Technische Universität München
TUM School of Computation, Information and Technology

GENE-3D simulations of plasma turbulence in stellarators

Felix Wilms

Vollständiger Abdruck der von der TUM School of Computation, Information and Technology der Technischen Universität München zur Erlangung eines Doktors der Naturwissenschaften (Dr. rer. nat.) genehmigten Dissertation.

Vorsitz: Prof. Dr.-Ing. Nils Thuerey

Prüfende der Dissertation:

1. Hon.-Prof. Dr. Frank Jenko
2. Prof. Dr. Eric Sonnendrücker

Die Dissertation wurde am 06.12.2023 bei der Technischen Universität München eingereicht und durch die TUM School of Computation, Information and Technology am 16.05.2024 angenommen.

Abstract

Magnetic confinement fusion could one day serve as a critical player in meeting humanity's energy demands in the future. The two most prominent approaches are the tokamak and stellarator concepts. One of the main challenges of these devices is the outflow of heat and particles within the fusion plasma due to turbulent fluctuations. Understanding and mitigating these losses is vital for designing a future power plant. The complex and nonlinear nature of plasma turbulence is largely studied via numerical simulations within the gyrokinetic framework. Although turbulence in the core of tokamak plasmas has been studied for decades, stellarator turbulence is understood far less. Due to the inherently three-dimensional magnetic field geometry, simulations have mainly been limited to small spatial domains, so-called flux-tubes, following a single magnetic field line once around the torus of the device.

This thesis aims at narrowing the knowledge gap. The GENE-3D code, the extension of the global gyrokinetic code GENE for stellarator geometries, has been improved to capture electromagnetic effects. Beyond the capability to simulate flux-tube domains, GENE-3D also allows for simulations of an entire torus surface at a time, so-called flux-surfaces, and even for radially global simulations up to the last closed flux-surface. The code upgrade allows studying global stellarator turbulence in the presence of a finite pressure gradient and enhances the numerical efficiency of (quasi-)electrostatic simulations using a kinetic electron model. A detailed discussion of the modifications to the physical model and the changes in the numerical schemes is provided, and verification studies in tokamak geometries against GENE are presented.

The new code version has been applied to study multiple topics linked to turbulence in the configurations of the Wendelstein 7-X stellarator. In the first step, it was shown that even moderate electromagnetic effects can significantly stabilise global ion temperature gradient (ITG) turbulence. Following that, the influence of nonlocal effects on ion temperature gradient turbulence, trapped electron mode (TEM) turbulence and hybrid scenarios of the two was studied by comparing transport predictions of flux-tube and full-flux-surface simulations. It was found that while flux-tube simulations can predict similar levels of transport as full-flux-surface simulations for some cases, there can be significant differences due to nonlocal effects in other cases. In a final step, radially global, full-flux-surface and flux-tube simulations of an experimental W7-X discharge were performed to show the existence of TEM turbulence in the form of ITG-TEM hybrids, primarily driven by the electron temperature gradient in the core of the plasma, which was hypothesised in the literature to be dominated solely by ITG on ion-scales. Furthermore, it was shown that electron temperature gradient (ETG) turbulence substantially contributes to the overall electron heat flux for the case under consideration.

Zusammenfassung

Kernfusion durch magnetischen Einschluss könnte eine entscheidende Rolle bei der Deckung des zukünftigen Energiebedarfs der Menschheit spielen. Die beiden bekanntesten Konzepte sind der Tokamak und der Stellarator. Eine der größten Herausforderungen dieser Anlagen ist der Verlust von Wärme und Teilchen aus dem Fusionsplasma aufgrund turbulenter Fluktuationen. Das Verständnis und die Reduzierung dieser Verluste sind von entscheidender Bedeutung für den Entwurf eines zukünftigen Kraftwerks. Die komplexe und nichtlineare Natur der Plasmaturbulenz wird weitgehend durch numerische Simulationen im Rahmen der Gyrokinetik untersucht. Während die Turbulenz im Kern von Tokamak-Plasmen seit Jahrzehnten untersucht wird, ist die Turbulenz in Stellaratoren weit weniger erforscht. Aufgrund der inhärenten dreidimensionalen Magnetfeldgeometrie beschränken sich die Simulationen hauptsächlich auf kleine räumliche Bereiche, so genannte Flussschläuche, die einer einzigen Magnetfeldlinie einmal um den Torus der Anlage folgen.

Die vorliegende Dissertation vertieft das theoretische Verständnis von Stellaratorturbulenz. Zu diesem Zweck wurde der Code GENE-3D, die Erweiterung des globalen gyrokinetischen Codes GENE für Stellaratorgeometrien, verbessert, um elektromagnetische Effekte miteinbeziehen zu können. Neben der Möglichkeit, Flussschläuche zu simulieren, erlaubt GENE-3D auch die Simulation ganzer Torusflächen, so genannter Flussflächen, und radial globale Simulationen bis hin zur letzten geschlossenen Flussfläche. Die Erweiterung des Codes ermöglicht nicht nur die Untersuchung globaler Stellaratorturbulenz bei endlichen Druckgradienten, sondern verbessert auch die numerische Effizienz von (quasi-)elektrostatischen Simulationen, welche ein kinetisches Elektronenmodell verwenden. Die Änderungen des physikalischen Modells und der numerischen Schemata werden ausführlich diskutiert und Verifikationsstudien gegen den GENE Code in Tokamakgeometrien vorgestellt.

Die neue Version des Codes wurde verwendet, um verschiedene Fragen bezüglich der Turbulenz in den Geometrien des Wendelstein 7-X Stellarators zu untersuchen. In einem ersten Schritt wurde gezeigt, dass selbst moderate elektromagnetische Effekte eine signifikante Stabilisierung auf globale, vom Ionentemperaturgradienten getriebene, Turbulenz (ITG) bewirken können.

Anschließend wurde der Einfluss nicht-lokaler Effekte auf Ionentemperaturgradiententurbulenz, Gefangene-Elektronen-Moden-Turbulenz (TEM) und hybride Szenarien der beiden untersucht, indem die Transportvorhersagen von Flussschlauch- und Flussflächensimulationen verglichen wurden. Es zeigte sich, dass Flussschlauchsimulationen zwar in einigen Fällen ähnliche Transportraten vorhersagen konnten wie Simulationen der gesamten Flussfläche, dass aber in anderen Fällen signifikante Unterschiede aufgrund nicht-lokaler Effekte auftreten können. In einem letzten Schritt wurden radial-globale Flussflächen- und Flussschlauchsimulationen einer experimentellen W7-X-Entladung durchgeführt. Entgegen Vorhersagen aus früherer Literatur, welche eine Dominanz von ITG-Turbulenz auf Ionenskalen postulier-

ten, wurde ein signifikanter Beitrag von TEM-Turbulenz zum Gesamtwärmestrom im Plasmakern in Form von ITG-TEM-Hybriden gezeigt, welche primär durch den Elektronentemperaturgradienten getrieben werden. Darüber hinaus wurde gezeigt, dass im betrachteten Fall die Elektronentemperaturgradienten-Turbulenz (ETG) einen wesentlichen Anteil am Gesamtwärmestrom der Elektronen im Plasmakern hat.

List of publications

First author

1. F. Wilms, G. Merlo, F. Sheffield, T. Görler, A. B. Navarro and F. Jenko, 'Implementation of magnetic compressional effects at arbitrary wavelength in the global version of GENE,' *Submitted to Computer Physics Communications*, 2023
2. F. Wilms, A. B. Navarro and F. Jenko, 'Full-flux-surface effects on electrostatic turbulence in Wendelstein 7-X-like plasmas,' *Nuclear Fusion*, 2023
3. F. Wilms, A. B. Navarro, G. Merlo, L. Leppin, T. Görler, T. Dannert, F. Hindenlang and F. Jenko, 'Global electromagnetic turbulence simulations of W7-X-like plasmas with GENE-3D,' *Journal of Plasma Physics*, 2021

Co-author

1. A. B. Navarro, G. Roberg-Clark, G. Plunk, D. Fernando, A. Di Siena, F. Wilms and F. Jenko, 'Assessing global ion thermal confinement in critical-gradient-optimized stellarators,' *arXiv preprint arXiv:2310.18705, submitted to Nuclear Fusion*, 2023
2. A. B. Navarro, A. Di Siena, J. Velasco, F. Wilms, G. Merlo, T. Windisch, L. LoDestro, J. Parker and F. Jenko, 'First-principles based plasma profile predictions for optimized stellarators,' *Nuclear Fusion*, 2023
3. E. Sanchez, A. B. Navarro, F. Wilms, M. Borchardt, R. Kleiber and F. Jenko, 'Instabilities and turbulence in stellarators from the perspective of global codes,' *Nuclear Fusion*, 2022
4. S. Hansen, M. Porkolab, J. Bähner, Z. Huang, A. von Stechow, O. Grulke, E. Edlund, F. Wilms, A. B. Navarro, F. Jenko et al., 'Development of a synthetic phase contrast imaging diagnostic for turbulence studies at Wendelstein 7-X,' *Plasma Physics and Controlled Fusion*, 2022
5. A. B. Navarro, G. Merlo, G. Plunk, P. Xanthopoulos, A. von Stechow, A. Di Siena, M. Maurer, F. Hindenlang, F. Wilms and F. Jenko, 'Global gyrokinetic simulations of ITG turbulence in the magnetic configuration space of the Wendelstein 7-X stellarator,' *Plasma Physics and Controlled Fusion*, 2020
6. J. A. Alcusón, P. Xanthopoulos, G. Plunk, P. Helander, F. Wilms, Y. Turkin, A. von Stechow and O. Grulke, 'Suppression of electrostatic micro-instabilities in maximum-J stellarators,' *Plasma Physics and Controlled Fusion*, 2020

Conference contributions

1. F. Wilms, A. B. Navarro and F. Jenko, 'Full-flux-surface effects on maximum-J stabilisation in Wendelstein 7-X,' *DPG-Frühjahrstagung (Oral)*, 2023

2. F. Wilms, A. B. Navarro and F. Jenko, 'Full-flux-surface effects on maximum-J stabilisation in Wendelstein 7-X,' *23rd International Stellarator and Heliotron Workshop (ISHW 2022) (Poster)*, 2022

3. F. Wilms, A. B. Navarro and F. Jenko, 'Turbulence in stellarators with GENE-3D,' *DPG-Frühjahrstagung (Poster)*, 2022

4. F. Wilms, A. B. Navarro, G. Merlo, L. Leppin, T. Görler, T. Dannert, F. Hindenlang and F. Jenko, 'Extension of GENE-3D to a global electromagnetic turbulence code for stellarators,' *DPG-Tagung der Sektion Materie und Kosmos (SMuK) (Poster)*, 2021

5. F. Wilms, A. B. Navarro, G. Merlo, L. Leppin, T. Görler, T. Dannert, F. Hindenlang and F. Jenko, 'Nonlinear global gyrokinetic stellarator simulations of GENE-3D with kinetic electrons,' *47th EPS Conference on Plasma Physics (Poster)*, 2021

Contents

Chapter 1

Introduction

1.1 Nuclear fusion as energy source

The continuous population growth and the tight link between societal advancement and energy consumption have put humanity in front of a global challenge. On the one hand, it is predicted that primary energy consumption will at least double during this century [1], requiring a drastic increase in its production worldwide. On the other hand, humanity must eliminate greenhouse gas emissions to mitigate the effects of climate change, thus having to move away from burning fossil fuels. In addition to renewable sources such as solar or wind power, using nuclear reactors poses a suitable way to meet current and future energy needs since their spatial energy density exceeds that of nonfossil-based power plants by more than one order of magnitude [2]. This can be done either in the form of nuclear fission or fusion. Fission reactions have been employed as an energy source since the 1950s [3], in which a heavy, radioactive nucleus is split by neutron bombardment into several fission products whose total mass is slightly lower than that of the reactants. The mass deficit Δm is transformed into energy ΔE, according to Einstein's famous formula

$$\Delta E = \Delta m c^2, \tag{1.1.1}$$

with c being the speed of light. Although nuclear fission is an established technology at this date, its future use is debated strongly, mainly due to safety concerns in cases of accidents within the reactor and the production of radioactive waste with half-life times on the order of 1000 to 10,000 years. The second type of nuclear reaction is the mechanism that powers the stars: fusion. In this process, two light nuclei fuse into a single nucleus, slightly lighter than the sum of the initial masses. Like in fission reactions, the mass deficit is converted into harnessable energy. The proton-proton chain, fuelling the Sun, requires protons to decay into neutrons and neutrinos via the weak nuclear force [4], which has a reaction cross-section that is too low for efficient use of this reaction chain as a terrestrial energy source.

The most promising reaction type to this date is that of deuterium and tritium, two heavy isotopes of hydrogen:

$$^2_1\mathrm{D} +^3_1 \mathrm{T} \rightarrow^4_2 \mathrm{He} +^1_0 \mathrm{n} + 17.6\,\mathrm{MeV}. \tag{1.1.2}$$

In this reaction, deuterium and tritium fuse into a helium nucleus and a neutron, where the latter carries approximately 80% of the 17.6 MeV released in the form of kinetic energy.

Ocean water contains approximately 0.015 mole% of deuterium [5] (1 deuterium atom per

6700 hydrogen atoms), thus being an abundant partial fuel source. On the other hand, the short-lived radioactive tritium must be synthesised in the laboratory. This can be achieved by neutron activation of lithium-6, a rare isotope of lithium:

$$^6_3\mathrm{Li} + ^1_0\mathrm{n} \rightarrow ^4_2\mathrm{He} + ^3_1\mathrm{T} + 4.8\,\mathrm{MeV}. \tag{1.1.3}$$

Lithium, in general, is largely found in the earth's crust and seawater.

Let us put the benefits of fusion energy into context. There are approximately 9.98×10^{21} atoms of deuterium in one litre of seawater and 6.59×10^{21} $^6_3$Li-atoms in one gram of lithium. Assuming a conversion efficiency of 33% from fusion energy to electricity, a typical value of steam turbines, it is straightforward to show that it only takes approximately 8.5 litres of seawater and 12.8 grams of lithium to match the yearly energy needs of an average German household [6]. Although this simplified scenario does not consider losses such as energy requirements for tritium breeding or efficiency losses through engineering constraints, nuclear fusion seems to provide an energy source with seemingly limitless amounts of fuel. In addition, fusion reactions do not produce any greenhouse gases such as CO_2 like the combustion of fossil materials. Fusion power plants would be inherently safer than those running on fission, as their reactions immediately cease in case of any disturbance such as a shutdown or damaging of the reactor [7]. Finally, the reactions themselves do not produce any long-lived radioactive materials. Only the fast neutrons will activate the reactor wall. In contrast to fission power plants, choosing materials that exhibit favourable activation properties is possible. As a result, most activated components are expected to possess relatively short half-lives, allowing for their recycling within less than 100 years of secure storage.

Whether a net energy production is achieved through fusion mainly depends on three parameters. The first one is the temperature, as the positively charged nuclei need sufficient kinetic energy to overcome the Coulomb repulsion and come close enough for the attractive strong nuclear force to induce the fusion reaction. Even though the quantum tunnelling effect lowers the classically required kinetic energy substantially, future reactors will still have to reach energies in the range of approximately 10 to 20 keV for a sufficient fusion rate, corresponding to temperatures between 100 and 200 million Kelvin [8]. At these temperatures, any type of matter is completely ionised and is in the plasma state. The second parameter is the plasma density. A higher density increases the frequency of the nuclei colliding with each other, raising the rate of fusion reactions per unit time. The third one is the so-called confinement time τ_E, which is a measure of how long the plasma can sustain conditions suitable for fusion reactions to occur. Through energy balance, one arrives at the so-called Lawson criterion [9], which states that, under simplified assumptions, the triple product between the three needs to exceed a value of

$$nT\tau_\mathrm{E} > 3 \times 10^{21}\,\frac{\mathrm{keV\,s}}{\mathrm{m}^3} \tag{1.1.4}$$

in order to obtain a net energy gain. Currently, two main approaches are being pursued to meet this constraint. The first one is that of inertial confinement fusion, in which lasers or ion beams are used to compress a fuel pellet to densities of $n \sim 10^{30}\,\mathrm{m}^{-3}$ and sustain this state for a short time $\tau_\mathrm{E} \sim 10^{-9}\,\mathrm{s}$. The alternative is magnetic confinement fusion, in which the plasma is kept at low densities $n \sim 10^{20}\,\mathrm{m}^{-3}$ for a much longer time $\tau_\mathrm{E} \sim 1\,\mathrm{s}$. The following section will discuss the basic ideas behind magnetic confinement fusion.

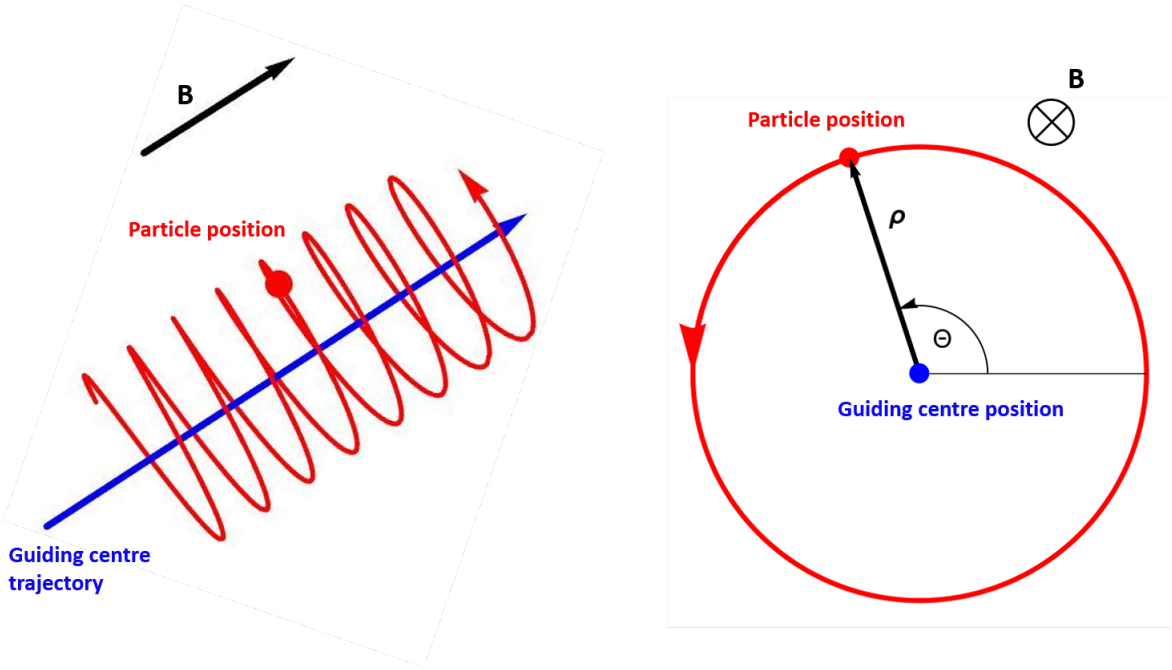

Figure 1.1: Sketch of Larmor motion of a positively charged particle in a uniform magnetic field (left), along with projection perpendicular to the magnetic field lines (right).

1.2 Magnetic confinement fusion: tokamaks and stellarators

In magnetic confinement fusion, a low-density gas of deuterium-tritium fuel is heated to approximately 100-200 million Kelvin, at which the gas becomes a plasma. Confining this state on the timescale of seconds is impossible using material walls since a plasma at such high temperatures would melt or corrode any material known to this day. Instead, it makes use of the fact that the plasma consists of charged particles, whose motion can be manipulated through a magnetic field $\mathbf{B} = B_0\mathbf{b}$ via the Lorentz force

$$\mathbf{F}_\mathrm{L} = \frac{q}{c}\mathbf{v} \times \mathbf{B}, \tag{1.2.1}$$

where q is the charge of a particle with mass m and velocity $\mathbf{v}$, and c is the speed of light.

Solving Newton's equations of motion, it is easy to show that a charged particle in a straight and uniform magnetic field will undergo a circular motion perpendicular to the magnetic field lines. In contrast, it can move freely parallel to them. This is exemplified in figure 1.1, where we have introduced the Larmor radius $\rho = v_\perp/\Omega$ with the Larmor frequency $\Omega = qB_0/(mc)$ and the particle velocity $v_\perp$ perpendicular to the magnetic field lines. A simple approach is bending the magnetic field to close on itself so that the particles can move in a toroidal orbit indefinitely. However, this results in an inhomogeneous magnetic field, causing additional outward drifts that ultimately terminate plasma confinement. The solution is incorporating a poloidal component into the purely toroidal magnetic field. This addition generates helical field lines that eliminate the average perpendicular drift over a complete orbit along the magnetic field, stabilising the plasma.

The first way to add a poloidal magnetic field is to use the transformer principle and drive

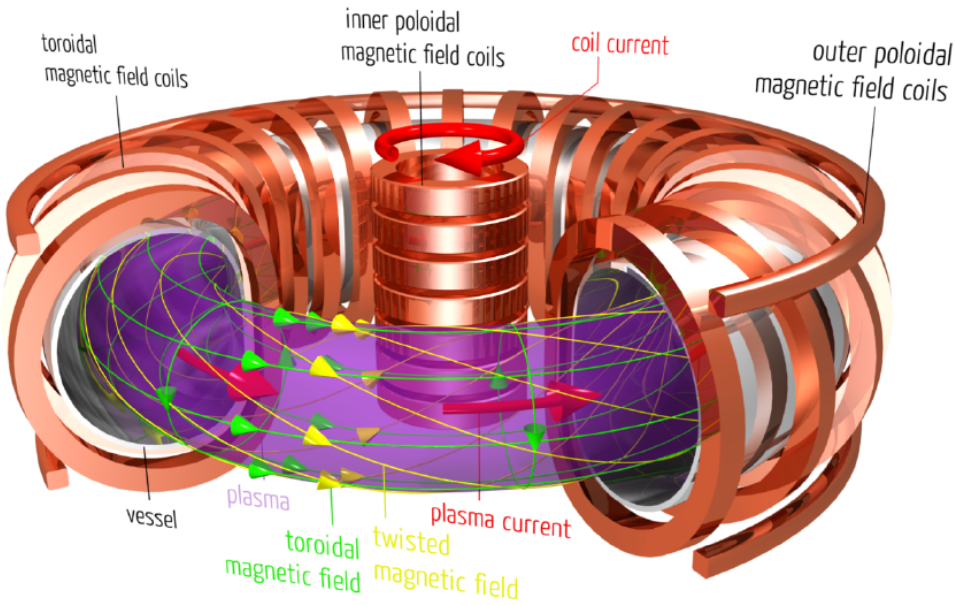

Figure 1.2: Schematic illustration of the tokamak principle. Source: IPP

a toroidal current in the plasma. For this, a solenoidal coil is placed in the centre of the plasma ring as the primary drive, using the plasma itself as the secondary coil. This approach is usually referred to as the 'tokamak' principle, following a Russian acronym for 'toroidal chamber with magnetic field coils'. Figure 1.2 shows a schematic picture of a tokamak. Although it is the most advanced magnetic confinement concept to date, tokamaks have several drawbacks. The transformer principle only allows for pulsed operation unless advanced current driving mechanisms, which are still being developed, are employed. Furthermore, tokamaks possess an intrinsic upper bound on the achievable plasma density known as the Greenwald limit [10], consequently limiting the triple product $nT\tau_{\mathrm{E}}$. The most prominent disadvantage of driving a plasma current is the possibility of various types of magnetohydrodynamic (MHD) instabilities, which can ultimately lead to a disruption of the plasma [11], in which the massive amount of energy stored in the plasma is released, potentially causing detrimental damage to the vessel wall.

All of these problems can be avoided if the poloidal magnetic field is not induced via a plasma current but via the magnetic field coils themselves. This is the basic principle of stellarators, of which a schematic picture is shown in figure 1.3. This comes at the expense of the magnetic field having an inherently three-dimensional structure, in contrast to the axisymmetric tokamak, with complex requirements for the coil design. The additional spatial variation, however, opens up the possibility of shaping the plasma substantially more than in tokamaks, opening up the potential for optimising plasma parameters.

1.3 Transport in magnetically confined fusion plasmas

Regardless of which type of magnetic field geometry is chosen, one of the key issues limiting current-day fusion experiments from reaching a net energy gain is the radial transport of

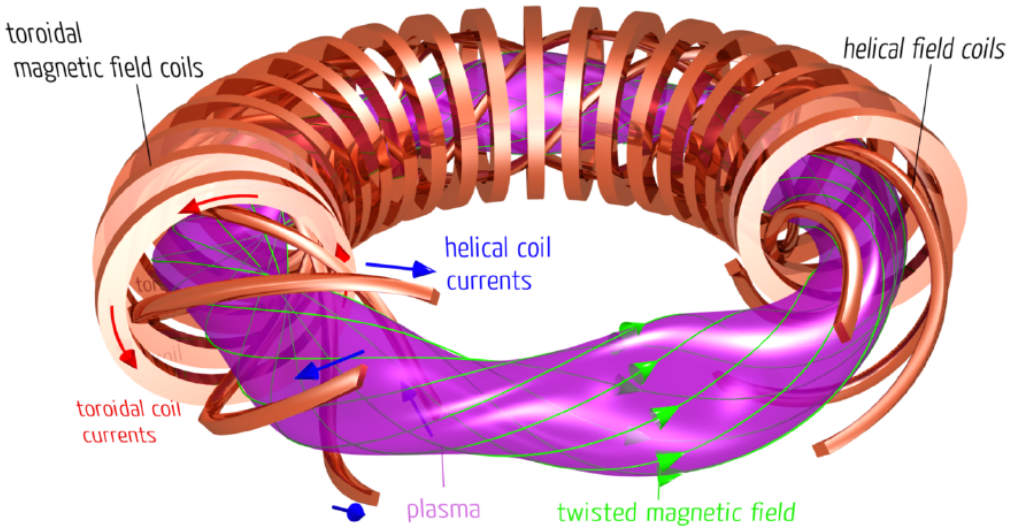

Figure 1.3: Schematic illustration of the stellarator principle. Source: IPP

particles and energy. This transport usually leads to severe reductions in the plasma confinement time and an overall degradation of the machine's fusion performance. Oftentimes, one considers transport to be mainly diffusive, so that Fick's law

$$\begin{aligned} \Gamma &= -D\nabla n \\ \chi &= -n\chi\nabla T \end{aligned} \tag{1.3.1}$$

is used to link the plasma density and temperature n and T to the particle and heat fluxes Γ and χ using the diffusion coefficients D, $\chi \sim a^2/\tau_\mathrm{E}$, where the (effective) minor radius a of the fusion device is often used as a characteristic lengthscale.

One usually distinguishes between three main types of transport based on its origin. The first one is the so-called 'classical' transport, which is caused by particles colliding with each other while moving along the magnetic field lines. Using a simple random-walk model

$$D_\mathrm{class} = \frac{\Delta x^2}{\Delta t}, \tag{1.3.2}$$

with $\Delta x \sim \rho$ being the distance a particle travels within a time step $\Delta t \sim 1/\nu_\mathrm{c}$ on the timescale of the Coulomb collision frequency ν_c, one finds $D_\mathrm{class} \sim 10^{-3}\,\mathrm{m}^2/\mathrm{s}$ for reactor-relevant conditions, which is far from the values $\sim 1\,\mathrm{m}^2/\mathrm{s}$ measured in today's experiments.

As mentioned before, the toroidal geometry in magnetic confinement devices induces additional drifts, which can cause radial fluxes. This type of transport caused by the toroidal magnetic geometry is usually referred to as 'neoclassical' transport and has been described extensively in [12]. While the magnetic field was originally designed to be twisted such that the averaged drift for particles that traverse the entire surface vanishes, this is only true for particles that are free to traverse around the entire device, referred to as passing particles.

There is a different class of particles, so-called trapped particles, whose averaged drift does not vanish and thus must be considered carefully. To understand their origin, consider a magnetic field whose strength varies periodically along the field lines, the direction which we label as z, according to

$$B(z) = \frac{1}{2}\left[(B_{\max} + B_{\min}) + (B_{\max} - B_{\min})\cos(z + \pi)\right]. \tag{1.3.3}$$

Due to the conservation of the kinetic energy $\mathcal{E} = m[v_{||}^2(z) + v_{\perp}^2(z)]/2$ and the magnetic moment $\mu = mv_{\perp}^2(z)/(2B(z))$, only particles with

$$\frac{v_{||}^2(0)}{v_{\perp}^2(0)} > 1 - \frac{B_{\min}}{B_{\max}} \tag{1.3.4}$$

can move along freely along the entire field. The others will bounce back and forth between points of equal magnetic field strength and are thus trapped along a field line. Collisional effects also influence this process due to the exchange of kinetic energy between particles. Neoclassical theory is, therefore, primarily driven by the plasma's collisionality and the details of the magnetic field geometry confining it.

Stellarators have been trailing behind tokamaks for a long time as a potentially viable concept for a future fusion reactor, as it has been shown that the lack of axisymmetry can induce significant amounts of neoclassical transport in comparison with tokamaks [12, 13], imposing a substantial limit on the overall performance of the device. However, the absence of axisymmetry allows far greater potential for shaping the magnetic field enclosing the plasma, giving rise to several decades of research on stellarator optimisation. These endeavours culminated in the design of the Wendelstein 7-X (W7-X) stellarator, whose construction in Greifswald, Germany, finished in 2015. The magnetic field is generated by 50 coils, divided into five identical modules, with an additional 20 planar coils for greater flexibility in shaping the magnetic field. The effective minor and major radii are $a = 0.55\,\mathrm{m}$ and $R_0 = 5.5\,\mathrm{m}$, respectively and is thus the largest stellarator built to this day. Besides other optimisation criteria, which are summarised in [14], it was shown in [15] that this machine is able to reduce neoclassical losses to the levels of tokamaks.

Even under these conditions, the diffusivities measured experimentally in either tokamak or stellarator can still be larger by one to two orders of magnitude than what is predicted by classical and neoclassical theory. The remaining transport is therefore categorised as 'anomalous', and it is widely accepted nowadays that it is caused by plasma turbulence. This type of turbulence is usually caused by so-called 'microinstabilities' with characteristic lengthscales perpendicular to the magnetic field comparable to the electron or ion Larmor radius. These instabilities usually arise due to density and temperature fluctuations δn and δT, which can cause electrostatic or electromagnetic fluctuations $\delta\phi$ and δA due to charge separation. The latter create additional drifts, which in turn can strengthen the initial perturbation if both are sufficiently out of phase with each other. The resulting instabilities can then form turbulent transport of particles and energy due to nonlinear interaction with the plasma.

1.4 Scope and outline of the thesis

In this section, we briefly introduce some of the theoretical studies on plasma turbulence within the core of Wendelstein 7-X. The overview is by no means complete but instead focuses on the topics relevant to this thesis.

With neoclassical losses substantially reduced, it was shown experimentally in [16] that plasma turbulence is the primary driver of heat and particle transport in the core of Wendelstein 7-X. As mentioned in the previous section, turbulence is caused by the nonlinear interaction of the plasma with different types of microinstabilities. The most prominent types of instabilities relevant to W7-X plasmas so far are the ion temperature gradient mode (ITG), electron temperature gradient mode (ETG) and trapped electron mode (TEM). Electromagnetic instabilities such as kinetic ballooning modes (KBM) might become relevant in highly electromagnetic regimes of future experiments [17]. Although a simplified picture of their linear excitation is given in [18], the complex magnetic geometries of stellarators, as well as the chaotic nonlinear interaction between plasma and instabilities, makes quantitative studies only possible in the context of numerical simulations based on so-called gyrokinetic theory.

Although studies of ETG turbulence in stellarators date back as early as 2002 [19], its impact on transport processes in Wendelstein 7-X is still debated today, with [20] arguing on the one hand that it should be negligible for W7-X but [21] concluding on the other hand that it could be the main contributor to the anomalous electron heat transport in the core of some experimental discharges.

In contrast, there have been extensive studies on turbulence driven by ITG and TEM. It was argued [22–24] that TEM turbulence should be relatively weak in W7-X due to most of the trapped electrons residing in regions of positive average magnetic field curvature, something referred to as the 'maximum-J' property. In the absence of TEMs, the so-called ion-driven trapped electron mode (iTEM) is supposed to emerge [25], having the characteristic structure of TEMs but propagating in the ion diamagnetic direction and using the bulk ions as a source of free energy. However, it was argued that iTEMs should contribute little to nonlinear transport compared to their 'classical' counterpart since they usually appear at smaller lengthscales. It is worth mentioning, however, that many, though not all, of those studies consider TEMs to be driven primarily by a finite density gradient and not by a finite electron temperature gradient.

As a result, the most significant contributor to turbulence in the core of W7-X was hypothesised to be ITG, with TEMs only expected to be found in the edge region, if at all [16, 26]. It was argued in [24] that equal density and temperature gradients lead to a regime of suppressed plasma turbulence referred to as a 'stability valley'. This situation could potentially be achieved in high-density scenarios. Consequently, the suppression of ITG turbulence was considered to explain record-high plasma performance [27] in W7-X during high-performance discharge, where pellet injection was used as a fuelling method.

Most of the theories mentioned above were derived based on gyrokinetic simulations that rely on some approximation. The most common one was using a flux-tube domain, mainly due to computational cost. Although flux-tube simulations mainly follow the general trends seen in the experiment, it is not clear that effects beyond their capabilities might not have a significant impact. In particular, since stellarators do not generally exhibit toroidal symmetry, it is not apparent which field line or field lines to choose to accurately characterise the mechanisms one is interested in.

This uncertainty facilitated the development of stellarator codes that can go beyond the

flux-tube domain. With the flux-surface version of the GENE code [28] providing some form of an interim solution, GENE-3D has been developed as the first code in the world to be able to simulate nonlinear stellarator turbulence in a global domain [29, 30], shortly followed by several other codes [31–33]. Using some of the world's most powerful supercomputers, these codes have helped advance the understanding of ITG transport mechanisms. However, all simulations have relied on the assumption of an adiabatic electron model up to this point, which has put the studies of trapped electron physics, one of the supposed key mechanisms in pellet scenarios, and the study of electromagnetic turbulence out of reach. With the improvements of GENE-3D performed throughout this project, it was possible to simulate global, electromagnetic stellarator turbulence with realistic electrons for the first time [34]. Besides the possibility of studying electromagnetic turbulence, the code was also capable of simulating electrostatic turbulence with significantly decreased cost, as stated in chapter 3, allowing us to test the validity of several of the above claims beyond the flux-tube limit. In particular, we test the impact of electromagnetic effects on global ITG turbulence in Wendelstein 7-X, showing a stabilising effect even when said effects are moderate. We furthermore show that a finite density gradient indeed also stabilises ITG turbulence in full-flux-surface simulations but find that the interplay between ITG and TEM turbulence proposed to explain the high performance in [23] is heavily affected by the presence of a finite electron temperature gradient. We also show that while heat flux predictions of flux-tube simulations agree quantitatively well with those considering an entire flux-surface in some cases, substantial disagreement between the two is found in other scenarios. Finally, we challenge the claims of weak TEM and ETG turbulence in the core of Wendelstein 7-X based on flux-tube, full-flux-surface and radially global simulations of one of its experimental discharges. We find that both types of turbulence are necessary to explain the experimentally measured electron heat fluxes. We find that TEMs appear hybrid with ITG turbulence and are primarily driven by the electron temperature gradient, a drive mechanism that has received far less attention in the literature than those driven by density gradients.

The rest of this thesis is structured as follows. In chapter 2, the fundamentals of gyrokinetic theory will be discussed, and the equations used by GENE-3D will be derived. Chapter 3 outlines the numerical algorithm used by GENE-3D. The description includes several new features added throughout this project, such as considering electromagnetic effects and using staggered-grid finite-difference schemes to discretise the field equations and electromagnetic verification studies against the global tokamak version of the GENE code. In chapter 4, global simulations in stellarator geometry are described to study the influence of electromagnetic effects on ITG turbulence. Chapter 5 describes studies on the interplay between ITG and TEM turbulence in stellarator geometries and the influence of a constant equilibrium electric field. For this, flux-tube as well as full-flux-surface simulations were performed, and their predictive capabilities were compared with each other. Chapter 6 analyses the turbulence characteristics of an experimental discharge of Wendelstein 7-X using radially global, full-flux-surface and flux-tube simulations. Finally, the results are summarised in chapter 7 and an outlook for future projects is given.

Chapter 2

Modern derivation of gyrokinetics

The description of the plasma dynamics via the individual particles' behaviour is unsuitable for fusion applications, as a particle density of the order of $10^{19}\,\mathrm{m}^{-3}$ puts such an approach out of reach computationally for any meaningful scenario. Instead, it proves to be advantageous to consider the bulk behaviour of the plasma via means of statistical physics. For this, each particle species σ, like ions, electrons, or others, is characterised by a distribution function $f_\sigma(\mathbf{x}, \mathbf{v}, t)$, being defined as the number of particles per unit volume in an infinitesimal hypervolume centred around the phase-space coordinate $(\mathbf{x}, \mathbf{v})$ at time t in the presence of self-consistently calculated electromagnetic fields. Conservation of particles then dictates that the total time derivative of f_σ has to vanish, giving rise to the so-called Vlasov equation [35]

$$\frac{df_\sigma}{dt} = \frac{\partial f_\sigma}{\partial t} + \dot{\mathbf{x}}_\sigma \cdot \nabla_{\mathbf{x}} f_\sigma + \dot{\mathbf{v}}_\sigma \cdot \nabla_{\mathbf{v}} f_\sigma = 0, \tag{2.0.1}$$

where $\dot{\mathbf{x}}_\sigma$ and $\dot{\mathbf{v}}_\sigma$ are the single-particle characteristics of species σ in $\mathbf{x}$- and $\mathbf{v}$-space. If one considers only electromagnetic forces acting on the particles, equation (2.0.1) can be shown to have the form

$$\frac{\partial f_\sigma}{\partial t} + \mathbf{v} \cdot \nabla_{\mathbf{x}} f_\sigma + \frac{q_\sigma}{m_\sigma} \left(\mathbf{E}(\mathbf{x}, t) + \frac{1}{c} \mathbf{v} \times \mathbf{B}(\mathbf{x}, t) \right) \cdot \nabla_{\mathbf{v}} f_\sigma = 0 \tag{2.0.2}$$

in the non-relativistic limit. This equation has to be coupled with Maxwell's equations

$$\begin{aligned} \nabla \cdot \mathbf{E} &= 4\pi \sum_\sigma \rho_\sigma \qquad & \nabla \cdot \mathbf{B} &= 0 \\ \nabla \times \mathbf{E} &= -\frac{1}{c} \frac{\partial \mathbf{B}}{\partial t} \qquad & \nabla \times \mathbf{B} &= \frac{4\pi}{c} \sum_\sigma \mathbf{j}_\sigma, \end{aligned} \tag{2.0.3}$$

where the displacement current $(1/c)(\partial \mathbf{E}/\partial t)$ has been neglected. The charge and current densities ρ_σ and $\mathbf{j}_\sigma$ are defined in terms of the distribution function as

$$\rho_\sigma(\mathbf{x}, t) = q_\sigma \int f_\sigma(\mathbf{x}, \mathbf{v}, t)\, d^3v \qquad \text{and} \qquad \mathbf{j}_\sigma = q_\sigma \int f_\sigma(\mathbf{x}, \mathbf{v}, t)\, \mathbf{v}\, d^3v. \tag{2.0.4}$$

Although providing an accurate description of any non-relativistic plasma, the kinetic equation (2.0.2) coupled with equations (2.0.3) and (2.0.4) does not provide a suitable tool in order to investigate the bulk behaviour of fusion plasmas, in particular of plasma turbulence,

either. The reason is that, especially in a fusion device, the plasma inherits a great variety of phenomena acting over a broad spectrum of length- and timescales. The spatial variations range from the size of the minor radius of a fusion device, on the order of a metre, down to the electron Larmor radius, typically 1-10 micrometres. The temporal variations range from the confinement timescales on the order of a second down to the electron Larmor frequency on the order of 10^{-10} seconds. Resolving five orders of magnitude in space and ten orders in time is out of reach for even the most powerful supercomputers to this date for any fusion-relevant application.

In order to overcome this issue, one has to find a theoretical framework in which the Larmor motion of the particles is eliminated through appropriate averaging procedures so that one does not consider the motion of the plasma particles themselves but rather the motion of their centres of rotation. This framework is largely known as gyrokinetic theory. Frieman and Chen did the original derivation of the system of nonlinear equations [36] using perturbation techniques, followed by numerous derivations using alternative approaches, such as variational methods. This chapter will provide a derivation largely based on the references [37–40].

In the following, we will introduce the underlying assumptions of gyrokinetic theory in section 2.1, followed by the derivation of the gyrokinetic Lagrangian describing the particle motion in an electromagnetic field in section 2.2. We will couple the single-particle dynamics to the Lagrangian of the dynamics of the electromagnetic fields induced by the plasma in section 2.3, from which we will then derive the equations of motion in section 2.4, which is necessary to establish the gyrokinetic equation describing the bulk behaviour of the plasma in section 2.5. Since the plasma is not only affected by electromagnetic fields but also creates them itself, one has to couple the gyrokinetic equation self-consistently with a system of equations determining the electric and magnetic potentials, which are derived in section 2.6. Finally, section 2.7 will discuss the approximations of the gyrokinetic model specific to the GENE-3D code, which will be the primary numerical tool used in this thesis and which will be introduced in detail in chapter 3.

2.1 Gyrokinetic ordering

The theoretical study of plasma turbulence in fusion devices mainly deals with phenomena that act on gyrokinetic length- and timescales. In order to understand what this entails in detail, we introduce the ordering parameter

$$\epsilon_{\mathrm{B}} = \frac{\rho_{\mathrm{s}}}{L_{\mathrm{ref}}} = \rho_s^* \ll 1, \tag{2.1.1}$$

where ρ_{s} usually refers to the thermal sound radius of the bulk ions. Assuming this parameter is small is equivalent to assuming that the plasma is strongly magnetised, as the deviation of a particle orbit from the magnetic field line is small compared with the reference lengthscale.

We will further split all quantities of interest $Q(\mathbf{x}, \mathbf{v}, t)$ into a stationary background $Q_0(\mathbf{x}, \mathbf{v})$ and a fluctuating perturbation $Q_1(\mathbf{x}, \mathbf{v}, t)$ with

$$\frac{Q_1}{Q_0} \sim \epsilon_\delta. \tag{2.1.2}$$

Although in the edge and scrape-off layer regions of a plasma fluctuations can reach levels of

$\epsilon_\delta \sim \mathcal{O}(1)$, it is usually well-justified to assume that $\epsilon_\delta \sim \epsilon_\mathrm{B} \ll 1$ when dealing with physics in the plasma core. However, turbulent fluctuations turn out to be highly anisotropic in space, as the Lorentz force causes the fluctuation wavelengths $k_\perp$ perpendicular to the magnetic field to be around 10 to 100 gyroradii, whereas, in the parallel direction, the associated wavelengths $k_{||}$ can extend up to several meters. In contrast, the background quantities are always assumed to vary on the equilibrium spatial scale L_ref. These statements can be turned into the ordering assumptions

$$\begin{aligned} &\rho_\mathrm{s}\nabla_\perp \ln(Q_1) \sim k_\perp \rho_\mathrm{s} \equiv \epsilon_\perp, \\ &\rho_\mathrm{s}\nabla_{||} \ln(Q_1) \sim k_{||} \sim \epsilon_B k_\perp \rho_\mathrm{s} = \epsilon_B \epsilon_\perp, \\ &\rho_\mathrm{s}\nabla \ln(Q_0) \sim \epsilon_B k_\perp \rho_\mathrm{s} = \epsilon_B \epsilon_\perp. \end{aligned} \tag{2.1.3}$$

The parameter $\epsilon_\perp$ helps distinguish between theories dealing with various kinds of plasma behaviour. In what is known as gyrokinetic theory, one assumes $\epsilon_\perp \sim \mathcal{O}(1)$. In contrast, driftkinetic theory, the fundamental theory used to describe neoclassical transport phenomena, assumes $\epsilon_\perp \ll 1$. Furthermore, one can also consider the so-called 'long-wavelength' approximation of gyrokinetic theory, in which only terms up to $\mathcal{O}(\epsilon_\perp^2)$ are retained.

As we wish to eliminate the rapid particle gyration around the magnetic field lines from our description of the plasma, we have to specify that we are only interested in phenomena that are in the range of a characteristic temporal frequency $\omega \sim v_\mathrm{th}/L_\mathrm{ref}$ with $\epsilon_\omega \equiv \omega/\Omega \sim \epsilon_\mathrm{B} \ll 1$.

2.2 Derivation of the gyrokinetic Lagrangian

2.2.1 Zeroth-order description

We start from the Lagrangian of a point particle with mass m and charge q, influenced by the electrostatic and electromagnetic potentials ϕ and $\mathbf{A}$, which is given by [41]

$$L(\mathbf{x}, \mathbf{v}, \dot{\mathbf{x}}, t) = \left(m\mathbf{v} + \frac{q}{c}\mathbf{A}(\mathbf{x}, t)\right) \cdot \dot{\mathbf{x}} - H(\mathbf{x}, \mathbf{v}, t), \tag{2.2.1}$$

where the Hamiltonian H is given by

$$H(\mathbf{x}, \mathbf{v}, t) = \frac{m}{2}v^2 + q\phi(\mathbf{x}, t). \tag{2.2.2}$$

In order to proceed, it is useful to introduce the Lagrangian one-form γ, which is defined via its relation to the Lagrangian as

$$\int L\, dt = \int \gamma,$$

which means it is given by

$$\gamma = \left(m\mathbf{v} + \frac{q}{c}\mathbf{A}(\mathbf{x}, t)\right) \cdot d\mathbf{x} - H(\mathbf{x}, \mathbf{v}, t)dt. \tag{2.2.3}$$

As was mentioned in the introduction, it is beneficial to transform the system into guiding

centre coordinates

$$\begin{aligned}
&\mathbf{X} = \mathbf{x} - \frac{mc}{qB_0(\mathbf{x})}\mathbf{b}(\mathbf{x}) \times \mathbf{v}, \quad \mu = \frac{mv_\perp^2}{2B_0(\mathbf{x})}, \quad v_{||} = \mathbf{v} \cdot \mathbf{b}(\mathbf{x}) \\
&\mathbf{x} = \mathbf{X} + \rho(\mathbf{X})\mathbf{a}(\Theta), \quad \mathbf{v} = v_{||}\mathbf{b} + v_\perp \mathbf{c}(\Theta), \quad \text{with } v_\perp = \sqrt{\frac{2\mu B_0(\mathbf{x})}{m}} \\
&\mathbf{a}(\Theta) = \mathbf{e}_1 \cos(\Theta) - \mathbf{e}_2 \sin(\Theta), \quad \mathbf{c}(\Theta) = \frac{\partial \mathbf{a}}{\partial \Theta} = -\mathbf{e}_1 \sin(\Theta) - \mathbf{e}_2 \cos(\Theta),
\end{aligned} \tag{2.2.4}$$

with $\mathbf{B}_0 = B_0\mathbf{b} = \nabla \times \mathbf{A}$.

In general the transformation of the one-form γ with the coordinate system (z^ν) into the one-form Γ with coordinate system (Z^μ) is done using

$$\Gamma_\mu = \gamma_\nu \frac{dz^\nu}{dZ^\mu}. \tag{2.2.5}$$

We identify

$$z^0 = t,\ z^1 = x,\ z^2 = y,\ z^3 = z,\ z^4 = v_x,\ z^5 = v_y,\ z^6 = v_z \tag{2.2.6}$$

and

$$Z^0 = t,\ Z^1 = X,\ Z^2 = Y,\ Z^3 = Z,\ Z^4 = v_{||},\ Z^5 = \mu,\ Z^6 = \Theta. \tag{2.2.7}$$

Notice that $\gamma_{\mathbf{v}} = 0$. Since the time coordinate t is not transformed, we have

$$\Gamma_t = \gamma_t = -H(\mathbf{X}, v_{||}, \mu) = -\left(\frac{mv_{||}^2}{2} + \mu B_0(\mathbf{X}) + q\phi(\mathbf{X})\right). \tag{2.2.8}$$

The spatial component of the one-form transforms as

$$\Gamma_i = \left(mv_{||}b_j + mv_\perp c_j(\Theta) + \frac{q}{c}A_j(\mathbf{X} + \rho(\mathbf{X})\mathbf{a}(\Theta))\right)\frac{dx^j}{dX^i}. \tag{2.2.9}$$

We can see that the last term in the bracket is much larger than the first two since

$$\frac{qA}{cmv_{||}} \sim \frac{q}{mc}\frac{B_0 L_{\text{ref}}}{v_{\text{th}}} \sim \frac{\Omega}{\omega} \gg 1, \tag{2.2.10}$$

so that we have to retain the first-order expansion in ρ of the term involving the vector potential. Expanding the vector potential for small gyroradii and evaluating the derivative,

we get

$$\begin{aligned}
\Gamma_i &= \left(mv_{||}b_j + mv_\perp c_j(\Theta) + \frac{q}{c}A_j(\mathbf{X}+\rho(\mathbf{X})\mathbf{a}(\Theta))\right)\frac{dx^j}{dX^i} \\
&\approx \left(mv_{||}b_j + mv_\perp c_j(\Theta) + \frac{q}{c}A_j(\mathbf{X}) + \frac{q\rho}{c}\left(\mathbf{a}(\Theta)\cdot\nabla\right)A_j(\mathbf{X})\right)\left(\delta_i^j + \frac{d}{dX^i}\frac{mcv_\perp}{qB_0(\mathbf{X})}a^j(\Theta)\right) \\
&= \left(mv_{||}b_j + mv_\perp c_j(\Theta) + \frac{q}{c}A_j(\mathbf{X}) + \frac{q\rho}{c}\left(\mathbf{a}(\Theta)\cdot\nabla\right)A_j(\mathbf{X})\right)\left(\delta_i^j + \frac{d}{dX^i}\frac{2c\mu}{qv_\perp}a^j(\Theta)\right) \\
&= \left(mv_{||}b_j + mv_\perp c_j(\Theta) + \frac{q}{c}A_j(\mathbf{X}) + \frac{q\rho}{c}\left(\mathbf{a}(\Theta)\cdot\nabla\right)A_j(\mathbf{X})\right)\left(\delta_i^j - \frac{2c\mu}{qv_\perp^2}a^j(\Theta)\frac{dv_\perp}{dX^i}\right) \\
&= \left(mv_{||}b_j + mv_\perp c_j(\Theta) + \frac{q}{c}A_j(\mathbf{X}) + \frac{q\rho}{c}\left(\mathbf{a}(\Theta)\cdot\nabla\right)A_j(\mathbf{X})\right)\left(\delta_i^j - \frac{\mu\, a^j(\Theta)}{\Omega(\mathbf{X})mv_\perp}\frac{dB_0}{dX^i}\right) \\
&= \left[\left(mv_{||}b_i + mv_\perp c_i(\Theta) + \frac{q}{c}A_i(\mathbf{X})\right) - \mathbf{A}\cdot\mathbf{a}(\Theta)\frac{\mu}{B_0(\mathbf{X})v_\perp}\frac{dB_0}{dX^i}\right] \\
&\quad + \frac{q\rho}{c}\left(\mathbf{a}(\Theta)\cdot\nabla\right)A_i(\mathbf{X}) + \frac{\mu\rho}{B_0(\mathbf{X})v_\perp}\frac{dB_0}{dX^i}\left(a^j(\Theta)a^1(\Theta)\frac{\partial}{\partial X^1} + a^j(\Theta)a^2(\Theta)\frac{\partial}{\partial X^2}\right)A_j(\mathbf{X}).
\end{aligned} \tag{2.2.11}$$

In order to obtain $\Gamma_{v_{||}}$, we notice that $v_{||}$ only appears in the transformation $(v_x, v_y, v_z) \to (v_{||}, \mu, \Theta)$ (in contrast to μ and Θ, which also appear in the space coordinate transformations). However, since we know that $\gamma_{\mathbf{v}} = 0$, $\Gamma_{v_{||}} = 0$ as well.

For Γ_μ we have

$$\begin{aligned}
\Gamma_\mu &= \left(mv_{||}b_j + mv_\perp c_j(\Theta) + \frac{q}{c}A_j(\mathbf{X}) + \frac{q\rho}{c}(\mathbf{a}(\Theta)\cdot\nabla)A_j(\mathbf{X})\right)\frac{dx^j}{d\mu} \\
&= \left(mv_{||}b_j + mv_\perp c_j(\Theta) + \frac{q}{c}A_j(\mathbf{X}) + \frac{q\rho}{c}(\mathbf{a}(\Theta)\cdot\nabla)A_j(\mathbf{X})\right)\frac{d}{d\mu}\frac{mcv_\perp}{qB_0(\mathbf{X})}a^j(\Theta) \\
&= \left(mv_{||}b_j + mv_\perp c_j(\Theta) + \frac{q}{c}A_j(\mathbf{X}) + \frac{q\rho}{c}(\mathbf{a}(\Theta)\cdot\nabla)A_j(\mathbf{X})\right)a^j(\Theta)\frac{B_0(\mathbf{X})}{\Omega(\mathbf{X})mv_\perp} \\
&= \frac{\mathbf{A}(\mathbf{X})\cdot\mathbf{a}(\Theta)}{v_\perp} + \frac{\rho}{v_\perp}\left(a^j(\Theta)a^1(\Theta)\frac{\partial}{\partial X^1} + a^j(\Theta)a^2(\Theta)\frac{\partial}{\partial X^2}\right)A_j(\mathbf{X}).
\end{aligned} \tag{2.2.12}$$

Finally, we get for Γ_Θ:

$$\begin{aligned}
\Gamma_\Theta &= \left(mv_{||}b_j + mv_\perp c_j(\Theta) + \frac{q}{c}A_j(\mathbf{X}) + \frac{q\rho}{c}(\mathbf{a}(\Theta)\cdot\nabla)A_j(\mathbf{X})\right)\frac{dx^j}{d\Theta} \\
&= \left(mv_{||}b_j + mv_\perp c_j(\Theta) + \frac{q}{c}A_j(\mathbf{X}) + \frac{q\rho}{c}(\mathbf{a}(\Theta)\cdot\nabla)A_j(\mathbf{X})\right)\frac{mcv_\perp}{qB_0(\mathbf{X})}\frac{da^j}{d\Theta} \\
&= \left(mv_{||}b_j + mv_\perp c_j(\Theta) + \frac{q}{c}A_j(\mathbf{X}) + \frac{q\rho}{c}(\mathbf{a}(\Theta)\cdot\nabla)A_j(\mathbf{X})\right)c^j(\Theta)\frac{mcv_\perp}{qB_0(\mathbf{X})} \\
&= \left(mv_\perp + \frac{q}{c}\mathbf{A}\cdot\mathbf{c}(\Theta) + \frac{q\rho}{c}\left(c^j(\Theta)a^1(\Theta)\frac{\partial}{\partial X^1} + c^j(\Theta)a^2(\Theta)\frac{\partial}{\partial X^2}\right)A_j(\mathbf{X})\right)\frac{v_\perp}{\Omega} \\
&= \left(\frac{mv_\perp^2}{\Omega} + \frac{qv_\perp}{\Omega c}\mathbf{A}\cdot\mathbf{c}(\Theta) + \frac{mv_\perp^2}{B_0(\mathbf{X})\Omega}\left(c^j(\Theta)a^1(\Theta)\frac{\partial}{\partial X^1} + c^j(\Theta)a^2(\Theta)\frac{\partial}{\partial X^2}\right)A_j(\mathbf{X})\right).
\end{aligned} \tag{2.2.13}$$

Since we want to obtain a one-form that is independent of the gyroangle Θ, we perform an

average over a full gyro-period, which we do by using the operator

$$\mathcal{G}\left\{...\right\} \equiv \frac{1}{2\pi}\int_0^{2\pi} (...)\, d\Theta.$$

Before we average the individual parts of the one-form, we mention the following relations, which are easy to prove:

$$\begin{aligned}
\mathcal{G}\left\{a^i a^j\right\} &= \frac{\delta^{ij}}{2}, \\
\mathcal{G}\left\{c^i c^j\right\} &= \frac{\delta^{ij}}{2}, \\
\mathcal{G}\left\{a^i c^j\right\} &= \frac{1}{2}\left(\delta^{i2}\delta^{j1} - \delta^{i1}\delta^{j,2}\right).
\end{aligned} \tag{2.2.14}$$

From this, it follows that

$$\mathcal{G}\left\{\left(a^j(\Theta)a^1(\Theta)\frac{\partial}{\partial X^1} + a^j(\Theta)a^2(\Theta)\frac{\partial}{\partial X^2}\right)\right\} = \frac{1}{2}\left(\delta^{j1}\frac{\partial}{\partial X^1} + \delta^{j2}\frac{\partial}{\partial X^2}\right) \tag{2.2.15}$$

and

$$\mathcal{G}\left\{\left(c^j(\Theta)a^1(\Theta)\frac{\partial}{\partial X^1} + c^j(\Theta)a^2(\Theta)\frac{\partial}{\partial X^2}\right)\right\} = \frac{1}{2}\left(\delta^{j2}\frac{\partial}{\partial X^1} - \delta^{j1}\frac{\partial}{\partial X^2}\right). \tag{2.2.16}$$

Using this, the gyroaveraged spatial parts of the one form become

$$\begin{aligned}
\mathcal{G}\left\{\Gamma_i\right\} &= \left[mv_{||}b_i + \frac{q}{c}A_i(\mathbf{X}) + \frac{\mu\rho}{2B_0(\mathbf{X})v_\perp}\frac{dB_0}{dX^i}\left(\frac{\partial A_1}{\partial X^1} + \frac{\partial A_2}{\partial X^2}\right)\right] \\
&= \left[mv_{||}b_i + \frac{q}{c}A_i(\mathbf{X}) + \frac{\mu\rho}{2B_0(\mathbf{X})v_\perp}\frac{dB_0}{dX^i}\nabla\cdot\mathbf{A}(\mathbf{X})\right] \\
&= \left[mv_{||}b_i + \frac{q}{c}A_i(\mathbf{X})\right],
\end{aligned} \tag{2.2.17}$$

where we have assumed a Coulomb gauge for the vector potential. Similarly, we find for the μ-component of the one-form that

$$\mathcal{G}\left\{\Gamma_\mu\right\} = 0, \tag{2.2.18}$$

so that the magnetic moment is conserved within the gyroaveraged dynamics. The one-form contribution of the gyroangle becomes

$$\begin{aligned}
\mathcal{G}\left\{\Gamma_\Theta\right\} &= \left[\frac{mv_\perp^2}{\Omega(\mathbf{X})} + \frac{mv_\perp^2}{2\Omega(\mathbf{X})B_0(\mathbf{X})}\left(-\frac{\partial A_2}{\partial X^1} + \frac{\partial A_1}{\partial X^2}\right)\right] d\Theta \\
&= \left[\frac{mv_\perp^2}{\Omega(\mathbf{X})} - \frac{mv_\perp^2}{2\Omega(\mathbf{X})B_0(\mathbf{X})}B_0(\mathbf{X})\right] d\Theta \\
&= \frac{\mu B_0(\mathbf{X})}{\Omega(\mathbf{X})}\, d\Theta.
\end{aligned} \tag{2.2.19}$$

With this, the gyroaveraged one-form $\mathcal{G}\left\{\Gamma\right\}$ up to second-order corrections in ϵ_B, which we

will denote as Γ_0 in the following, takes the form [42]

$$\Gamma_0 = \left(mv_{||}\mathbf{b} + \frac{q}{c}\mathbf{A}(\mathbf{X})\right)\cdot d\mathbf{X} + \frac{\mu B_0(\mathbf{X})}{\Omega(\mathbf{X})}\,d\Theta - \left(\frac{mv_{||}^2}{2} + \mu B_0(\mathbf{X}) + q\phi(\mathbf{X})\right)dt. \tag{2.2.20}$$

2.2.2 Adding field perturbations

As a next step, we add rapidly varying fluctuations to the electromagnetic fields. That is, now we assume

$$\begin{aligned}\mathbf{A}(\mathbf{x},t) &= \mathbf{A}_0(\mathbf{x}) + \mathbf{A}_1(\mathbf{x},t)\\ \phi(\mathbf{x},t) &= \phi_0(\mathbf{x}) + \phi_1(\mathbf{x},t),\end{aligned}$$

where the relation of the field to the ordering parameters was discussed in section 2.1.

We can split the one form γ into two parts γ_0 and γ_1, where the first part contains the slowly varying background

$$\gamma_0 = \left(m\mathbf{v} + \frac{q}{c}\mathbf{A}_0(\mathbf{x})\right)\cdot d\mathbf{x} - \left(\frac{m}{2}v^2 + q\phi_0(\mathbf{x})\right)dt \tag{2.2.21}$$

and the second part

$$\gamma_1 = \frac{q}{c}\mathbf{A}_1(\mathbf{x},t)\cdot d\mathbf{x} - q\phi_1(\mathbf{x},t)\,dt \tag{2.2.22}$$

the rapidly varying fluctuations.

We will introduce new velocity coordinates

$$\begin{aligned}v_{||,*} &= v_{||} + \frac{q}{mc}\widetilde{A_{1,||}},\\ \mathbf{v}_{\perp,*} &= \mathbf{v}_\perp + \frac{q}{mc}\mathbf{A}_{1,\perp},\end{aligned} \tag{2.2.23}$$

where the tilde indicates the gyroangle-dependent part:

$$\widetilde{A_{1,||}} = A_{1,||} - \mathcal{G}\left\{A_{1,||}\right\}. \tag{2.2.24}$$

With this, the one-form γ can be written as

$$\begin{aligned}\gamma = &\left(m\mathbf{v}_* + \frac{q}{c}\mathbf{A}_0(\mathbf{x})\right)\cdot d\mathbf{x} - \left(\frac{mv_*^2}{2} + q\phi_0(\mathbf{x})\right)dt\\ &+ \frac{q}{c}\mathcal{G}\left\{A_{1,||}\right\}\mathbf{b}\cdot d\mathbf{x} - \left(q\phi_1(\mathbf{x},t) - \frac{qv_{||,*}}{c}\widetilde{A_{1,||}} - \frac{q}{c}\mathbf{v}_{\perp,*}\cdot\mathbf{A}_{1,\perp}\right)dt\\ &- \frac{q^2}{2mc^2}\left(\widetilde{A_{1,||}}^2 + |\mathbf{A}_{1,\perp}|^2\right)dt.\end{aligned} \tag{2.2.25}$$

Transforming the one-form into guiding centre coordinates yields the one-forms $\Gamma = \Gamma_0 + \Gamma_1 +$

Γ_2 with the three components

$$\begin{aligned}
\Gamma_0 =& \left(mv_{||,*}\mathbf{b} + \frac{q}{c}\mathbf{A}_0(\mathbf{X}+\boldsymbol{\rho})\right)\cdot d\mathbf{X} + \frac{\mu_* B_0(\mathbf{X}+\boldsymbol{\rho})}{\Omega(\mathbf{X}+\boldsymbol{\rho})}\, d\Theta \\
&- \left(\frac{mv_{||,*}^2}{2} + \mu_* B_0(\mathbf{X}+\boldsymbol{\rho}) + q\phi_0(\mathbf{X}+\boldsymbol{\rho})\right) dt, \\
\Gamma_1 =& \frac{q}{c}\mathcal{G}\left\{A_{1,||}(\mathbf{X}+\boldsymbol{\rho},t)\right\}\mathbf{b}\cdot d\mathbf{X} - \left(q\phi_1(\mathbf{X}+\boldsymbol{\rho},t) - \frac{qv_{||,*}}{c}\widetilde{A_{1,||}}(\mathbf{X}+\boldsymbol{\rho},t)\right) dt \\
&+ \frac{q}{c}\mathbf{v}_{\perp,*}\cdot\mathbf{A}_{1,\perp}(\mathbf{X}+\boldsymbol{\rho},t)dt, \\
\Gamma_2 =& -\frac{q^2}{2mc^2}\left(\left[\widetilde{A_{1,||}}(\mathbf{X}+\boldsymbol{\rho},t)\right]^2 + |\mathbf{A}_{1,\perp}(\mathbf{X}+\boldsymbol{\rho},t)|^2\right) dt.
\end{aligned} \tag{2.2.26}$$

Just like before, we wish to remove the $\Theta-$dependence from the one-form. In contrast to the previous efforts, however, expressing the field perturbations via a truncated Taylor expansion for small gyroradii is not appropriate, as all terms of the expansion are of the same order due to the assumption $k_\perp\rho_\mathrm{s} = \epsilon_\perp \sim \mathcal{O}(1)$ from section 2.1.

A convenient way to obtain a one-form independent of the gyroangle is to use so-called Lie transformations [43, 44], a special kind of near-identity transformation in extended phase space. We introduce a new set of coordinates $\overline{Z}$, which we will call gyrocentre coordinates, together with the smallness parameter ε, which are implicitly defined by the differential equation

$$\frac{\partial\overline{Z}^\nu(\mathbf{Z},\varepsilon)}{\partial\varepsilon} = G^\nu(\overline{\mathbf{Z}}(\mathbf{Z},\varepsilon)), \tag{2.2.27}$$

with the generating functions $G^\nu(\overline{Z}(Z,\varepsilon))$ and the index ν running over all phase-space indices. If we consider the initial condition $\overline{Z}^\nu(\mathbf{Z},0) = Z^\nu$, which is the basic property of a near-identity transformation, the above equation can be rewritten as

$$\overline{Z}^\nu(\mathbf{Z},\varepsilon) = T(\varepsilon)Z^\nu, \tag{2.2.28}$$

where the operator T is given by $T(\varepsilon) = \exp(\varepsilon G^\nu)$. Using again equation (2.2.5), we obtain the one-form in the new coordinate system

$$\overline{\Gamma}_\mu(\overline{Z},\varepsilon) = \frac{dZ^\nu}{d\overline{Z}^\mu}\Gamma_\nu(\mathbf{Z}(\overline{\mathbf{Z}},\varepsilon)). \tag{2.2.29}$$

Before continuing, we note the useful identity

$$\begin{aligned}
&\mathbf{Z} = \mathbf{Z}(\overline{\mathbf{Z}}(\mathbf{Z},\varepsilon),\varepsilon) \\
\Rightarrow &\frac{dZ^\nu}{d\varepsilon} = 0 = \frac{\partial Z^\nu}{\partial\varepsilon} + \frac{dZ^\nu}{d\overline{Z}^\mu}\frac{\partial\overline{Z}^\mu}{\partial\varepsilon} = \frac{\partial Z^\nu}{\partial\varepsilon} + \frac{dZ^\nu}{d\overline{Z}^\mu}G^\mu,
\end{aligned}$$

so that we have

$$\frac{\partial Z^\nu}{\partial\varepsilon}(\overline{\mathbf{Z}},\varepsilon) = -\frac{dZ^\nu}{d\overline{Z}^\mu}(\overline{\mathbf{Z}},\varepsilon)G^\mu(\overline{\mathbf{Z}}). \tag{2.2.30}$$

Applying $\partial/\partial\varepsilon$ to equation (2.2.29) gives us

$$\begin{aligned}\frac{\partial\overline{\Gamma}_\mu}{\partial\varepsilon} &= -\Gamma_\nu\frac{d}{d\overline{Z}^\mu}\left[\frac{dZ^\nu}{d\overline{Z}^\lambda}G^\lambda\right] - \frac{dZ^\nu}{d\overline{Z}^\mu}G^\lambda\left[\frac{d\Gamma_\nu}{dZ^\sigma}\frac{dZ^\sigma}{d\overline{Z}^\lambda}\right] \\ &= -\Gamma_\nu\frac{d}{d\overline{Z}^\mu}\left[\frac{dZ^\nu}{d\overline{Z}^\lambda}G^\lambda\right] - \frac{dZ^\nu}{d\overline{Z}^\mu}G^\lambda\frac{d\Gamma_\nu}{d\overline{Z}^\lambda},\end{aligned} \tag{2.2.31}$$

which can be rearranged to be

$$\begin{aligned}\frac{\partial\overline{\Gamma}_\mu}{\partial\varepsilon} &= -\Gamma_\nu\frac{d}{d\overline{Z}^\mu}\left[\frac{dZ^\nu}{d\overline{Z}^\lambda}G^\lambda\right] - \frac{dZ^\nu}{d\overline{Z}^\mu}G^\lambda\frac{d\Gamma_\nu}{d\overline{Z}^\lambda} \\ &= -\frac{d}{d\overline{Z}^\mu}\left[\overline{\Gamma}_\lambda G^\lambda\right] - G^\lambda\left[\frac{d\overline{\Gamma}_\mu}{d\overline{Z}^\lambda} - \frac{d\overline{\Gamma}_\lambda}{d\overline{Z}^\mu}\right],\end{aligned} \tag{2.2.32}$$

where we have used equation (2.2.29). Therefore, if we define the operator L_G, applied to a one-form $\overline{\Gamma}$, as

$$L_\mathrm{G}\overline{\Gamma} = G^\lambda\left[\frac{\partial\overline{\Gamma}_\mu}{\partial\overline{Z}^\lambda} - \frac{d\overline{\Gamma}_\lambda}{d\overline{Z}^\mu}\right], \tag{2.2.33}$$

we get that

$$\frac{\partial\overline{\Gamma}}{\partial\varepsilon} = -L_\mathrm{G}\overline{\Gamma} - d(\overline{\Gamma}\cdot G), \tag{2.2.34}$$

where the second term on the right hand side is a one-form with components $d(\overline{\Gamma}\cdot G)_\mathrm{i}) = \partial(\overline{\Gamma}\cdot G)_\mathrm{i})/\partial\overline{Z}_\mathrm{i}$. It is easy to show that any product of the operators L_G and d vanish so that

$$\frac{\partial^\mathrm{n}\overline{\Gamma}}{\partial\varepsilon^\mathrm{n}} = (-L_\mathrm{G})^\mathrm{n}\overline{\Gamma} + (-dG\cdot)^\mathrm{n}\overline{\Gamma}. \tag{2.2.35}$$

Prescribing the initial condition that $\overline{\Gamma} = \Gamma$ for $\varepsilon = 0$, the solution is given by

$$\overline{\Gamma} = T_*^{-1}(\varepsilon)\Gamma + dS, \tag{2.2.36}$$

with

$$T_*^{-1}(\varepsilon) = \exp\left(-\varepsilon L_\mathrm{G}\right). \tag{2.2.37}$$

The term dS is an exact differential arising from the second term in equation (2.2.35). The explicit form of S does not matter, as it will not alter the equations of motion given through the one-form. It can be considered a gauge function chosen to obtain an easily tractable one-form. Expanding equation (2.2.36) in powers of the smallness parameter and collecting terms order by order, we obtain up to second order [44]

$$\begin{aligned}\overline{\Gamma}_0 &= \Gamma_0 + dS_0 = \Gamma_0, \\ \overline{\Gamma}_1 &= \Gamma_1 - L_1\Gamma_0 + dS_1, \\ \overline{\Gamma}_2 &= \Gamma_2 - L_1\Gamma_1 + \left(\frac{1}{2}L_1^2 - L_2\right)\Gamma_0 + dS_2.\end{aligned} \tag{2.2.38}$$

In the following, we will only consider first-order perturbations, which means we will only calculate the form of $\overline{\Gamma}_1$. Therefore, for any particular component of the gyrocenter one-form,

we have to use

$$\overline{\Gamma}_{1,\nu} = \Gamma_{1,\nu} - G_1^{\sigma}\left[\frac{\partial \Gamma_{0,\nu}}{\partial Z^{\sigma}} - \frac{\partial \Gamma_{0,\sigma}}{\partial Z^{\nu}}\right] + \frac{\partial S_1}{\partial Z^{\nu}}. \tag{2.2.39}$$

Notice here that we take the derivatives with respect to the old coordinates due to the expansion, as $\overline{\mathbf{Z}} = \mathbf{Z}$ at $\varepsilon = 0$.

For the magnetic moment, we have

$$\begin{aligned}\overline{\Gamma}_{1,\mu_*} =& \cancelto{0}{\Gamma_{1,\mu_*}} - G_1^{\mathbf{X}}\left[\frac{\partial}{\partial \mathbf{X}}\cancelto{0}{\Gamma_{0,\mu}} - \frac{\partial \cancelto{0}{\Gamma_{0,\mathbf{X}}}}{\partial \mu}\right] - G_1^{v_{||,*}}\left[\frac{\partial}{\partial v_{||,*}}\cancelto{0}{\Gamma_{0,\mu_*}} - \frac{\partial}{\partial \mu_*}\cancelto{0}{\Gamma_{0,v_{||,*}}}\right] \\ & - G_1^{\Theta}\left[\frac{\partial}{\partial \Theta}\cancelto{0}{\Gamma_{0,\mu_*}} - \frac{\partial}{\partial \mu_*}\Gamma_{0,\Theta}\right] + \frac{\partial S_1}{\partial \mu_*} \\ =& G_1^{\Theta}\frac{mc}{q} + \frac{\partial S_1}{\partial \mu_*}.\end{aligned} \tag{2.2.40}$$

Since we want the magnetic moment to be conserved even in the presence of rapidly varying perturbations, we need to impose that $\overline{\Gamma}_{1,\mu_*} = 0$, which means that

$$G_1^{\Theta} = -\frac{q}{mc}\frac{\partial S_1}{\partial \mu_*}. \tag{2.2.41}$$

In an analogous way to that, we can get

$$G_1^{\mu_*} = \frac{q}{mc}\frac{\partial S_1}{\partial \Theta} \tag{2.2.42}$$

and

$$G_1^{\mathbf{X}} \cdot \mathbf{b} = -\frac{1}{m}\frac{\partial S_1}{\partial v_{||,*}} \tag{2.2.43}$$

by imposing that $\overline{\Gamma}_{1,\Theta} = 0$ and $\overline{\Gamma}_{1,v_{||,*}} = 0$, respectively.

The spatial component of the first-order one-form is given by

$$\overline{\Gamma}_{1,\mathbf{X}} = \frac{q}{c}\mathcal{G}\left\{A_{1,||}(\overline{\mathbf{X}} + \boldsymbol{\rho}, t)\right\}\mathbf{b} + \frac{q}{c}G_1^{\mathbf{X}} \times \mathbf{B}_* - mG_1^{v_{||,*}}\mathbf{b} + \nabla S_1, \tag{2.2.44}$$

where we have used that $\mathbf{B}_0^* = \mathbf{B}_0 + \mathcal{O}(\epsilon B_0)$. The goal is to choose the three unknown functions in such a way that $\overline{\Gamma}_{1,\mathbf{X}}$ is independent of the gyroangle Θ, i.e. that $\overline{\Gamma}_{1,\mathbf{X}} = (q/c)\mathcal{G}\left\{A_{1,||}(\mathbf{X} + \boldsymbol{\rho}, t)\right\}\mathbf{b}$, which is known as the $||-$symplectic gyrocentre model [37]. Therefore, we require that

$$\frac{q}{c}G_1^{\mathbf{X}} \times \mathbf{B}^* - mG_1^{v_{||,*}}\mathbf{b} + \nabla S_1 = 0, \tag{2.2.45}$$

with $\mathbf{B}^* = \nabla \times \mathbf{A}^*$. Taking the dot product equation (2.2.45) with $\mathbf{B}^*$, one obtains

$$G_1^{v_{||,*}} = \frac{1}{mB_{||}^*}\nabla S_1 \cdot \mathbf{B}^*. \tag{2.2.46}$$

On the other hand, taking the cross product of equation (2.2.45) with $\mathbf{b}$, one obtains a relation

for $G_1^{\mathbf{X}}$, which reads

$$G_1^{\mathbf{X}} = -\frac{1}{B_{||}^*}\left[\frac{1}{m}\frac{\partial S_1}{\partial v_{||,*}}\mathbf{B}^* + \frac{c}{q}\mathbf{b}\times\nabla S_1\right]. \tag{2.2.47}$$

Inserting all solutions of the generating function into the Hamiltonian part of the one-form, one obtains an expression that can be used to determine the gauge function S_1. The Hamiltonian part of the gyrocentre one-form then reads up to second-order corrections

$$\begin{aligned}\overline{\Gamma}_{1,t} =& -\left[q\phi_1(\mathbf{X}+\boldsymbol{\rho},t) - \frac{qv_{||,*}}{c}\widetilde{A_{1,||}}(\mathbf{X}+\boldsymbol{\rho},t) - \frac{q}{c}\mathbf{v}_{\perp,*}\cdot\mathbf{A}_{1,\perp}(\mathbf{X}+\boldsymbol{\rho},t)\right] + \Omega\frac{\partial S_1}{\partial\Theta}\\ &+\left(\frac{1}{B_{||}^*}\left[\frac{1}{m}\frac{\partial S_1}{\partial v_{||,*}}\mathbf{B}^* + \frac{c}{q}\mathbf{b}\times\nabla S_1\right]\cdot\nabla(\mu_* B_0 + q\phi_0) + \frac{v_{||,*}}{B_{||,*}}\nabla S_1\cdot\mathbf{B}^* + \frac{\partial S_1}{\partial t}\right).\end{aligned} \tag{2.2.48}$$

If we assume that the gauge function also obeys the gyrokinetic ordering concerning its spatio-temporal variation shown in section 2.1, we can show that all terms in the second row of equation (2.2.48) are of order $\epsilon_\delta\epsilon_B$, $\epsilon_\delta\epsilon_\omega$ or higher orders thereof. Therefore, if we only want to keep the terms that are of order ϵ_δ, we are left with

$$\begin{aligned}\overline{\Gamma}_{1,t} =& -q\mathcal{G}\left\{\phi_1(\mathbf{X}+\boldsymbol{\rho},t)\right\} + \frac{qv_{\perp,*}}{c}\mathcal{G}\left\{\mathbf{A}_{1,\perp}(\mathbf{X}+\boldsymbol{\rho},t)\cdot\mathbf{c}(\Theta)\right\}\\ &-q\tilde{\phi}_1(\mathbf{X}+\boldsymbol{\rho},t) + \frac{qv_{||,*}}{c}\widetilde{A_{1,||}}(\mathbf{X}+\boldsymbol{\rho},t) + \frac{qv_{\perp,*}}{c}\widetilde{\mathbf{A}_{1,\perp}\cdot\mathbf{c}}(\Theta)(\mathbf{X}+\boldsymbol{\rho},t) + \Omega\frac{\partial S_1}{\partial\Theta}.\end{aligned} \tag{2.2.49}$$

If one chooses the gauge function S_1 such that

$$\frac{\partial S_1}{\partial\Theta} = \frac{1}{\Omega}\left[q\tilde{\phi}_1 - \frac{qv_{||,*}}{c}A_{1,||}\widetilde{(\mathbf{X}+\boldsymbol{\rho},t)} - \frac{qv_{\perp,*}}{c}\widetilde{\mathbf{A}_{1,\perp}\cdot\mathbf{c}}(\Theta)\right], \tag{2.2.50}$$

the perturbed gyroaveraged Hamiltonian takes the simple form

$$\overline{H}_1 = q\mathcal{G}\left\{\phi_1(\mathbf{X}+\boldsymbol{\rho},t)\right\} - \frac{q}{c}\mathcal{G}\left\{\mathbf{A}_{1,\perp}(\mathbf{X}+\boldsymbol{\rho},t)\cdot\mathbf{v}_{\perp,*}(\Theta)\right\}. \tag{2.2.51}$$

Putting all components together, the full gyrokinetic one-form, up to second-order corrections, can be written as

$$\begin{aligned}\overline{\Gamma} =& \overline{\Gamma}_0 + \overline{\Gamma}_1\\ =& \left[mv_{||,*}\mathbf{b} + \frac{q}{c}\mathbf{A}_0 + \frac{q}{c}\mathcal{G}\left\{A_{1,||}\right\}\mathbf{b}\right]\cdot d\mathbf{X} + \frac{\mu_* B_0}{\Omega}\,d\Theta\\ &-\left(\frac{mv_{||*}^2}{2} + q\phi_0 + q\mathcal{G}\left\{\phi_1\right\} + \mu_* B_0 - \frac{q}{c}\mathcal{G}\left\{\mathbf{A}_{1,\perp}\cdot\mathbf{v}_{\perp,*}\right\}\right)dt.\end{aligned} \tag{2.2.52}$$

As we shall see in section 2.6, the contribution of the electromagnetic fields to the total Lagrangian of the system is quadratic in the field perturbations ϕ_1 and $\mathbf{A}_1$. Therefore, we also need to take the second-order correction of the gyrocentre Hamiltonian into account to derive the gyrokinetic field equations consistent with the desired order of accuracy. These corrections can be obtained by considering again equation (2.2.38) and calculating the second-order Lie operator and gauge function in such a way that $\overline{\Gamma}_2 = 0$. We will skip this step for brevity, as it can be done analogously. The leading terms of the second-order corrections turn

out to be of the form [37]

$$\overline{H}_2 = -\frac{q^2}{2B_0}\frac{\partial}{\partial \mu_*}\mathcal{G}\left\{\tilde{\chi}_1^2\right\} + \frac{q^2}{2mc^2}\left(\mathcal{G}\left\{\widetilde{A_{1,||}}^2\right\} + \mathcal{G}\left\{|\mathbf{A}_{1,\perp}|^2\right\}\right), \tag{2.2.53}$$

where

$$\tilde{\chi}_1 = \tilde{\phi}_1 - \frac{v_{||,*}}{c}\tilde{A}_{1,||} - \frac{v_{\perp,*}}{c}\widetilde{\mathbf{A}_{1,\perp}\cdot\mathbf{c}}(\Theta). \tag{2.2.54}$$

It becomes apparent from equation (2.2.23) that the transformation of quantities from gyrocentre to particle space involves a nonlinear coupling to the perturbed vector potential. For example, the transformation $\mathbf{x} \leftrightarrow \mathbf{X} + \boldsymbol{\rho}(\mathbf{X}, \mu_*, \Theta)$ would involve explicit evaluation of the perpendicular vector potential, which is prohibitively expensive to do. Therefore, most gyrokinetic codes today use the approximation $\mathbf{v}_* \approx \mathbf{v}$, meaning that the ϵ_δ-correction of the velocities is dropped. Doing so results in the final form of the Lagrangian, including second-order corrections used throughout this thesis, which reads

$$\begin{aligned}\mathcal{L} = &\left(\frac{q}{c}\mathbf{A}_0^* + \frac{q}{c}\mathcal{G}\left\{A_{1,||}\right\}\mathbf{b}\right)\cdot\dot{\mathbf{X}} + \frac{\mu B_0}{\Omega}\dot{\Theta} - \left(\frac{mv_{||}^2}{2} + \mu B_0 + q\phi_0 + q\mathcal{G}\left\{\psi_1\right\}\right)\\ &+ \frac{q_\sigma^2}{2B_0}\frac{\partial}{\partial\mu}\mathcal{G}\left\{\tilde{\chi}_1^2\right\} - \frac{q^2}{2mc^2}\left(\mathcal{G}\left\{\widetilde{A_{1,||}}^2\right\} + \mathcal{G}\left\{|\mathbf{A}_{1,\perp}|^2\right\}\right),\end{aligned} \tag{2.2.55}$$

where the variables

$$\mathbf{A}_0^* \equiv \mathbf{A}_0 + (mc/q)\, v_{||}\mathbf{b} \tag{2.2.56}$$

and

$$\psi_1 \equiv \phi_1 - \frac{\mathbf{v}_\perp\cdot\mathbf{A}_{1,\perp}}{c} \tag{2.2.57}$$

were introduced for convenience.

Finally, one can use the symplectic part of the Lagrangian to calculate the Jacobian for the transformation between particle and gyrocentre space as

$$\mathcal{J} = \sqrt{\det\left(\frac{\partial\overline{\Gamma}_\nu^{\text{symp.}}}{\partial\overline{Z}^\lambda} - \frac{\partial\overline{\Gamma}_\lambda^{\text{symp.}}}{\partial\overline{Z}^\nu}\right)} = \frac{B_{||,\varepsilon}^*}{m}, \tag{2.2.58}$$

with

$$\begin{aligned}&\mathbf{B}_\varepsilon^* = \mathbf{B}_0^* + \nabla\times\left(\mathcal{G}\left\{A_{1,||}\right\}\mathbf{b}\right),\\ &B_{\varepsilon,||}^* = \mathbf{b}\cdot\mathbf{B}_\varepsilon^* = B_{0,||}^* + \mathcal{G}\left\{A_{1,||}\right\}\mathbf{b}\cdot(\nabla\times\mathbf{b}).\end{aligned} \tag{2.2.59}$$

Therefore, the infinitesimal phase-space element transforms as

$$d^3x d^3v = \frac{B_{\varepsilon,||}^*}{m} d^3X d\Theta d\mu_* dv_{||,*}. \tag{2.2.60}$$

The previously mentioned approximation $\mathbf{v}_* \approx \mathbf{v}$ leaves us with the approximate Jacobian

$$\mathcal{J} \approx \frac{B_{0,||}^*}{m},$$

so that we will use the phase-space transformation

$$d^3x d^3v \approx \frac{B^*_{0,||}}{m} d^3X d\Theta d\mu dv_{||}. \tag{2.2.61}$$

Although it should be noted that this approximation will violate the conservation of phase-space volume, as it is incompatible with the symplectic part of the one-form (2.2.52), its effects seem to be manageable for most gyrokinetic simulations, as benchmarks of parallel-symplectic codes show good agreement with those using a canonical model [45].

2.3 The gyrokinetic action functional

In order to derive the governing equations of the gyrokinetic Vlasov-Maxwell system in an energy-preserving manner, one needs to obtain them through a consistent minimisation procedure. Here, we will follow the derivation of [46] with the addition of introducing a splitting of the distribution function later in this section.

If we introduce the modified distribution function $\mathcal{F}_\sigma(\mathbf{Z},t) \equiv \mathcal{J}(\mathbf{Z},t)F_\sigma(\mathbf{Z},t)$, the entire dynamical behaviour of the gyrokinetic system can be described through the Lagrangian of the system:

$$\begin{aligned}\mathcal{L}_{\text{total}} = \sum_\sigma & \underbrace{\int d^6Z_0\, \mathcal{F}_\sigma(\mathbf{Z}_0,t_0)\mathcal{L}_\sigma(\mathbf{Z}_\sigma\left(\mathbf{Z}_0,t_0;t\right),\dot{\mathbf{Z}}_\sigma\left(\mathbf{Z}_0,t_0;t\right),t)}_{=:\,\mathcal{L}_{\text{part},\sigma}} \\ & + \underbrace{\int d^3x\, \frac{1}{8\pi}\left(|\nabla\phi(\mathbf{x},t)|^2 + |\nabla\times\mathbf{A}(\mathbf{x},t)|^2\right)}_{=:\,\mathcal{L}_{\text{f}}}.\end{aligned} \tag{2.3.1}$$

The particle Lagrangian of species σ is determined via the modified distribution function $\mathcal{F}_\sigma(\mathbf{Z}_0,t_0)$ at an arbitrary point in time t_0 and the single particle Lagrangian given by equation (2.2.55), evaluated at the characteristics $\mathbf{Z}_\sigma\left(\mathbf{Z}_0,t_0;t\right)$ with the initial conditions $\mathbf{Z}_\sigma\left(\mathbf{Z}_0,t_0;t_0\right) = \mathbf{Z}_0$. Additionally, $\mathcal{L}_{\text{f}}$ is the Lagrangian of the electromagnetic field.

With this, we can then introduce the gyrokinetic action functional

$$I[\phi_1,\mathbf{A}_1,\mathbf{Z}_\sigma] = \sum_\sigma \int_{t_1}^{t_2} \mathcal{L}_{\text{part},\sigma}[\phi_1,\mathbf{A}_1,\mathbf{Z}_\sigma;t]dt + \int_{t_1}^{t_2} \mathcal{L}_{\text{f}}[\phi_1,\mathbf{A}_1;t]dt. \tag{2.3.2}$$

Similar to what is done in classical mechanics, the governing equations of the system are derived by minimising the action functional (2.3.2) with respect to the quantities of interest. In particular, minimising (2.3.2) with respect to ϕ_1, $\mathbf{A}_1$ and $\mathbf{Z}_\sigma$ will give the gyrokinetic Poisson's and Ampère's equations as well as the nonlinear characteristics of motion $\mathbf{Z}_\sigma$ of the so-called "full-f" model of gyrokinetics. Once the characteristics are known, conservation of probability then dictates that the modified distribution function $\mathcal{F}_\sigma$ at any point in time is given by

$$\mathcal{F}(\mathbf{Z},t) = \int \mathcal{F}_\sigma(\mathbf{Z}_0,t_0)\,\delta^6\left(\mathbf{Z}-\mathbf{Z}_\sigma(\mathbf{Z}_0,t_0;t)\right)\,d^6Z_0. \tag{2.3.3}$$

Additionally, if we require that the Jacobian satisfies Liouville's theorem

$$\frac{\partial \mathcal{J}}{\partial t} + \nabla_{\mathbf{Z}} \cdot \left(\mathcal{J}(\mathbf{Z}) \dot{\mathbf{Z}} \right) = 0, \tag{2.3.4}$$

it is then easy to prove from equation (2.3.3) that $F_\sigma(\mathbf{X}, v_{||}, \mu, t)$ satisfies the gyrokinetic equation

$$\frac{\partial F_\sigma}{\partial t} + \dot{\mathbf{X}}_\sigma \cdot \nabla F_\sigma + \dot{v}_{||,\sigma} \frac{\partial F_\sigma}{\partial v_{||}} + \dot{\mu}_\sigma \frac{\partial F_\sigma}{\partial \mu_\sigma} = 0, \tag{2.3.5}$$

where $\dot{\mathbf{X}}_\sigma$ and $\dot{v}_{||,\sigma}$ are the total time derivatives of the characteristics $\mathbf{X}_\sigma(\mathbf{Z}, t)$ and $v_{||}(\mathbf{Z}, t)$. Notice here that we replaced the exact Jacobian with an approximation in section 2.2, which will not satisfy the Liouville theorem exactly. Therefore, our model is not strictly conservative unless we retain the exact Jacobian. However, the deviation is of order $\epsilon_\delta \epsilon_{\mathrm{B}}^2$ and might therefore be small enough on turbulent timescales for numerical simulations to agree sufficiently with Hamiltonian frameworks [45]. It might nevertheless be worth exploring if conservation is still kept to sufficient levels when running gyrokinetic simulations on timescales comparable to the confinement time.

We will additionally introduce a splitting of the distribution function $F_\sigma(\mathbf{X}, v_{||}, \mu, t) = F_{0,\sigma}(\mathbf{X}, v_{||}, \mu) + F_{1,\sigma}(\mathbf{X}, v_{||}, \mu, t)$ with $F_{1,\sigma}/F_{0,\sigma} \sim \mathcal{O}(\epsilon_\delta)$. We will then truncate the total Lagrangian at order ϵ_δ^3. Therefore, we get

$$I_{\mathrm{trunc}} = \sum_\sigma \left(I^{(\mathrm{lin})}_{\mathrm{part},\sigma}[\phi_1, \mathbf{A}_1, \mathbf{Z}_\sigma] + I^{(\mathrm{nonlin})}_{\mathrm{part},\sigma}[\phi_1, \mathbf{A}_1, \mathbf{Z}_\sigma] \right) + I_{\mathrm{field}}[\phi_1, \mathbf{A}_1]. \tag{2.3.6}$$

Finally, we wish to neglect the nonlinear motion terms arising from the second-order Hamiltonian $\overline{H}_{2,\sigma}$ and only retain its contributions to the electromagnetic field equations. This can be accomplished by approximating $I^{(\mathrm{nonlin})}_{\mathrm{part},\sigma}[\phi_1, \mathbf{A}_1, \mathbf{Z}_\sigma] \to I^{(\mathrm{nonlin})}_{\mathrm{part},\sigma}[\phi_1, \mathbf{A}_1]$. A similar procedure was used in [47], although there a constrained Eularian variation with respect to the distribution function $\mathcal{F}_\sigma$ was performed instead of a variation with respect to the characteristics $\mathbf{Z}_\sigma$.

With all of these modifications, the total gyrokinetic action functional can be written as

$$I_{\mathrm{total}}[\phi_1, \mathbf{A}_1, \mathbf{Z}_\sigma] = \sum_\sigma \left(I^{(\mathrm{lin})}_{\mathrm{part},\sigma}[\phi_1, \mathbf{A}_1, \mathbf{Z}_\sigma] + I^{(\mathrm{nonlin})}_{\mathrm{part},\sigma}[\phi_1, \mathbf{A}_1] \right) + I_{\mathrm{field}}[\phi_1, \mathbf{A}_1], \tag{2.3.7}$$

with

$$
\begin{aligned}
I^{(\mathrm{lin})}_{\mathrm{part},\sigma}[\phi_1, \mathbf{A}_1, \mathbf{Z}_\sigma] &= \int_{\mathrm{t}_1}^{\mathrm{t}_2} \int (\mathcal{F}_{0,\sigma} + \mathcal{F}_{1,\sigma}) \left[\frac{q_\sigma}{c} \left(\mathbf{A}_0^* + \mathcal{G} \left\{ A_{1,||} \right\} \mathbf{b} \right) \cdot \dot{\mathbf{X}} + \frac{\mu B_0}{\Omega_\sigma} \dot{\Theta} \right] d^6 Z_0 \, dt \\
&\quad - \int_{\mathrm{t}_1}^{\mathrm{t}_2} \int (\mathcal{F}_{0,\sigma} + \mathcal{F}_{1,\sigma}) \left[\overline{H}_{0,\sigma} + \overline{H}_{1,\sigma} \right] d^6 Z_0 \, dt, \\
I^{(\mathrm{nonlin})}_{\mathrm{part},\sigma}[\phi_1, \mathbf{A}_1] &= - \int_{\mathrm{t}_1}^{\mathrm{t}_2} \int \overline{\mathrm{H}}_{2,\sigma}(\mathbf{Z}_0, \mathrm{t}) \mathcal{F}_{0,\sigma}(\mathbf{Z}_0) \, \mathrm{d}^6 \mathrm{Z}_0 \, \mathrm{dt}, \\
I_{\mathrm{field}}[\phi_1, \mathbf{A}_1] &= \frac{1}{8\pi} \int_{t_1}^{t_2} \int \left(|\nabla \phi_0(\mathbf{x}) + \nabla \phi_1(\mathbf{x}, t)|^2 - |\nabla \times \mathbf{A}_0(\mathbf{x}) + \nabla \times \mathbf{A}_1(\mathbf{x}, t)|^2 \right) d^3x \, dt.
\end{aligned}
\tag{2.3.8}
$$

2.4 Equations of motion

As was stated before, the equations of motion are obtained by minimising the total action (2.3.7) with respect to $\mathbf{Z}_\sigma(\mathbf{Z}_0, t)$.

$$
\begin{aligned}
&\frac{\delta I_{\mathrm{total}}}{\delta \mathbf{Z}_\sigma(\mathbf{Z}_0, t_0; t)} = \frac{\delta I^{(\mathrm{lin})}_{\mathrm{part},\sigma}}{\delta \mathbf{Z}_\sigma(\mathbf{Z}_0, t_0; t)} \\
=& \frac{\delta}{\delta \mathbf{Z}_\sigma(\mathbf{Z}_0, t_0; t)} \cdot \int_{\mathrm{t}_1}^{\mathrm{t}_2} \int (\mathcal{F}_{0,\sigma} + \mathcal{F}_{1,\sigma}) \, \mathcal{L}^{\mathrm{lin}}_\sigma(\mathbf{Z}_\sigma(\mathbf{Z}'_0, t_0; t'), \dot{\mathbf{Z}}_\sigma(\mathbf{Z}'_0, t_0; t'), t') \delta \mathbf{Z}_\sigma \, d^6 Z'_0 dt' \\
=& \int_{\mathrm{t}_1}^{\mathrm{t}_2} \int (\mathcal{F}_{0,\sigma} + \mathcal{F}_{1,\sigma}) \left[\frac{\partial \mathcal{L}^{\mathrm{lin}}_\sigma}{\partial \mathbf{Z}_\sigma} \delta^6 \left(\mathbf{Z}_0 - \mathbf{Z}'_0 \right) \delta(t - t') + \frac{\partial \mathcal{L}^{\mathrm{lin}}_\sigma}{\partial \dot{\mathbf{Z}}_\sigma} \cdot \frac{\delta \dot{\mathbf{Z}}_\sigma}{\delta \mathbf{Z}_\sigma} \right] d^6 Z'_0 dt' \\
=& \int_{\mathrm{t}_1}^{\mathrm{t}_2} \int (\mathcal{F}_{0,\sigma} + \mathcal{F}_{1,\sigma}) \, \delta(t - t') \delta^6 \left(\mathbf{Z}_0 - \mathbf{Z}'_0 \right) \left[\frac{\partial \mathcal{L}^{\mathrm{lin}}_\sigma}{\partial \mathbf{Z}_\sigma} - \frac{d}{dt'} \frac{\partial \mathcal{L}^{\mathrm{lin}}_\sigma}{\partial \dot{\mathbf{Z}}_\sigma} \right] d^6 Z'_0 dt' \\
=& (\mathcal{F}_{0,\sigma} + \mathcal{F}_{1,\sigma}) \left[\frac{\partial \mathcal{L}^{\mathrm{lin}}_\sigma}{\partial \mathbf{Z}_\sigma} - \frac{d}{dt'} \frac{\partial \mathcal{L}^{\mathrm{lin}}_\sigma}{\partial \dot{\mathbf{Z}}_\sigma} \right].
\end{aligned}
\tag{2.4.1}
$$

Therefore, the minimisation of the gyrokinetic action functional tells us that we have to calculate the particle trajectories using the Euler-Lagrange equations

$$
\frac{d}{dt} \frac{\partial \mathcal{L}}{\partial \dot{Z}_i} = \frac{\partial \mathcal{L}}{\partial Z_i},
\tag{2.4.2}
$$

from the linear Lagrangian $\mathcal{L}^{\mathrm{lin}}_\sigma$, which is the Lagrangian (2.2.55) without the contribution coming from $\overline{H}_2$. If we drop the index σ for now, obtaining the equations of motion from the

Lagrangian is straightforward. The ones for μ, Θ and $X_{||}$ are

$$\dot{\mu} = 0, \tag{2.4.3}$$

$$\dot{\Theta} = \Omega + \frac{q\Omega}{B_0}\frac{\partial}{\partial \mu}\mathcal{G}\left\{\chi_1\right\}, \tag{2.4.4}$$

$$\mathbf{b}\cdot\dot{\mathbf{X}} = v_{||}. \tag{2.4.5}$$

Furthermore, we have

$$\begin{aligned}
\frac{\partial \mathcal{L}}{\partial \dot{\mathbf{X}}} &= \left(\frac{q}{c}\mathbf{A}_0^* + \frac{q}{c}\mathcal{G}\left\{A_{1,||}\right\}\mathbf{b}\right), \\
\frac{\partial \mathcal{L}}{\partial \mathbf{X}} &= \frac{q}{c}\nabla\left[\left(\mathbf{A}_0^* + \mathcal{G}\left\{A_{1,||}\right\}\mathbf{b}\right)\cdot\dot{\mathbf{X}}\right] - \left(\mu\nabla B_0 + q\nabla\phi_0 + q\nabla\mathcal{G}\left\{\psi_1\right\}\right),
\end{aligned}$$

so that

$$\begin{aligned}
&m\dot{v}_{||}\mathbf{b} + \frac{q}{c}\left[\left(\dot{\mathbf{X}}\cdot\nabla\right)\mathbf{A}_0^* - \nabla\left(\mathbf{A}_0^*\cdot\dot{\mathbf{X}}\right)\right] + \frac{q}{c}\left[\left(\dot{\mathbf{X}}\cdot\nabla\right)\mathcal{G}\left\{A_{1,||}\right\}\mathbf{b} - \nabla\left(\mathcal{G}\left\{A_{1,||}\right\}\mathbf{b}\cdot\dot{\mathbf{X}}\right)\right] \\
=&m\dot{v}_{||}\mathbf{b} - \frac{q}{c}\dot{\mathbf{X}}\times\left(\mathbf{B}_0^* + \left[\nabla\times\left(\mathcal{G}\left\{A_{1,||}\right\}\mathbf{b}\right)\right]\right) \\
=&m\dot{v}_{||}\mathbf{b} - \frac{q}{c}\dot{\mathbf{X}}\times\mathbf{B}_\varepsilon^* \\
=&-\left(\mu\nabla B_0 + q\nabla\phi_0 + q\nabla\mathcal{G}\left\{\psi_1\right\}\right) - \frac{q}{c}\frac{\partial}{\partial t}\mathcal{G}\left\{A_{1,||}\right\}\mathbf{b}.
\end{aligned}$$

Applying the operation $(\mathbf{b}\times)$ to the equation above gives the expressions for $\dot{\mathbf{X}}$, which reads

$$\begin{aligned}
\dot{\mathbf{X}} =&\frac{\mathbf{B}_\varepsilon^*}{B_{||,\varepsilon}^*}v_{||} + \frac{c}{qB_{||,\varepsilon}^*}\mathbf{b}\times\left(\mu\nabla B_0 + q\nabla\phi_0 + q\nabla\mathcal{G}\left\{\psi_1\right\}\right) \\
=&v_{||}\mathbf{b} + \frac{m_\sigma B_0}{\mathcal{J}}\left(\mathbf{v}_{E_0} + \mathbf{v}_\chi + \mathbf{v}_{\nabla B} + \mathbf{v}_c + \frac{v_{||}\mathcal{G}\left\{A_{1,||}\right\}}{B_0}\left(\nabla\times\mathbf{b}\right)_\perp\right),
\end{aligned} \tag{2.4.6}$$

where we expressed $B_{\varepsilon,||}^*$ in terms of the (exact) gyrokinetic phase-space Jacobian $\mathcal{J} = B_{\varepsilon,||}^*/m$ defined in equation (2.2.59). Furthermore, we introduced the drift velocities

$$\begin{aligned}
&\mathbf{v}_{\mathrm{E}_0} \equiv \frac{c}{B_0^2}\mathbf{B}_0\times\nabla\phi_0 \qquad \mathbf{v}_\chi \equiv \frac{c}{B_0^2}\mathbf{B}_0\times\nabla\mathcal{G}\{\chi_1\} \\
&\mathbf{v}_{\nabla\mathrm{B}} \equiv \frac{\mu c}{qB_0^2}\mathbf{B}_0\times\nabla B_0 \qquad \mathbf{v}_\mathrm{c} \equiv \frac{v_{||}^2}{\Omega}\left(\nabla\times\mathbf{b}\right)_\perp = \frac{v_{||}^2}{\Omega}\left(\mathbf{b}_0\times\left(\nabla\ln(B_0) + \frac{\beta}{2}\nabla\ln(p_0)\right)\right),
\end{aligned} \tag{2.4.7}$$

with the gyrokinetic potential being defined as $\chi_1 \equiv \psi_1 - \left(v_{||}/c\right)A_{1,||} = \phi_1 - \left(v_{||}/c\right)A_{1,||} - \mathbf{v}_\perp\cdot\mathbf{A}_{1,\perp}/c$. On the other hand, applying the operation $\left(\dot{\mathbf{X}}\cdot\right)$ gives the form of $\dot{v}_{||}$:

$$\dot{v}_{||} = -\frac{q\dot{\mathbf{X}}}{mv_{||}}\cdot\left(\nabla\phi_0 + \nabla\mathcal{G}\left\{\psi_1\right\} + \frac{1}{c}\frac{\partial\mathcal{G}\left\{A_{1,||}\right\}}{\partial t}\mathbf{b} + \frac{\mu}{q}\nabla B_0\right). \tag{2.4.8}$$

2.5 The gyrokinetic equation

Having derived the characteristics in phase-space along which the distribution function F_σ of species σ is advected, it is straightforward to combine equations (2.3.5) and equations (2.4.3)-(2.4.8) together with the splitting $F_\sigma = F_{0,\sigma} + F_{1,\sigma}$ to give

$$\begin{aligned}
&\frac{\partial F_{1,\sigma}}{\partial t} + \left[v_{||}\mathbf{b} + \frac{m_\sigma B_0}{\mathcal{J}} \left(\mathbf{v}_{E_0} + \mathbf{v}_\chi + \mathbf{v}_{\nabla B} + \mathbf{v}_c + \frac{v_{||}\mathcal{G}\left\{A_{1,||}\right\}}{B_0} \left(\nabla \times \mathbf{b}\right)_\perp \right) \right] \cdot \nabla \left(F_{0,\sigma} + F_{1,\sigma} \right) \\
&- \frac{q_\sigma}{m_\sigma v_{||}} \left[v_{||}\mathbf{b} + \frac{m_\sigma B_0}{\mathcal{J}} \left(\mathbf{v}_{E_0} + \mathbf{v}_\chi + \mathbf{v}_{\nabla B} + \mathbf{v}_c + \frac{v_{||}\mathcal{G}\left\{A_{1,||}\right\}}{B_0} \left(\nabla \times \mathbf{b}\right)_\perp \right) \right] \cdot \Bigg(\nabla \phi_0 \\
&+ \nabla \mathcal{G}\left\{\psi_1\right\} + \frac{1}{c}\frac{\partial \mathcal{G}\left\{A_{1,||}\right\}}{\partial t}\mathbf{b} + \frac{\mu}{q_\sigma}\nabla B_0 \Bigg) \frac{\partial}{\partial v_{||}} \left(F_{0,\sigma} + F_{1,\sigma} \right) = 0.
\end{aligned} \tag{2.5.1}$$

Setting all rapidly fluctuating contributions to zero gives an equation for the background distribution function, which then reads

$$\left[v_{||}\mathbf{b} + \frac{m_\sigma B_0}{\mathcal{J}} \left(\mathbf{v}_{E_0} + \mathbf{v}_{\nabla B} + \mathbf{v}_c \right) \right] \cdot \left(\nabla F_{0,\sigma} - \frac{q_\sigma}{m_\sigma v_{||}} \left(\nabla \phi_0 + \frac{\mu}{q_\sigma}\nabla B_0 \right) \frac{\partial F_{0,\sigma}}{\partial v_{||}} \right) = 0. \tag{2.5.2}$$

After some algebra and using the fact that, for example, $\mathbf{v}_{E_0} \cdot \nabla \mathcal{G}\left\{\chi_1\right\} = -\mathbf{v}_\chi \cdot \nabla \phi_0$, we can collect all terms that are of first order in the perturbation parameters ϵ_B, ϵ_δ and ϵ_ω, which gives

$$\begin{aligned}
\frac{\partial F_{1,\sigma}}{\partial t} =& - \left[v_{||}\mathbf{b} + \frac{m_\sigma B_0}{\mathcal{J}} \left(\mathbf{v}_\chi + \mathbf{v}_{\nabla \mathrm{B}} + \mathbf{v}_\mathrm{c} \right) \right] \cdot \nabla F_{1,\sigma} + \mathbf{b} \cdot \left(\nabla \phi_0 + \frac{\mu}{m_\sigma}\nabla B_0 \right) \frac{\partial F_{1,\sigma}}{\partial v_{||}} \\
&- \frac{m_\sigma B_0}{\mathcal{J}} \mathbf{v}_\chi \cdot \nabla F_{0,\sigma} + \frac{q_\sigma}{m_\sigma v_{||}} \frac{\partial F_{0,\sigma}}{\partial v_{||}} \left[v_{||}\mathbf{b} + \frac{m_\sigma B_0}{\mathcal{J}} \left(\mathbf{v}_\chi + \mathbf{v}_{\nabla \mathrm{B}} + \mathbf{v}_\mathrm{c} \right) \right] \cdot \nabla \mathcal{G}\{\psi_1\} \\
&+ \frac{q_\sigma}{m_\sigma c} \frac{\partial F_{0,\sigma}}{\partial v_{||}} \frac{\partial \mathcal{G}\{A_{1,||}\}}{\partial t} - \frac{m_\sigma B_0}{\mathcal{J}} \mathbf{v}_{\mathrm{E}_0} \cdot \left(\nabla F_{1,\sigma} + \frac{q_\sigma v_{||}}{c} \nabla \mathcal{G}\{A_{1,||}\} \right) \\
&- \frac{m_\sigma B_0}{\mathcal{J}} \left(\mathbf{v}_{\nabla \mathrm{B}} + \mathbf{v}_\mathrm{c} \right) \cdot \nabla F_{0,\sigma}.
\end{aligned} \tag{2.5.3}$$

It should be noted that neglecting the higher-order terms will make the underlying system non-conservative. However, it was concluded in [48] that the impact on the final heat flux is negligible, although retaining higher-order terms seems important in terms of entropy balance.

2.6 Gyrokinetic field equations

As was stated already in section 2.3, one obtains the gyrokinetic field equations by minimising the gyrokinetic action functional with respect to the electromagnetic fields ϕ_1, $A_{1,||}$ and $\mathbf{A}_{1,\perp}$,

which we will do in this section. We will start with the field action

$$I_{\text{field}}[\phi_1, \mathbf{A}_1] = \frac{1}{8\pi} \int_{t_1}^{t_2} \int \left(|\nabla\phi_0(\mathbf{x}') + \nabla\phi_1(\mathbf{x}', t')|^2 - |\nabla \times \mathbf{A}_0(\mathbf{x}') + \nabla \times \mathbf{A}_1(\mathbf{x}', t')|^2 \right) d^3x'\, dt',$$

given by equation (2.3.8). We will assume that the plasma background is quasineutral, equivalent to neglecting the gradient of ϕ_0. Furthermore, we will only retain gradients perpendicular to the magnetic field, as they are much larger than their parallel counterparts, as stated in section 2.1. Minimising the field action with respect to ϕ_1 will then give

$$\begin{aligned}
\frac{\delta I_{\text{field}}}{\delta\phi_1(\mathbf{x}, t)} =& \frac{1}{8\pi} \int_{t_1}^{t_2} \int \frac{\delta|\nabla_\perp\phi_1(\mathbf{x}', t')|^2}{\delta\phi_1(\mathbf{x}, t)}\, d^3x'\, dt' \\
=& \frac{1}{4\pi} \int_{t_1}^{t_2} \nabla_\perp\phi_1(\mathbf{x}', t') \cdot \nabla_\perp\delta(\mathbf{x} - \mathbf{x}')\delta(t - t')\, d^3x'\, dt' \\
=& -\frac{1}{4\pi} \int_{t_1}^{t_2} \nabla_\perp^2\phi_1(\mathbf{x}', t')\delta(\mathbf{x} - \mathbf{x}')\delta(t - t')\, d^3x'\, dt' \\
=& -\frac{1}{4\pi}\nabla_\perp^2\phi_1(\mathbf{x}, t).
\end{aligned} \tag{2.6.1}$$

Similarly, we get

$$\begin{aligned}
\frac{\delta I_{\text{field}}}{\delta\mathbf{A}_1(\mathbf{x}, t)} =& \frac{1}{4\pi} \int_{t_1}^{t_2} \int \left[\mathbf{B}_0(\mathbf{x}) + \mathbf{B}_1(\mathbf{x}', t')\right] \cdot \left[\nabla_\perp \times \delta(\mathbf{x} - \mathbf{x}')\delta(t - t')\right] d^3x'\, dt' \\
=& -\frac{1}{4\pi} \int_{t_1}^{t_2} \int \nabla_\perp \times \left[(\mathbf{B}_0 + \mathbf{B}_1)\right] \delta(\mathbf{x} - \mathbf{x}')\delta(t - t')\, d^3x' dt' \\
=& -\frac{1}{4\pi}\nabla_\perp \times \left[\mathbf{B}_0(\mathbf{x}) + \mathbf{B}_1(\mathbf{x}, t)\right].
\end{aligned} \tag{2.6.2}$$

Next, we have to look at the linear particle contribution to the total action, providing the gyrocenter moments of the field equations. Using equation (2.4.5) we can rewrite the particle

action functional as

$$
\begin{aligned}
I^{(\mathrm{lin})}_{\mathrm{part},\sigma}[\phi_1, \mathbf{A}_1, \mathbf{Z}_\sigma] =& \int_{\mathrm{t}_1}^{\mathrm{t}_2} \int \left(\mathcal{F}_{0,\sigma} + \mathcal{F}_{1,\sigma}\right) \left[\left(\frac{q_\sigma}{c} \mathbf{A}_0^* + \frac{q_\sigma}{c} \mathcal{G}\left\{ A_{1,||} \right\} \mathbf{b} \right) \cdot \dot{\mathbf{X}} + \frac{\mu B_0}{\Omega_\sigma} \dot{\Theta} \right] d^6 Z_0 \, dt' \\
& - \int_{\mathrm{t}_1}^{\mathrm{t}_2} \int \left(\mathcal{F}_{0,\sigma} + \mathcal{F}_{1,\sigma}\right) \left[\overline{H}_{0,\sigma} + \overline{H}_{1,\sigma} \right] d^6 Z_0 \, dt' \\
=& \int_{\mathrm{t}_1}^{\mathrm{t}_2} \int \left(\mathcal{F}_{0,\sigma} + \mathcal{F}_{1,\sigma}\right) \left[\frac{q_\sigma}{c} \mathbf{A}_0^* \cdot \dot{\mathbf{X}} + \frac{q_\sigma}{c} \mathcal{G}\left\{ A_{1,||} \right\} v_{||} + \frac{\mu B_0}{\Omega_\sigma} \dot{\Theta} \right] d^6 Z_0 \, dt' \\
& - \int_{\mathrm{t}_1}^{\mathrm{t}_2} \int \left(\mathcal{F}_{0,\sigma} + \mathcal{F}_{1,\sigma}\right) \left[\overline{H}_{0,\sigma} + \overline{H}_{1,\sigma} \right] d^6 Z_0 \, dt' \\
=& \int_{\mathrm{t}_1}^{\mathrm{t}_2} \int \left(\mathcal{F}_{0,\sigma} + \mathcal{F}_{1,\sigma}\right) \left[\mathcal{L}_{0,\sigma} - q_\sigma \mathcal{G}\left\{ \chi_1 \right\} \right] d^6 Z_0 \, dt',
\end{aligned}
\tag{2.6.3}
$$

where $\mathcal{L}_{0,\sigma}$ contains all the perturbation-free contributions of the single-particle Lagrangian (2.2.55). We can use conservation of probability density, so that $d\mathcal{F}_\sigma/dt = 0$, along the trajectories $\mathbf{Z}_\sigma(\mathbf{Z}_0, t_0; t)$, so that $\mathcal{F}_\sigma(\mathbf{Z}_0, t_0) = \mathcal{F}_\sigma(\mathbf{Z}_\sigma(\mathbf{Z}_0, t_0; t), t)$, which we will just abbreviate as $\mathcal{F}_\sigma(\mathbf{Z}, t)$ for convenience. We can further introduce the four-vectors $\mathcal{A}_\lambda = \left(\phi_1, A_{1,||}, \mathbf{A}_{1,\perp}\right)$ and $v_\lambda = (c, v_{||}, \mathbf{v}_\perp)$, so that χ_1 can be expressed as $\chi_1 = -\mathcal{A}_\lambda v^\lambda / c$ using a Minkowski metric.

Therefore, we can write the functional derivative of the linear action functional as

$$
\begin{aligned}
\frac{\delta I^{(\mathrm{lin})}_{\mathrm{part},\sigma}}{\delta \mathcal{A}_\nu(\mathbf{x}, t)} =& - q_\sigma \int_{\mathrm{t}_1}^{\mathrm{t}_2} \int \left(\mathcal{F}_{0,\sigma}(\mathbf{X}) + \mathcal{F}_{1,\sigma}(\mathbf{X}, v_{||}, \mu, t) \right) \frac{\delta}{\delta \mathcal{A}_\nu(\mathbf{x}, t)} \mathcal{G}\left\{ \chi_1\left(\mathbf{X} + \boldsymbol{\rho}, v_{||}, \mu, t' \right) \right\} d^6 Z_0 dt' \\
=& \frac{q_\sigma}{2\pi c} \int_{\mathrm{t}_1}^{\mathrm{t}_2} \int_0^{2\pi} \int \left(\mathcal{F}_{0,\sigma}(\mathbf{X}) + \mathcal{F}_{1,\sigma}(\mathbf{X}, v_{||}, \mu, t) \right) v^\lambda \frac{\delta \mathcal{A}_\lambda\left(\mathbf{X} + \boldsymbol{\rho}(\Theta'), v_{||}, \mu, t' \right)}{\delta \mathcal{A}_\nu(\mathbf{x}, t)} d^6 Z_0 d\Theta' dt' \\
=& \frac{q_\sigma}{2\pi c} \int_{\mathrm{t}_1}^{\mathrm{t}_2} \int_0^{2\pi} \int \left(\mathcal{F}_{0,\sigma}(\mathbf{X}) + \mathcal{F}_{1,\sigma}(\mathbf{X}, v_{||}, \mu, t) \right) v^\lambda \delta(t - t') \delta\left(\mathbf{X} + \boldsymbol{\rho} - \mathbf{x} \right) \delta^\nu_\lambda \, d^6 Z_0 d\Theta' dt' \\
=& \frac{2\pi q_\sigma}{2\pi c} \int_{-\infty}^{\infty} \int_0^{\infty} \int_0^{2\pi} \int \left(\mathcal{F}_{0,\sigma}(\mathbf{X}) + \mathcal{F}_{1,\sigma}(\mathbf{X}, v_{||}, \mu, t) \right) v^\nu \delta\left(\mathbf{X} + \boldsymbol{\rho} - \mathbf{x} \right) d^3 X_0 d\Theta' d\mu dv_{||} \\
\equiv& \frac{2\pi q_\sigma}{c} \int_{-\infty}^{\infty} \int_0^{\infty} \mathcal{K}\left\{ \left(\mathcal{F}_{0,\sigma} + \mathcal{F}_{1,\sigma} \right) v^\nu \right\} d\mu dv_{||},
\end{aligned}
\tag{2.6.4}
$$

where we have introduced the pull-back gyroaverage operator

$$\mathcal{K}\left\{u\right\}(\mathbf{x}) = \frac{1}{2\pi}\int \int_0^{2\pi} u(\mathbf{X})\delta(\mathbf{X}+\boldsymbol{\rho}-\mathbf{x})\,d\Theta d^3X = \frac{1}{2\pi}\int_0^{2\pi} u(\mathbf{x}-\boldsymbol{\rho})\,d\Theta \tag{2.6.5}$$

and renamed the variable Θ' to Θ.

Analogously, we have to perform the minimisation of the nonlinear contribution to the action functional, which reads

$$\begin{aligned} I^{(\mathrm{nonlin})}_{\mathrm{part},\sigma}[\phi_1,\mathbf{A}_1] = &\int_{t_1}^{t_2}\int \frac{q_\sigma^2}{2B_0c^2}\frac{\partial}{\partial\mu}\mathcal{G}\left\{\widetilde{(-\mathcal{A}_\lambda v^\lambda)}^{\,2}\right\}\mathcal{F}_{0,\sigma}(\mathbf{Z}_0)\,d^6Z_0\,dt' \\ &-\int_{t_1}^{t_2}\int \frac{q_\sigma^2}{2m_\sigma c^2}\mathcal{G}\left\{\widetilde{A_{1,\|}}^{\,2}\right\}\mathcal{F}_{0,\sigma}(\mathbf{Z}_0)\,d^6Z_0\,dt' \\ &-\int_{t_1}^{t_2}\int \frac{q_\sigma^2}{2m_\sigma c^2}\mathcal{G}\left\{|\mathbf{A}_{1,\perp}|^2\right\}\mathcal{F}_{0,\sigma}(\mathbf{Z}_0)\,d^6Z_0\,dt'. \end{aligned} \tag{2.6.6}$$

If we only focus on the first integral, we get

$$\begin{aligned} &\frac{\delta}{\delta\mathcal{A}_\nu(\mathbf{x},t)}\int_{t_1}^{t_2}\int \frac{q_\sigma^2}{2B_0c^2}\frac{\partial}{\partial\mu}\mathcal{G}\left\{\widetilde{(-\mathcal{A}_\lambda v^\lambda)}^{\,2}\right\}\mathcal{F}_{0,\sigma}(\mathbf{Z}_0)\,d^6Z_0\,dt' \\ &= -\frac{\delta}{\delta\mathcal{A}_\nu(\mathbf{x},t)}\int_{t_1}^{t_2}\int \frac{q_\sigma^2}{2B_0c^2}\frac{\partial\mathcal{F}_{0,\sigma}(\mathbf{Z}_0)}{\partial\mu}\left[\mathcal{G}\left\{\left(\mathcal{A}_\lambda v^\lambda\right)^2\right\}-\mathcal{G}\left\{\left(\mathcal{A}_\lambda v^\lambda\right)\right\}^2\right]d^6Z_0\,dt' \\ &= -\int \frac{q_\sigma^2}{c^2}\mathcal{G}\left\{\frac{\partial\mathcal{F}_{0,\sigma}(\mathbf{Z}_0)}{\partial\mu}\left(\mathcal{A}_\lambda v^\lambda\right)\frac{\delta\mathcal{A}_\lambda(\mathbf{X}+\boldsymbol{\rho},t)}{\delta\mathcal{A}_\nu(\mathbf{x},t)}\frac{v^\lambda}{B_0}\right\}d^6Z_0 \\ &\quad+\int \frac{q_\sigma^2}{c^2}\mathcal{G}\left\{\frac{\delta\mathcal{A}_\lambda(\mathbf{X}+\boldsymbol{\rho},t)}{\delta\mathcal{A}_\nu(\mathbf{x},t)}\frac{v^\lambda}{B_0}\mathcal{G}\left\{\mathcal{A}_\lambda v^\lambda\right\}\frac{\partial\mathcal{F}_{0,\sigma}(\mathbf{Z}_0)}{\partial\mu}\right\}d^6Z_0 \\ &= -\int \frac{q_\sigma^2}{c^2}\mathcal{G}\left\{\frac{\partial\mathcal{F}_{0,\sigma}}{\partial\mu}\left(\mathcal{A}_\lambda v^\lambda\right)\delta^\nu_\lambda\frac{v^\lambda}{B_0}\delta\left(\mathbf{X}+\boldsymbol{\rho}-\mathbf{x}\right)\right\}d^6Z_0 \\ &\quad+\int \frac{q_\sigma^2}{c^2}\mathcal{G}\left\{\delta^\nu_\lambda\frac{v^\lambda}{B_0}\delta\left(\mathbf{X}+\boldsymbol{\rho}-\mathbf{x}\right)\frac{\partial\mathcal{F}_{0,\sigma}}{\partial\mu}\mathcal{G}\left\{\mathcal{A}_\lambda v^\lambda\right\}\right\}d^6Z_0. \end{aligned} \tag{2.6.7}$$

Here, we have used that the gyroaverage of a gyroaveraged function is the function itself and that $\mathcal{F}_{0,\sigma}$ does not depend on Θ in the second-to-last row. Using again the pull-back

gyroaverage operator, we can rewrite the minimisation (2.6.7) as

$$\begin{aligned}
&-\frac{q_\sigma^2}{c^2}\int_{-\infty}^{\infty}\int_{0}^{\infty}\int_{0}^{2\pi}\left[\frac{\partial \mathcal{F}_{0,\sigma}}{\partial \mu}\left(\mathcal{A}_\lambda v^\lambda\right)\frac{v^\nu}{B_0}-\mathcal{K}\left\{\frac{\partial \mathcal{F}_{0,\sigma}}{\partial \mu}\frac{v^\nu}{B_0}\mathcal{G}\left\{\mathcal{A}_\lambda v^\lambda\right\}\right\}\right]\, d\Theta d\mu dv_{||}\\
=&\frac{q_\sigma^2}{c}\int_{-\infty}^{\infty}\int_{0}^{\infty}\int_{0}^{2\pi}\left[\frac{\partial \mathcal{F}_{0,\sigma}}{\partial \mu}\chi_1\frac{v^\nu}{B_0}-\mathcal{K}\left\{\frac{\partial \mathcal{F}_{0,\sigma}}{\partial \mu}\frac{v^\nu}{B_0}\mathcal{G}\left\{\chi_1\right\}\right\}\right]\, d\Theta d\mu dv_{||}.
\end{aligned} \tag{2.6.8}$$

Similarly, we obtain

$$\begin{aligned}
&-\frac{\delta}{\delta A_{1,||}(\mathbf{x},t)}\int_{t_1}^{t_2}\int \frac{q_\sigma^2}{2m_\sigma c^2}\mathcal{G}\left\{\widetilde{A_{1,||}}^2\right\}\mathcal{F}_{0,\sigma}(\mathbf{Z}_0)\, d^6Z_0\, dt\\
=&-\frac{q_\sigma^2}{m_\sigma c^2}\int_{-\infty}^{\infty}\int_{0}^{\infty}\int_{0}^{2\pi}\left[A_{1,||}(\mathbf{x},t)\mathcal{F}_{0,\sigma}-\mathcal{K}\left\{\mathcal{F}_{0,\sigma}\mathcal{G}\left\{A_{1,||}\right\}\right\}\right]\, d\Theta d\mu dv_{||}\\
=&-\frac{q_\sigma^2}{m_\sigma c^2}\left[n_{0,\sigma}A_{1,||}(\mathbf{x},t)-2\pi\int_{-\infty}^{\infty}\int_{0}^{\infty}\mathcal{K}\left\{\mathcal{F}_{0,\sigma}\mathcal{G}\left\{A_{1,||}\right\}\right\}\, d\mu dv_{||}\right]
\end{aligned} \tag{2.6.9}$$

and

$$\begin{aligned}
&-\frac{\delta}{\delta \mathbf{A}_{1,\perp}(\mathbf{x},t)}\int_{t_1}^{t_2}\int \frac{q_\sigma^2}{2m_\sigma c^2}\mathcal{G}\left\{|\mathbf{A}_{1,\perp}|^2\right\}\mathcal{F}_{0,\sigma}(\mathbf{Z}_0)\, d^6Z_0\, dt'\\
=&-\frac{q_\sigma^2}{m_\sigma c^2}\int_{-\infty}^{\infty}\int_{0}^{\infty}\int_{0}^{2\pi}\mathcal{F}_{0,\sigma}\, d\Theta d\mu dv_{||}\mathbf{A}_{1,\perp}(\mathbf{x},t)\\
=&-\frac{q_\sigma^2 n_{0,\sigma}}{m_\sigma c^2}\mathbf{A}_{1,\perp}(\mathbf{x},t).
\end{aligned} \tag{2.6.10}$$

Putting everything together, we can, therefore, write the gyrokinetic Poisson equation as

$$\begin{aligned}
&-\frac{1}{4\pi}\nabla_\perp^2\phi_1-\sum_\sigma q_\sigma^2\int_{-\infty}^{\infty}\int_{0}^{\infty}\int_{0}^{2\pi}\left[\frac{1}{B_0}\frac{\partial \mathcal{F}_{0,\sigma}}{\partial \mu}\phi_1-\mathcal{K}\left\{\frac{1}{B_0}\frac{\partial \mathcal{F}_{0,\sigma}}{\partial \mu}\mathcal{G}\left\{\phi_1\right\}\right\}\right]d\Theta d\mu dv_{||}\\
=&-\sum_\sigma\frac{q_\sigma^2}{c}\int_{-\infty}^{\infty}\int_{0}^{\infty}\int_{0}^{2\pi}v_{||}\left[\frac{1}{B_0}\frac{\partial \mathcal{F}_{0,\sigma}}{\partial \mu}A_{1,||}-\mathcal{K}\left\{\frac{1}{B_0}\frac{\partial \mathcal{F}_{0,\sigma}}{\partial \mu}\mathcal{G}\left\{A_{1,||}\right\}\right\}\right]d\Theta d\mu dv_{||}\\
&-\sum_\sigma\frac{q_\sigma^2}{c}\int_{-\infty}^{\infty}\int_{0}^{\infty}\int_{0}^{2\pi}\left[\frac{1}{B_0}\frac{\partial \mathcal{F}_{0,\sigma}}{\partial \mu}\mathbf{A}_{1,\perp}\cdot\mathbf{v}_\perp(\mu,\Theta)-\mathcal{K}\left\{\frac{1}{B_0}\frac{\partial \mathcal{F}_{0,\sigma}}{\partial \mu}\mathcal{G}\left\{\mathbf{A}_{1,\perp}\cdot\mathbf{v}_\perp(\mu,\Theta)\right\}\right\}\right]d\Theta d\mu dv_{||}\\
&+2\pi\sum_\sigma q_\sigma\int_{-\infty}^{\infty}\int_{0}^{\infty}\mathcal{K}\left\{\mathcal{F}_{0,\sigma}+\mathcal{F}_{1,\sigma}\right\}\, d\mu dv_{||}.
\end{aligned} \tag{2.6.11}$$

We can additionally use that $\sum_\sigma q_\sigma \int_{-\infty}^{\infty}\int_0^\infty \mathcal{K}\{\mathcal{F}_{0,\sigma}\}\, d\mu dv_{||} = \sum_\sigma q_\sigma n_{0,\sigma} = 0$, since we assumed quasineutrality of the background earlier. Furthermore, integration over Θ will make the first term containing $\mathbf{A}_{1,\perp}$ in equation (2.6.11) vanish. Therefore, the gyrokinetic Poisson equation can be written as:

$$\begin{aligned}
&-\frac{1}{4\pi}\nabla_\perp^2\phi_1 - 2\pi\sum_\sigma q_\sigma^2 \int_{-\infty}^{\infty}\int_0^\infty \left[\frac{1}{B_0}\frac{\partial \mathcal{F}_{0,\sigma}}{\partial \mu}\phi_1 - \mathcal{K}\left\{\frac{1}{B_0}\frac{\partial \mathcal{F}_{0,\sigma}}{\partial \mu}\mathcal{G}\{\phi_1\}\right\}\right] d\mu dv_{||} \\
=&-2\pi\sum_\sigma \frac{q_\sigma^2}{c}\int_{-\infty}^{\infty}\int_0^\infty v_{||}\left[\frac{1}{B_0}\frac{\partial \mathcal{F}_{0,\sigma}}{\partial \mu}A_{1,||} - \mathcal{K}\left\{\frac{1}{B_0}\frac{\partial \mathcal{F}_{0,\sigma}}{\partial \mu}\mathcal{G}\{A_{1,||}\}\right\}\right] d\mu dv_{||} \\
&+2\pi\sum_\sigma \frac{q_\sigma^2}{c}\int_{-\infty}^{\infty}\int_0^\infty \mathcal{K}\left\{\frac{1}{B_0}\frac{\partial \mathcal{F}_{0,\sigma}}{\partial \mu}\mathcal{G}\{\mathbf{A}_{1,\perp}\cdot\mathbf{v}_\perp(\mu,\Theta)\}\right\} d\mu dv_{||} \\
&+2\pi\sum_\sigma q_\sigma \int_{-\infty}^{\infty}\int_0^\infty \mathcal{K}\{\mathcal{F}_{1,\sigma}\}\, d\mu dv_{||}.
\end{aligned} \tag{2.6.12}$$

Ampère's law, on the other hand, reads

$$\begin{aligned}
&-\frac{1}{4\pi}\nabla_\perp\times[\mathbf{B}_0+\mathbf{B}_1] + \sum_\sigma \frac{q_\sigma^2}{c}\int_{-\infty}^{\infty}\int_0^\infty\int_0^{2\pi}\left[\frac{1}{B_0}\frac{\partial \mathcal{F}_{0,\sigma}}{\partial \mu}\chi_1\mathbf{v} - \mathcal{K}\left\{\frac{1}{B_0}\frac{\partial \mathcal{F}_{0,\sigma}}{\partial \mu}\mathbf{v}\mathcal{G}\{\chi_1\}\right\}\right] d\Theta d\mu dv_{||} \\
&-\sum_\sigma \frac{q_\sigma^2}{m_\sigma c^2}\mathbf{b}\left[n_{0,\sigma}A_{1,||}(\mathbf{x},t) - 2\pi\int_{-\infty}^{\infty}\int_0^\infty \mathcal{K}\left\{\mathcal{F}_{0,\sigma}\mathcal{G}\left\{A_{1,||}\right\}\right\} d\mu dv_{||}\right] - \sum_\sigma \frac{q_\sigma^2 n_{0,\sigma}}{m_\sigma c^2}\mathbf{A}_{1,\perp}(\mathbf{x},t) \\
=&-2\pi\sum_\sigma \frac{q_\sigma}{c}\int_{-\infty}^{\infty}\int_0^\infty \mathcal{K}\{\mathbf{v}(\mathcal{F}_{0,\sigma}+\mathcal{F}_{1,\sigma})\}\, d\mu dv_{||}.
\end{aligned} \tag{2.6.13}$$

One can simplify equation (2.6.13) again by noticing that it is an equation for the total magnetic field. However, it is easy to identify the equilibrium current as

$$\mathbf{J}_{0,\sigma} \equiv 2\pi q_\sigma \int_{-\infty}^{\infty}\int_0^\infty \mathcal{K}\{\mathbf{v}\mathcal{F}_{0,\sigma}\}\, d\mu dv_{||} = 2\pi q_\sigma \int_{-\infty}^{\infty}\int_0^\infty \mathbf{v}\mathcal{F}_{0,\sigma}\, d\mu dv_{||},$$

which we assume satisfies Maxwell's equations on equilibrium scales, so that this term and

the one containing the curl of $\mathbf{B}_0$ will cancel each other. Furthermore, we have

$$\begin{aligned}
&\int_{-\infty}^{\infty}\int_{0}^{\infty}\int_{0}^{2\pi} \frac{1}{B_0}\frac{\partial \mathcal{F}_{0,\sigma}}{\partial \mu}\chi_1 \mathbf{v}\, d\Theta d\mu dv_{||} \\
=&\int_{-\infty}^{\infty}\int_{0}^{\infty}\int_{0}^{2\pi} \frac{1}{B_0}\frac{\partial \mathcal{F}_{0,\sigma}}{\partial \mu}\left[\phi_1 - \frac{v_{||}}{c}A_{1,||} - \frac{1}{c}\mathbf{v}_\perp\cdot\mathbf{A}_{1,\perp}\right]\left[v_{||}\mathbf{b}+\mathbf{v}_\perp\right]\, d\Theta d\mu dv_{||} \\
=&2\pi\int_{-\infty}^{\infty}\int_{0}^{\infty} \frac{1}{B_0}\frac{\partial \mathcal{F}_{0,\sigma}}{\partial \mu}\left[\mathbf{b}\left(v_{||}\phi_1 - \frac{v_{||}^2}{c}A_{1,||}\right) - \frac{v_\perp^2}{2c}\mathbf{A}_{1,\perp}\right] d\mu\, dv_{||} \\
=&2\pi\int_{-\infty}^{\infty}\int_{0}^{\infty} \frac{\mathbf{b}}{B_0}\frac{\partial \mathcal{F}_{0,\sigma}}{\partial \mu}\left(v_{||}\phi_1 - \frac{v_{||}^2}{c}A_{1,||}\right) d\mu\, dv_{||} + 2\pi\int_{-\infty}^{\infty}\int_{0}^{\infty}\frac{\mathcal{F}_{0,\sigma}}{m_\sigma c}\mathbf{A}_{1,\perp}\, d\mu\, dv_{||} \\
=&2\pi\int_{-\infty}^{\infty}\int_{0}^{\infty} \frac{\mathbf{b}}{B_0}\frac{\partial \mathcal{F}_{0,\sigma}}{\partial \mu}\left(v_{||}\phi_1 - \frac{v_{||}^2}{c}A_{1,||}\right) d\mu\, dv_{||} + \frac{n_{0,\sigma}}{m_\sigma c}\mathbf{A}_{1,\perp},
\end{aligned} \tag{2.6.14}$$

where we have used that $\mathbf{A}_{1,\perp} = A_1^1\mathbf{e}_1 + A_1^2\mathbf{e}_2$ and $\mathbf{v}_\perp = v_\perp \mathbf{c}(\Theta) = v_\perp(-\mathbf{e}_1\cos(\Theta) - \mathbf{e}_2\sin(\Theta))$.

Therefore, Ampère's law for the perturbed magnetic field $\mathbf{B}_1$ can be written as

$$\begin{aligned}
&-\frac{1}{4\pi}\nabla_\perp\times\mathbf{B}_1 \\
&+\mathbf{b}\sum_\sigma \frac{2\pi q_\sigma^2}{c}\int_{-\infty}^{\infty}\int_{0}^{\infty} v_{||}\left[\frac{1}{B_0}\frac{\partial \mathcal{F}_{0,\sigma}}{\partial \mu}\phi_1 - \mathcal{K}\left\{\frac{1}{B_0}\frac{\partial \mathcal{F}_{0,\sigma}}{\partial \mu}\mathcal{G}\left\{\phi_1\right\}\right\}\right] d\mu\, dv_{||} \\
&-\mathbf{b}\sum_\sigma \frac{2\pi q_\sigma^2}{c^2}\int_{-\infty}^{\infty}\int_{0}^{\infty} v_{||}\left[\mathcal{K}\left\{\frac{1}{B_0}\frac{\partial \mathcal{F}_{0,\sigma}}{\partial \mu}\mathcal{G}\left\{\mathbf{v}_\perp\cdot\mathbf{A}_{1,\perp}\right\}\right\}\right] d\mu\, dv_{||} \\
&-\mathbf{b}\sum_\sigma \frac{2\pi q_\sigma^2}{c^2}\int_{-\infty}^{\infty}\int_{0}^{\infty} v_{||}^2\left[\frac{1}{B_0}\frac{\partial \mathcal{F}_{0,\sigma}}{\partial \mu}A_{1,||} - \mathcal{K}\left\{\frac{1}{B_0}\frac{\partial \mathcal{F}_{0,\sigma}}{\partial \mu}\mathcal{G}\left\{A_{1,||}\right\}\right\}\right] d\mu\, dv_{||} \\
&-\mathbf{b}\sum_\sigma \frac{2\pi q_\sigma^2}{m_\sigma c^2}\int_{-\infty}^{\infty}\int_{0}^{\infty} \left[\mathcal{F}_{0,\sigma}A_{1,||} - \mathcal{K}\left\{\mathcal{F}_{0,\sigma}\mathcal{G}\left\{A_{1,||}\right\}\right\}\right] d\mu\, dv_{||} \\
&-\sum_\sigma \frac{2\pi q_\sigma^2}{c}\int_{-\infty}^{\infty}\int_{0}^{\infty} \mathcal{K}\left\{\frac{1}{B_0}\frac{\partial \mathcal{F}_{0,\sigma}}{\partial \mu}\mathbf{v}_\perp\mathcal{G}\left\{\chi_1\right\}\right\} d\mu\, dv_{||} \\
=&-2\pi\mathbf{b}\sum_\sigma \frac{q_\sigma}{c}\int_{-\infty}^{\infty}\int_{0}^{\infty} v_{||}\mathcal{K}\left\{\mathcal{F}_{1,\sigma}\right\} d\mu dv_{||} - 2\pi\sum_\sigma\frac{q_\sigma}{c}\int_{-\infty}^{\infty}\int_{0}^{\infty}\mathcal{K}\left\{\mathbf{v}_\perp\mathcal{F}_{1,\sigma}\right\} d\mu dv_{||}.
\end{aligned} \tag{2.6.15}$$

Both equations (2.6.12) and (2.6.15) can be further simplified by transforming the dependence on the vector quantity $\mathbf{A}_{1,\perp}$ into dependencies on the scalar parallel magnetic field $B_{1,||} = \nabla_\perp \times \mathbf{A}_{1,\perp}$. To do so, we first consider the quantity $(q_\sigma/c)\mathcal{G}\left\{\mathbf{A}_{1,\perp}\cdot\mathbf{v}_\perp\right\}$, which can

be rewritten as

$$\frac{q_\sigma}{c}\mathcal{G}\left\{\mathbf{A}_{1,\perp}(\mathbf{X}+\boldsymbol{\rho},t)\cdot\mathbf{v}_\perp(\Theta)\right\}=\frac{q_\sigma}{2c\pi}\int_0^{2\pi}\mathbf{A}_{1,\perp}\cdot\mathbf{v}_\perp\,d\Theta=\frac{q_\sigma\Omega_\sigma}{2c\pi}\int_0^{2\pi}\mathbf{A}_{1,\perp}\cdot\left[\boldsymbol{\rho}(\Theta)\times\mathbf{b}\right]d\Theta. \tag{2.6.16}$$

One can then interpret this expression as integrating $A_{1,\perp}$ along a gyroring perpendicular to the magnetic field with the differential line element $d\mathbf{l}=[\boldsymbol{\rho}(\Theta)\times\mathbf{b}]\,d\Theta$. Using Stokes' theorem, this integral can be transformed into an integral of the surface contained by a given gyroring, namely

$$\begin{aligned}\int_0^{2\pi}\mathbf{A}_{1,\perp}\cdot\left[\boldsymbol{\rho}(\Theta)\times\mathbf{b}\right]d\Theta&=-\int_0^{2\pi}\left[\int_0^{\rho}(\nabla\times\mathbf{A}_{1,\perp})\cdot\mathbf{b}\,\rho' d\rho'\right]d\Theta\\&=-\int_0^{2\pi}\left[\int_0^{\rho}B_{1,\parallel}\,\rho' d\rho'\right]d\Theta.\end{aligned} \tag{2.6.17}$$

We now introduce the "gyrodisk-integral" operator

$$\mathcal{G}_\mathrm{D}\left\{u\right\}\equiv\frac{q_\sigma\Omega_\sigma}{2\pi c}\int_0^{2\pi}\int_0^{\rho}u(\mathbf{X}+\boldsymbol{\rho}'(\Theta))\rho' d\rho'\,d\Theta, \tag{2.6.18}$$

so that equation (2.6.16) can be written as

$$\frac{q_\sigma\Omega_\sigma}{2\pi c}\int_0^{2\pi}\mathbf{A}_{1,\perp}\cdot\left[\boldsymbol{\rho}(\Theta)\times\mathbf{b}\right]d\Theta=-\mathcal{G}_\mathrm{D}\left\{B_{1,\parallel}(\mathbf{X}+\boldsymbol{\rho},t)\right\}. \tag{2.6.19}$$

Using the identity

$$\oint_{\partial S}g d\mathbf{l}=-\int_S\nabla g\times d\mathbf{S} \tag{2.6.20}$$

for a function g and a surface S, we can derive the following relations in analogy:

$$\mathcal{G}\left\{g\mathbf{v}_\perp\right\}=\frac{c}{q_\sigma}\mathcal{G}_\mathrm{D}\left\{\nabla_\perp g\times\mathbf{b}\right\}, \tag{2.6.21}$$

$$\mathcal{K}\left\{g\mathbf{v}_\perp\right\}=-\frac{c}{q_\sigma}\mathcal{K}_\mathrm{D}\left\{\nabla_\perp g\times\mathbf{b}\right\}, \tag{2.6.22}$$

where we have introduced the pull-back gyrodisk-integral operator

$$\mathcal{K}_\mathrm{D}\left\{u\right\}\equiv\frac{q_\sigma\Omega_\sigma}{2\pi c}\int_0^{2\pi}\int_0^{\rho}u(\mathbf{x}-\boldsymbol{\rho}'(\Theta))\rho' d\rho'\,d\Theta. \tag{2.6.23}$$

The difference in the sign between equations (2.6.21) and (2.6.22) arises from the fact that the orbits in both cases will run in opposite directions. This can be understood by using the relation between $\mathbf{x}$, $\mathbf{X}$, and $\boldsymbol{\rho}$ from equation (2.2.4). With this, we can express the line element

as $d\mathbf{l} = [(\mathbf{x} - \mathbf{X}) \times \mathbf{b}]\, d\Theta$. The gyroaverage is evaluated at constant gyrocentre position $\mathbf{X}$, which means one can transform into a coordinate system where the gyrocentre sits at the origin, meaning that $\mathbf{X} = 0$. In this system, the line element will be given by $d\mathbf{l} = [\mathbf{x} \times \mathbf{b}]\, d\Theta$ which means the curve will run in a counter-clockwise manner relative to $\mathbf{b}$. On the other hand, the pull-back average is evaluated at constant particle position so that one can choose a coordinate system where $\mathbf{x} = 0$. In there, the line element will be $d\mathbf{l} = [(-\mathbf{X}) \times \mathbf{b}]\, d\Theta$, which means that the curve will now run clockwise relative to the magnetic field vector $\mathbf{b}$.

With the help of the disk integrals, Poisson's equation (2.6.12) can be rewritten as

$$\begin{aligned}
&-\frac{1}{4\pi}\nabla_\perp^2\phi_1 - 2\pi\sum_\sigma q_\sigma^2 \int_{-\infty}^{\infty}\int_0^{\infty}\left[\frac{1}{B_0}\frac{\partial\mathcal{F}_{0,\sigma}}{\partial\mu}\phi_1 - \mathcal{K}\left\{\frac{1}{B_0}\frac{\partial\mathcal{F}_{0,\sigma}}{\partial\mu}\mathcal{G}\left\{\phi_1\right\}\right\}\right] d\mu dv_{||} \\
&= -2\pi\sum_\sigma \frac{q_\sigma^2}{c}\int_{-\infty}^{\infty}\int_0^{\infty} v_{||}\left[\frac{1}{B_0}\frac{\partial\mathcal{F}_{0,\sigma}}{\partial\mu}A_{1,||} - \mathcal{K}\left\{\frac{1}{B_0}\frac{\partial\mathcal{F}_{0,\sigma}}{\partial\mu}\mathcal{G}\left\{A_{1,||}\right\}\right\}\right] d\mu dv_{||} \\
&- 2\pi\sum_\sigma q_\sigma \int_{-\infty}^{\infty}\int_0^{\infty}\mathcal{K}\left\{\frac{1}{B_0}\frac{\partial\mathcal{F}_{0,\sigma}}{\partial\mu}\mathcal{G}_{\mathrm{D}}\left\{B_{1,||}\right\}\right\} d\mu dv_{||} \\
&+ 2\pi\sum_\sigma q_\sigma \int_{-\infty}^{\infty}\int_0^{\infty}\mathcal{K}\left\{\mathcal{F}_{1,\sigma}\right\}\, d\mu dv_{||}.
\end{aligned} \tag{2.6.24}$$

Ampère's law can be solved more easily by splitting it into its parallel and perpendicular components. The parallel component reads

$$\begin{aligned}
&-\frac{1}{4\pi}\left(\nabla_\perp \times \mathbf{B}_1\right)\cdot\mathbf{b} \\
&+\sum_\sigma \frac{2\pi q_\sigma^2}{c}\int_{-\infty}^{\infty}\int_0^{\infty} v_{||}\left[\frac{1}{B_0}\frac{\partial\mathcal{F}_{0,\sigma}}{\partial\mu}\phi_1 - \mathcal{K}\left\{\frac{1}{B_0}\frac{\partial\mathcal{F}_{0,\sigma}}{\partial\mu}\mathcal{G}\left\{\phi_1\right\}\right\}\right] d\mu\, dv_{||} \\
&+\sum_\sigma \frac{2\pi q_\sigma^2}{c}\int_{-\infty}^{\infty}\int_0^{\infty} v_{||}\mathcal{K}\left\{\frac{1}{q_\sigma B_0}\frac{\partial\mathcal{F}_{0,\sigma}}{\partial\mu}\mathcal{G}_{\mathrm{D}}\left\{B_{1,||}\right\}\right\} d\mu\, dv_{||} \\
&-\sum_\sigma \frac{2\pi q_\sigma^2}{c^2}\int_{-\infty}^{\infty}\int_0^{\infty} v_{||}^2\left[\frac{1}{B_0}\frac{\partial\mathcal{F}_{0,\sigma}}{\partial\mu}A_{1,||} - \mathcal{K}\left\{\frac{1}{B_0}\frac{\partial\mathcal{F}_{0,\sigma}}{\partial\mu}\mathcal{G}\left\{A_{1,||}\right\}\right\}\right] d\mu\, dv_{||} \\
&-\sum_\sigma \frac{2\pi q_\sigma^2}{m_\sigma c^2}\int_{-\infty}^{\infty}\int_0^{\infty}\left[\mathcal{F}_{0,\sigma}A_{1,||} - \mathcal{K}\left\{\mathcal{F}_{0,\sigma}\mathcal{G}\left\{A_{1,||}\right\}\right\}\right] d\mu\, dv_{||} \\
&= -2\pi\sum_\sigma \frac{q_\sigma}{c}\int_{-\infty}^{\infty}\int_0^{\infty} v_{||}\mathcal{K}\left\{\mathcal{F}_{1,\sigma}\right\}\, d\mu dv_{||}.
\end{aligned} \tag{2.6.25}$$

On the other hand, the perpendicular component of Ampère's law can now be expressed as

an equation for $B_{1,||}$:

$$\begin{aligned}
&-\frac{1}{4\pi}\left(\nabla_\perp \times \mathbf{B}_1\right)_\perp = -\frac{1}{4\pi}\nabla_\perp B_{1,||} \times \mathbf{b} \\
&= -2\pi\left[\sum_\sigma \int_{-\infty}^{\infty}\int_0^\infty \mathcal{K}_\mathrm{D}\left\{\nabla_\perp\left(\frac{q_\sigma}{B_0}\frac{\partial \mathcal{F}_{0,\sigma}}{\partial \mu}\mathcal{G}\left\{\chi_1\right\}\right)\right\} d\mu\, dv_{||}\right] \times \mathbf{b} \\
&+ 2\pi\left[\sum_\sigma \int_{-\infty}^{\infty}\int_0^\infty \mathcal{K}_\mathrm{D}\left\{\nabla_\perp \mathcal{F}_{1,\sigma}\right\}\, d\mu dv_{||}\right] \times \mathbf{b}.
\end{aligned} \tag{2.6.26}$$

If we now use the assumption of gyrokinetic theory that $k_\perp/L \ll 1$, pulling the perpendicular gradient out of the disk integrals and therefore factoring it out of the entire equation is justified. This approximation can also be made on the Lagrangian level already if the Lagrangian is written in terms of $B_{1,||}$ instead of $\mathbf{A}_{1,\perp}$ and the gradient is taken out of the disk integral there. Therefore, the perpendicular component of Ampère's law can be rewritten in its final form, which reads

$$\begin{aligned}
&\frac{B_{1,||}}{4\pi} - 2\pi\sum_\sigma \int_{-\infty}^{\infty}\int_0^\infty \mathcal{K}_\mathrm{D}\left\{\left(\frac{1}{B_0}\frac{\partial \mathcal{F}_{0,\sigma}}{\partial \mu}\mathcal{G}_\mathrm{D}\left\{B_{1,||}\right\}\right)\right\} d\mu\, dv_{||} \\
&= \sum_\sigma \int_{-\infty}^{\infty}\int_0^\infty \mathcal{K}_\mathrm{D}\left\{\mathcal{F}_{1,\sigma}\right\}\, d\mu dv_{||} + 2\pi\sum_\sigma \int_{-\infty}^{\infty}\int_0^\infty \mathcal{K}_\mathrm{D}\left\{\left(\frac{q_\sigma}{B_0}\frac{\partial \mathcal{F}_{0,\sigma}}{\partial \mu}\mathcal{G}\left\{\phi_1\right\}\right)\right\} d\mu\, dv_{||} \\
&- 2\pi\sum_\sigma \int_{-\infty}^{\infty}\int_0^\infty \mathcal{K}_\mathrm{D}\left\{\left(\frac{q_\sigma v_{||}}{B_0 c}\frac{\partial \mathcal{F}_{0,\sigma}}{\partial \mu}\mathcal{G}\left\{A_{1,||}\right\}\right)\right\} d\mu\, dv_{||}.
\end{aligned} \tag{2.6.27}$$

2.7 Choice of Maxwellian background and other assumptions in GENE-3D

In this section, we will introduce additional assumptions employed by the codes of the GENE family. For most applications dealing with gyrokinetic turbulence in the core of fusion devices, a popular choice of a background distribution function is that of a local Maxwellian, meaning that we choose

$$F_{0,\sigma} = F_{\mathrm{M},\sigma} = n_{0,\sigma}(x)\left(\frac{2\pi T_{0,\sigma}(x)}{m_\sigma}\right)^{-3/2}\exp\left(-\frac{m_\sigma v_{||}^2/2 + \mu B_0(\mathbf{X})}{T_{0,\sigma}(x)}\right), \tag{2.7.1}$$

where the density is given by $n_{0,\sigma}(x) = N_{0,\sigma}(x)\exp(-q_\sigma\phi_0(\mathbf{X})/T_{0,\sigma}(x))$ for some function $N_{0,\sigma}(x)$. This choice of this function can be motivated by considering plasmas at low collisionality [13]. It follows immediately from the quasineutrality condition $\sum_\sigma n_{0,\sigma} = 0$ that the background potential ϕ_0 can only depend on the flux-surface label, meaning that $\phi_0 = \phi_0(x)$.

In addition, we can easily express the derivatives of $F_{0,\sigma}$ in terms of the function itself, via

$$\begin{aligned}
\frac{\partial F_{\mathrm{M},\sigma}}{\partial v_{||}} &= -\frac{m_\sigma v_{||}}{T_{0,\sigma}} F_{\mathrm{M},\sigma}, \\
\frac{\partial F_{\mathrm{M},\sigma}}{\partial \mu} &= -\frac{B_0}{T_{0,\sigma}} F_{\mathrm{M},\sigma}, \\
\nabla F_{\mathrm{M},\sigma} &= \left[\nabla \ln(n_{0,\sigma}) + \nabla \ln(T_{0,\sigma}) \left(\frac{m_\sigma v_{||}^2/2 + \mu B_0}{T_{0,\sigma}} - \frac{3}{2} \right) - \nabla \ln(B_0) \frac{\mu B_0}{T_{0,\sigma}} \right] F_{\mathrm{M},\sigma}.
\end{aligned} \tag{2.7.2}$$

Furthermore, we neglect the contribution of magnetic field curvature to the perturbed magnetic field, meaning that we will assume that $\mathbf{B}_{1,\perp} = \nabla_\perp \times (A_{1,||}\mathbf{b}) \approx \nabla_\perp A_{1,||} \times \mathbf{b}$. This approximation is of no concern for the gyrokinetic equation (2.5.3), where the corresponding terms were already eliminated. Although this approximation can be done on the Lagrangian level in terms of the electromagnetic field equations, it results in the perturbed magnetic field to be not divergence-free anymore [39]. Therefore, it will be interesting to test whether there are scenarios in which retaining the corresponding terms in Ampère's law will have an impact on turbulence dynamics in the future.

Finally, we will use the approximation $B^*_{\varepsilon,||} \approx B_0$, meaning we will only retain the leading-order term. We discussed already in section 2.2 that the Jacobian will be approximated to not depend on the perturbed vector potential $A_{1,||}$ not having a significant impact when simulations are compared with those using a canonical model, which is by nature free of this dependence. However, retaining the curvature term of $B^*_{0,||}$ will also result in higher-order corrections than the ones that are retained in the gyrokinetic equation (2.5.3). Therefore, we assume $B^*_{\varepsilon,||} \approx B_0$, which means we will approximate the phase-space Jacobian as $\mathcal{J} \approx B_0/m_\sigma$. Therefore, the modified distribution function takes the form $\mathcal{F}_{0,\sigma} \approx F_{\mathrm{M},\sigma} B_0/m_\sigma$.

Using these assumptions, the gyrokinetic Maxwell's equation and the gyrokinetic Vlasov equation simplify significantly. Starting from equation (2.5.3) the latter can be written as

$$\begin{aligned}
\frac{\partial F_{1,\sigma}}{\partial t} =& - \left[v_{||}\mathbf{b}_0 + (\mathbf{v}_\chi + \mathbf{v}_{\nabla \mathrm{B}} + \mathbf{v}_\mathrm{c}) \right] \cdot \nabla F_{1,\sigma} + \frac{\mu}{m_\sigma} \mathbf{b}_0 \cdot \nabla B_0 \frac{\partial F_{1,\sigma}}{\partial v_{||}} \\
& - \mathbf{v}_\chi \cdot \left[\nabla \ln(n_{0,\sigma}) + \nabla \ln(T_{0,\sigma}) \left(\frac{m_\sigma v_{||}^2/2 + \mu B_0}{T_{0,\sigma}} - \frac{3}{2} \right) \right] F_{\mathrm{M},\sigma} \\
& - \frac{q_\sigma F_{\mathrm{M},\sigma}}{T_{0,\sigma}} \left[v_{||}\mathbf{b}_0 + (\mathbf{v}_\chi + \mathbf{v}_{\nabla \mathrm{B}} + \mathbf{v}_\mathrm{c}) \right] \cdot \nabla \mathcal{G}\{\psi_1\} \\
& - \frac{q_\sigma v_{||}}{c} \frac{F_{\mathrm{M},\sigma}}{T_{0,\sigma}} \frac{\partial \mathcal{G}\{A_{1,||}\}}{\partial t} - \mathbf{v}_{\mathrm{E}_0} \cdot \left(\nabla F_{1,\sigma} + \frac{q_\sigma v_{||}}{c} \nabla \mathcal{G}\{A_{1,||}\} \right) \\
& - (\mathbf{v}_{\nabla \mathrm{B}} + \mathbf{v}_\mathrm{c}) \cdot \left[\nabla \ln(n_{0,\sigma}) + \nabla \ln(T_{0,\sigma}) \left(\frac{m_\sigma v_{||}^2/2 + \mu B_0}{T_{0,\sigma}} - \frac{3}{2} \right) \right] F_{\mathrm{M},\sigma}.
\end{aligned} \tag{2.7.3}$$

The terms in the last row, representing the interaction between gyrokinetic and neoclassical physics, are usually neglected. Furthermore, we can now express the gyrokinetic potentials

in terms of $B_{1,||}$ instead of $\mathbf{A}_{1,\perp}$ as

$$\begin{aligned}\mathcal{G}\left\{\psi_1\right\} &\equiv \mathcal{G}\left\{\phi_1\right\} + \frac{\widetilde{\mathcal{G}_{\mathrm{D}}}\left\{B_{1,||}\right\}}{q_\sigma},\\ \mathcal{G}\left\{\chi_1\right\} &= \mathcal{G}\left\{\psi_1\right\} - \frac{v_{||}}{c}\mathcal{G}\left\{A_{1,||}\right\} = \mathcal{G}\left\{\phi_1\right\} - \frac{v_{||}}{c}\mathcal{G}\left\{A_{1,||}\right\} + \frac{\widetilde{\mathcal{G}_{\mathrm{D}}}\left\{B_{1,||}\right\}}{q_\sigma}.\end{aligned} \tag{2.7.4}$$

We can also see that all terms in the field equations (2.6.24), (2.6.25) and (2.6.27) that depend on $\mathcal{F}_{0,\sigma}$ and are linear in $v_{||}$ will vanish upon integration over said coordinate. This simplifies the parallel component of Ampère's law the most, as it will remove all couplings to the other field equations and read

$$\nabla_\perp^2 A_{1,||} = -8\pi^2 \sum_\sigma \frac{q_\sigma}{m_\sigma c} \int_{-\infty}^{\infty}\int_{0}^{\infty} v_{||}\mathcal{K}\left\{B_0 F_{1,\sigma}\right\}\, d\mu dv_{||}. \tag{2.7.5}$$

On the other hand, Poisson's equation will still be coupled with the perpendicular component of Ampère's law. They will constitute a system of the form

$$\begin{pmatrix} C_{11} & C_{12} \\ C_{21} & C_{22}\end{pmatrix}\begin{pmatrix}\phi_1 \\ B_{1,||}\end{pmatrix} = \sum_\sigma \frac{8\pi^2}{m_\sigma}\int_{-\infty}^{\infty}\int_{0}^{\infty}\begin{pmatrix} q_\sigma\mathcal{K}\left\{B_0F_{1,\sigma}\right\} \\ -\widetilde{\mathcal{K}}_{\mathrm{D}}\left\{(B_0F_{1,\sigma})\right\}\end{pmatrix} dv_{||}d\mu. \tag{2.7.6}$$

Here, the four operators from the left hand side are given by

$$\begin{aligned} C_{11}\phi_1 &= -\nabla_\perp^2\phi_1 + 8\pi^2\sum_\sigma \frac{q_\sigma^2}{m_\sigma}\int_{-\infty}^{\infty}\int_{0}^{\infty}\left(\frac{F_{\mathrm{M},\sigma}B_0}{T_{0,\sigma}}\phi_1 - \mathcal{K}\left\{\frac{F_{\mathrm{M},\sigma}B_0}{T_{0,\sigma}}\mathcal{G}\left\{\phi_1\right\}\right\}\right) dv_{||}d\mu,\\ C_{12}B_{1,||} &= -8\pi^2\sum_\sigma \frac{q_\sigma}{m_\sigma}\int_{-\infty}^{\infty}\int_{0}^{\infty}\left[\mathcal{K}\left\{\frac{F_{\mathrm{M},\sigma}B_0}{T_{0,\sigma}}\widetilde{\mathcal{G}_{\mathrm{D}}}\left\{B_{1,||}\right\}\right\}\right] dv_{||}d\mu,\\ C_{21}\phi_1 &= 8\pi^2\sum_\sigma \frac{q_\sigma}{m_\sigma}\int_{-\infty}^{\infty} dv_{||}\int_{0}^{\infty} d\mu\left[\widetilde{\mathcal{K}}_{\mathrm{D}}\left\{\left(\frac{F_{\mathrm{M},\sigma}B_0}{T_{0,\sigma}}\mathcal{G}\left\{\phi_1\right\}\right)\right\}\right],\\ C_{22}B_{1,||} &= B_{1,||} + 8\pi^2\sum_\sigma \frac{1}{m_\sigma}\int_{-\infty}^{\infty} dv_{||}\int_{0}^{\infty} d\mu\,\widetilde{\mathcal{K}}_{\mathrm{D}}\left\{\left(\frac{F_{\mathrm{M},\sigma}B_0}{T_{0,\sigma}}\widetilde{\mathcal{G}}_{\mathrm{D}}\left\{B_{1,||}\right\}\right)\right\}.\end{aligned} \tag{2.7.7}$$

In all applications of this thesis dealing with turbulence on ion scales, the plasma is assumed to be quasineutral, which means that the first term appearing in $C_{11}\phi_1$ is neglected. Furthermore, GENE-3D currently assumes $B_{1,||} = 0$, so that equation (2.7.6) reduces to an equation for ϕ_1 only.

Furthermore, it will be beneficial to express the particle distribution functions in terms of that for the gyrocenters. If a scalar $\overline{U}$ is given in gyrocentre coordinates, the transformation into the guiding centre frame is done using the pull-back operator T_* defined in equation (2.2.37). Considering only first-order corrections, the transformation is performed using the

generating functions G_1^ν derived in section 2.2.2 according to

$$\begin{aligned} U(\mathbf{Z}) =& T_*\overline{U} \approx \overline{U}_0 + \overline{U}_1 + \sum_{\nu=0}^{5} G_1^\nu \frac{\partial \overline{U}_0}{\partial Z^\nu} \\ \approx& \overline{U}_0 + \overline{U}_1 + + \frac{1}{B_0}\left(q_\sigma \tilde{\phi}_1 - \mu \mathcal{G}_\mathrm{D}\left\{B_{1,||}\right\}\right)\frac{\partial \overline{U}_0}{\partial \mu} + \widetilde{A_{1,||}}\ \left(\frac{q_\sigma}{m_\sigma c}\frac{\partial \overline{U}_0}{\partial v_{||}} - \frac{q_\sigma v_{||}}{B_0 c}\frac{\partial \overline{U}_0}{\partial \mu}\right), \end{aligned} \tag{2.7.8}$$

where we only retained leading-order contributions of the generating functions. The transformation into particle coordinates then follows according to

$$u(\mathbf{x}, \mathbf{v}) = \int \delta\left(\mathbf{X} + \boldsymbol{\rho} - \mathbf{x}\right) T_*\overline{U}\, d^3X. \tag{2.7.9}$$

If we use the assumptions $B_{1,||} = 0$ and $F_{0,\sigma} = F_{\mathrm{M},\sigma}$, this means that the perturbed particle distribution function $f_{1,\sigma}$ can be expressed in terms of the gyrocentre distribution function as

$$\begin{aligned} f_{1,\sigma}(\mathbf{x}, \mathbf{v}, t) =& \int \delta\left(\mathbf{X} + \boldsymbol{\rho} - \mathbf{x}\right) F_{1,\sigma}(\mathbf{X}, v_{||}, \mu, t) d^3X \\ & - \int \delta\left(\mathbf{X} + \boldsymbol{\rho} - \mathbf{x}\right) \frac{q_\sigma F_{\mathrm{M},\sigma}(\mathbf{X}, v_{||}, \mu)}{T_{0,\sigma}(\mathbf{X})} \left[\phi_1(\mathbf{x}, t) - \mathcal{G}\left\{\phi_1\right\}(\mathbf{X}, t)\right] d^3X. \end{aligned} \tag{2.7.10}$$

Finally, we note that GENE-3D can use an adiabatic electron model, in which the electrons are assumed to be massless compared with the bulk ion species, $m_\mathrm{e}/m_\mathrm{i} \to 0$, making them infinitely fast and causing a perfect force balance between a perturbed electric field parallel to the field line and the parallel pressure gradient. This allows us to approximate the perturbed electron density by a modified Boltzmann response

$$\frac{n_{1,\mathrm{e}}}{n_{0,\mathrm{e}}} = \frac{e}{T_{0,\mathrm{e}}}\left(\phi_1(\mathbf{x}, t) - \langle\phi_1\rangle_\mathrm{FS}(x, t)\right), \tag{2.7.11}$$

where we have introduced the flux-surface average [49]

$$\langle u\rangle_\mathrm{FS}(x) = \frac{\partial}{\partial V}\int\limits_V u(\mathbf{x})\, dV' = \frac{1}{A(x)}\int\limits_{\partial V(x)} u(\mathbf{x})\, dS, \tag{2.7.12}$$

where V and $A(x) = V'(x) = \int\limits_{\partial V(x)} dS$ are the volume and surface area enclosed by a toroidal surface at radial coordinate x. Assuming a quasineutral plasma in the electrostatic limit, equation (2.7.6) then reduces to

$$\begin{aligned} & \frac{e^2 n_{0,\mathrm{e}}}{T_{0,\mathrm{e}}}\left(\phi_1 - \langle\phi_1\rangle_\mathrm{FS}\right) + \sum_{\sigma\neq e}\frac{q_\sigma^2}{m_\sigma}\int\limits_{-\infty}^{\infty}\int\limits_{0}^{\infty}\left(\frac{F_{\mathrm{M},\sigma}B_0}{T_{0,\sigma}}\phi_1 - \mathcal{K}\left\{\frac{F_{\mathrm{M},\sigma}B_0}{T_{0,\sigma}}\mathcal{G}\left\{\phi_1\right\}\right\}\right) dv_{||}d\mu \\ & = \sum_{\sigma\neq e}\frac{q_\sigma}{m_\sigma}\int\limits_{-\infty}^{\infty}\int\limits_{0}^{\infty}\mathcal{K}\left\{B_0 F_{1,\sigma}\right\}\, dv_{||}d\mu. \end{aligned} \tag{2.7.13}$$

On the other hand, one can also consider a short-wavelength limit, where the averages

over ion gyromotion are assumed to vanish. In that case, the ion density can be approximated as

$$\frac{n_{1,\mathrm{i}}}{n_{0,\mathrm{i}}} = -\frac{q_\mathrm{i}}{T_{0,\mathrm{i}}}\phi_1, \tag{2.7.14}$$

So that the polarisation matrix C_{11} reduces to

$$C_{11}\phi_1 \approx -\nabla_\perp^2\phi_1 + 4\pi\sum_{\sigma\neq e}\frac{q_\sigma^2 n_{0,\sigma}}{T_{0,\sigma}}\phi_1 + \frac{8\pi^2 e^2}{m_\mathrm{e}}\int_{-\infty}^{\infty}\int_{0}^{\infty}\left(\frac{F_{\mathrm{M,e}}B_0}{T_{0,\mathrm{e}}}\phi_1 - \mathcal{K}\left\{\frac{F_{\mathrm{M,e}}B_0}{T_{0,\mathrm{e}}}\mathcal{G}\left\{\phi_1\right\}\right\}\right) dv_{||}d\mu. \tag{2.7.15}$$

The rest of the Poisson-Ampère system (2.7.5)-(2.7.6) can be kept, but the summation over species is replaced by the electron contributions only.

Although both approximations can significantly ease the computational effort, as they eliminate the necessity to resolve ion- and electron-timescales simultaneously, their range of validity is very limited, especially the approximation of adiabatic electrons. Therefore, unless explicitly stated otherwise, all particle species will be treated as being kinetic throughout this work.

2.8 Induction field equation

One particular feature of symplectic gyrokinetic models is the explicit time derivative of the perturbed vector potential in the right hand side of the gyrokinetic equation (2.5.3). For a long time this issue was dealt with in GENE by introducing a new distribution function $g_\sigma = F_{1,\sigma} + \left(q_\sigma v_{||} F_{\mathrm{M},\sigma} A_{1,||}\right) / \left(T_{0,\sigma} c\right)$ and solving the corresponding gyrokinetic system for g_σ instead of $F_{1,\sigma}$ [50]. However, it was shown in [51] that such a scheme becomes numerically unstable in nonlinear simulations at high plasma-β, although being stable linearly. An alternative scheme was proposed in the same publication, similar to the one presented in [52]. The same approach is also used in GENE-3D and will be presented in the following for a Maxwellian background distribution, as the extension to other equilibrium distributions is straightforward.

We begin by defining the parallel inductive electric field as

$$E_{||}^{\mathrm{ind}} \equiv -\frac{1}{c}\frac{\partial A_{1,||}}{\partial t}, \tag{2.8.1}$$

and rewrite the gyrokinetic equation (2.7.3) into

$$\frac{\partial F_{1,\sigma}}{\partial t} = R_\sigma + q_\sigma v_{||}\frac{F_{\mathrm{M},\sigma}}{T_{0,\sigma}}\mathcal{G}\left\{E_{||}^{\mathrm{ind}}\right\}, \tag{2.8.2}$$

where the term R_σ contains all the contributions to the right hand side except the one accounting for the parallel inductive electric field. We can then take the partial time derivative of Ampère's law (2.7.5) and multiply by $(-1/c)$, which will give a differential equation for $E_{||}^{\mathrm{ind}}$:

$$-\frac{1}{c}\nabla_\perp^2\frac{\partial A_{1,||}}{\partial t} = \nabla_\perp^2 E_{||}^{\mathrm{ind}} = 8\pi^2\sum_\sigma\frac{q_\sigma}{m_\sigma c^2}\int_{-\infty}^{\infty}\int_{0}^{\infty} v_{||}\mathcal{K}\left\{B_0\frac{\partial F_{1,\sigma}}{\partial t}\right\} d\mu dv_{||}. \tag{2.8.3}$$

Inserting definition (2.8.2) into equation (2.8.3) eliminates the explicit coupling of the equation to the particle distribution function $F_{1,\sigma}$. Therefore, one obtains an equation that treats the inductive electric field as an independent electromagnetic field:

$$\begin{aligned}&\nabla_{\perp}^{2} E_{||}^{\mathrm{ind}} - \frac{8\pi^{2}}{c^{2}} \sum_{\sigma} \frac{q_{\sigma}^{2}}{m_{\sigma}} \int_{-\infty}^{\infty} \int_{0}^{\infty} v_{||}^{2} \mathcal{K} \left\{ \frac{B_{0} F_{\mathrm{M},\sigma}}{T_{0,\sigma}} \mathcal{G} \left\{ E_{||}^{\mathrm{ind}} \right\} \right\} d\mu dv_{||} \\ &= 8\pi^{2} \sum_{\sigma} \frac{q_{\sigma}}{m_{\sigma} c^{2}} \int_{-\infty}^{\infty} \int_{0}^{\infty} v_{||} \mathcal{K} \left\{ B_{0} R_{\sigma} \right\} d\mu dv_{||}.\end{aligned} \tag{2.8.4}$$

2.9 Chapter summary

The previous chapter introduced the foundation of gyrokinetics, which forms the underlying theoretical framework for the remainder of this thesis. The general Lagrangian description of the motion of an electrically charged particle in an electromagnetic field was used as a starting point to derive a fully self-consistent set of equations describing the behaviour of a plasma under the ordering assumptions of gyrokinetics, including finite magnetic compressional effects as well as the possibility of an arbitrary background distribution function. Finally, several approximations to the model, such as the choice of a Maxwellian background distribution function or the choice of a simplified phase-space Jacobian, which are specific to GENE-3D, have been introduced. The numerical discretisation and implementation into the code will be given in the next chapter.

Chapter 3

The GENE-3D code

This chapter discusses the inner mechanisms of the GENE-3D code, which was used for most of the work presented in this thesis. Although it is an independent code, it can be seen as the extension of the radially global GENE code [50] for non-axisymmetric magnetic fields, as there is a large amount of legacy from one code to the other. The main difference between the two is the treatment of one of the spatial coordinates. Since the global version of GENE deals with tokamaks only, it exploits the inherent axisymmetry to use a Fourier representation in the binormal direction, leading to a much more efficient numerical treatment. In contrast, as GENE-3D is meant to simulate systems with broken axisymmetry, a real-space representation of all spatial coordinates was considered the most efficient approach.

The first publication involving GENE-3D simulations was [29], shortly followed by [30], which contains a description of the algorithm itself. At the beginning of this project, the code was well-tested for adiabatic electron simulations, with only a few linear kinetic electron simulations being run in tokamaks and stellarators with an artificially large electron-to-ion mass ratio. One major bottleneck at the time was that the code only solved purely electrostatic systems. This shortcoming does not only limit the range of possible physical applications but also introduces severe limitations on the maximum allowable numerical time step employed due to the so-called $\omega_{\mathrm{H}}-$mode [53], which can be avoided if the plasma-β is finite but small enough not to have any impact on the physics.

Thus, one of the project's first tasks was to upgrade GENE-3D to a code that can treat electromagnetic effects stemming from magnetic flutter, retaining finite $A_{1,||}$ fluctuations in the simulation. While adding this capability, it was discovered that it is necessary for some stellarator applications to use additional advanced finite-difference schemes to ensure numerical stability, which will be explained below. Furthermore, a methodology was developed to include effects arising through a finite $B_{1,||}$ in global simulations at arbitrary wavelengths. The algorithm has only been implemented in GENE by an external collaborator and has yet to be in GENE-3D due to time limitations. Nevertheless, we will outline it in this work and plan to implement this feature into GENE-3D in the near future.

The rest of this chapter is structured as follows: we introduce the coordinate system used in GENE-3D in section 3.1, followed by the introduction of the normalisations and the corresponding unitless equations that are solved by the code in section 3.2. Section 3.4 discusses the collision operator model currently implemented in GENE-3D. The current grid structure and corresponding boundary conditions of the phase-space variables in GENE-3D are outlined in section 3.5, an essential prerequisite for understanding the construction of the gyroaverage

and gyrodisk operators presented in sections 3.6 and 3.7, respectively. Further numerical schemes, such as numerical differentiation and integration, specifics to global simulations, as well as the introduction of mimetic finite-difference schemes, are discussed in section 3.8. Finally, the upgrades to include electromagnetic effects are verified in section 3.9 in linear as well as nonlinear electromagnetic tokamak simulations against the global version of the GENE code. The details about the implementation of the upgrade, as well as the verification tests, have been published in [34].

3.1 Choice of coordinates

The large spatial anisotropy of gyrokinetic fluctuations discussed in section 2.1 motivates the choice of a coordinate system that accounts for an efficient numerical treatment of the different spatial scales. A popular choice is a Clebsh-type coordinate system (ψ, α, θ^*). It can be shown [13, 49] that the magnetic field can be expressed as

$$\mathbf{B}_0 = \nabla\psi \times \nabla\alpha. \tag{3.1.1}$$

Here, the toroidal flux ψ serves as a radial coordinate. The field-line label α is defined via

$$\alpha = q(\psi)\theta^* - \phi, \tag{3.1.2}$$

where ϕ is the geometrical toroidal angle and the poloidal PEST angle θ^* [54] is used to serve as a coordinate parallel to the magnetic field lines. Furthermore, $q = q(\psi)$ is the so-called safety factor and is defined via

$$q(\psi) = \frac{d\phi}{d\theta^*}. \tag{3.1.3}$$

This choice saves several orders of magnitude in computing resources compared to using a mesh that disregards the magnetic field structure. In GENE-3D, one modifies said coordinate system further and introduces the coordinates

$$\begin{aligned} x &= \rho_{\mathrm{tor}} a = \sqrt{\frac{\psi}{\psi_{\mathrm{edge}}}}\, a, \\ y &= \sigma_{B_\mathrm{p}} C_\mathrm{y} \alpha = \sigma_{B_\mathrm{p}} C_\mathrm{y} \left(q(x)\theta^* - \phi\right), \\ z &= \sigma_{B_\mathrm{p}} \theta^*. \end{aligned} \tag{3.1.4}$$

Here, ψ_{edge} denotes the toroidal flux at the last closed flux-surface, and $a = \sqrt{\psi_{\mathrm{edge}}/(\pi B_{\mathrm{axis}})}$ defines an effective minor radius. σ_{B_p} is the sign of the poloidal magnetic field and ensures that the covariant basis vector $\mathbf{e}_\mathrm{z}$ is always parallel to the magnetic field lines and $C_\mathrm{y} = x_0/|q_0|$ has been introduced so that y is a length in contrast to the angle-like coordinate α. The subscript '0' indicates that the quantity is evaluated at reference position x_0. The magnetic field can be written as

$$\mathbf{B}_0 = \mathcal{C}(x)\nabla x \times \nabla y, \tag{3.1.5}$$

with

$$\mathcal{C}(x) = \frac{x}{|q(x)|}\frac{B_{\mathrm{axis}}}{C_\mathrm{y}}. \tag{3.1.6}$$

It then becomes obvious that the spatial Jacobian $\sqrt{g}$ is given by

$$\sqrt{g} = (\nabla x \times \nabla y) \cdot \nabla z = \frac{\mathbf{B}_0 \cdot \nabla z}{\mathcal{C}}, \tag{3.1.7}$$

and the metric elements are given by

$$g^{\mathrm{ij}} = \nabla u^{\mathrm{i}} \cdot \nabla u^{\mathrm{j}}, \tag{3.1.8}$$

where u^{i} is any of the $(x, y, z)-$coordinates. We will further introduce the abbreviations

$$\begin{aligned} \gamma_1 &= g^{\mathrm{xx}} g^{\mathrm{yy}} - g^{\mathrm{xy}} g^{\mathrm{yx}}, \\ \gamma_2 &= g^{\mathrm{xx}} g^{\mathrm{yz}} - g^{\mathrm{yx}} g^{\mathrm{xz}}, \\ \gamma_3 &= g^{\mathrm{xy}} g^{\mathrm{yz}} - g^{\mathrm{yy}} g^{\mathrm{xz}}. \end{aligned} \tag{3.1.9}$$

One can then see that the outer vector products, related to the drift velocities in (2.4.7) can be expressed as

$$\begin{aligned} \frac{1}{B_0^2} (\mathbf{B}_0 \times \nabla \xi) \cdot \nabla =& \frac{\mathcal{C}}{B_0^2} \frac{\partial \xi}{\partial u^{\mathrm{i}}} \left([\nabla x \times \nabla y] \times \nabla u^{\mathrm{i}} \right) \cdot \nabla u^{\mathrm{j}} \frac{\partial}{\partial u^{\mathrm{j}}} \\ =& \frac{1}{\mathcal{C}} \frac{g^{\mathrm{xi}} g^{\mathrm{yj}} - g^{\mathrm{yi}} g^{\mathrm{xj}}}{\gamma_1} \frac{\partial \xi}{\partial u^{\mathrm{i}}} \frac{\partial}{\partial u^{\mathrm{j}}}, \end{aligned} \tag{3.1.10}$$

where ξ is representative of any scalar whose gradients enter in the drift velocities (2.4.7), such as $c\phi_0$ in $\mathbf{v}_{\mathrm{E}_0}$. In the same way, parallel derivatives can be expressed as

$$\mathbf{B}_0 \cdot \nabla = \mathcal{C} \left[\nabla x \times \nabla y \right] \cdot \nabla u^{\mathrm{i}} \frac{\partial}{\partial u^{\mathrm{i}}} = \frac{\mathcal{C}}{\sqrt{g}} \frac{\partial}{\partial z}. \tag{3.1.11}$$

Using these relations, one can then express the gyrokinetic equation (2.7.3) in the $(x, y, z)-$coordinate system, which will be expressed in normalised units in the next section.

3.2 Normalisations

Although equations (2.7.3)-(2.7.7) are correct in the limits that they are derived in, it is impractical to use them for numerical studies. While the main reason for that is that computers can use unit-less quantities with magnitude of order one a lot easier than potentially very large or small dimensioned quantities, it is also worth noting that certain quantities are only relevant in relation to each other, such as the finite-size parameter ρ^*, introduced in section 2.1. Therefore, we will define appropriate normalisations for all physical quantities, which will be split into a dimensioned reference part usually identifiable by an index 'ref' and the remaining dimensionless value, which will be marked with a hat.

The fundamental reference values required are the elementary charge e, a reference density n_{ref} and temperature T_{ref}, which are typically chosen to be the equilibrium electron density and temperature in the centre of the radial domain, a reference mass m_{ref}, typically chosen to be the mass of the bulk ion species, a reference magnetic field strength B_{ref}, which in GENE-3D is given by the magnetic field strength on the magnetic axis B_{axis} of the device, and a reference lengthscale L_{ref}, typically given by the effective minor radius

a introduced in section 3.1. With this, one can then define a reference sound velocity as $c_{\mathrm{ref}} = \sqrt{T_{\mathrm{ref}}/m_{\mathrm{ref}}}$ and a reference Larmor frequency $\Omega_{\mathrm{ref}} = eB_{\mathrm{ref}}/(m_{\mathrm{ref}}c)$, where c is the speed of light. From this, we then obtain a reference gyroradius $\rho_{\mathrm{ref}} = c_{\mathrm{ref}}/\Omega_{\mathrm{ref}}$. With these expressions, one can identify three derived parameters appearing in the normalised gyrokinetic equation. They are the finite-size parameter $\rho^*_{\mathrm{ref}} = \rho_{\mathrm{ref}}/a$, the reference ratio between thermodynamic and magnetic field pressure, also known as plasma-β, which is given by $\beta = \beta_{\mathrm{ref}} = 8\pi n_{\mathrm{ref}} T_{\mathrm{ref}}/B^2_{\mathrm{ref}}$ and the normalised reference collision frequency $\nu_{\mathrm{ref}} = \pi e^4 n_{\mathrm{ref}} L_{\mathrm{ref}}/(2^{2/3}T^2_{\mathrm{ref}}) \cdot \left[24 - \ln\left(\sqrt{n_{\mathrm{ref}}[10^{19}/m^3] \cdot 10^{13}}/(T_{\mathrm{ref}}[\mathrm{keV}] \cdot 10^3)\right)\right]$, where the expression in square brackets is the Coulomb logarithm $\ln\Lambda$ [55]. Furthermore, we will split the background density and temperature profiles into a unique reference value, a species-dependent normalisation and a dimensionless profile according to $n_{0,\sigma}(x) = n_{\mathrm{ref}}\hat{n}_{0,\sigma}(x_0)\hat{n}_{\mathrm{p},\sigma}(x)$ and $T_{0,\sigma}(x) = T_{\mathrm{ref}}\hat{T}_{0,\sigma}(x_0)\hat{T}_{\mathrm{p},\sigma}(x)$.

Based on these definitions, we can write the space and time coordinates as

$$x = \rho_{\mathrm{ref}}\hat{x}, \qquad y = \rho_{\mathrm{ref}}\hat{y}, \qquad z = \hat{z}, \qquad t = \frac{L_{\mathrm{ref}}}{c_{\mathrm{ref}}}\hat{t}, \tag{3.2.1}$$

whereas the velocity-space coordinates will have a species-dependent normalisation of the form

$$v_{||} = c_{\mathrm{ref}}\hat{v}_{\mathrm{th},\sigma}(x_0)\hat{v}_{||}, \qquad \mu = \frac{T_{\mathrm{ref}}}{B_{\mathrm{ref}}}\hat{T}_{0,\sigma}(x_0)\hat{\mu}, \tag{3.2.2}$$

with $\hat{v}_{\mathrm{th},\sigma} = \sqrt{2\hat{T}_{0,\sigma}(x_0)/\hat{m}_\sigma}$ being the normalised thermal velocity of species σ. Quantities related to the geometry are assumed to vary slowly in space so that they will be normalised with respect to L_{ref}:

$$\gamma_1 = \hat{\gamma}_1, \qquad \gamma_2 = \frac{1}{L_{\mathrm{ref}}}\hat{\gamma}_2, \qquad \gamma_3 = \frac{1}{L_{\mathrm{ref}}}\hat{\gamma}_3, \qquad \sqrt{g} = L_{\mathrm{ref}}\sqrt{\hat{g}}, \qquad \mathcal{C} = B_{\mathrm{ref}}\hat{\mathcal{C}}. \tag{3.2.3}$$

The electromagnetic fields and potentials are given by

$$\phi_1 = \frac{\rho_{\mathrm{ref}}}{L_{\mathrm{ref}}}\frac{T_{\mathrm{ref}}}{e}\hat{\phi}_1, \qquad A_{1,||} = \frac{\rho_{\mathrm{ref}}}{L_{\mathrm{ref}}}B_{\mathrm{ref}}\rho_{\mathrm{ref}}\hat{A}_{1,||}, \qquad B_{1,||} = \frac{\rho_{\mathrm{ref}}}{L_{\mathrm{ref}}}B_{\mathrm{ref}}\hat{B}_{1,||}. \tag{3.2.4}$$

Finally, the distribution functions $F_{0,\sigma}$ and $F_{1,\sigma}$ are normalised according to

$$F_{0,\sigma} = \frac{n_{\mathrm{ref}}}{c^3_{\mathrm{ref}}}\frac{\hat{n}_{0,\sigma}(x_0)}{\hat{v}^3_{\mathrm{th},\sigma}}\hat{F}_{0,\sigma}, \qquad F_{1,\sigma} = \frac{\rho_{\mathrm{ref}}}{L_{\mathrm{ref}}}\frac{n_{\mathrm{ref}}}{c^3_{\mathrm{ref}}}\frac{\hat{n}_{0,\sigma}(x_0)}{\hat{v}^3_{\mathrm{th},\sigma}}\hat{F}_{1,\sigma}, \tag{3.2.5}$$

where in this case, we choose a normalised Maxwellian as the background distribution function so that

$$\hat{F}_{0,\sigma} = \hat{F}_{\mathrm{M},\sigma} = \frac{\hat{n}_{\mathrm{p},\sigma}(x)}{\left(\pi\hat{T}_{\mathrm{p},\sigma}(x)\right)^{3/2}}\exp\left(-\frac{\hat{v}^2_{||} + \hat{\mu}\hat{B}_0(\mathbf{x})}{\hat{T}_{\mathrm{p},\sigma}(x)}\right). \tag{3.2.6}$$

With this, the normalised gyrokinetic equation takes the form

$$\begin{aligned}\frac{\partial \hat{F}_{1,\sigma}}{\partial \hat{t}} =& -\hat{v}_{\mathrm{th},\sigma}\frac{\hat{\mathcal{C}}}{\sqrt{\hat{g}}\hat{B}_0}\hat{v}_{||}\hat{\Gamma}_{\mathrm{z},\sigma} + \frac{\hat{v}_{\mathrm{th},\sigma}}{2}\frac{\hat{\mathcal{C}}}{\sqrt{\hat{g}}\hat{B}_0}\hat{\mu}\frac{\partial \hat{B}_0}{\partial \hat{z}}\frac{\partial \hat{F}_{1,\sigma}}{\partial \hat{v}_{||}} \\ &- \frac{\hat{T}_{0,\sigma}(x_0)}{\hat{q}_\sigma}\frac{2\hat{v}_{||}^2+\hat{\mu}\hat{B}_0}{\hat{B}_0}\hat{K}_{\mathrm{x}}\hat{\Gamma}_{\mathrm{x},\sigma} \\ &- \left[\frac{\hat{T}_{0,\sigma}(x_0)}{\hat{q}_\sigma}\frac{2\hat{v}_{||}^2+\hat{\mu}\hat{B}_0}{\hat{B}_0}\hat{K}_{\mathrm{y}} - \beta_{\mathrm{ref}}\frac{\hat{p}_0}{\hat{B}_0^2}\frac{\hat{T}_{0,\sigma}(x_0)}{\hat{q}_\sigma}\frac{\hat{v}_{||}^2}{\hat{\mathcal{C}}}\hat{\omega}_{\mathrm{p},\sigma}\right]\hat{\Gamma}_{\mathrm{y},\sigma} \\ &- \frac{1}{\hat{\mathcal{C}}}\left[\hat{\omega}_{\mathrm{n},\sigma} + \hat{\omega}_{\mathrm{T},\sigma}\left(\frac{\hat{v}_{||}^2+\hat{\mu}\hat{B}_0}{\hat{T}_{\mathrm{p},\sigma}} - \frac{3}{2}\right)\right]\hat{F}_{\mathrm{M},\sigma}\frac{\partial}{\partial \hat{y}}\mathcal{G}\left\{\hat{\chi}_1\right\} \\ &- \frac{1}{\hat{\mathcal{C}}}\left[\left\{\hat{F}_{1,\sigma}, \mathcal{G}\left\{\hat{\chi}_1\right\}\right\}_{\mathrm{x,y}} + \frac{\hat{q}_\sigma \hat{F}_{\mathrm{M},\sigma}}{\hat{T}_{0,\sigma}(x_0)\hat{T}_{\mathrm{p},\sigma}}\left\{\mathcal{G}\left\{\hat{\psi}_1\right\}, \mathcal{G}\left\{\hat{\chi}_1\right\}\right\}_{\mathrm{x,y}}\right] \\ &- \frac{\hat{E}_{\mathrm{r}}}{\hat{\mathcal{C}}}\left(\frac{\partial \hat{F}_{1,\sigma}}{\partial \hat{y}} + \frac{\hat{q}_\sigma \hat{v}_{||}}{\hat{v}_{\mathrm{th},\sigma}}\frac{\hat{F}_{\mathrm{M},\sigma}}{\hat{T}_{\mathrm{p},\sigma}}\frac{\partial}{\partial \hat{y}}\mathcal{G}\left\{\hat{A}_{1,||}\right\}\right) \\ &+ \frac{\hat{q}_\sigma \hat{v}_{||}\sqrt{2}}{\sqrt{\hat{m}_\sigma \hat{T}_{0,\sigma}(x_0)}}\frac{\hat{F}_{\mathrm{M},\sigma}}{\hat{T}_{\mathrm{p},\sigma}}\mathcal{G}\left\{\hat{E}_{||}^{\mathrm{ind}}\right\} \\ &+ C\left[\hat{F}_{1,\sigma}\right].\end{aligned} \tag{3.2.7}$$

Here, we have introduced the abbreviations

$$\begin{aligned}\hat{\omega}_{\mathrm{n},\sigma} &= -L_{\mathrm{ref}}\frac{\partial \ln(\hat{n}_{\mathrm{p},\sigma})}{\partial x}, \qquad \hat{\omega}_{\mathrm{T},\sigma} = -L_{\mathrm{ref}}\frac{\partial \ln(\hat{T}_{\mathrm{p},\sigma})}{\partial x}, \\ \hat{\omega}_{\mathrm{p}} &= -L_{\mathrm{ref}}\frac{\partial \ln(\hat{p}_0)}{\partial x}, \qquad \hat{E}_{\mathrm{r}} = -\frac{eL_{\mathrm{ref}}}{T_{\mathrm{ref}}}\frac{\partial \phi_0}{\partial x}\end{aligned} \tag{3.2.8}$$

for the normalised gradient lengths of the equilibrium background fields. We additionally have defined

$$\hat{K}_{\mathrm{x}} = -\frac{1}{\hat{\mathcal{C}}}\frac{L_{\mathrm{ref}}}{B_{\mathrm{ref}}}\left(\frac{\partial B_0}{\partial y} + \frac{\gamma_2}{\gamma_1}\frac{\partial B_0}{\partial z}\right), \qquad \hat{K}_{\mathrm{y}} = -\frac{1}{\hat{\mathcal{C}}}\frac{L_{\mathrm{ref}}}{B_{\mathrm{ref}}}\left(\frac{\partial B_0}{\partial x} - \frac{\gamma_3}{\gamma_1}\frac{\partial B_0}{\partial z}\right), \tag{3.2.9}$$

containing gradients of the equilibrium magnetic field. Furthermore, we have used

$$\hat{\Gamma}_{\mathrm{i},\sigma} = \frac{\partial \hat{F}_{1,\sigma}}{\partial \hat{x}_{\mathrm{i}}} + \frac{\hat{q}_\sigma \hat{F}_{\mathrm{M},\sigma}}{\hat{T}_{0,\sigma}(x_0)\hat{T}_{\mathrm{p},\sigma}}\frac{\partial}{\partial \hat{x}_{\mathrm{i}}}\mathcal{G}\{\hat{\psi}_1\} \tag{3.2.10}$$

with the normalised potentials and fields

$$\begin{aligned}&\mathcal{G}\left\{\hat{\psi}_1\right\} = \mathcal{G}\left\{\hat{\phi}_1\right\} + \frac{\hat{T}_{0,\sigma}(x_0)}{\hat{q}_\sigma}\hat{\mathcal{G}}_{\mathrm{D}}\left\{\hat{B}_{1,||}\right\}, \quad \mathcal{G}\left\{\hat{\chi}_1\right\} = \mathcal{G}\left\{\hat{\psi}_1\right\} - \hat{v}_{\mathrm{th},\sigma}\hat{v}_{||}\mathcal{G}\left\{\hat{A}_{1,||}\right\}, \\ &\mathcal{G}\left\{\hat{E}_{||}^{\mathrm{ind}}\right\} = -\frac{\partial}{\partial \hat{t}}\mathcal{G}\left\{\hat{A}_{1,||}\right\}\end{aligned} \tag{3.2.11}$$

and $\hat{\mathcal{G}}_{\mathrm{D}} = [B_{\mathrm{ref}}/(T_{\mathrm{ref}}\hat{T}_{0,\sigma}(x_0))]\mathcal{G}_{\mathrm{D}}$ being the normalised gyrodisk-integral operator. Lastly, we have added the normalised collision operator $C[\hat{F}_{1,\sigma}]$ to the right-hand side of the gyrokinetic equation, which will be discussed in more detail in section 3.4. Finally, the nonlinear terms

$$\mathcal{N}_\sigma = -\frac{1}{\hat{\mathcal{C}}}\left[\left\{\hat{F}_{1,\sigma}, \mathcal{G}\left\{\hat{\chi}_1\right\}\right\}_{\mathrm{x,y}} + \frac{\hat{q}_\sigma \hat{F}_{\mathrm{M},\sigma}}{\hat{T}_{0,\sigma}(x_0)\hat{T}_{\mathrm{p},\sigma}}\left\{\mathcal{G}\left\{\hat{\psi}_1\right\}, \mathcal{G}\left\{\hat{\chi}_1\right\}\right\}_{\mathrm{x,y}}\right] \tag{3.2.12}$$

require the evaluation of Poisson brackets $\{.,.\}_{\mathrm{x,y}}$, whose treatment will be discussed in section 3.8.5.

Equation (3.2.7) is then coupled self-consistently to the normalised field equations, which can be shown to be of the form

$$\hat{\nabla}_\perp^2 \hat{A}_{1,||} = -\frac{\beta_{\mathrm{ref}}}{2}\sum_\sigma \hat{q}_\sigma \hat{n}_{0,\sigma}(x_0)\hat{v}_{\mathrm{th},\sigma}\pi \int_0^\infty \int_{-\infty}^\infty \mathcal{K}\left\{\hat{F}_{1,\sigma}\hat{B}_0\right\}\, \hat{v}_{||}\, d\hat{v}_{||}d\hat{\mu} \tag{3.2.13}$$

for the parallel vector potential,

$$\begin{aligned}&\hat{\nabla}_\perp^2 \hat{E}_{||}^{\mathrm{ind}} - \beta_{\mathrm{ref}}\sum_\sigma \frac{\hat{q}_\sigma^2 \hat{n}_{0,\sigma}(x_0)}{\hat{m}_\sigma}\pi \int_0^\infty \int_{-\infty}^\infty \mathcal{K}\left\{\frac{\hat{v}_{||}^2 \hat{B}_0 \hat{F}_{\mathrm{M},\sigma}}{\hat{T}_{\mathrm{p},\sigma}}\mathcal{G}\left\{\hat{E}_{||}^{\mathrm{ind}}\right\}\right\}\, d\hat{v}_{||}d\hat{\mu} \\ =&\frac{\beta_{\mathrm{ref}}}{2}\sum_\sigma \hat{q}_\sigma \hat{n}_{0,\sigma}(x_0)\hat{v}_{\mathrm{th},\sigma}\pi \int_0^\infty \int_{-\infty}^\infty \mathcal{K}\left\{\hat{R}_\sigma \hat{B}_0\right\}\, \hat{v}_{||}\, d\hat{v}_{||}d\hat{\mu}\end{aligned} \tag{3.2.14}$$

for its time derivative and

$$\begin{pmatrix}\hat{C}_{11} & \hat{C}_{12}\\ \hat{C}_{21} & \hat{C}_{22}\end{pmatrix}\begin{pmatrix}\hat{\phi}_1\\ \hat{B}_{1,||}\end{pmatrix} = \sum_\sigma \hat{n}_{0,\sigma}(x_0)\,\pi \int_{-\infty}^\infty \int_0^\infty \begin{pmatrix}\hat{q}_\sigma \hat{\mathcal{K}}\left\{\hat{B}_0\hat{F}_{1,\sigma}\right\}\\ -\frac{\beta_{\mathrm{ref}}\hat{T}_{0,\sigma}(x_0)}{2}\hat{\mathcal{K}}_{\mathrm{D}}\left\{\left(\hat{B}_0\hat{F}_{1,\sigma}\right)\right\}\end{pmatrix} d\hat{v}_{||}d\hat{\mu} \tag{3.2.15}$$

for the electrostatic potential and the parallel magnetic field with

$$\begin{aligned}\hat{C}_{11}\hat{\phi}_1 &= \sum_\sigma \hat{q}_\sigma^2 \hat{n}_{0,\sigma}(x_0)\,\pi \int_{-\infty}^\infty d\hat{v}_{||} \int_0^\infty d\hat{\mu}\, \left[\frac{\hat{F}_{0,\sigma}\hat{B}_0}{\hat{T}_{0,\sigma}(x_0)\hat{T}_{\mathrm{p},\sigma}}\hat{\phi}_1 - \hat{\mathcal{K}}\left\{\frac{\hat{F}_{0,\sigma}\hat{B}_0}{\hat{T}_{0,\sigma}(x_0)\hat{T}_{\mathrm{p},\sigma}}\hat{\mathcal{G}}\left\{\hat{\phi}_1\right\}\right\}\right],\\ \hat{C}_{12}\hat{B}_{1,||} &= -\sum_\sigma \hat{q}_\sigma \hat{n}_{0,\sigma}(x_0)\pi \int_{-\infty}^\infty d\hat{v}_{||} \int_0^\infty d\hat{\mu}\, \hat{\mathcal{K}}\left\{\frac{\hat{F}_{0,\sigma}\hat{B}_0}{\hat{T}_{\mathrm{p},\sigma}}\hat{\mathcal{G}}_{\mathrm{D}}\left\{\hat{B}_{1,||}\right\}\right\},\\ \hat{C}_{21}\hat{\phi}_1 &= \frac{\beta_{\mathrm{ref}}}{2}\sum_\sigma \hat{q}_\sigma \hat{n}_{0,\sigma}(x_0)\pi \int_{-\infty}^\infty d\hat{v}_{||} \int_0^\infty d\hat{\mu}\, \hat{\mathcal{K}}_{\mathrm{D}}\left\{\frac{\hat{F}_{0,\sigma}\hat{B}_0}{\hat{T}_{\mathrm{p},\sigma}}\hat{\mathcal{G}}\left\{\hat{\phi}_1\right\}\right\},\\ \hat{C}_{22}\hat{B}_{1,||} &= \left[\hat{B}_{1,||} + \frac{\beta_{\mathrm{ref}}}{2}\sum_\sigma \hat{n}_{0,\sigma}(x_0)\hat{T}_{0,\sigma}(x_0)\,\pi \int_{-\infty}^\infty d\hat{v}_{||} \int_0^\infty d\hat{\mu}\, \hat{\mathcal{K}}_{\mathrm{D}}\left\{\frac{\hat{F}_{0,\sigma}\hat{B}_0}{\hat{T}_{\mathrm{p},\sigma}}\hat{\mathcal{G}}_{\mathrm{D}}\left\{\hat{B}_{1,||}\right\}\right\}\right].\end{aligned} \tag{3.2.16}$$

At the current stage, parallel magnetic field fluctuations cannot be considered yet in GENE-3D, which means that from now on, we will assume $\mathcal{G}\left\{\hat{\psi}_1\right\} \to \mathcal{G}\left\{\hat{\phi}_1\right\}$ and equation

(3.2.15) will reduce to the electrostatic quasineutrality equation

$$\begin{aligned}&\sum_{\sigma} \hat{q}_{\sigma}^{2}\hat{n}_{0,\sigma}(x_0)\,\pi \int_{-\infty}^{\infty} d\hat{v}_{||} \int_{0}^{\infty} d\hat{\mu}\, \left[\frac{\hat{F}_{0,\sigma}\hat{B}_0}{\hat{T}_{0,\sigma}(x_0)\hat{T}_{\mathrm{p},\sigma}}\hat{\phi}_1 - \hat{\mathcal{K}}\left\{\frac{\hat{F}_{0,\sigma}\hat{B}_0}{\hat{T}_{0,\sigma}(x_0)\hat{T}_{\mathrm{p},\sigma}}\hat{\mathcal{G}}\left\{\hat{\phi}_1\right\}\right\}\right] \\ &= \sum_{\sigma} \hat{n}_{0,\sigma}(x_0)\,\pi \int_{-\infty}^{\infty}\int_{0}^{\infty} \hat{q}_{\sigma}\hat{\mathcal{K}}\left\{\hat{B}_0\hat{F}_{1,\sigma}\right\} d\hat{v}_{||}d\hat{\mu}.\end{aligned} \tag{3.2.17}$$

3.3 Macroscopic observables

Although the individual particle species' distribution functions describe the entire dynamical behaviour, the amount of information contained in their time evolution is too large for most practical considerations. Instead, one often considers appropriate velocity space moments to provide suitable quantities that can be compared against experimental measurements. These moments are of the form

$$\begin{aligned}M_{\mathrm{ab},\sigma}(\mathbf{x},t) =& \int v_{||}^{a}\, v_{\perp}^{b}\, f_{1,\sigma}(\mathbf{x},\mathbf{v},t)\, d^3v \\ =& \int_0^{\infty}\int_{-\infty}^{\infty}\int_0^{2\pi}\int \delta\left(\mathbf{X}-\boldsymbol{\rho}-\mathbf{x}\right)\left(\frac{2B_0}{m_\sigma}\right)^{\frac{\mathrm{b}}{2}} T^{*}F_{1,\sigma}v_{||}^{\mathrm{a}}\mu^{\frac{\mathrm{b}}{2}}\frac{B_0}{m_\sigma}\, d^3X d\theta dv_{||}d\mu \\ =& \pi\int_0^{\infty}\int_{-\infty}^{\infty} \mathcal{K}\left\{\left(\frac{2B_0}{m_\sigma}\right)^{\frac{\mathrm{b}}{2}+1} T^{*}F_{1,\sigma}v_{||}^{\mathrm{a}}\mu^{\frac{\mathrm{b}}{2}}\right\} dv_{||}d\mu,\end{aligned} \tag{3.3.1}$$

where we have used the relation between particle distribution function $f_{1,\sigma}$ and gyrocentre distribution function $F_{1,\sigma}$ given by equation (2.7.10). With this expression, one can derive a form of the moments in terms of the distribution function $F_{1,\sigma}$ and the electromagnetic fields, as shown in [56]. Here, we give their final expression, using the normalisations introduced in section 3.2:

$$M_{\mathrm{ab},\sigma}(\mathbf{x},t) = \rho_{\mathrm{ref}}^{*} n_{\mathrm{ref}}\hat{n}_{0,\sigma}c_{\mathrm{ref}}^{\mathrm{a+b}}\hat{v}_{\mathrm{th},\sigma}^{\mathrm{a+b}}\hat{M}_{\mathrm{ab},\sigma}(\mathbf{x},t), \tag{3.3.2}$$

with the dimensionless velocity space moment

$$\begin{aligned}\hat{M}_{\mathrm{ab},\sigma}(\mathbf{x},t) =& \pi\int_0^{\infty}\int_{-\infty}^{\infty} \mathcal{K}\left\{\hat{B}_0^{\frac{\mathrm{b}}{2}+1}\hat{F}_{1,\sigma}\hat{v}_{||}^{\mathrm{a}}\hat{\mu}^{\frac{\mathrm{b}}{2}}\right\} d\hat{v}_{||}d\hat{\mu} \\ &- \hat{q}_\sigma\frac{\hat{n}_{\mathrm{p},\sigma}\hat{T}_{\mathrm{p},\sigma}^{\frac{\mathrm{a+b}}{2}}}{\hat{T}_{0,\sigma}\hat{T}_{\mathrm{p},\sigma}}\Upsilon(a)\Gamma\left(\frac{b}{2}+1\right)\hat{\phi}_1 \\ &+ \frac{\hat{q}_\sigma}{\hat{T}_{0,\sigma}}\Upsilon(a)\int_0^{\infty}\mathcal{K}\left\{\frac{\hat{n}_{\mathrm{p},\sigma}\hat{B}_0\hat{T}_{\mathrm{p},\sigma}^{\frac{\mathrm{a+b}}{2}}}{\hat{T}_{\mathrm{p},\sigma}^{2}}\left(\frac{\hat{\mu}\hat{B}_0}{\hat{T}_{\mathrm{p},\sigma}}\right)^{\frac{\mathrm{b}}{2}} e^{-\frac{\hat{\mu}\hat{B}_0}{\hat{T}_{\mathrm{p},\sigma}}}\,\mathcal{G}\left\{\hat{\phi}_1\right\}\right\} d\hat{\mu}.\end{aligned} \tag{3.3.3}$$

Here, $\Gamma(b) = \int_0^\infty y^{b-1}\exp(-y)\,dy$ is the Gamma function [57] and $\Upsilon(a)$ is defined as

$$\Upsilon(a) = \frac{1+(-1)^a}{2\sqrt{\pi}}\Gamma\left(\frac{1+a}{2}\right) = \begin{cases} 1, & a=0 \\ 0, & a\,\text{odd} \\ \frac{(a-1)!!}{\sqrt{2}^a}, & a\,\text{even} \end{cases} = \begin{cases} 1, & a=0 \\ 0, & a\,\text{odd} \\ \frac{1\cdot 3\cdot\ldots\cdot(a-1)}{\sqrt{2}^a}, & a\,\text{even}. \end{cases} \tag{3.3.4}$$

With this definition, it is easy to see that

$$\begin{aligned} n_{1,\sigma}(\mathbf{x},t) &= M_{00,\sigma}(\mathbf{x},t), \\ j_{1,||,\sigma}(\mathbf{x},t) &= q_\sigma M_{10,\sigma}(\mathbf{x},t). \end{aligned} \tag{3.3.5}$$

Furthermore, one can introduce the radial turbulent heat and particle fluxes, defined as [58]

$$\begin{aligned} \Gamma_\sigma(\mathbf{x},t) &= \int \mathbf{v}_\chi \cdot \nabla x f_{1,\sigma}(\mathbf{x},\mathbf{v},t)\,d^3v, \\ Q_\sigma(\mathbf{x},t) &= \int \frac{m_\sigma v^2}{2}\mathbf{v}_\chi \cdot \nabla x f_{1,\sigma}(\mathbf{x},\mathbf{v},t)\,d^3v. \end{aligned} \tag{3.3.6}$$

Both will be of great interest when analysing nonlinear simulations in later chapters. Here, $\mathbf{v}_\chi$ is the $\nabla\chi$-drift introduced in equation (2.4.7). Using equation (3.1.10), one can show that the radial component of this drift is given by

$$\mathbf{v}_\chi \cdot \nabla x = -\frac{1}{\mathcal{C}}\left(c\frac{\partial\phi_1}{\partial y} - v_{||}\frac{\partial A_{1,||}}{\partial y}\right). \tag{3.3.7}$$

One can further split the fluxes into electrostatic and electromagnetic parts, which are distinguished based on the drift contribution of ϕ_1 and $A_{1,||}$, respectively. After some algebra, one finds that

$$\begin{aligned} \frac{\Gamma_{\text{es},\sigma}(\mathbf{x},t)}{\Gamma_{\text{GB}}} &= -\frac{\hat{n}_{0,\sigma}}{\hat{\mathcal{C}}(x)}\left(\frac{\partial\hat{\phi}_1}{\partial\hat{y}}(\mathbf{x},t)\hat{M}_{00,\sigma}(\mathbf{x},t)\right), \\ \frac{\Gamma_{\text{em},\sigma}(\mathbf{x},t)}{\Gamma_{\text{GB}}} &= \frac{\hat{n}_{0,\sigma}\hat{v}_{\text{th},\sigma}}{\hat{\mathcal{C}}(x)}\left(\frac{\partial\hat{A}_{1,||}}{\partial\hat{y}}(\mathbf{x},t)\hat{M}_{20,\sigma}(\mathbf{x},t)\right), \\ \frac{Q_{\text{es},\sigma}(\mathbf{x},t)}{Q_{\text{GB}}} &= -\frac{\hat{n}_{0,\sigma}\hat{T}_{0,\sigma}}{\hat{\mathcal{C}}(x)}\left[\frac{\partial\hat{\phi}_1}{\partial\hat{y}}(\mathbf{x},t)\left(\hat{M}_{20,\sigma}(\mathbf{x},t) - \hat{M}_{02,\sigma}(\mathbf{x},t)\right)\right], \\ \frac{Q_{\text{em},\sigma}(\mathbf{x},t)}{Q_{\text{GB}}} &= \frac{\hat{n}_{0,\sigma}\hat{T}_{0,\sigma}\hat{v}_{\text{th},\sigma}}{\hat{\mathcal{C}}(x)}\left[\frac{\partial\hat{A}_{1,||}}{\partial\hat{y}}(\mathbf{x},t)\left(\hat{M}_{30,\sigma}(\mathbf{x},t) + \hat{M}_{12,\sigma}(\mathbf{x},t)\right)\right], \end{aligned} \tag{3.3.8}$$

where the so-called Gyrobohm units

$$\begin{aligned} \Gamma_{\text{GB}} &= n_{\text{ref}}c_{\text{ref}}(\rho^*_{\text{ref}})^2, \\ Q_{\text{GB}} &= n_{\text{ref}}T_{\text{ref}}c_{\text{ref}}(\rho^*_{\text{ref}})^2 \end{aligned} \tag{3.3.9}$$

have been introduced for normalisation. As the fluxes are still functions of the position $\mathbf{x}$,

one often considers the flux-surface averages

$$\begin{aligned}\Gamma_\sigma(x,t) &= \langle \Gamma_\sigma(\mathbf{x},t)\rangle_{\mathrm{FS}} = \frac{1}{A(x)}\int \Gamma_\sigma(x,y,z,t)\sqrt{g}\,dydz,\\ Q_\sigma(x,t) &= \langle Q_\sigma(\mathbf{x},t)\rangle_{\mathrm{FS}} = \frac{1}{A(x)}\int Q_\sigma(x,y,z,t)\sqrt{g}\,dydz,\end{aligned} \tag{3.3.10}$$

where we have used definition (2.7.12) of the flux-surface average, together with the definition of the area $A(x) = V'(x) = \int \sqrt{g}\,dydz$ of the flux-surface.

3.4 The collision operator

High-temperature, low-density plasmas often exhibit negligible collisional effects. However, under certain parameter regimes, such as detrapping of trapped particle modes and collisional damping of zonal flows, collisional effects can become significant. A collision operator must be added to the right hand side of equation (2.5.3). Different collision operators have been developed in the literature. GENE-3D currently uses a linearised Landau-Boltzmann collision operator [59], $C[F_{1\sigma}]$, which is also used in the global tokamak version of GENE. In our linearised model, we neglect the equilibrium operator $C[F_{0\sigma}, F_{0\sigma'}]$ between particle species σ and σ', and only retain the test particle operator, $C[F_{1\sigma}, F_{0\sigma'}]$, and the field particle operator, $C[F_{0\sigma}, F_{1\sigma'}]$, which can be expressed as

$$\sum_{\sigma'}\big(C[F_{1\sigma}, F_{0\sigma'}] + C[F_{0\sigma}, F_{1\sigma'}]\big). \tag{3.4.1}$$

The test particle operator, given by

$$C[F_{1\sigma}, F_{0\sigma'}] = \frac{\partial}{\partial \mathbf{v}}\cdot\left(\mathsf{D}_{\sigma\sigma'}\cdot\frac{\partial}{\partial\mathbf{v}} - \mathbf{R}_{\sigma\sigma'}\right)F_{1\sigma} \equiv C^T_{\sigma\sigma'}\left[F_{1\sigma}\right], \tag{3.4.2}$$

is then transformed into gyrocentre coordinates, and the velocity derivatives are taken with respect to $v_\parallel$ and μ. The diffusion tensor, $\mathsf{D}_{\sigma\sigma'}$, and dynamical friction, $\mathbf{R}_{\sigma\sigma'}$, are defined as

$$\mathsf{D}_{\sigma\sigma'} = \frac{\gamma_{\sigma\sigma'} n_{\sigma'} T_{\sigma'}}{m_\sigma^2 m_{\sigma'}}\frac{1}{v^3}\left[\mathbf{1}_{\mathbf{v}}\Phi_1(u_{\sigma'}) + 3\frac{\mathbf{vv}}{v^2}\Phi_2(u_{\sigma'})\right], \quad \mathbf{R}_{\sigma\sigma'} = -\frac{\gamma_{\sigma\sigma'} n_{\sigma'}}{m_\sigma m_{\sigma'}}\frac{\mathbf{v}}{v^3}\Phi_3(u_{\sigma'}). \tag{3.4.3}$$

Here, the variable $u_{\sigma'} \equiv v/v_{\mathrm{th},\sigma'}$ is the normalised velocity, where $v_{\mathrm{th},\sigma'} = \sqrt{2T_{0,\sigma'}/m_{\sigma'}}$ is the thermal velocity of species σ'. Above, the shorthand notations

$$\Phi_1(u_{\sigma'}) = u_{\sigma'}\,\mathrm{erf}'\left(u_{\sigma'}\right) + \left(2u_{\sigma'}^2 - 1\right)\mathrm{erf}\left(u_{\sigma'}\right), \tag{3.4.4}$$

$$\Phi_2(u_{\sigma'}) = \left(1 - 2u_{\sigma'}^2/3\right)\mathrm{erf}\left(u_{\sigma'}\right) - u_{\sigma'}\,\mathrm{erf}'\left(u_{\sigma'}\right), \tag{3.4.5}$$

$$\Phi_3(u_{\sigma'}) = \Phi_1(u_{\sigma'}) + 3\Phi_2\left(u_{\sigma'}\right), \tag{3.4.6}$$

$$\gamma_{\sigma\sigma'} = 2\pi q_\sigma^2 q_{\sigma'}^2 \ln\Lambda, \tag{3.4.7}$$

have been introduced with the Coulomb logarithm $\ln\Lambda$ and the error function $\mathrm{erf}(u_{\sigma'}) = (2/\sqrt{\pi})\int_0^{u_{\sigma'}}\exp\left(-u^2\right)\mathrm{d}u$.

As in GENE, the field particle operator is not evaluated explicitly but replaced by a model operator to ensure that the collision operator as a whole conserves energy, particles,

and momentum along the background magnetic field. In particular,

$$C[F_{0\sigma}, F_{1\sigma'}] = \frac{v_\parallel F_{0\sigma}}{m_\sigma I_{5,\sigma\sigma'}} \delta\dot{\mathcal{P}}_{\parallel\sigma'\sigma} + \frac{I_{1,\sigma\sigma'} u_{\sigma'}^2 - I_{2,\sigma\sigma'}}{I_{3,\sigma\sigma'} I_{1,\sigma\sigma'} - I_{2,\sigma\sigma'} I_{4,\sigma\sigma'}} \frac{F_{0\sigma}}{m_\sigma} \delta\dot{\mathcal{E}}_{\sigma'\sigma}, \tag{3.4.8}$$

where the collisional parallel momentum transfer $\delta\dot{\mathcal{P}}_{\parallel\sigma'\sigma}$ and energy transfer $\delta\dot{\mathcal{E}}_{\sigma'\sigma}$ are given by

$$\delta\dot{\mathcal{P}}_{\parallel\sigma'\sigma} = -\int C^T_{\sigma'\sigma}[F_{1\sigma}] m_{\sigma'} v_\parallel \mathrm{d}^3 v\,, \quad \delta\dot{\mathcal{E}}_{\sigma'\sigma} = -\int C^T_{\sigma'\sigma}[F_{1\sigma}] m_{\sigma'} v^2 \mathrm{d}^3 v. \tag{3.4.9}$$

The integrals $I_{1,\sigma\sigma'}$, $I_{2,\sigma\sigma'}$, $I_{3,\sigma\sigma'}$, $I_{4,\sigma\sigma'}$, and $I_{5,\sigma\sigma'}$ are evaluated as

$$I_{1,\sigma\sigma'} = \int F_{0\sigma} \mathrm{d}^3 v\,, \qquad I_{2,\sigma\sigma'} = \int F_{0\sigma} u_{\sigma'}^2 \mathrm{d}^3 v, \tag{3.4.10}$$

$$I_{3\sigma\sigma'} = \int v^2 F_{0\sigma} u_{\sigma'}^2 \mathrm{d}^3 v, \qquad I_{4,\sigma\sigma'} = \int v^2 F_{0\sigma} \mathrm{d}^3 v, \tag{3.4.11}$$

$$I_{5,\sigma\sigma'} = \int v_\parallel^2 F_{0\sigma} \mathrm{d}^3 v. \tag{3.4.12}$$

3.5 Numerical grids and boundary conditions

Naturally, the coordinate system introduced in section 3.1 is discretised on a finite grid in GENE-3D. These grids come with a set of boundary conditions specific to each coordinate. Both the discretisation and the boundary conditions applied in GENE-3D will be introduced in the following.

3.5.1 Binormal direction

GENE-3D employs periodic boundary conditions in the binormal direction given by the y-grid. Considering equation (3.1.4), the periodicity condition

$$f(x, y + L_\mathrm{y}, z) = f(x, y, z) \tag{3.5.1}$$

is equivalent to

$$f(\rho_\mathrm{tor}, \phi + \frac{2\pi}{n_0}, \theta^*) = f(\rho_\mathrm{tor}, \phi, \theta^*), \tag{3.5.2}$$

where $L_\mathrm{y} = 2\pi C_\mathrm{y}/n_0$ and n_0 is a positive integer that describes the discrete toroidal symmetry of the configuration at hand. If $n_0 = 1$, the simulation domain will cover the entire area of a given set of flux surfaces. However, such a large domain is prohibitively expensive to simulate in many cases. In practice, one can exploit discrete symmetries intrinsic to the magnetic configuration at hand. For example, since Wendelstein 7-X consists of five identical modules, it has a five-fold symmetry. Hence, any simulation involving a W7-X-based geometry can be run with n_0 being a multiple of 5.

3.5.2 Parallel direction

The spatial direction parallel to the magnetic field, represented in GENE-3D by the z-coordinate, requires a more delicate treatment of its boundary. If again expressed in the

$(\rho_{\mathrm{tor}}, \phi, \theta^*)$-coordinate system, the parallel boundary condition reads

$$f(\rho_{\mathrm{tor}}, \phi, \theta^* + 2\pi) = f(\rho_{\mathrm{tor}}, \phi, \theta^*). \tag{3.5.3}$$

However, it is easy to see from equation (3.1.4) that this implies for the flux-coordinate system that

$$f(x, y + 2\pi C_{\mathrm{y}} q(x), z + 2\pi) = f(x, y, z). \tag{3.5.4}$$

These so-called "twist-and-shift" boundary conditions [60] impose a coupling between the y- and the z-grid. Since the shifted position in the binormal direction will not necessarily coincide with points on the grid, GENE-3D currently uses a third-order Catmull-Rom spline interpolation to overcome this issue.

3.5.3 Radial direction

At the current stage, GENE-3D can use Dirichlet or periodic boundary conditions in the radial direction. In global simulations, the former are employed, implying that turbulence is modelled to decay towards the domain boundaries with

$$f(x \leq x_0 - \frac{L_{\mathrm{x}}}{2}, y, z) = f(x \geq x_0 + \frac{L_{\mathrm{x}}}{2}, y, z) = 0. \tag{3.5.5}$$

In the case of radially local simulations, one has the choice between Dirichlet and periodic boundary conditions. The latter is the standard assumption in most flux-tube codes as well since almost all background quantities are assumed to be constant over the entire radial domain in this direction. However, in order to include the effect of magnetic shear, one linearises the safety factor q appearing in the twist-and-shift boundary condition (3.5.4):

$$q(x) \approx q(x_0) + \frac{dq}{dx}(x_0)(x - x_0) = q_0 \left(1 + \hat{s}\frac{x - x_0}{x_0}\right), \tag{3.5.6}$$

with $\hat{s} = x_0(dq/dx)$ being the magnetic shear. In this case, the twist-and-shift condition is only compatible with radial periodicity if the shift in the y-direction will be periodic in the radial direction as well, which is equivalent to

$$2\pi C_{\mathrm{y}} \frac{q_0}{x_0} \hat{s} L_{\mathrm{x}} = 2\pi \hat{s} L_{\mathrm{x}} = N L_{\mathrm{y}}, \quad N \in \mathbb{N}. \tag{3.5.7}$$

This quantisation can make local simulations of low-shear geometries prohibitively expensive, as the radial box sizes can become much larger than the actual machine size itself.

Alternatively, one can use Dirichlet boundary conditions in this context to circumvent the restriction on L_{x}. In this case, no periodicity in the radial direction is required for the binormal shift given by equation (3.5.4) so that the linearisation given in equation (3.5.6) can be performed without introducing the quantisation of L_{x}. However, this alleviation comes at the cost of introducing numerical sources and buffer zones, which will be discussed in section 3.8.6, just like in a global simulation.

3.5.4 Velocity directions

In gyrokinetic theory, it is assumed that turbulent fluctuations vanish for infinitely large velocities. Hence, zero-Dirichlet boundary conditions are employed for the grids in the velocity

space parallel to the magnetic field lines $v_{||}-$ and the magnetic moment μ. The former is partitioned on an equidistant grid. In contrast, multiple grids are available for the latter, such as equidistant partitioning or a partitioning based on a Gauss quadrature scheme with Gauss-Laguerre weights and knots [57]. The latter is the default option, as derivatives in this direction are only calculated if collisional effects are retained. Therefore, it is reasonable to choose a grid that is optimised for numerical integration.

3.6 Implementation of the gyroaverage operator

Several terms in the gyrokinetic equation (2.5.3) involve the evaluation of gyroaveraged quantities of the form

$$\mathcal{G}\left\{u\right\}(\mathbf{X}) = \frac{1}{2\pi}\int_0^{2\pi} u(\mathbf{X}+\boldsymbol{\rho})\, d\Theta, \tag{3.6.1}$$

requiring high-accuracy approximations of numerical integrals. One particular challenge is that the calculation requires knowledge of the quantity of interest at positions that will not necessarily coincide with numerical grid points. GENE-3D deals with this issue by employing a finite-element representation

$$u\left(x(\mathbf{X}+\boldsymbol{\rho}), y(\mathbf{X}+\boldsymbol{\rho}), z(\mathbf{X}+\boldsymbol{\rho})\right) \approx \sum_{\mathrm{i,j}}^{\mathrm{n_x,n_y}} u_{\mathrm{ij}}(z(\mathbf{X}))\, \Lambda_{\mathrm{ij}}\left(x(\mathbf{X}+\boldsymbol{\rho}), y(\mathbf{X}+\boldsymbol{\rho})\right) \tag{3.6.2}$$

that can then be used easily for interpolation between grid points. Here, u_{ij} denotes the finite-element coefficient corresponding to its respective basis function Λ_{ij}, and n_{x} and n_{y} denote the number of grid points in the x- and y-direction, respectively. Furthermore, we assumed that the function u will only vary slowly in z, in accordance with the gyrokinetic ordering, so that its variation along this direction over the course of a gyroradius can be neglected.

In order to ease the computational effort, the basis functions should have compact support, and the finite-element coefficients should coincide with the values of the function or its derivatives evaluated on the numerical grid. Alternative approaches, such as using a spline basis, require the additional solution of a potentially large linear system.

In GENE-3D, a representation with third-order Hermite polynomials with compact support is chosen, which takes the form

$$u(x,y,z) \approx \sum_{\mathrm{i,j}}^{\mathrm{n_x,n_y}} \left(H_{\mathrm{ij}}^{0,0}(x,y) + H_{\mathrm{ij}}^{1,0}(x,y)\partial_{\mathrm{x}} + H_{\mathrm{ij}}^{0,1}(x,y)\partial_{\mathrm{y}} + H_{\mathrm{ij}}^{1,1}(x,y)\partial_{\mathrm{x,y}}\right) u_{\mathrm{ij}}(z), \tag{3.6.3}$$

inside the support and zero outside, where the operator $\partial_{\mathrm{n,m}} u_{\mathrm{ij}}$ represents the n-th derivative in the x- and the m-th derivative in the y-direction of the function u at $(x_{\mathrm{i}}, y_{\mathrm{j}})$. The functions $H_{\mathrm{ij}}^{\mathrm{n,m}}$ are defined in the following way:

$$\begin{aligned}
H_{\mathrm{ij}}^{0,0} =& \left(1-\sigma_{\mathrm{x}}\delta x\right)^2 \left(1+2\sigma_{\mathrm{x}}\delta x\right) \left(1-\sigma_{\mathrm{y}}\delta y\right)^2 \left(1+2\sigma_{\mathrm{y}}\delta y\right), \\
H_{\mathrm{ij}}^{1,0} =& \Delta x \left(1-\sigma_{\mathrm{x}}\delta x\right)^2 \left(1-\sigma_{\mathrm{y}}\delta y\right)^2 \left(1+2\sigma_{\mathrm{y}}\delta y\right), \\
H_{\mathrm{ij}}^{0,1} =& \Delta y \left(1-\sigma_{\mathrm{x}}\delta x\right)^2 \left(1-\sigma_{\mathrm{y}}\delta y\right)^2 \left(1+2\sigma_{\mathrm{x}}\delta x\right), \\
H_{\mathrm{ij}}^{1,1} =& \Delta x \Delta y \left(1-\sigma_{\mathrm{x}}\delta x\right)^2 \left(1-\sigma_{\mathrm{y}}\delta y\right)^2.
\end{aligned} \tag{3.6.4}$$

Here, $\Delta x = x - x_\mathrm{i}$, $\delta x = \Delta x/(x_{\mathrm{i}+1} - x_\mathrm{i})$, and $\sigma_\mathrm{x} = \mathrm{sgn}(x - x_\mathrm{i})$. These quantities are calculated analogously for y. Introducing the vector representation $\mathbf{u} = \{u_\mathrm{ij}\}$, the function u is then approximated as

$$u(x,y,z) \approx \mathbf{\Lambda}(x,y)\mathbf{u}(z) = \left(\mathbf{H}^{0,0}(x,y) + \mathbf{H}^{1,0}(x,y)\mathbf{D}_\mathrm{x} + \mathbf{H}^{0,1}(x,y)\mathbf{D}_\mathrm{y} + \mathbf{H}^{1,1}(x,y)\mathbf{D}_\mathrm{x,y}\right)\cdot\mathbf{u}(z), \tag{3.6.5}$$

where $\mathbf{D}_\mathrm{n,m}$ are numerical approximations of the n-th and m-th derivative in the x- and y-direction, respectively, which in GENE-3D is chosen to be through a central finite-difference scheme.

In a similar manner, the gyroaverage of the function u, evaluated at discrete points $\mathbf{X}_\mathrm{kl} = (X^1_\mathrm{k}, X^2_\mathrm{l})$, can now be approximated as

$$\left\{\mathcal{G}\left\{u(\mathbf{X}+\boldsymbol{\rho})\right\}(\mathbf{X}_\mathrm{kl})\right\}_\mathrm{k,l} \approx \frac{1}{2\pi}\int_0^{2\pi} \mathbf{\Lambda}\left(x(\mathbf{X}+\boldsymbol{\rho}(\Theta)), y(\mathbf{X}+\boldsymbol{\rho}(\Theta))\right) d\Theta\ \mathbf{u}(z) \equiv \boldsymbol{\mathcal{G}}\cdot\mathbf{u}. \tag{3.6.6}$$

The last step is to map the function values at positions $(\mathbf{X}+\boldsymbol{\rho})$ to the field-aligned $(x,y)-$grid used in the code in order to insert them into the finite element basis. Since the mapping between the two systems is done numerically and only known at a finite number of positions $\{\mathbf{X}_\mathrm{n}\}_\mathrm{n}$, an exact mapping of the gyrorings would be very demanding computationally.

As a more practical approach, the mapping between the two coordinate systems is linearised under the assumption of small gyroradii as

$$\begin{aligned} x(\mathbf{X}+\boldsymbol{\rho}(\Theta)) &\approx x(\mathbf{X}) + \boldsymbol{\rho}(\Theta)\cdot\nabla x + \mathcal{O}(\rho^2),\\ y(\mathbf{X}+\boldsymbol{\rho}(\Theta)) &\approx y(\mathbf{X}) + \boldsymbol{\rho}(\Theta)\cdot\nabla y + \mathcal{O}(\rho^2). \end{aligned} \tag{3.6.7}$$

To do so, one can introduce the orthonormal basis

$$\begin{aligned} \mathbf{e}^1 &= \frac{\nabla x}{||\nabla x||} = \frac{\nabla x}{\sqrt{g^{\mathrm{xx}}}},\\ \mathbf{e}^3 &= \mathbf{b},\\ \mathbf{e}^2 &= \mathbf{e}^3\times\mathbf{e}^1 = \frac{\nabla x\times\nabla y}{\sqrt{\gamma_1}}\times\frac{\nabla x}{\sqrt{g^{\mathrm{xx}}}} = \frac{1}{\sqrt{\gamma_1}}\left(\sqrt{g^{\mathrm{xx}}}\nabla y - \frac{g^{\mathrm{xy}}}{\sqrt{g^{\mathrm{xx}}}}\nabla x\right), \end{aligned} \tag{3.6.8}$$

so that $\boldsymbol{\rho}$ can be written as $\boldsymbol{\rho}(\Theta) = \rho\left(\mathbf{e}_1\cos(\Theta) - \mathbf{e}_2\sin(\Theta)\right)$, with $\rho = \sqrt{2\mu B_0/m_\sigma}\Big/\Omega_\sigma = \sqrt{2\hat{\mu}\hat{m}_\sigma\hat{T}_{0,\sigma}(x_0)/(\hat{q}^2_\sigma\hat{B}_0)}\,\rho_\mathrm{ref}$.

The particle position can then be expressed as

$$\begin{aligned} x(\mathbf{X}+\boldsymbol{\rho}(\Theta)) &\approx x(\mathbf{X}) + \boldsymbol{\rho}(\Theta)\cdot\nabla x = x(\mathbf{X}) + \rho\sqrt{g^{\mathrm{xx}}}\cos(\Theta),\\ y(\mathbf{X}+\boldsymbol{\rho}(\Theta)) &\approx y(\mathbf{X}) + \boldsymbol{\rho}(\Theta)\cdot\nabla y = y(\mathbf{X}) + \frac{\rho}{\sqrt{g^{\mathrm{xx}}}}\left(g^{\mathrm{xy}}\cos(\Theta) - \sqrt{\gamma_1}\sin(\Theta)\right). \end{aligned} \tag{3.6.9}$$

We remark that, as discussed in [58], the linearisation used in equation (3.6.9) breaks down close to the magnetic axis. A solution for tokamak scenarios, using a higher order approach, has already been provided in [58] and will be explored in the future for GENE-3D.

As shown in section 2.6, one also needs to evaluate the operator

$$\mathcal{K}\{u\}(\mathbf{x}) = \frac{1}{2\pi}\int_0^{2\pi}\int \delta\left(\mathbf{X}-\mathbf{x}+\boldsymbol{\rho}\right)\, u(\mathbf{X})\, d^3X d\Theta, \tag{3.6.10}$$

when computing the electromagnetic fields. For a discrete point $\mathbf{x}_{\mathrm{kl}} = (x^1_{\mathrm{k}}, x^2_{\mathrm{l}})$, the operator can be approximated by the finite element basis as

$$\mathcal{K}\{u\}(\mathbf{x}_{\mathrm{kl}}) \approx \frac{1}{2\pi}\sum_{\mathrm{i,j}} u_{\mathrm{ij}} \int_0^{2\pi}\int \delta\left(\mathbf{X}-\mathbf{x}_{\mathrm{kl}}+\boldsymbol{\rho}\right)\Lambda_{\mathrm{ij}}(\mathbf{X})\, d\Theta = \frac{1}{2\pi}\sum_{\mathrm{i,j}} u_{\mathrm{ij}} \int_0^{2\pi}\Lambda_{\mathrm{ij}}(\mathbf{x}_{\mathrm{kl}}-\boldsymbol{\rho})\, d\Theta. \tag{3.6.11}$$

Since the basis functions $\Lambda_{\mathrm{ij}}(\mathbf{x})$ are the same except for a shift of the support region, one could also write them by introducing the function

$$\Lambda_0(\mathbf{x}-\mathbf{x}_{\mathrm{ij}}) \equiv \Lambda_{\mathrm{ij}}(\mathbf{x}). \tag{3.6.12}$$

This allows us to write the expression for $\mathcal{K}\{u\}$ as

$$\begin{aligned}
\mathcal{K}\{u\}(\mathbf{x}_{\mathrm{kl}}) \approx & \frac{1}{2\pi}\sum_{\mathrm{i,j}} u_{\mathrm{ij}} \int_0^{2\pi}\Lambda_0(\mathbf{x}_{\mathrm{kl}}-\boldsymbol{\rho}-\mathbf{x}_{\mathrm{ij}})\, d\Theta \\
= & \frac{1}{2\pi}\sum_{\mathrm{i,j}} u_{\mathrm{ij}} \int_0^{2\pi}\Lambda_0(\boldsymbol{\rho}+\mathbf{x}_{\mathrm{ij}}-\mathbf{x}_{\mathrm{kl}})\, d\Theta \\
= & \frac{1}{2\pi}\sum_{\mathrm{i,j}} u_{\mathrm{ij}} \int_0^{2\pi}\Lambda_{\mathrm{kl}}(\boldsymbol{\rho}+\mathbf{x}_{\mathrm{ij}})\, d\Theta \\
= & \sum_{\mathrm{i,j}} \mathcal{G}_{\mathrm{ij,kl}}\, u_{\mathrm{ij}} \\
= & \sum_{\mathrm{i,j}} \mathcal{G}^{\dagger}_{\mathrm{kl,ij}}\, u_{\mathrm{ij}},
\end{aligned} \tag{3.6.13}$$

Where $\mathcal{G}_{\mathrm{kl,ij}}$ is the (kl,ij)-element of the gyromatrix $\boldsymbol{\mathcal{G}}$ defined in equation (3.6.6). Therefore, if we adopt a matrix-vector notation again, we can see that the pull-back gyroaverage can be expressed in terms of the gyromatrices via

$$\left\{\mathcal{K}\{u\}(\mathbf{x}_{\mathrm{kl}})\right\}_{\mathrm{kl}} = \boldsymbol{\mathcal{K}}\cdot\mathbf{u} = \boldsymbol{\mathcal{G}}^{\dagger}\cdot\mathbf{u}. \tag{3.6.14}$$

Doing so ensures that the approximations of equations (3.2.14) and (3.2.17) will be symmetric.

3.7 Construction of the gyrodisk operators

While the idea of introducing gyrodisk-operators into the analytical form of the gyrokinetic equation has already been proposed in [61, 62], the actual implementation in global gyrokinetic

codes has always relied on using a long-wavelength or Padé-approximation. Only recently, an approach valid at arbitrary wavelengths has been implemented in the GEM code [63] using pseudo-spectral methods. In the following, we will discuss an implementation that works entirely in real-space, especially suited for Eulerian codes, as the grid structure of the phase-space representation enables us to represent the disk integrals as matrix-vector products. Although not yet implemented in GENE-3D, the model has been tested successfully in GENE [64] and will be used to include magnetic compression effects in GENE-3D in the future.

We begin by considering the linearised metric (3.6.9) introduced in section 3.6. We can see that the particle orbits form a sheared ellipse shape if represented in the coordinate system of GENE-3D. Defining $x' = x(\mathbf{X} + \boldsymbol{\rho}) - x(\mathbf{X})$ and $y' = y(\mathbf{X} + \boldsymbol{\rho}) - y(\mathbf{X})$, one can derive the polar representation of the particle orbit as

$$\begin{aligned} r &= \sqrt{x'^2 + y'^2}, \\ \vartheta &= \arctan\left(\frac{y'}{x'}\right), \end{aligned} \tag{3.7.1}$$

where the polar angle ϑ is not to be confused with the gyroangle Θ. The transformation of the infinitesimal surface element then reads as

$$dx'dy' = \frac{r(\vartheta)}{\sqrt{\gamma_1}} dr d\vartheta, \tag{3.7.2}$$

where the factor $1/\sqrt{\gamma_1}$ appears since the (x, y)-coordinate system used in GENE-3D is non-Cartesian. We now wish to express the spatial integral in terms of the Larmor radius ρ and the gyroangle Θ in order to link it to the gyroaverage. It is straightforward to show that

$$\begin{aligned} \frac{\partial r}{\partial \rho} &= \sqrt{g^{\mathrm{xx}} \cos^2(\Theta) + \left[\frac{1}{\sqrt{g^{\mathrm{xx}}}} \left(g^{\mathrm{xy}} \cos(\Theta) - \sqrt{\gamma_1} \sin(\Theta)\right)\right]^2}, \\ \frac{\partial \vartheta}{\partial \Theta} &= \frac{1}{1 + \left(\frac{g^{\mathrm{xy}}}{g^{\mathrm{xx}}} - \frac{\sqrt{\gamma_1}}{g^{\mathrm{xx}}} \tan(\Theta)\right)^2} \frac{\sqrt{\gamma_1}}{g^{\mathrm{xx}}} \frac{1}{\cos^2(\Theta)}, \end{aligned} \tag{3.7.3}$$

where a minus sign in the latter equation is absent due to the orientation of the gyroangle Θ as defined in GENE. As ϑ does not depend on ρ, the off-diagonal contribution to the Jacobian vanished, and the transformation to the new coordinate system reads thus

$$\begin{aligned} \frac{r(\vartheta)}{\sqrt{\gamma_1}} dr d\vartheta =& \frac{\left(g^{\mathrm{xx}} \cos^2(\Theta) + \left[\frac{1}{\sqrt{g^{\mathrm{xx}}}} \left(g^{\mathrm{xy}} \cos(\Theta) - \sqrt{\gamma_1} \sin(\Theta)\right)\right]^2\right)}{1 + \left(\frac{g^{\mathrm{xy}}}{g^{\mathrm{xx}}} - \frac{\sqrt{\gamma_1}}{g^{\mathrm{xx}}} \tan(\Theta)\right)^2} \frac{1}{g^{\mathrm{xx}}} \frac{1}{\cos^2(\Theta)} \rho d\rho d\Theta \\ =& \rho \, d\rho \, d\Theta. \end{aligned} \tag{3.7.4}$$

Therefore, although the gyro-orbits have an elliptical shape in GENE-3D, the integration over a gyrodisk is performed in the same way as if the orbits were circular. Note that this is not necessarily true if a different representation of the particle position than (3.6.9) is chosen.

As a final step, we can express the Larmor radius ρ as a function of the phase-space

coordinate μ:

$$\begin{aligned} &\rho^2 = \rho^2(\mathbf{X}, \mu) \\ =&\frac{v_\perp^2(\mathbf{X}, \mu)}{\Omega^2(\mathbf{X})} = 2\mu \frac{c}{q\Omega(\mathbf{X})} \\ \Rightarrow &\rho d\rho = \frac{1}{2} d(\rho^2) = \frac{c}{q\Omega(\mathbf{X})} d\mu. \end{aligned} \tag{3.7.5}$$

With this, we can then bring the gyrodisk-integral into the final form

$$\begin{aligned} \mathcal{G}_\mathrm{D}\{u\}(\mathbf{X}, v_{||}, \mu, t) =& \frac{q_\sigma \Omega_\sigma}{2\pi c} \int_0^{2\pi} \int_0^{\rho} u(\mathbf{X} + \boldsymbol{\rho}'(\Theta), v_{||}, \mu, t)\ \rho'\, d\rho' d\Theta \\ =& \frac{1}{2\pi} \int_0^{2\pi} \int_0^{\mu} u(\mathbf{X} + \boldsymbol{\rho}'(\Theta), v_{||}, \mu, t)\, d\mu' d\Theta \\ =& \int_0^{\mu} \mathcal{G}_{\mu'}\{u\}\ d\mu', \end{aligned} \tag{3.7.6}$$

where $\mathcal{G}_{\mu'}\{\cdot\}$ represents the gyroaverage for a Larmor radius determined by μ'. It is important to note that the integral over μ' is still done with u being evaluated at fixed μ as the disk integral is only an integral in position space.

As for the calculation of the gyroaverage matrices in section 3.6, one can then introduce a finite-element basis $u(x, y, z) \approx \boldsymbol{\Lambda}(x, y)\mathbf{u}(z)$, so that one can describe the gyrodisk-integral as a matrix-vector product between the matrix $\boldsymbol{\mathcal{G}}_\mathbf{D}$ and the finite-element coefficients $\mathbf{u}$. In particular, for a given Larmor radius associated with a given magnetic moment μ, the gyrodisk-integral matrix $\boldsymbol{\mathcal{G}}_{\mathbf{D},\boldsymbol{\mu}}$ is given by

$$\begin{aligned} \boldsymbol{\mathcal{G}}_{\mathbf{D},\boldsymbol{\mu}} =& \int_0^{\mu} \mathcal{G}\left\{\boldsymbol{\Lambda}(x(\mathbf{X} + \boldsymbol{\rho}(\mu', \Theta)), y(\mathbf{X} + \boldsymbol{\rho}(\mu', \Theta)))\right\}\ d\mu' \\ \approx& \sum_{\mathrm{m}'=1}^{\mathrm{m}} \mathcal{G}\left\{\boldsymbol{\Lambda}(x(\mathbf{X} + \boldsymbol{\rho}(\mu_{\mathrm{m}'}, \Theta)), y(\mathbf{X} + \boldsymbol{\rho}(\mu_{\mathrm{m}'}, \Theta)))\ \right\}\ w_\mu(m') \end{aligned} \tag{3.7.7}$$

for appropriate quadrature points and weights m' and $w_\mu(m')$. In analogy to the gyromatrices in section 3.6, one can make use of the symmetry properties of the finite-element basis to show that the pull-back gyrodisk-integral $\boldsymbol{\mathcal{K}}_{\mathbf{D},\boldsymbol{\mu}}$ can be expressed as $\boldsymbol{\mathcal{K}}_{\mathbf{D},\boldsymbol{\mu}} = \boldsymbol{\mathcal{G}}_{\mathbf{D},\boldsymbol{\mu}}{}^\dagger$.

The model for this approach has been developed throughout this thesis and adapted for a Fourier representation in the binormal direction, which has then been implemented in GENE by Gabriele Merlo (The University of Texas at Austin). In order to test the validity of this model, it has been compared in flux-tube simulations against the fully local version of the code, where the gyrodisks are represented by Bessel functions. In figure 3.1, the linear growth rates and mode frequencies between the fully local and the so-called LILO version of the code, in which the global algorithm is used, but radial variations of the background are neglected, are compared for a CBC-like parameter setup (see section 3.9 for more details), showing excellent agreement, indicating that the prescribed approach is implemented correctly.

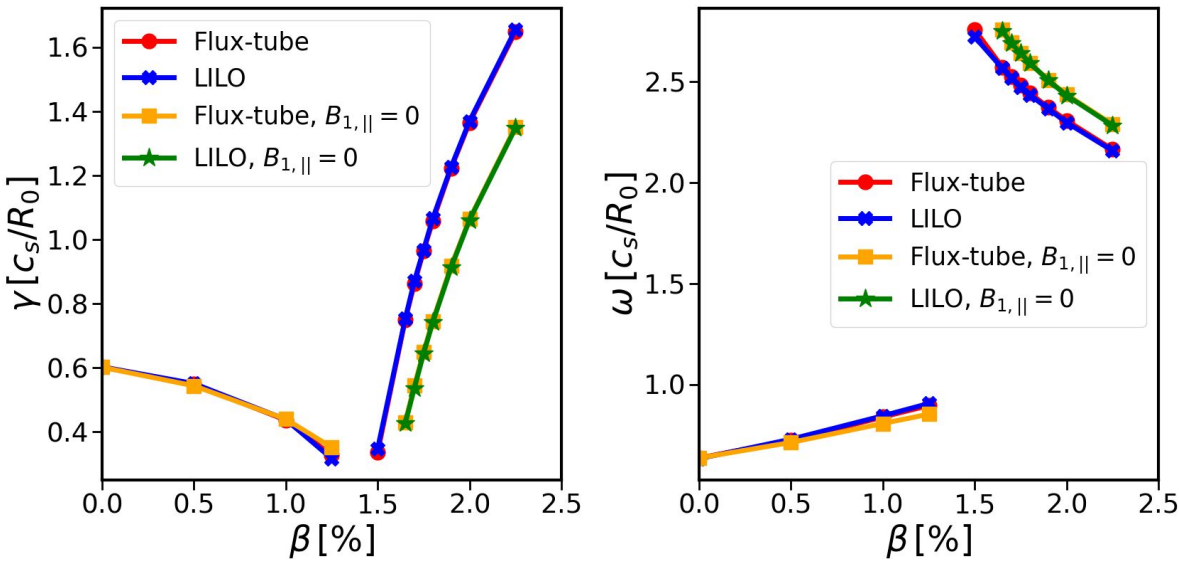

Figure 3.1: Linear growth rates (left) and real frequencies (right) of the $n_0 = 19$ mode ($k_y \simeq 0.3$) for local simulations with CBC-like parameters as a function of β. Blue crosses (resp. red circles) show the results obtained by the LILO (resp. local) version of GENE. For comparison, results neglecting $B_{1,||}$ are also shown via green stars (resp. orange squares) for the LILO version (resp. local).

3.8 Further numerical schemes

The normalised gyrokinetic Vlasov-Maxwell equations given in section 3.2 form an integro-differential system that requires appropriate methods of discretising derivatives and integrals. The following sections will briefly describe the methods employed in GENE-3D.

3.8.1 Time-stepping scheme

In order to evolve the distribution function $F_{1,\sigma}$ in time according to equation

$$\frac{\partial F}{\partial t} = \mathcal{V}(t, F), \tag{3.8.1}$$

with the right hand side operator given by equation (3.2.7), GENE-3D uses explicit Runge-Kutta methods. The default option is a fourth-order scheme (RK4),

$$F_{\mathrm{n}+1} = F_{\mathrm{n}} + \frac{\Delta t_{\mathrm{n}}}{6}\left(k_1 + k_2 + k_3 + k_4\right), \tag{3.8.2}$$

with $t_{\mathrm{n}+1} = t_{\mathrm{n}} + \Delta t_{\mathrm{n}}$, $F_{\mathrm{n}} = F(t = t_{\mathrm{n}})$. The coefficients k_{i} are calculated according to

$$\begin{aligned} k_1 &= \mathcal{V}(t_{\mathrm{n}}, F_{\mathrm{n}}), \\ k_2 &= \mathcal{V}\left(t_{\mathrm{n}} + \frac{\Delta t_{\mathrm{n}}}{2}, F_{\mathrm{n}} + \frac{k_1 \Delta t_{\mathrm{n}}}{2}\right), \\ k_3 &= \mathcal{V}\left(t_{\mathrm{n}} + \frac{\Delta t_{\mathrm{n}}}{2}, F_{\mathrm{n}} + \frac{k_2 \Delta t_{\mathrm{n}}}{2}\right), \\ k_4 &= \mathcal{V}\left(t_{\mathrm{n}} + \Delta t_{\mathrm{n}}, F_{\mathrm{n}} + k_3 \Delta t_{\mathrm{n}}\right). \end{aligned} \tag{3.8.3}$$

As in all explicit time integrators, a CFL-like limit on the time step Δt_{n} is required to guarantee the numerical stability of the algorithm. For linear simulations, an estimate is based on an upper limit of the normalised advection velocities in each direction given in equation (3.2.7). The time step is then chosen according to the stability region of the underlying Runge-Kutta scheme.

While the numerical time step is held constant in linear simulations, adjusting it for each step in nonlinear runs is necessary. The reason is the nonlinear $\nabla\chi$-drift, acting as a time-dependent advection velocity. To this end, a nonlinear time step adaptation is performed according to

$$\Delta t_{\max} = s_c \min(\Delta t_{\mathrm{lin}}, \Delta t_{\mathrm{NL}}), \tag{3.8.4}$$

where Δt_{lin} is the linear time step calculated at the beginning and Δt_{NL} is the time step limit under the assumption that there is only the nonlinear $\nabla\chi$-drift. As the superposition of these two limits is a rather crude approximation, a safety factor s_c, usually set to ≈ 0.5, is also introduced. Additionally, it was reported in [65] that adapting the time step at each iteration will lead to numerical artefacts if the time step is determined via the nonlinear estimate. Therefore, it is only changed if $0.8 \leq \Delta t / \Delta t_{\max} \leq 1.2$, leading to much smoother simulations.

3.8.2 Phase-space derivatives

GENE-3D uses a real-space representation of all phase-space coordinates. As such, a finite-difference approach is used, with a fourth-order central-difference scheme

$$\frac{\partial f}{\partial u} \approx \frac{f(u_{\mathrm{i}-2}) - 8f(u_{\mathrm{i}-1}) + 8f(u_{\mathrm{i}+1}) - f(u_{\mathrm{i}+2})}{12\Delta u} \tag{3.8.5}$$

shown to be the best compromise between computational cost and numerical accuracy. Here, u is any of the phase-space variables x, y, z or $v_{||}$, as no explicit calculation of derivatives in μ is required.

In order to avoid unphysical high-wavenumber modes that arise due to the central-difference approximations acting on the distribution function $F_{1,\sigma}$, one can introduce numerical hyperdiffusion terms to the right hand side of the gyrokinetic equation to dampen these modes. The hyperdiffusion terms in the x, y, z and $v_{||}$ direction are all fourth-order accurate with second-order stencils, meaning that they are of the form

$$\mathcal{H}_{\mathrm{u_i}} = \eta_{\mathrm{u}} \frac{-F_{1,\sigma}(u_{\mathrm{i}-2}) + F_{1,\sigma}(u_{\mathrm{i}-1}) - 6F_{1,\sigma}(u_{\mathrm{i}}) + 4F_{1,\sigma}(u_{\mathrm{i}+1}) - F_{1,\sigma}(u_{\mathrm{i}-2})}{16\Delta u}, \tag{3.8.6}$$

where the damping amplitude η_{u} can be set for each coordinate individually as input by the user.

3.8.3 Phase-space integrals

While a standard trapezoidal rule

$$\int_{-L_\mathrm{u}/2}^{L_\mathrm{u}/2} f(u)\,du \approx \sum_\mathrm{i} f(u_\mathrm{i})\Delta u \tag{3.8.7}$$

is employed for integration over any spatial direction, an extended Simpson's rule [66] is used in the $v_{||}-$direction. In the $\mu-$direction, a Gaussian quadrature scheme is used so that the Gauss-Laguerre knots are used. However, alternative quadrature schemes are also possible in accordance with the different choices of the underlying grid.

3.8.4 The necessity for conservative finite-difference methods

As mentioned in section 3.5, multiple choices are available for the grid used in the μ-direction. It was additionally stated that the default option is to use Gauss-Laguerre quadrature points, as they have proven to be the most efficient option for integration in GENE due to an expected exponential decay of functions in this coordinate. However, it turns out that for many full-flux-surface or global simulations, the polarisation matrix C_{11} defined in equation (3.2.17) becomes inaccurate, which results in discontinuities in the electrostatic potential along the magnetic field line, as can be seen in figure 3.2, ultimately leading to the simulations becoming unstable.

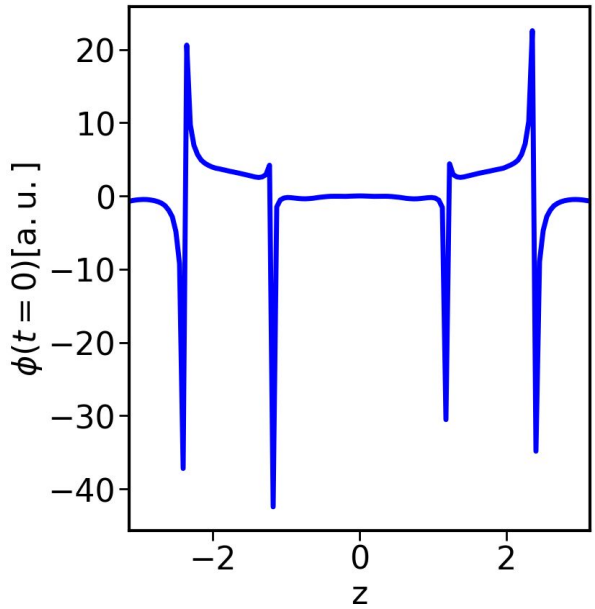

Figure 3.2: Electrostatic potential at t=0, averaged over all field lines, for a typical full-flux-surface simulation with kinetic electrons, using the full polarisation model.

We have found that using an equidistant grid alleviates this issue, at the cost of using a significantly higher resolution in μ up to a point which impacts performance [67]. It was found that while the polarisation matrix can become inaccurate, computing the right hand

side of the gyrokinetic equation (3.2.7) seems to be well-behaved under the given quadrature rule. While investigations into alternative grid types are still ongoing, a replacement of the full polarisation operator C_{11} by either a long-wavelength

$$C_{11,\mathrm{LWA}}\,\phi_1 = -\nabla_\perp \cdot \left[\sum_\sigma \left(\frac{m_\sigma n_{0,\sigma}}{B_0^2}\right) \nabla_\perp \phi_1\right] \tag{3.8.8}$$

or Padé approximation

$$C_{11,\mathrm{Padé}}\,\phi_1 = -\left(1 - \nabla_\perp \cdot \left[\sum_\sigma \left(\frac{T_{0,\sigma} m_\sigma}{q_\sigma^2 B_0^2}\right) \nabla_\perp\right]\right)^{-1} \nabla_\perp \cdot \left[\sum_\sigma \left(\frac{m_\sigma n_{0,\sigma}}{B_0^2}\right) \nabla_\perp \phi_1\right] \tag{3.8.9}$$

was implemented as a practical solution. The resulting Laplacian-like operators, however, need to be discretised with great care. The same applies to the Laplacian employed in Ampère's law and the induction equation, which we will use to explain the underlying challenge.

The Laplacian operator can be written in a coordinate-independent version as

$$\nabla^2 u = \frac{1}{\sqrt{g}} \frac{\partial}{\partial x^i} \left(g^{ij} \sqrt{g} \frac{\partial u}{\partial x^j}\right), \tag{3.8.10}$$

where $\sqrt{g}$ is the Jacobain and g^{ij} are the metric coefficients. Applying the chain rule gives

$$\nabla^2 u = \frac{1}{\sqrt{g}} \left(\frac{\partial}{\partial x^i} \sqrt{g} g^{ij}\right) \frac{\partial u}{\partial x^j} + g^{ij} \frac{\partial^2 u}{\partial x^i \partial x^j}.$$

Similar to what was done in GENE, the earliest implementation in GENE-3D assumed that the variation of the metric elements and the Jacobian is much smaller than that of the function u itself, so the first term on the right hand side could be dropped. Furthermore, only the symmetric part of the approximate Laplacian was retained for the operators to still have purely real eigenvalues. The operator that has, therefore, been used is of the form

$$\left[\nabla^2 - \frac{1}{\sqrt{g}} \left(\frac{\partial}{\partial x^i} \sqrt{g} g^{ij}\right) \frac{\partial}{\partial x^j}\right]_{\mathrm{symm}} u, \tag{3.8.11}$$

which might be interpreted as something close to an advection-diffusion operator rather than a purely elliptical Laplacian, which might be dominated by the term containing first derivatives of u if the derivatives of the metric elements become large, an issue that has already been known for tokamak simulations close to the magnetic axis or small devices due to the singularity of the chosen coordinate system at the radial origin [68].

Therefore, a numerical approximation of the Laplacian was implemented throughout this project that does not make any assumptions about the variation of the metric elements while still preserving the self-adjointness of the operator. The solution for that is to use finite-difference methods on staggered grids. In the following, we will explain the idea for a one-dimensional case using an equidistant grid. A more complete introduction can be found in [69].

Consider the differential diffusion equation

$$-\frac{d}{dx}\left(K(x)\frac{du}{dx}\right) = f(x), \quad x \in (a,b), \tag{3.8.12}$$

with boundary conditions being discussed later. A different formulation of this is given by

$$-\operatorname{div}\left(K(x)\operatorname{grad}\left(u\right)\right) = f(x), \quad x \in (a,b). \tag{3.8.13}$$

Assuming the matrix K is symmetric positive definite, the entire operator will be symmetric positive definite. That is, introducing the inner product

$$(u,v)_{\mathrm{H}} = \int_{\mathrm{a}}^{\mathrm{b}} u(x)v(x)\,dx,$$

and considering functions that are zero at the boundary, we have

$$\left(-\operatorname{div}\left(K\operatorname{grad}\left(u\right)\right),v\right)_{\mathrm{H}} = \left(u,-\operatorname{div}\left(K\operatorname{grad}\left(v\right)\right)\right)_{\mathrm{H}}$$

and

$$\left(-\operatorname{div}\left(K\operatorname{grad}\left(u\right)\right),u\right)_{\mathrm{H}} \geq 0.$$

This can be seen by the identity

$$\int_{\mathrm{a}}^{\mathrm{b}} \operatorname{grad}\left(u\right)\cdot\mathbf{A}\,dx + \int_{\mathrm{a}}^{\mathrm{b}} u\operatorname{div}\left(\mathbf{A}\right)\,dx = 0, \tag{3.8.14}$$

if u is zero at the boundary.

If one, therefore, constructs finite-difference operators $\mathrm{D_x}$ and $\mathcal{D}_{\mathrm{x}}$ to approximate the operators grad and div, respectively, in such a way that they fulfil the discrete analogue of equation (3.8.14), the matrix

$$-\mathcal{D}_{\mathrm{x}}K\mathrm{D_x}$$

will be symmetric positive given that K is symmetric positive definite. As was shown in [69], the way to achieve this is to define the operator $\mathrm{D_x}$ as a finite-difference operator that approximates the first derivative at half-cell positions. That is, we want

$$\mathrm{D_x}:\ u(x_{\mathrm{i}}) \to \frac{\partial u}{\partial x}|_{\mathrm{x}=\mathrm{x}_{\mathrm{i}+1/2}} \tag{3.8.15}$$

to our desired order of accuracy. In order to approximate the diffusive flow $K(x)\partial u/\partial x$ correctly, the matrix K, representing the diffusion coefficient, should be given by

$$K_{\mathrm{ij}} = K(\mathrm{x}_{\mathrm{i}+1/2})\,\delta_{\mathrm{ij}}. \tag{3.8.16}$$

The 'derived' operator $\mathcal{D}_{\mathrm{x}}$, constituting the approximation of the divergence, is then chosen in such a way that it takes the function values at half-cell positions and maps them back to the original grid, that is

$$\mathcal{D}_{\mathrm{x}}:\ v(x_{\mathrm{i}+1/2}) \to \frac{\partial v}{\partial x}|_{\mathrm{x}=\mathrm{x}_{\mathrm{i}}}. \tag{3.8.17}$$

While the rigorous method of constructing $\mathcal{D}_\mathrm{x}$ was presented in [69], we note that intuitively it makes sense that it is given by

$$\mathcal{D}_\mathrm{x} = -\mathrm{D}_\mathrm{x}^\mathrm{T}$$

in order to make the composite operator symmetric. As can be shown easily, a fourth-order accurate approximation of the gradient at $x_{\mathrm{i}+1/2}$ using a finite-difference scheme is given by

$$(\mathrm{D}_\mathrm{x}u)_{\mathrm{i}+1/2} = \frac{1}{24\Delta x}\left(u_{\mathrm{i}-1} - 27u_\mathrm{i} + 27u_{\mathrm{i}+1} - u_{\mathrm{i}+2}\right), \tag{3.8.18}$$

which means that the divergence operator is given by

$$(\mathcal{D}_\mathrm{x}v)_\mathrm{i} = -\frac{1}{24\Delta x}\left(-v_{\mathrm{i}-3/2} + 27v_{\mathrm{i}-1/2} - 27v_{\mathrm{i}+1/2} + v_{\mathrm{i}+3/2}\right). \tag{3.8.19}$$

It becomes apparent that, in order to calculate the Laplacian close to and at the grid boundaries, one needs information about the function values outside of the domain. In GENE-3D, we assume that all functions of interest are periodic or zero beyond the domain boundaries.

If our domain is from $[x_1, x_{\mathrm{N}-1}]$, so that x_0 and x_N are the boundary points, then we see that the Laplacian at our domain grids is given by

$$\begin{aligned}
(\mathcal{D}_\mathrm{x}D_\mathrm{x}u)_1 &= \frac{1}{24\Delta x}\left((D_\mathrm{x}u)_{-1/2} + 27(D_\mathrm{x}u)_{1/2} - (D_\mathrm{x}u)_{3/2} + (D_\mathrm{x}u)_{5/2}\right), \\
(\mathcal{D}_\mathrm{x}D_\mathrm{x}u)_{\mathrm{N}-1} &= \frac{1}{24\Delta x}\left((D_\mathrm{x}u)_{\mathrm{N}-5/2} + 27(D_\mathrm{x}u)_{\mathrm{N}-3/2} - (D_\mathrm{x}u)_{\mathrm{N}-1/2} + (D_\mathrm{x}u)_{\mathrm{N}+1/2}\right).
\end{aligned} \tag{3.8.20}$$

It becomes apparent that we need to calculate gradients at half-cells that are no longer in our domain. From equation (3.8.18), we see that we require knowledge of the ghost-cells u_{-2}, u_{-1} and $u_{\mathrm{N}+1}$, which are determined through the choice of boundary conditions as discussed in section 3.5.

An extension of this formalism to two dimensions was given in [70] and [71] for a second- and fourth-order accurate algorithm, respectively. Both stencils are implemented in GENE-3D, where the fourth-order accurate stencil is used as default and reads

$$\begin{aligned}
(\mathrm{D}_\mathrm{x}u)_{\mathrm{i}+1/2,\mathrm{j}+1/2} =& \frac{1}{384\Delta x}\begin{bmatrix} 243\left(T_{i+1,j+1} + T_{i+1,j} - T_{i,j+1} - T_{i,j}\right) \\ +27\left(T_{i,j+2} + T_{i,j-1} - T_{i+1,j+2} - T_{i+1,j-1}\right) \\ +9\left(T_{i-1,j+1} + T_{i-1,j} - T_{i+2,j+1} - T_{i+2,j}\right) \\ +\left(T_{i+2,j+2} + T_{i+2,j-1} - T_{i-1,j+2} - T_{i-1,j-1}\right) \end{bmatrix}, \\
(\mathrm{D}_\mathrm{y}u)_{\mathrm{i}+1/2,\mathrm{j}+1/2} =& \frac{1}{384\Delta x}\begin{bmatrix} 243\left(T_{i+1,j+1} - T_{i+1,j} + T_{i,j+1} - T_{i,j}\right) \\ -9\left(T_{i,j+2} - T_{i,j-1} + T_{i+1,j+2} - T_{i+1,j-1}\right) \\ -27\left(T_{i-1,j+1} - T_{i-1,j} + T_{i+2,j+1} - T_{i+2,j}\right) \\ +\left(T_{i+2,j+2} - T_{i+2,j-1} + T_{i-1,j+2} - T_{i-1,j-1}\right) \end{bmatrix}.
\end{aligned} \tag{3.8.21}$$

The divergence operators are given by $\mathcal{D}_\mathrm{x} = -D_\mathrm{x}^\mathrm{T}$ and $\mathcal{D}_\mathrm{y} = -D_\mathrm{y}^\mathrm{T}$, respectively, and the Laplacian is then

$$\nabla_\perp^2 u \approx \frac{1}{\sqrt{g}}\left[\mathcal{D}_\mathrm{x}\left(\sqrt{g}g^{\mathrm{xx}}D_\mathrm{x}u + \sqrt{g}g^{\mathrm{xy}}D_\mathrm{y}u\right) + \mathcal{D}_\mathrm{y}\left(\sqrt{g}g^{\mathrm{yy}}D_\mathrm{y}u + \sqrt{g}g^{\mathrm{xy}}D_\mathrm{x}u\right)\right]. \tag{3.8.22}$$

The respective field equations are then multiplied by $\sqrt{g}$ in order to make the operator symmetric.

As a result, in contrast to the standard Laplacian, this symmetric formulation produces reasonable solutions of the field equations, as shown in figure 3.3, resulting in numerically stable simulations.

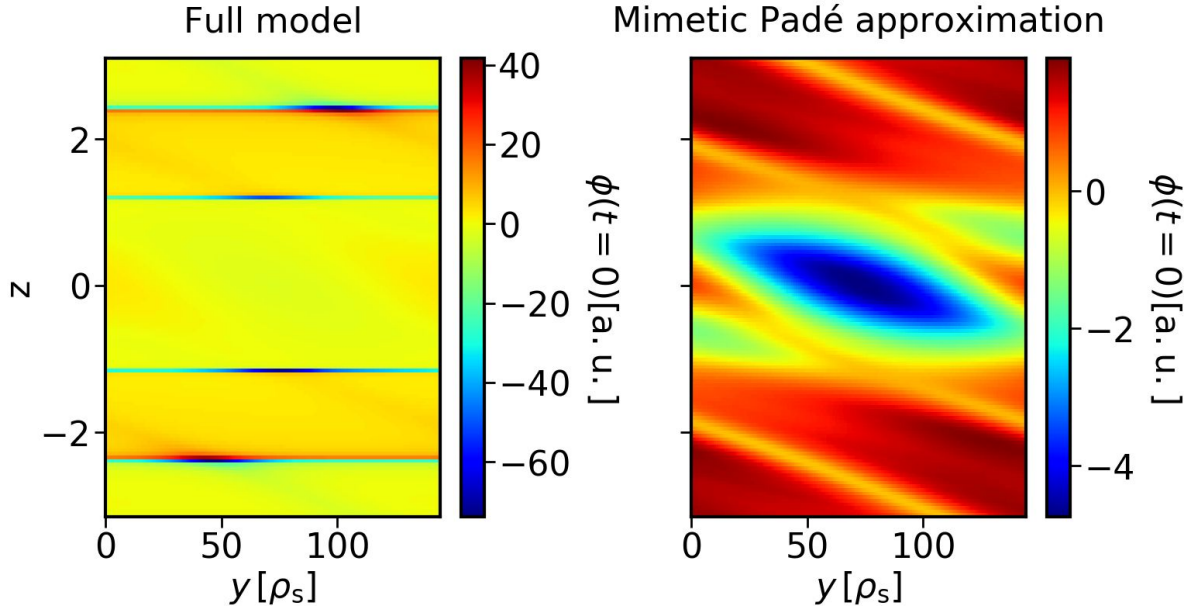

Figure 3.3: Left: the same electrostatic potential as in figure 3.2, as a function of y and z; right: electrostatic potential at t=0 of the same simulation setup, but with a mimetic Padé approximation of the polarisation matrix.

3.8.5 Treatment of the nonlinear terms

As already mentioned in section 3.2, the nonlinear interaction between distribution functions and electromagnetic fields can be expressed in terms of Poisson brackets

$$\{F, G\}_{\mathrm{x,y}} = \frac{\partial F}{\partial x}\frac{\partial G}{\partial y} - \frac{\partial F}{\partial y}\frac{\partial G}{\partial x}. \tag{3.8.23}$$

However, simple evaluation of the derivatives via finite-difference approximation results in numerically unstable simulations. It was shown in [72] that such an approach does not conserve the system's free energy. In the same paper, an alternative scheme was proposed, numerically satisfying

$$\int \{F, G\}_{\mathrm{x,y}}\, dxdy = 0, \qquad \int F\, \{F, G\}_{\mathrm{x,y}}\, dxdy = 0, \qquad \int G\, \{F, G\}_{\mathrm{x,y}}\, dxdy = 0, \tag{3.8.24}$$

and conserving free energy. The same scheme has been implemented in GENE-3D and uses a finite-difference approximation of

$$\{F, G\}_{\mathrm{x,y}} = \frac{1}{3}\left[\{F, G\}_{\mathrm{x,y}} + \frac{\partial}{\partial x}\left(F\frac{\partial G}{\partial y} - G\frac{\partial F}{\partial y}\right) + \frac{\partial}{\partial y}\left(G\frac{\partial F}{\partial x} - F\frac{\partial G}{\partial x}\right)\right]. \tag{3.8.25}$$

3.8.6 Sources and sinks

In a nonlinear setup, turbulent heat and particle fluxes arise in the system, which naturally causes the transport of particle densities and temperatures, especially in the radial direction. If periodicity of the radial domain is assumed, any quantity of interest leaving through one side of the domain will automatically reenter through the other side. Thus, the radial average of particle densities and temperatures will remain constant. This is no longer the case if Dirichlet boundary conditions are employed. In this case, the system naturally tries to relax the profiles to a sub-critical state where turbulence is suppressed, which has to be avoided in gradient-driven simulations, as they aim to calculate turbulent quantities for a fixed set of profiles.

In order to combat this relaxation, numerical heat and particle sources are added to the right hand side of the gyrokinetic equation. GENE-3D uses sources of the form

$$S_{\mathrm{P},\sigma} = -\kappa_{\mathrm{P}} \frac{\left\langle F_{\mathrm{M},\sigma}(\mathbf{X}, |v_{||}|, \mu) \right\rangle_{\mathrm{FS}}}{\sum\limits_{\sigma} \left\langle \int F_{\mathrm{M},\sigma}(\mathbf{X}, |v_{||}|, \mu)\, d^3v \right\rangle_{\mathrm{FS}}} \sum_{\sigma} \left\langle \int \left\langle F_{1,\sigma}(\mathbf{X}, |v_{||}|, \mu, t) \right\rangle_{\mathrm{FS}} d^3v \right\rangle_{\mathrm{FS}} \tag{3.8.26}$$

in the case of the particle source and

$$S_{\mathrm{H},\sigma} = -\kappa_{\mathrm{H}} \left[\left\langle F_{1,\sigma}(\mathbf{X}, |v_{||}|, \mu, t) \right\rangle_{\mathrm{FS}} - \frac{\left\langle \int \left\langle F_{1,\sigma}(\mathbf{X}, |v_{||}|, \mu, t) \right\rangle_{\mathrm{FS}} d^3v \right\rangle_{\mathrm{FS}}}{\left\langle \int \left\langle F_{\mathrm{M},\sigma}(\mathbf{X}, |v_{||}|, \mu) \right\rangle_{\mathrm{FS}} d^3v \right\rangle_{\mathrm{FS}}} \left\langle F_{\mathrm{M},\sigma}(\mathbf{X}, |v_{||}|, \mu) \right\rangle_{\mathrm{FS}} \right] \tag{3.8.27}$$

for the heat source, with

$$F_{1,\sigma}(\mathbf{X}, |v_{||}|, \mu, t) = \frac{F_{1,\sigma}(\mathbf{X}, v_{||}, \mu, t) + F_{1,\sigma}(\mathbf{X}, -v_{||}, \mu, t)}{2}.$$

The symmetrisation of the distribution function with respect to $v_{||}$ in equation (3.8.27) ensures the conservation of parallel momentum and the terms proportional $\left\langle \int (...) \right\rangle_{\mathrm{FS}} / \left\langle \int (...) \right\rangle_{\mathrm{FS}}$ avoids the unwanted numerical injection of particles [73]. The coefficients κ_{P} and κ_{H} are specified by the user and should be chosen to be around 5-10% of the maximum linear growth rate of the system [58].

Nevertheless, avoiding profile relaxation altogether is impossible in practical applications, as the sources are only active once finite relaxation occurs. In such instances, small profile variations close to the boundaries might generate large gradients, resulting in significant fluctuation levels incompatible with the Dirichlet condition. In order to avoid this, one additionally introduces Krook-type damping terms of the form

$$K_{\mathrm{x}} = -\nu(x) F_{1,\sigma} \tag{3.8.28}$$

to the gyrokinetic equation, where the damping factor $\nu(x)$ is implemented as a fourth-order polynomial with compact support within a buffer region at the radial boundaries, typically 5-10% at each side of the domain.

3.9 Numerical benchmarks of the electromagnetic upgrade

Having introduced the general framework of GENE-3D along with the electromagnetic upgrades performed throughout this work, the following sections will provide benchmark scenarios of GENE-3D against its tokamak counterpart, GENE. At the time of the upgrade, no other global stellarator code was able to include electromagnetic effects in its considerations. Therefore, the logical option was to benchmark GENE-3D against its long-established tokamak-counterpart GENE in global, electromagnetic tokamak simulations. In particular, we consider a modified version of the so-called Cyclone Base Case (CBC) [74, 75], which constitutes the most widely used setup for benchmarks of gyrokinetic tokamak codes. In particular, one considers a tokamak geometry with circular, concentric flux-surfaces, as it provides an easy test case with an analytical magnetic field geometry. The magnetic field on axis B_{ref} is chosen to be 2.0 T and the major radius considered here is $R_0 = 1.67\,\mathrm{m}$ with an aspect ratio of $a/R_0 = 0.36$. The safety factor profile is chosen to be

$$q(x) = 0.86 - 0.16(x/a) + 2.52(x/a)^2 \tag{3.9.1}$$

and the temperatures at the reference point $x_0/a = 0.5$ are chosen to be $T_{\mathrm{i}}(x_0) = T_{\mathrm{e}}(x_0) = 2.14\,\mathrm{keV}$. As a first step, we perform linear simulations at fixed wavenumber, varying the plasma-β with both the radially global version of GENE and GENE-3D in section 3.9.1, showing excellent agreement between the codes. We then take it a step further in section 3.9.2 and compare nonlinear heat fluxes predicted by both codes, only showing small discrepancies. Both tests together give confidence that the implementation of finite $A_{1,||}$ in GENE-3D is correct and that the code is able to simulate electromagnetic plasma turbulence.

3.9.1 Linear β-scan in global tokamak geometry

For the linear scans, the background density and temperature profiles are the same as in [45], namely of the form

$$\frac{A}{A(x_0)} = \exp\left[-\kappa_{\mathrm{A}} w_{\mathrm{A}} \frac{a}{R_0} \tanh\left(\frac{x - x_0}{w_{\mathrm{A}} a}\right)\right] \tag{3.9.2}$$

for both, electrons and ions, where $A = (n, T_{\mathrm{i}}, T_{\mathrm{e}})$. The corresponding normalised logarithmic gradients are

$$\frac{R_0}{L_{\mathrm{A}}} = -R_0 \frac{\partial \ln(A)}{\partial x} = \kappa_{\mathrm{A}} \cosh^{-2}\left(\frac{x - x_0}{w_{\mathrm{A}} a}\right), \tag{3.9.3}$$

The reference density $n_{\mathrm{ref}} = n(x_0)$ is adjusted for each case such that the corresponding plasma-β at the reference position is equal to the desired value. The remaining free parameters of the profiles are chosen to be $\kappa_{\mathrm{T_i}} = \kappa_{\mathrm{T_e}} = 6.96$, $w_{\mathrm{T_i}} = w_{\mathrm{T_e}} = 0.3$, $\kappa_{\mathrm{n_i}} = \kappa_{\mathrm{n_e}} = 2.23$ and $w_{\mathrm{n_i}} = w_{\mathrm{n_e}} = 0.3$. The plasma consists of Deuterium as ionic species and electrons with twice their realistic mass to keep the ion-to-electron mass ratio to that of a hydrogen plasma. The box lengths are chosen to be $(L_{\mathrm{x}}, L_{\mathrm{v}_{||}}, L_\mu) = (80\,\rho_{\mathrm{s}}, 3\,v_{\mathrm{th},\sigma}(x_0), 9\,T_{0,\sigma}(x_0)/B_{\mathrm{ref}})$ and $L_{\mathrm{y}} = 21.13\,\rho_{\mathrm{s}}$, which results in resolving multiples of the toroidal mode number $n_0 = 19$.

For the GENE-3D simulations, a resolution of $(1344 \times 16 \times 16 \times 64 \times 32)$ points in $(x, y, z, v_{||}, \mu)$ were used, together with hyperdiffusion parameters set to $\eta_{\mathrm{x}} = 2.0$, $\eta_{\mathrm{y}} = 0.05$, $\eta_{\mathrm{z}} = 2.0$ and $\eta_{\mathrm{v}_{||}} = 0.2$, respectively. The same parameters were used for performing the GENE simulations, except that, due to the Fourier representation in y, only one Fourier mode and no hyperdiffusion in y was used.

Figure 3.4 shows the linear growth and the corresponding linear frequency of the $n_0 = 19$ mode for various values of β. Red data points indicate results obtained by GENE, whereas blue represents results obtained by GENE-3D. Both codes show excellent agreement in growth rates and mode frequencies, with a relative error between both codes being less than 3%.

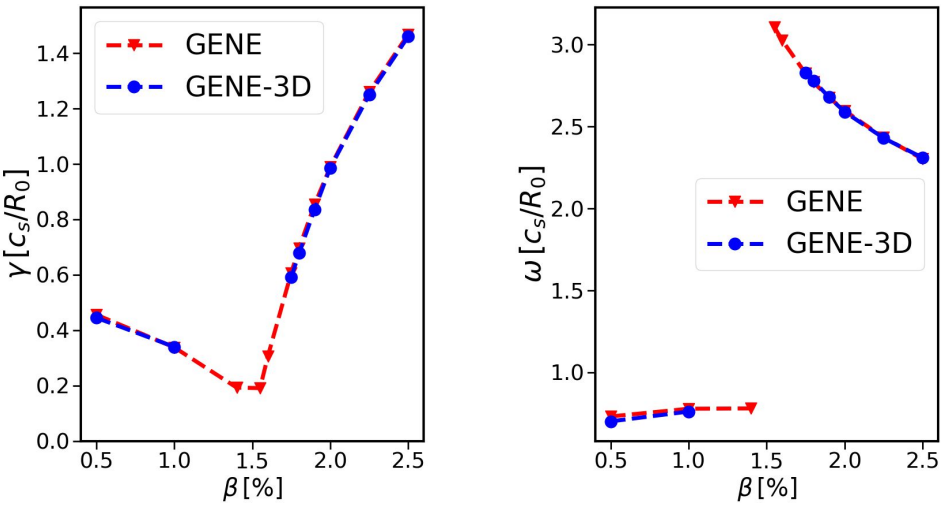

Figure 3.4: Linear growth rates (left) and mode frequencies (right) of the $n_0 = 19$ mode for various values of β. Red shows the results obtained with GENE, and blue the ones obtained with GENE-3D.

In particular, one can observe a reduction of the linear growth rate, which is caused by ITG instabilities, through increasing β, up to $\beta \approx 1.4\%$, where a transition to KBM instabilities can be observed, which is indicated by the rapid increase in mode frequency.

In order to further verify the results of GENE-3D, the radial and parallel mode structures of the instability at $\beta = 2.5\%$ are compared for both codes in figure 3.5, again showing excellent agreement with each other.

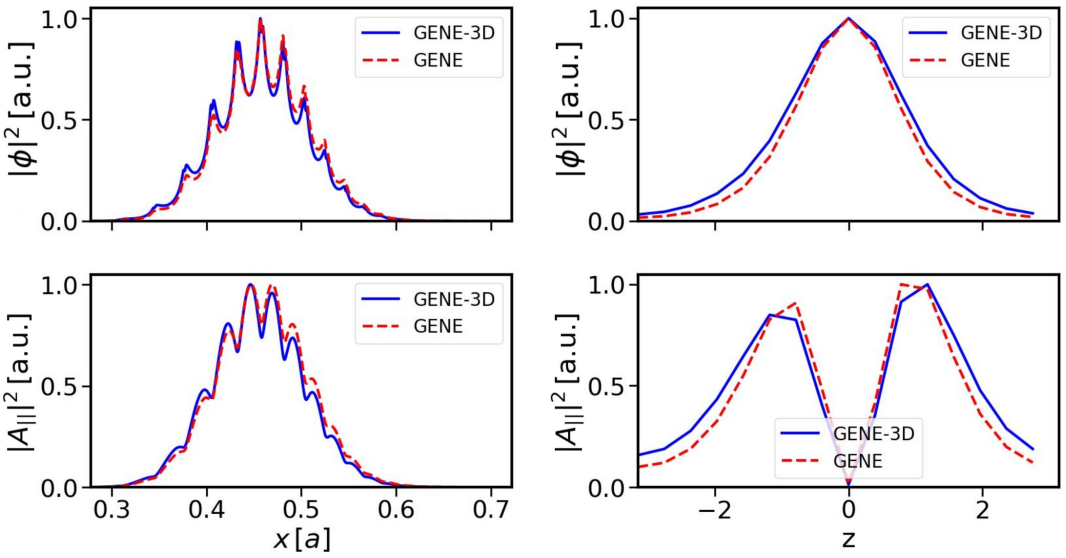

Figure 3.5: Normalised squares of the electrostatic and parallel vector potential for the scenario using $\beta = 2.5\%$; top: radial (left) and parallel (right) structures of the electrostatic potential, bottom: radial (left) and parallel (right) structures of the parallel vector potential. The red dashed line shows the results obtained by GENE, and the blue solid line the ones obtained with GENE-3D.

3.9.2 Nonlinear turbulence at finite plasma-β in a tokamak

In order to fully verify the correct implementation of all additional terms of the electromagnetic upgrade, one has to perform nonlinear simulations and compare them against an established code, which in this case is GENE again.

While the geometry being used is kept the same in this section, using a broader profile than the one in the last subsection is helpful in order to reduce the amount of unwanted profile relaxation that naturally occurs in gradient-driven simulations.

Therefore, new plasma profiles of the form

$$\frac{A}{A(x_0)} = \left[\frac{\cosh\left(\frac{x-x_0+\Delta_\mathrm{A}}{w_\mathrm{A}}\right)}{\cosh\left(\frac{x-x_0-\Delta_\mathrm{A}}{w_\mathrm{A}}\right)}\right]^{-\frac{\kappa_\mathrm{A} w_\mathrm{A}}{2}\frac{a}{R_0}} \tag{3.9.4}$$

are chosen, with $x_0/a = 0.5$, $\kappa_{\mathrm{T_i}} = \kappa_{\mathrm{T_e}} = 6.66$, $\kappa_n = 2.20$, $w_{\mathrm{T_i}} = w_{\mathrm{T_e}} = w_\mathrm{n} = 0.04$ and $\Delta_{\mathrm{T_i}} = \Delta_{\mathrm{T_e}} = \Delta_\mathrm{n} = 0.8$. Furthermore, the plasma pressure is such that $\beta_\mathrm{e}(x_0) = 0.75\%$. In order to save computational time, the simulations were performed further increasing the electron-to-ion mass ratio to $m_\mathrm{e}/m_\mathrm{i} = 0.01$ and a finite-size parameter $\rho_\mathrm{s}^* = \rho_\mathrm{s}/L_\mathrm{ref} = \rho_\mathrm{s}/R_0 = 0.01$. The simulation covers the radial domain $0.1 \leq x/a \leq 0.9$, using buffer zones of 10% at each side, with normalised box sizes being $(L_\mathrm{x}, L_\mathrm{y}, L_{\mathrm{v}_{||}}, L_\mu) = (80.0\,\rho_\mathrm{s}, 111.4\,\rho_\mathrm{s}, 3\,v_{\mathrm{th},\sigma}(x_0), 9\,T_{0,\sigma}(x_0)/B_\mathrm{ref})$ and a resolution of $(n_\mathrm{x}, n_{\mathrm{k_y}}, n_\mathrm{z}, n_{\mathrm{v}_{||}}, n_\mu) = (160 \times 64 \times 24 \times 64 \times 24)$ for GENE and $(n_\mathrm{x}, n_\mathrm{y}, n_\mathrm{z}, n_{\mathrm{v}_{||}}, n_\mu) = (160 \times 256 \times 24 \times 64 \times 24)$ for GENE-3D, respectively. Finally, heat and particle sources were added with amplitudes being $\kappa_\mathrm{H} = \kappa_\mathrm{P} = 0.1$ and hyperdiffusion was set $\eta_\mathrm{x} = \eta_\mathrm{y} = 0.05$, $\eta_\mathrm{z} = 2.0$ and $\eta_{\mathrm{v}_{||}} = 0.2$.

In order to compare the results of the two nonlinear simulations, we compare the nonlinear

Heat flux $[Q_{\mathrm{GB}}]$	GENE	GENE-3D
$Q_{\mathrm{es,ions}}$	$76. \pm 7$	75 ± 11
$Q_{\mathrm{es,electrons}}$	60 ± 5	55 ± 6
$Q_{\mathrm{em,ions}}$	-1.07 ± 0.13	-1.13 ± 0.15
$Q_{\mathrm{em,electrons}}$	-1.70 ± 0.32	-1.65 ± 0.33

Table 3.1: Time-averaged heat flux contributions of GENE and GENE-3D.

heat fluxes defined in section 3.3. Figure 3.6 shows the volume-averaged time traces of the ion and electron heat flux contributions, each split into their electrostatic and electromagnetic components. Since the time traces show large fluctuations in their amplitudes, a simple comparison between the mean values and the standard deviations obtained by GENE and GENE-3D is not helpful, as the latter quantity will be of the order of the mean value itself. In order to obtain a quantitative comparison, the time traces in the range $t \in [100, 345]\, R_0/c_{\mathrm{s}}$, roughly containing the same number of bursts for both codes, are divided into disjoint intervals, each approximately three autocorrelation times long. By taking the mean for each section individually, one can obtain an ensemble average and variance for the heat flux that is statistically meaningful in the context of an inter-code comparison.

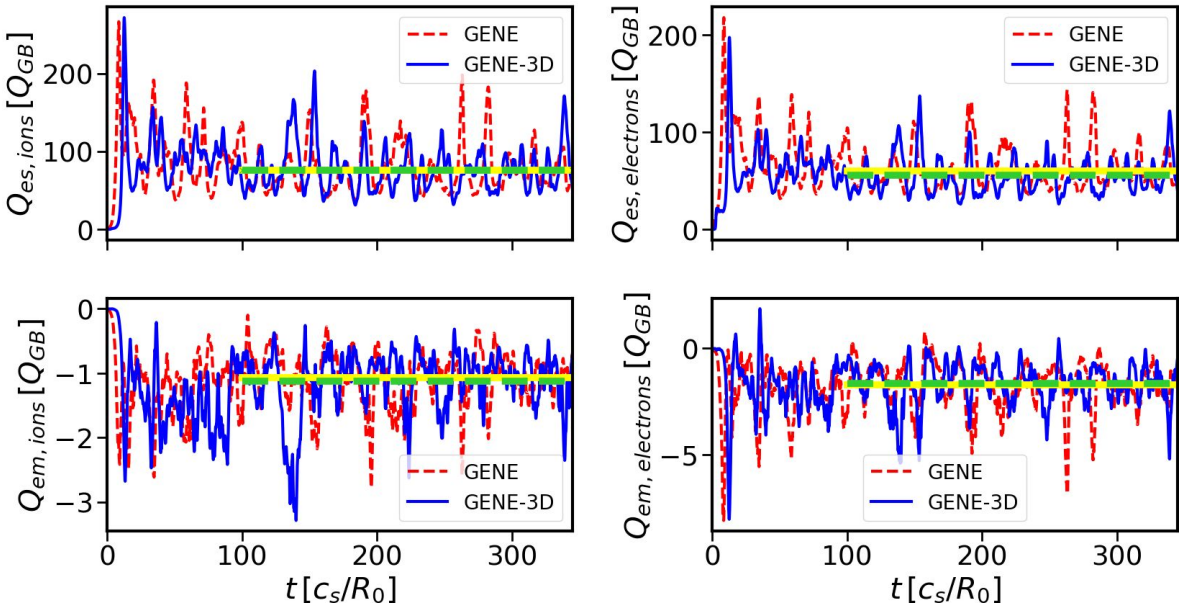

Figure 3.6: Time traces of the volume-averaged electron and ion heat fluxes. Yellow and green lines indicate the average over the given time interval for GENE and GENE-3D, respectively. Electrostatic heat flux of ions (top left) and electrons (top right), and electromagnetic heat flux of ions (bottom left) and electrons (bottom right).

The results are presented in table 3.1. Both simulations are in good agreement with each other, as the relative difference between their respective ensemble mean values is below 10 % for all components.

Further inspection of the radial heat flux profiles, shown in figure 3.7, show excellent agreement between the two codes. In there, one can see that the electrostatic contribu-

tions dominate the fluxes, peaking around $x/a = 0.6$. At this position, GENE predicts the heat fluxes to be $Q_{\text{es,ions}} = 103.24\, Q_{\text{GB}}$, $Q_{\text{es,electrons}} = 80.09\, Q_{\text{GB}}$, whereas GENE-3D gives $Q_{\text{es,ions}} = 104.72\, Q_{\text{GB}}$ and $Q_{\text{es,electrons}} = 75.41\, Q_{\text{GB}}$. Both results differ by less than 6%, giving additional confidence in the numerical implementation of the latter code.

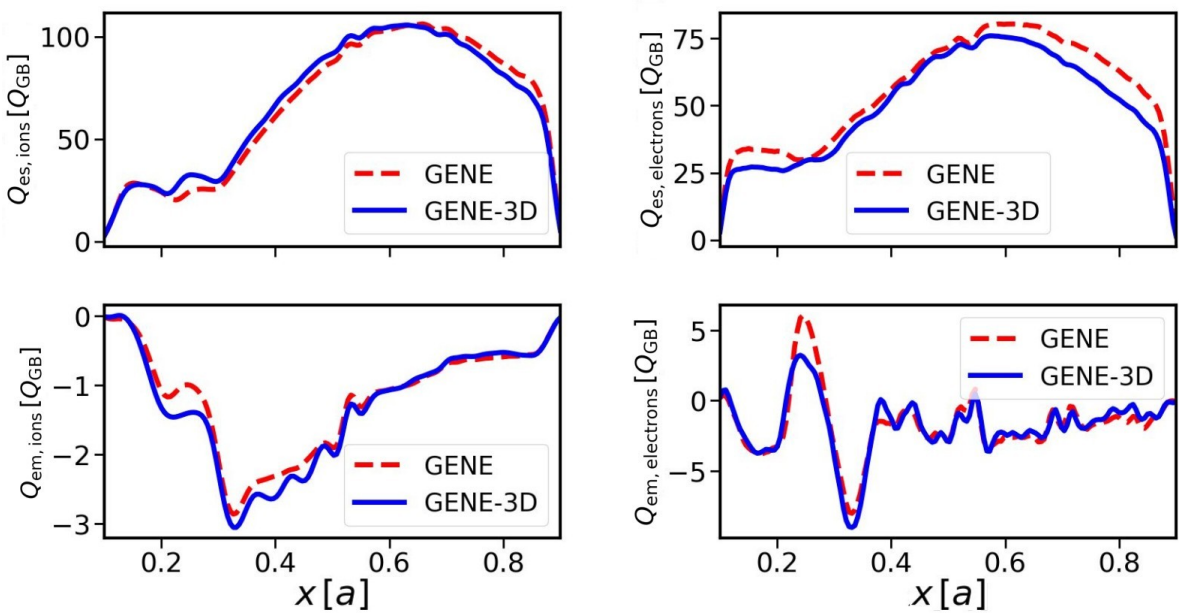

Figure 3.7: Radial profiles of heat flux contributions. Electrostatic heat flux of ions (top left) and electrons (top right), and electromagnetic heat flux of ions (bottom left) and electrons (bottom right).

Finally, the spectra of the electrostatic heat fluxes at $x/a = 0.6$ are compared in figure 3.8, showing only minor deviations between both codes at the smallest scale, which can be attributed to the different representations of the binormal coordinate.

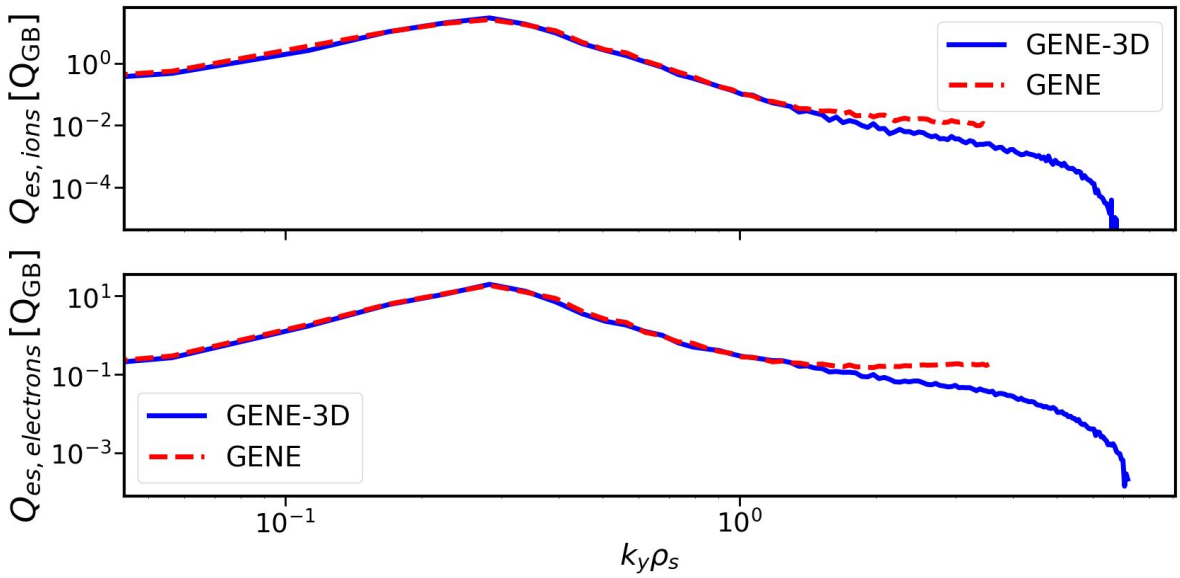

Figure 3.8: k_y-spectra of the electrostatic heat fluxes, evaluated at $x/a = 0.6$.

Overall, these results show excellent agreement of the spectra in the wavenumber interval where most of the transport is located. Therefore, the linear and nonlinear verification studies of GENE-3D can be considered successful.

3.10 Chapter summary

The present chapter outlined the numerical techniques used in GENE-3D to discretise the gyrokinetic Vlasov-Maxwell system. The steps necessary to upgrade the code to an electromagnetic turbulence code, including parallel vector potential and possible techniques to implement parallel magnetic field perturbations in the future, have been outlined. Furthermore, a mimetic finite-difference scheme based on the support-operator method for the Laplacian operator has been introduced as a necessary tool to run non-local simulations with kinetic electrons in GENE-3D. Linear and nonlinear verification studies with global, electromagnetic tokamak simulations against GENE have shown excellent agreement between the two codes so that the implementation of the improved model can be considered successful.

Thanks to the upgrades performed within this project, GENE-3D can accurately simulate a broad range of electrostatic as well as electromagnetic phenomena, making it possible to investigate most of the parameter space of core turbulence considered in the operational phases of Wendelstein 7-X to this date.

Chapter 4

Electromagnetic effects on ITG turbulence in Wendelstein 7-X-like plasmas

In gyrokinetics, a crucial dimensionless parameter is the plasma-β, which was defined in section 3.2. It serves as a measure of the impact of electromagnetic effects on the overall system, given the explicit dependence of the normalised Ampére's law (3.2.13) on this parameter. The effects encompass, amongst other things, both stabilising and destabilising influences on turbulence, as well as the excitation of instabilities like kinetic ballooning modes (KBM). Since fusion performance scales favourably with an increasing β [9], the corresponding plasma regimes need to be well understood for the design of future fusion power plants. Although finite electromagnetic effects were already incorporated routinely in flux-tube simulations, comprehensive studies of global stellarator turbulence at finite β were largely absent, with only a single study using artificially heavy electrons [76] was published at the time. However, flux-tube and global simulations of tokamaks were shown to predict substantially different characteristics regarding the saturation of electromagnetic ITG and KBM turbulence in [77]. The reason for the discrepancy was found to be additional global entropy transfer for the latter model, emphasising the need to study such phenomena globally for stellarators as well. While such studies are out of the scope of this chapter, the successful verification of the electromagnetic upgrade of GENE-3D in section 3.9 allows us to gain a first insight into the influence of electromagnetic effects on ITG turbulence in Wendelstein 7-X-like geometries at moderate values of β already. The results presented here follow what was published in [34].

The rest of this chapter is structured as follows: we introduce the numerical setup of all simulations performed throughout this chapter in section 4.1. In section 4.2, we present the stabilisation of global, linear ITG instabilities through finite plasma-β, followed by an analysis of the impact of β on nonlinear ITG turbulence in section 4.3.

4.1 Numerical setup

All simulations throughout this chapter are performed using the standard configuration [78] of Wendelstein 7-X. The normalised density and temperature profiles are chosen to be the same for all simulations and are shown in figure 4.1. Therefore, in order to change the plasma-β, only the reference density n_{ref} has to be changed.

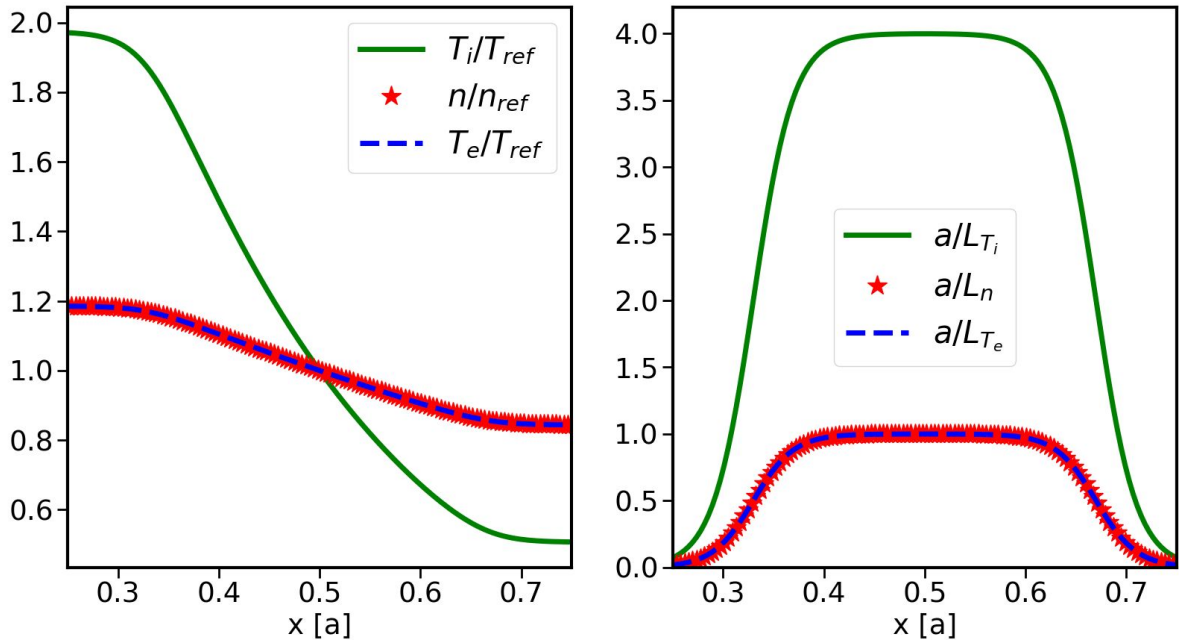

Figure 4.1: Left: initial density and temperature profiles. Right: initial normalised density and temperature gradient profiles.

As can be seen in the right plot of figure 4.1, the profiles are chosen such that most of the drive is localised around the centre of the plasma volume with no significant contributions towards the radial boundaries, which allows us to get an accurate representation while only using a limited radial domain, thus saving computational cost. Furthermore, the ion temperature gradient is chosen to be significantly larger than the electron temperature and density gradients, thus mainly destabilising ITG modes. The specific form of the density and temperature profiles is given by

$$\frac{A}{A(x_0)} = \left[\frac{\cosh\left(\frac{x-x_0+\Delta_\mathrm{A}}{w_\mathrm{A}}\right)}{\cosh\left(\frac{x-x_0-\Delta_\mathrm{A}}{w_\mathrm{A}}\right)}\right]^{-\frac{\kappa_\mathrm{A} w_\mathrm{A}}{2}}, \tag{4.1.1}$$

with the defining parameters set to $\kappa_{\mathrm{T_i}} = 4.0$, $\kappa_{\mathrm{T_e}} = 1.0$, $w_{\mathrm{T_i}} = w_{\mathrm{T_e}} = 0.04$, $\Delta_{\mathrm{T_i}} = \Delta_{\mathrm{T_e}} = 0.17$, $\kappa_\mathrm{n} = 1.0$, $w_\mathrm{n} = 0.04$ and $\Delta_\mathrm{n} = 0.17$. The reference position x_0 is chosen to be at half-radius $x_0/a = 0.5$. In order to test the influence of electromagnetic effects on ITG activity, we compare two scenarios. The first one employs $\beta = 0.01\%$ and can be considered an electrostatic limit. The second scenario uses $\beta = 0.5\%$, similar to what can be found in experiments of the first operational phase of W7-X [79]. The specific geometries in this chapter were generated using the MHD-equilibrium code GVEC [80] to match the background profiles and prescribed plasma pressures. The plasma is a hydrogen plasma with realistic electron mass, and the reference temperature is $T_\mathrm{ref} = 4.0\,\mathrm{keV}$. The reference values of $B_\mathrm{ref} = 2.28\,\mathrm{T}$ and $L_\mathrm{ref} = a = 0.52\,\mathrm{m}$ result in a finite-size parameter of $\rho^*_\mathrm{ref} = \rho_\mathrm{s}/a = 1/184$. The simulations consider a radial domain of $0.25 \leq x/a \leq 0.75$, with buffer zones covering 10% of each side. Moreover, the simulations make use of the five-fold symmetry of W7-X by analysing only one fifth of the toroidal domain.

4.2 Linear simulations

As a starting point, we performed linear simulations for both scenarios to compare their respective growth rates. However, compared to tokamaks, all toroidal modes are coupled even in linear scenarios in a stellarator. To understand this, consider the following simplified picture of the linear gyrokinetic equation

$$\frac{d}{dt} f(y,t) = \mathcal{L}(y,t) f(y,t), \tag{4.2.1}$$

where $\mathcal{L}$ is a linear integrodifferential operator representing the right hand side of the gyrokinetic equation such that it contains all linear terms and its dependence on the electromagnetic fields are expressed through another integrodifferential operator acting on the distribution function f whose specific form is not relevant to the argument. Taking the Fourier transform in space of this equation will result in

$$\mathcal{F}_{y\to k_y}\left\{\frac{d}{dt} f(y,t)\right\} \equiv \frac{d}{dt}\hat{f}(k_y,t) = \mathcal{F}_{y\to k_y}\left\{\mathcal{L}(y,t) f(y,t)\right\} = \int_{-\infty}^{\infty} \hat{\mathcal{L}}(k_y',t)\hat{f}(k_y - k_y',t)\, dk_y', \tag{4.2.2}$$

where $\hat{f}$ and $\hat{\mathcal{L}}$ are the Fourier transforms of f and $\mathcal{L}$ and k_y is the wavelength associated with the spatial coordinate y. From this, we see that even for a linear model, all modes are coupled to each other unless the linear operator does not depend on y itself, $\mathcal{L} = \mathcal{L}(t)$ so that $\hat{\mathcal{L}} \sim \delta(k_y')$. As such, the only thing that GENE-3D will produce is the fastest-growing linear mode that is resolved appropriately within a set of toroidal modes determined by the resolution being used. Such modes, however, often have a large wavenumber that usually gives only small contributions to the total nonlinear transport, as seen later in this section.

To somewhat overcome this issue, one can lower the resolution in the y-direction to a point where the strongest binormal mode is not resolved anymore while still properly resolving the magnetic field geometry so that the second strongest mode will dominate. An alternative is to use a numerical filter to single out the desired mode, as is done, for example, in the EUTERPE code. In this work, we chose the former approach, but it was shown in [81] that both methods agree with each other. Nevertheless, one should interpret such simulations with great care, as it is unclear for both approaches how much the coupling to the neglected modes will influence the results.

Three simulations were performed for each case, using a resolution of $(120 \times 128 \times 64 \times 24)$ points in $(x, z, v_{||}, \mu)$, with box lengths of size
$(L_\mathrm{x}, L_\mathrm{y}, L_{\mathrm{v}_{||}}, L_\mu) = (92.22\,\rho_\mathrm{s}, 100.64\,\rho_\mathrm{s}, 4.2\,v_{\mathrm{th},\sigma}(x_0), 17.7\,T_{0,\sigma}(x_0)/B_\mathrm{ref})$ and hyperdiffusion parameters $\eta_\mathrm{x} = \eta_\mathrm{y} = 0.05$, $\eta_\mathrm{z} = 2.0$ and $\eta_{\mathrm{v}_{||}} = 0.2$. The binormal resolution was set to $(48, 75, 240)$, respectively, to resolve different linear modes. This setup produces linear growth rates for both scenarios shown in figure 4.2. One can see a clear decrease induced by electromagnetic effects. The precise numerical values are listed in table 4.1, together with the ratio between the ion and electron heat fluxes, which will be used later for comparison with the nonlinear results.

$k_y\rho_s$	γ_{max} $[c_s/a]$	$Q_{es,e}/Q_{es,i}$
0.5	0.155	0.13
0.62	0.176	0.15
1.37	0.231	0.17

(a) Electrostatic case

$k_y\rho_s$	γ_{max} $[c_s/a]$	$Q_{es,e}/Q_{es,i}$
0.5	0.116	0.15
0.81	0.155	0.19
1.37	0.179	0.22

(b) Electromagnetic ($\beta = 0.5\%$) case

Table 4.1: Linear results of electrostatic and electromagnetic W7-X simulations.

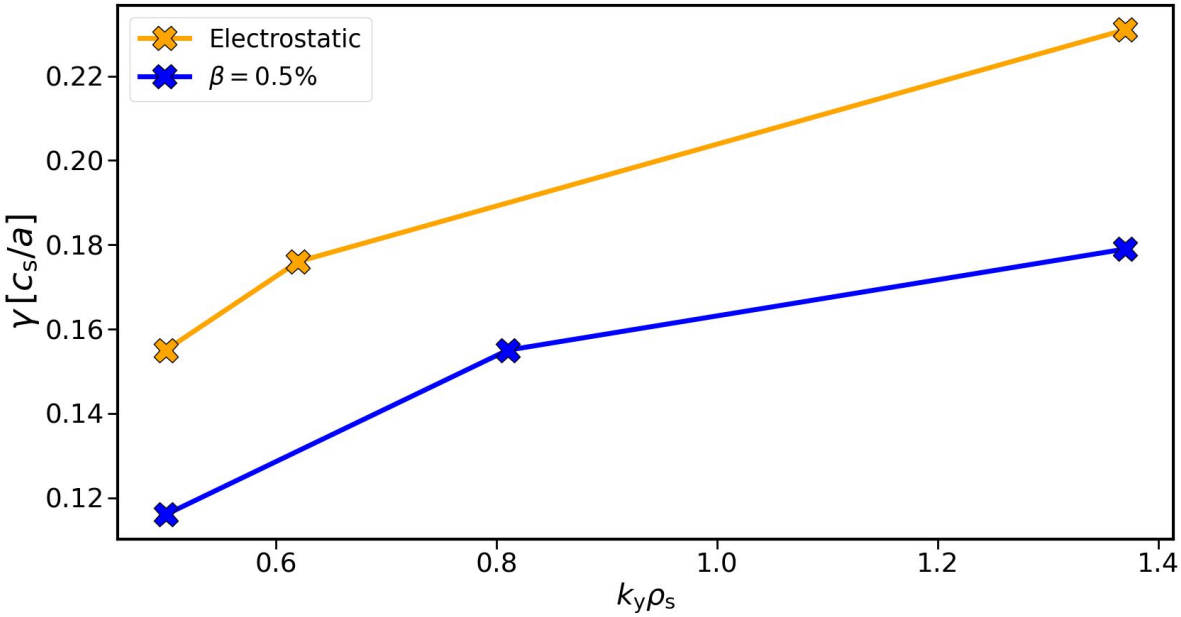

Figure 4.2: Linear growth rates as a function of the binormal wavenumber of both electrostatic and electromagnetic cases.

The growth rates are overall reduced by approximately 20-25%, with the strongest one going from 0.231 c_s/a to 0.179 c_s/a. Figure 4.3 compares the radial and poloidal mode structures of the fastest-growing modes in both scenarios for completeness. With only a tiny variation between the electrostatic and the electromagnetic cases, all fields peak radially close to $x/a = 0.6$. Furthermore, the parallel vector potential of the electromagnetic simulation covers the entire domain parallel to the magnetic field lines, whereas the electrostatic potential is highly localised at $z = 0$ in both cases.

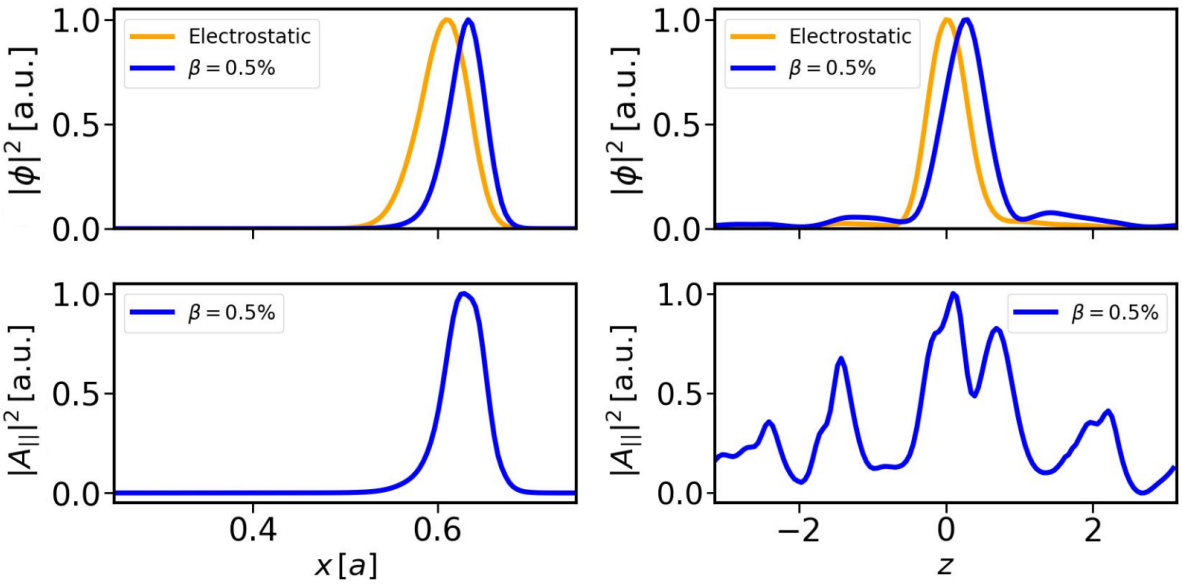

Figure 4.3: Normalised squares of the electrostatic and parallel vector potential of the fastest growing modes for the electrostatic and electromagnetic scenarios; top: radial (left) and poloidal (right) structures of the electrostatic potential, bottom: radial (left) and poloidal (right) structures of the parallel vector potential. The orange lines show the structures of the electrostatic simulation, whereas the blue lines correspond to those of the electromagnetic setup.

4.3 Nonlinear simulations

Having observed a stabilisation of linear ITG modes through electromagnetic effects, we now test whether this also holds true in nonlinear scenarios. For this, we reuse the setup of the linear cases, except fixing the binormal resolution to $n_y = 120$. Additionally, we employ heat and particle sources $\kappa_H = \kappa_P = 0.03$. Later in figure 4.5, we see that this keeps the background profiles nearly identical to the initial ones with only minor deviations.

The volume-averaged time traces of the heat fluxes from the electromagnetic and electrostatic simulations are shown in Figure 4.4. The electromagnetic case exhibits lower levels of turbulent heat fluxes than the electrostatic case at 200 time units or when saturation is reached. There, one can see a reduction of heat flux in all channels for the electromagnetic case compared with the electrostatic one.

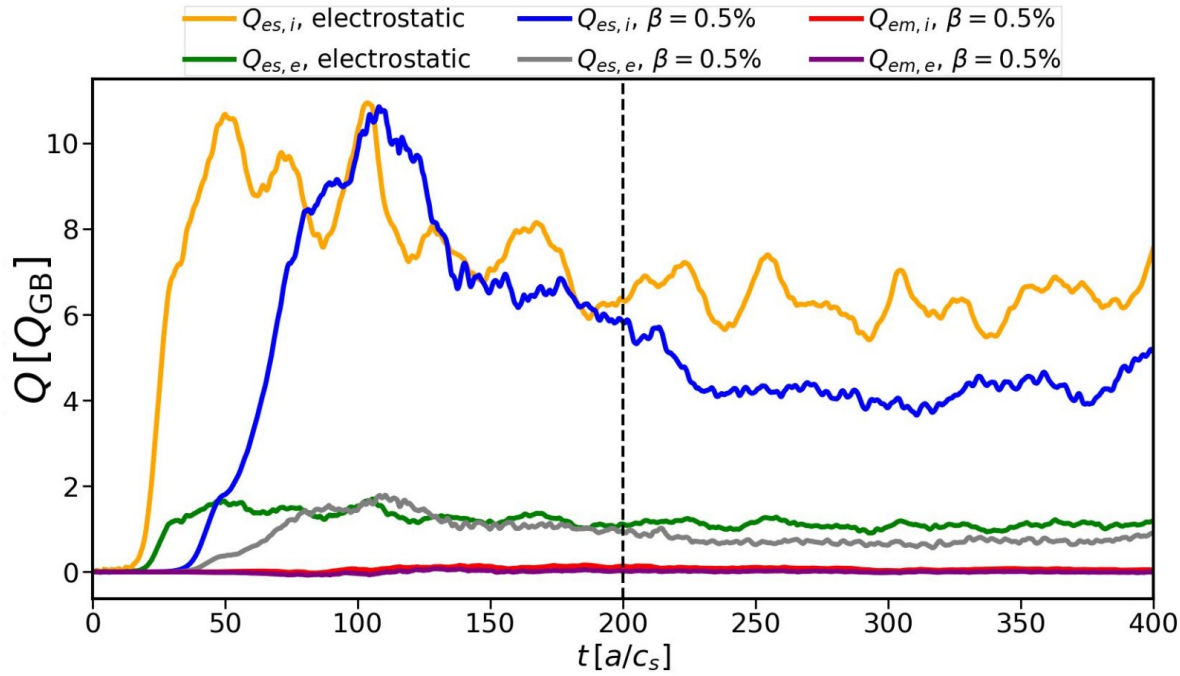

Figure 4.4: Time traces of the volume-averaged heat fluxes; dashed black line indicates the beginning of time interval used for averaging.

In order to make sure the stabilisation is caused by the electromagnetic effects and not by relaxation of the background profiles, the final profiles are shown in figure 4.5, showing only slight variations from the initial ones, so that it can also be concluded that the heat and particle sources have been chosen appropriately.

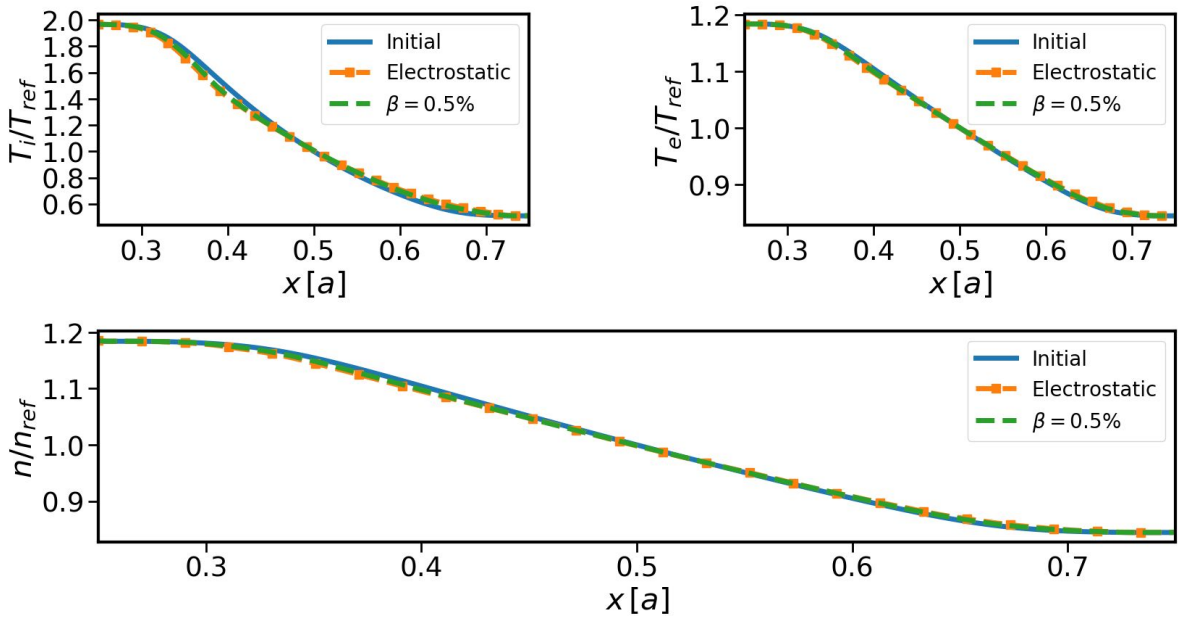

Figure 4.5: Time-average of the background density and temperature profiles.

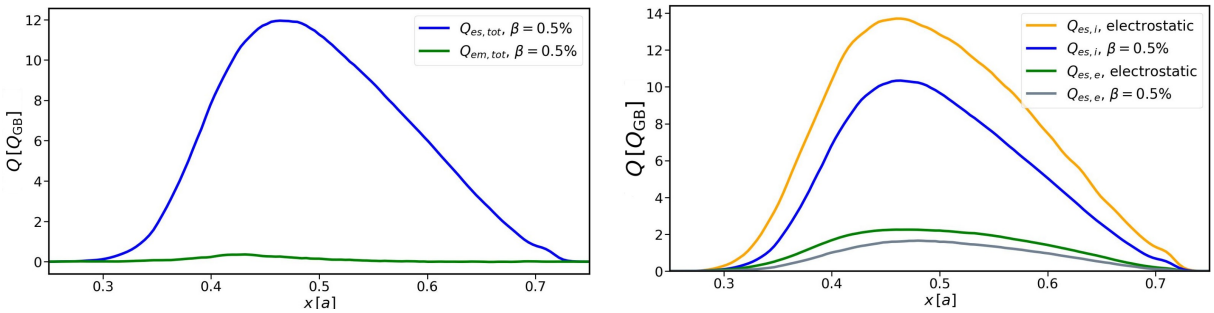

Figure 4.6: Time-average of the radial heat flux profiles. Left: electrostatic and electromagnetic heat fluxes; right: electrostatic ion and electron heat fluxes.

Going into a more detailed analysis of the different transport levels, we can compare the radial profiles of the total electrostatic and electromagnetic heat fluxes in figure 4.6. The total transport of the electromagnetic case is still mainly of electrostatic nature, with a peak value of 11.99 Q_{GB}, in comparison with the maximum electromagnetic heat flux of 0.36 Q_{GB}. One can further compare the flux contributions from the different species in the right plot of figure 4.6, showing the radial profiles of the electrostatic heat fluxes of both scenarios. All flux profiles are peaking approximately at $x/a = 0.46$, close to where the normalised background gradients are largest (see figure 4.1). The fact that turbulence is mostly electrostatic and mainly driven by the ion channel indicates that the turbulence at hand is still mainly driven by ITG. Both ion and electron fluxes are reduced by approximately 25%, in line with the linear behaviour seen in table 4.1. In particular, the peak ion heat flux decreases from 13.70 Q_{GB} to 10.34 Q_{GB} and the electron flux from 2.25 Q_{GB} to 1.65 Q_{GB}. The nonlinear results are also in line with the linear precursors in terms of the electron-to-ion flux ratio, which is approximately $Q_{es,e}/Q_{es,i} = 0.15$ for both, the electrostatic and electromagnetic scenario. However, prior linear runs deviate slightly for larger k_y in the electromagnetic simulation. This is not a problem, as most of the transport is produced by modes peaking around $k_y\rho_s \sim 0.3$, as can be seen in figure 4.7, with only minor contributions coming from $k_y\rho_s > 0.75$.

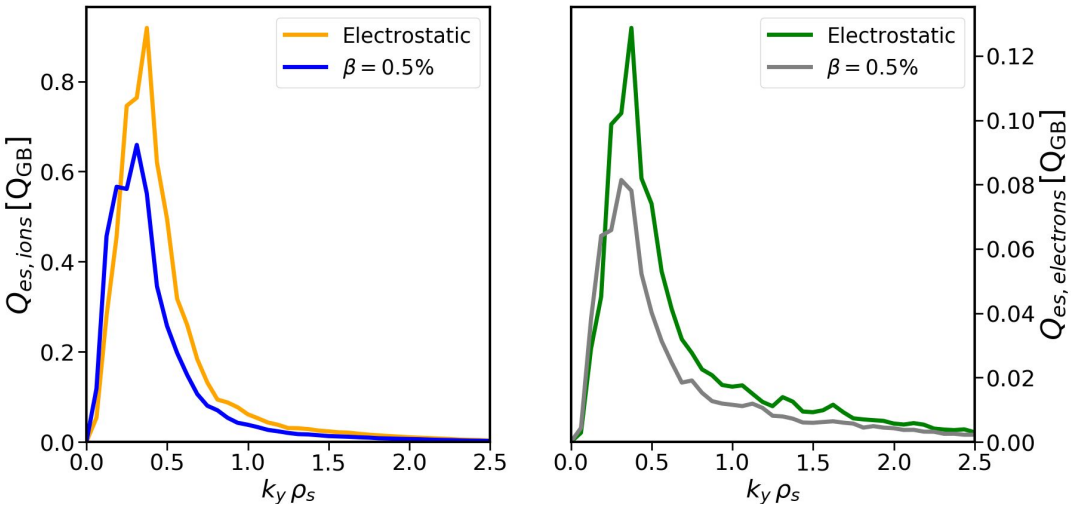

Figure 4.7: Wavenumber spectra of electrostatic ion and electron heat fluxes, evaluated at $x/a = 0.46$.

4.4 Chapter summary

This chapter presented the first global electromagnetic simulations in stellarator geometry using the GENE-3D code. The aim was to investigate the stabilising influence of finite plasma-β on ITG activity in a W7-X-like geometry. Both linear and nonlinear simulations have shown that even a moderate β of 0.5%, which is well within the parameter regime of the first operational phase of W7-X, leads to a reduction of approximately 25% of the linear growth rates and similar reduction of the nonlinear ion and electron heat fluxes. Such significant stabilisation and the eventual excitation of kinetic ballooning modes at higher β highlight the importance of electromagnetic effects for future investigations of reactor-relevant scenarios.

Chapter 5

Full-flux-surface effects on electrostatic turbulence in Wendelstein 7-X-like plasmas

Experimental discharges in the first operational campaign of W7-X have shown standard, ECRH-heated plasmas with gas-puff fuelling have a clamped ion core temperature at around 1.5 keV [82]. This issue was overcome transiently through the injection of hydrogen pellets as fuelling method, along with an increase in heating power. In contrast to tokamak scenarios, a significant reduction of turbulent transport was observed in W7-X for such modes of operation [83]. In [23], two mechanisms were provided as means to explain the improved performance: one of the main drivers of turbulent transport in W7-X has been identified to be ITG. Through the injection of pellets, there is a rise of the density gradient in the plasma core, bringing the temperature-to-density-gradient ratio $\eta_\mathrm{i} = L_\mathrm{n}/L_{\mathrm{T_i}}$ closer to 1, which is known to have a stabilising effect on this kind of turbulence [22] for tokamaks as well as stellarators. Unlike in tokamaks, however, it was hypothesised that for W7-X, the increase in density gradient does not lead to the excitation of trapped electron turbulence as trapped particles are considered to reside in regions of positive magnetic curvature [84, 85]. To show this, linear flux-tube simulations with a kinetic-electron model were performed, showing a transition from ITG instabilities in the pre-pellet phase to the so-called ion-driven trapped electron mode (iTEM) in the post-pellet phase, causing less transport, as indicated by subsequent nonlinear simulations. A second effect was mentioned based on simulations with the full-flux-surface version of the GENE code: it was suggested in [28] that ITG turbulence is highly localised around the outboard-midplane. Based on this, it was argued in [23] that the pellet injection causes an increase in the radial electric field produced by neoclassical transport, which in turn will dislocate the turbulent fluctuations into regions of weaker field curvature, therefore reducing the drive of ITG instabilities. A significant shift in the peak position was shown. However, the stabilising effect was considered secondary. While already giving some insight, both explanations fall short in some regard. Although it is a known effect in tokamaks already, the stabilisation of ITG through a finite density gradient was only shown for stellarator geometries using flux-tube simulations, considering only a single field line at a time. While being a reasonable approach in tokamaks due to axisymmetry, the fact that different modes can potentially reside in different positions on the magnetic surface is neglected, leaving open the question of whether turbulence is stabilised or just moved to

a different binormal position. Furthermore, the question about the impact of geometrical variations on nonlinear mechanisms, such as interaction with zonal flows, is left open. On the other hand, the full-flux-surface simulations performed in [23] only employed an adiabatic electron model. As such, the impact of a radial electric field on trapped-particle dynamics, which are known to influence ITG turbulence even in the absence of an explicit electron drive [22], as well as on ITG-TEM-hybrid scenarios is left unexplored.

In the following, we will combine both approaches to overcome these limitations by performing full-flux-surface simulations with a kinetic electron model and comparing the results to their flux-tube counterparts. Furthermore, we will investigate the influence of a constant radial electric field on various types of turbulence and address the aforementioned localisation of turbulence and the influence of magnetic field geometry. In part, this chapter follows [86].

The rest of this chapter is structured as follows: in section 5.1, we introduce the numerical setup of the simulations performed in this study. We show that the stabilisation of ITG-dominated turbulence through a finite density gradient, predicted by flux-tube simulations in [23], is reproduced in a nonlinear, full-flux-surface setup. We also investigate the spatial distribution of turbulent fluctuations, finding a significantly larger extension on the surface than what was reported, for example, in [28], which we show cannot be explained by the different treatment of the electrons. After that, we take a look at the configurational effects on ITG stabilisation through a density gradient in the context of the Low-Mirror configuration of W7-X in section 5.2. In there, we observe the same qualitative behaviour as for the cases shown in section 5.1. However, there is a significant fraction of trapped particles in regions of negative magnetic curvature. We attribute this to the fact that the driving background gradients are not large enough to highlight the configurational differences between the two geometries with respect to density gradient-driven ITG stabilisation. In section 5.3, we give an overview of the influence of a neoclassical electric field on the different types of turbulence under consideration. We show that its effect on the heat flux is small compared with the variation of the background gradients and that the dislocation of turbulent density fluctuations is small. Finally, we study the influence of a finite electron temperature gradient in section 5.4. When comparing flux-tube and full-flux-surface simulations for the parameters under consideration, we find substantial disagreement between the two models, which cannot be remedied by increasing the number of flux-tubes used to compare against the higher-fidelity model.

5.1 Density-gradient-induced ITG stabilisation in local and full-flux-surface simulations

We begin this study by investigating the influence of full-flux-surface effects on the stabilsation of ITG turbulence in W7-X through a finite density gradient. In order to avoid systematic differences, we use GENE-3D for both flux-tube and full-flux-surface simulations. We consider the standard configuration (EIM) [78] of Wendelstein 7-X at the radial position $x/a = 0.65$. We furthermore assume a collisionless and electrostatic ($\beta_\mathrm{e} = 10^{-4}$) limit, as the stabilisation of ITG is also discussed frequently in this simplified setting. Furthermore we use a reference temperature $T_\mathrm{ref} = 3.41\,\mathrm{keV}$ and $T_\mathrm{e} = T_\mathrm{i}$, which will result in a finite-size parameter $\rho_\mathrm{s}^* = 1/200$, which is somewhat larger than the values obtained from profiles of typical W7-X discharges at this position [79]. However, [28] showed that for a similar setup, good agreement between flux-tube and full-flux-surface simulations of ITG turbulence was attained for

even larger values of ρ_{s}^{*}. This influence will be addressed more for an experimental setting in chapter 6. While the full-flux-surface simulations will cover one-fifth of the entire surface, exploiting the five-fold symmetry of W7-X - the flux-tube simulations will only consider the bean-shaped ($\alpha = 0$) flux-tube unless stated explicitly otherwise. The phase space domain chosen for all simulations in this and the following sections is $(L_{\mathrm{x}}, L_{\mathrm{y}}, L_{\mathrm{v}_{||}}, L_{\mu}) = (225\,\rho_{\mathrm{s}}, 145.157\,\rho_{\mathrm{s}}, 2\pi, 3.0\,v_{\mathrm{th},\sigma}(x_0), 9.0\,T_{\sigma}/B_{\mathrm{ref}})$ with a resolution of $\left(n_{\mathrm{x}}, n_{\mathrm{y}}, n_{\mathrm{z}}, n_{\mathrm{v}_{||}}, n_{\mu}\right) = (225, 198, 128, 32, 9)$. Since Dirichlet boundary conditions were employed in the radial direction, numerical heat and particle sources with an amplitude of $\kappa_{\mathrm{H}} = \kappa_{\mathrm{P}} = 0.02$ were added to the equations in order to retain the background density and temperature profiles [58].

We take into account three scenarios to examine the turbulence stabilisation connected to a finite density gradient: in the first scenario, all background gradients are set to zero except for the ion temperature gradient of $a/L_{\mathrm{T_i}} = 2.5$. Doing this will make the turbulence entirely ITG-driven and serve as a reference case. As a comparison at the other end of the spectrum, the second scenario is a solely density-gradient driven TEM with $a/L_{\mathrm{n}} = 2.5$ and $a/L_{\mathrm{T_i}} = 0$. While the first two situations give a free-energy source for only ITG and ∇n-driven TEM turbulence, respectively, we also explore a third example with a mixed drive that lies in between the other two. The background gradients are chosen to be $a/L_{\mathrm{T_i}} = a/L_{\mathrm{n}} = 2.5$, which according to [24, 87] is considered to be a favourable parameter set for turbulence suppression since $\eta_{\mathrm{i}} = L_{\mathrm{n}}/L_{\mathrm{T_i}} = 1$. We set the electron temperature gradient to zero for all three situations for the time being and save the analysis of its effects for section 5.4. Table 5.1 summarises the gradients and the corresponding labelling of the cases for convenience.

Case label	$a/L_{\mathrm{T_i}}$	a/L_{n}	η_{i}
ITG	2.5	0.0	∞
TEM	0.0	2.5	0.0
Mixed	2.5	2.5	1.0

Table 5.1: Choice of normalised gradients for the different turbulence scenarios used in this chapter. Unless stated otherwise, the electron temperature gradient is assumed to be zero.

The heat flux levels of these setups can be compared with each other in figure 5.1. We reproduce the density gradient-driven turbulence reduction in flux-tube simulations suggested by linear theory [24, 84] and confirmed for nonlinear flux-tube simulations in [88]. In particular, we find that the ITG scenario has by far the largest ion and total transport. Compared with that, the turbulence of density-driven TEM seems much more benign, which is understood to be caused by the trapped electrons primarily residing in regions of positive average curvature [84]. Additionally, the Mixed case has the lowest transport of all flux-tube simulations, regardless of the total transport or that of each channel. This is consistent with the linear results shown in [23] and [24]. In contrast to the previous publications, however, we can additionally show in figure 5.1 that this stabilisation is also present in surface-global simulations. In particular, the full-flux-surface simulation results follow the same trends as those of their flux-tube counterparts, with the ITG case having the highest amount of transport, followed by the TEM case and the Mixed case having the lowest transport overall.

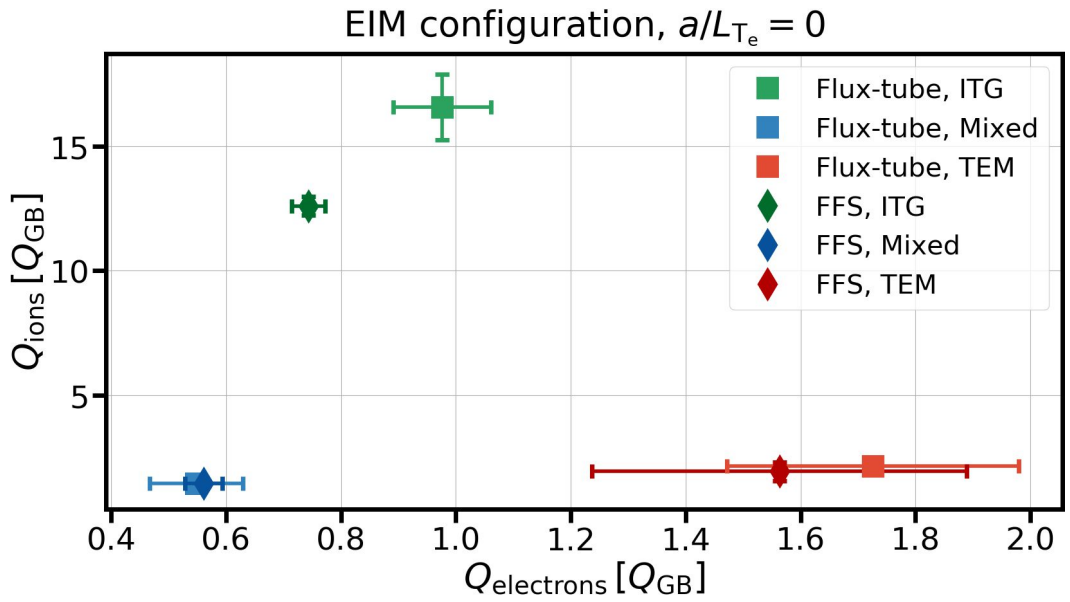

Figure 5.1: Averaged ion and electron heat fluxes of all three turbulence scenarios for flux-tube and full-flux-surface simulations.

Since surface simulations in GENE-3D are much more expensive than flux-tube simulations in GENE due to the absence of a Fourier representation of the binormal direction, it is natural to ask how well the latter model can approximate the results of the former. To this end, the averaged ion and electron heat fluxes obtained by the full-flux-surface simulations are displayed as a function of the field-line label α in figure 5.2 for all three cases. On top, the corresponding flux-tube results are marked by crosses.

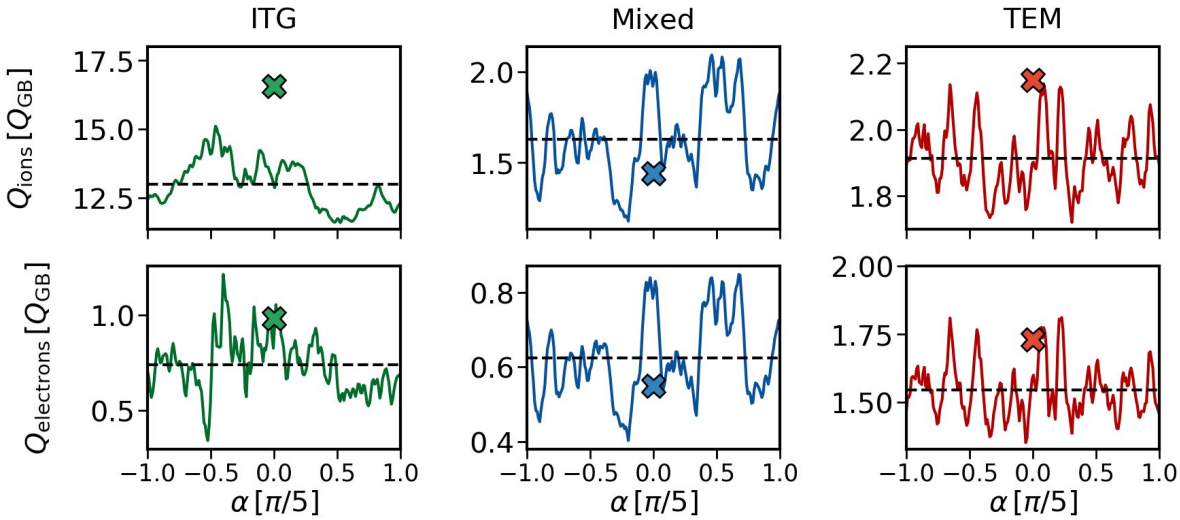

Figure 5.2: Variation of the ion and electron heat fluxes for the three turbulence scenarios as a function of the field-line label. The dashed black lines indicate the mean value, whereas the crosses represent the heat flux obtained by the corresponding flux-tube simulation.

With a variance that is always below 20% from the corresponding mean value, the heat

flux is relatively homogeneous for all scenarios under study. Nevertheless, it can be seen in figure 5.2 that the flux-tube results are within the range of attained flux-surface values of heat fluxes for the Mixed and TEM cases. Together with the previously mentioned relatively uniform distribution over the different field-line labels, it is reasonable to assume that flux-tube simulations can provide a good proxy for these two scenarios. However, we can see that for the ITG case, the local and flux-surface results differ by up to 30%, indicating that combining multiple independent local simulations could yield different results than the full-flux-surface approach. This contrasts what was shown in [28], where a similar setup with an adiabatic electron model produced a good agreement between flux-tube and surface simulations. To test the influence of the electron model, we repeated the simulation of the ITG case with adiabatic electrons. A comparison of the ion heat flux structure can be found in figure 5.3.

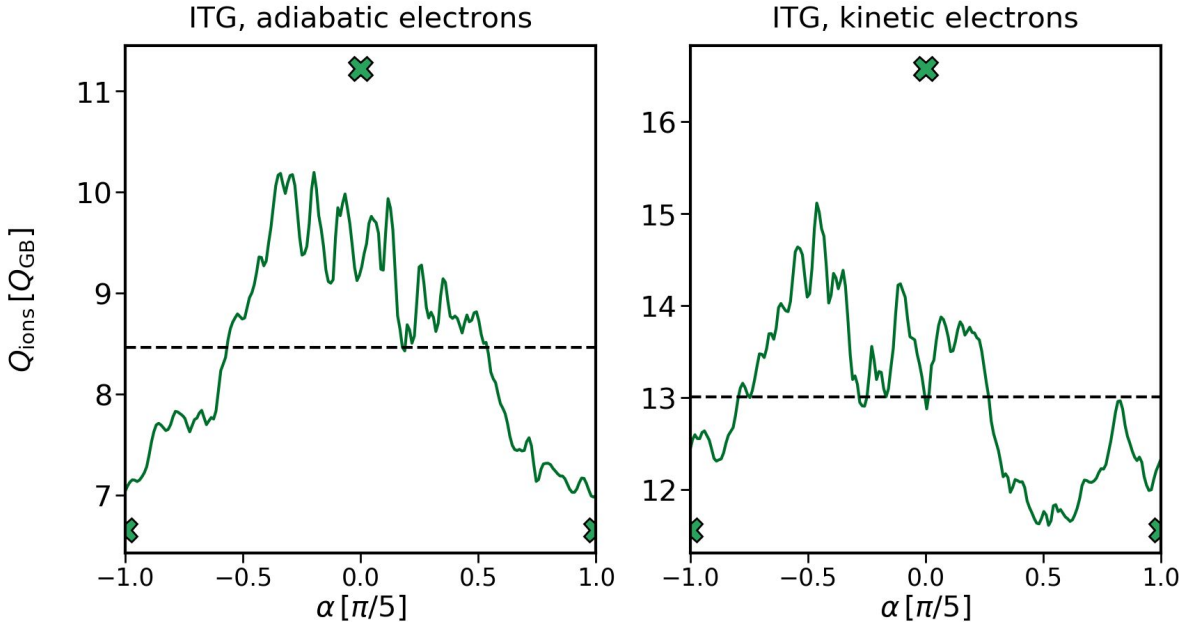

Figure 5.3: Variation of the ion heat flux for the ITG turbulence scenarios as a function of the field-line label. The dashed black lines indicate the mean value, whereas the crosses represent the heat flux obtained by the corresponding flux-tube simulation. The left plot shows the results obtained with an adiabatic electron model, whereas the results on the right are obtained with kinetic electrons.

One can see there that the flux-tube and full-flux-surface results agree much better when using adiabatic electrons than their kinetic counterpart, especially due to the clear maximum towards the $\alpha = 0$-field line for the former heat flux. Due to this, the differences between flux-tube and full-flux-surface simulations reduce to approximately 10% for the adiabatic electron model, in contrast to the 30% mentioned previously. In contrast, the surface simulation with kinetic electrons produces a rather uniform flux distribution. This could indicate that using an adiabatic electron model overstates the localisation of turbulence, which remains to be further investigated in the future. Figure 5.3 also shows that for both electron models, flux-tube simulations produce significantly more transport towards the $\alpha = 0$-tube, which in combination with the adiabatic electron model's peaked structure could be one reason for the

good agreement between flux-tube and full-flux-surface simulations that was shown in [28].

Beyond the one-dimensional structure of the heat fluxes, one can also study the structure of density fluctuations. Such investigations are of great interest, as previous studies like [23, 28, 87, 89, 90] have indicated that turbulent fluctuations peak only in a slim region around the outboard-midplane in Wendelstein 7-X and also other stellarators. A localisation with a maximum-to-minimum fluctuation ratio between a factor of 7-10 could cause difficulty for experimental measurement in that a slight misalignment of the detector with the peak position might significantly underestimate the fluctuation levels at play. However, all of the previously mentioned publications used an adiabatic electron model, which, as we have seen before, can give substantially different results than the more realistic kinetic electron model. Furthermore, global simulations performed by GENE-3D and EUTERPE with adiabatic electrons have also found the fluctuation amplitudes to vary by a factor of two rather than 7-10 in [91].

To shed more light on this discussion, we plot the density fluctuations of all three full-flux-surface scenarios given in table 5.1 as a function of the poloidal and toroidal PEST angles θ^* and ϕ [54], assuming a right-handed system, in figure 5.4.

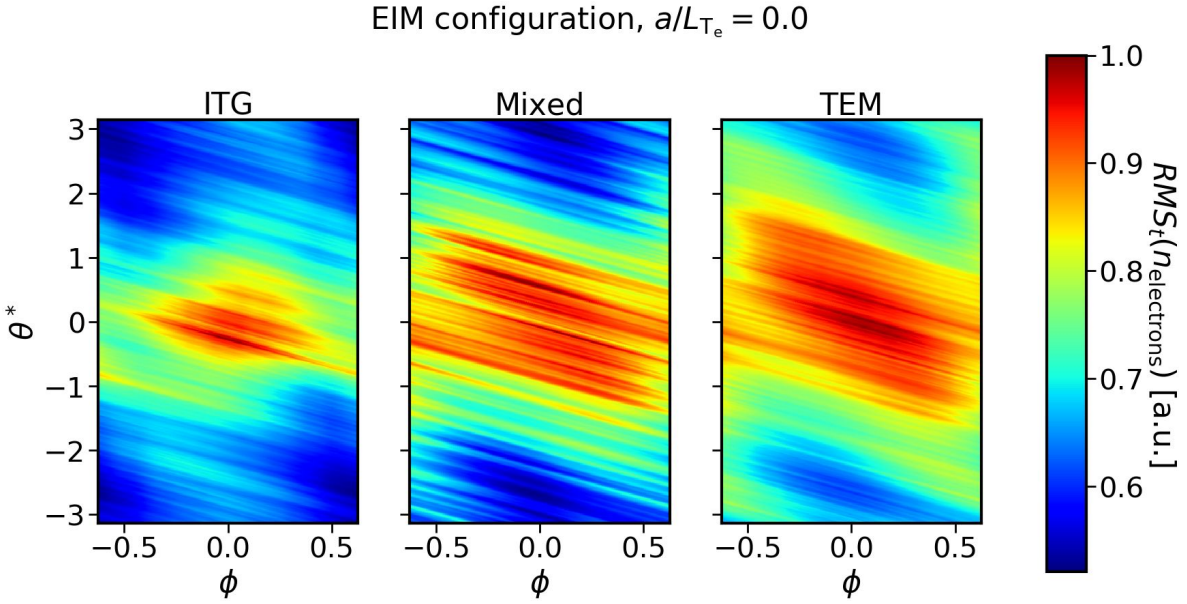

Figure 5.4: Root mean squared density fluctuations of the ITG, Mixed and TEM case, normalised to their respective maximum value, as a function of the poloidal and toroidal PEST angles.

As can be seen there, our results are in qualitative agreement with the simulations presented in [91] in so far as that the fluctuations seem to be fairly extended in both the poloidal and toroidal directions for all three cases, with the fluctuation level over the surface varying by at most around a factor of two. In order to test the influence of the treatment of the electrons further, we additionally compare the spatial distribution of density fluctuations between the adiabatic and kinetic electron simulation of the ITG scenario in figure 5.5. Although having a slightly larger ratio between maximum and minimum amplitude, the results obtained with adiabatic electrons are still far more extended than what was shown in [23, 28, 87, 89, 90], again being in line with [91]. What causes the difference in the spatial structures between

the previously mentioned models remains to be understood.

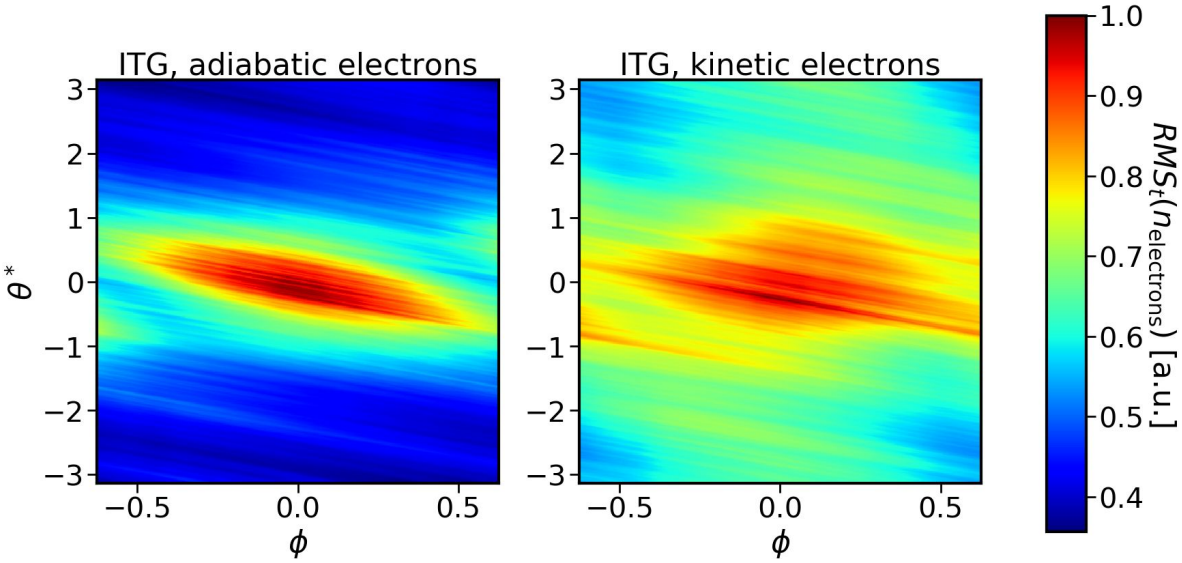

Figure 5.5: Root mean squared density fluctuations of the ITG case, simulated with adiabatic (left) and kinetic (right) electrons, normalised to their respective maximum value, as a function of the poloidal and toroidal PEST angles.

5.2 Comparison between standard and low-mirror configuration

Following the argument presented in the introduction that trapped electron mode turbulence is weak is caused by the electrons mainly residing in regions of positive magnetic curvature in W7-X, it has been hypothesised that one would observe a similar behaviour as in a tokamak in field configurations where the overlap is large. One such configuration is the low-mirror configuration (AIM), which has a local minimum of the magnetic field strength on the outboard midplane, where the field curvature is the most negative, as can be seen in figure 5.6. However, when simulating the scenarios introduced in the previous section in the mow-mirror configuration, we can see from figure 5.7 that ITG is also stabilised here, while TEM turbulence is kept benign.

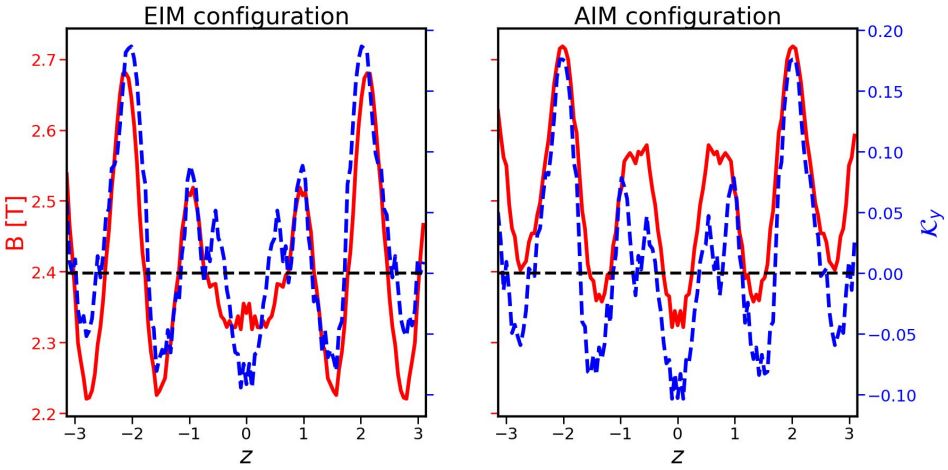

Figure 5.6: Comparison of the geometries of the standard (EIM) and low-mirror (AIM) configuration at $x/a = 0.65$, $\alpha = 0$. The magnetic field strength is marked in red, and the curvature-drive term $\mathcal{K}_y$ is marked in blue. The black line indicates $\mathcal{K}_y = 0$.

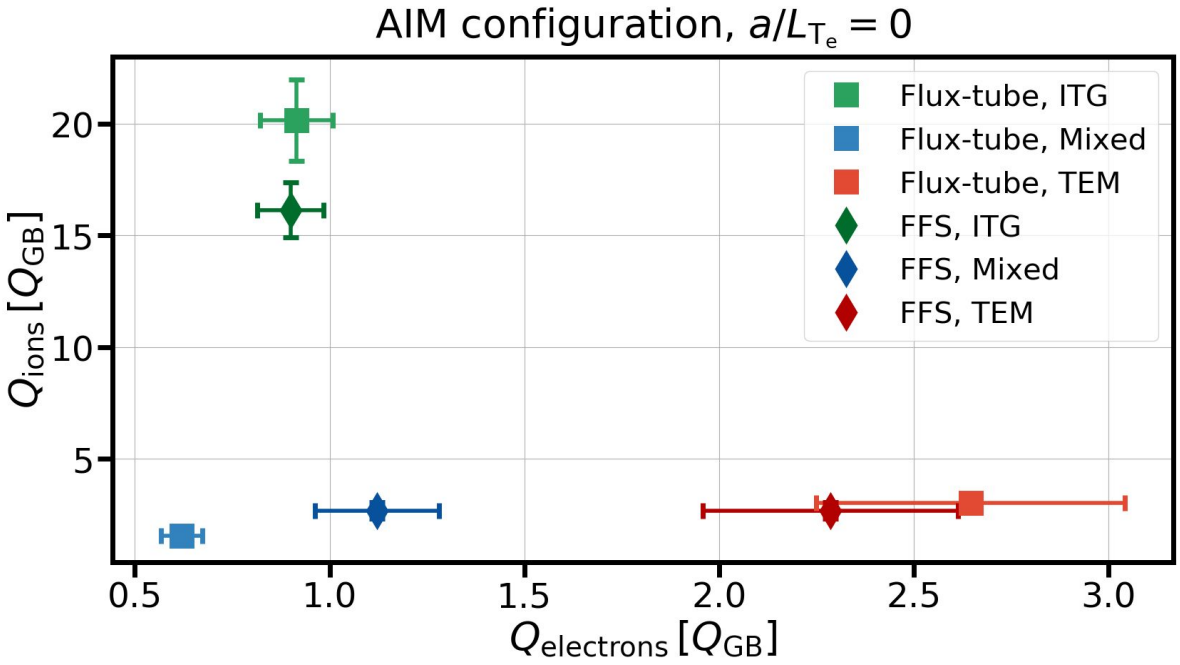

Figure 5.7: Averaged ion and electron heat fluxes of all three turbulence scenarios for flux-tube and full-flux-surface simulations in the low-mirror (AIM) configuration.

The overall transport of all cases seems to be larger than the heat fluxes obtained in the simulations of the standard configuration. The cause for this could be the previously mentioned more extensive overlap between regions of bad curvature and magnetic wells, which can act as a destabilising mechanism of trapped-particle dynamics, even if no TEM drive is available. However, one still observes a substantial decrease of both flux channels when adding a density gradient to the ITG scenario, as in figure 5.1. We argue that, for the gradients under consideration, all configurations of W7-X considered in [24] should benefit from

increasing the density gradient, bringing η_i closer to 1 [87]. As seen in [24], geometrical effects in stabilisation trends only become apparent at significantly larger gradients. To support this further, we mention that a reduction of ITG turbulence through a finite density gradient was even shown for the NCSX stellarator in [88], a machine whose quasi-axisymmetric nature results in largely unfavourable electron curvature drifts, therefore providing more drive of trapped-electron modes.

We can furthermore compare the structure of the electron density fluctuations on the surface again in figure 5.8, observing qualitative agreement with the structure shown in figure 5.4 for the standard configuration.

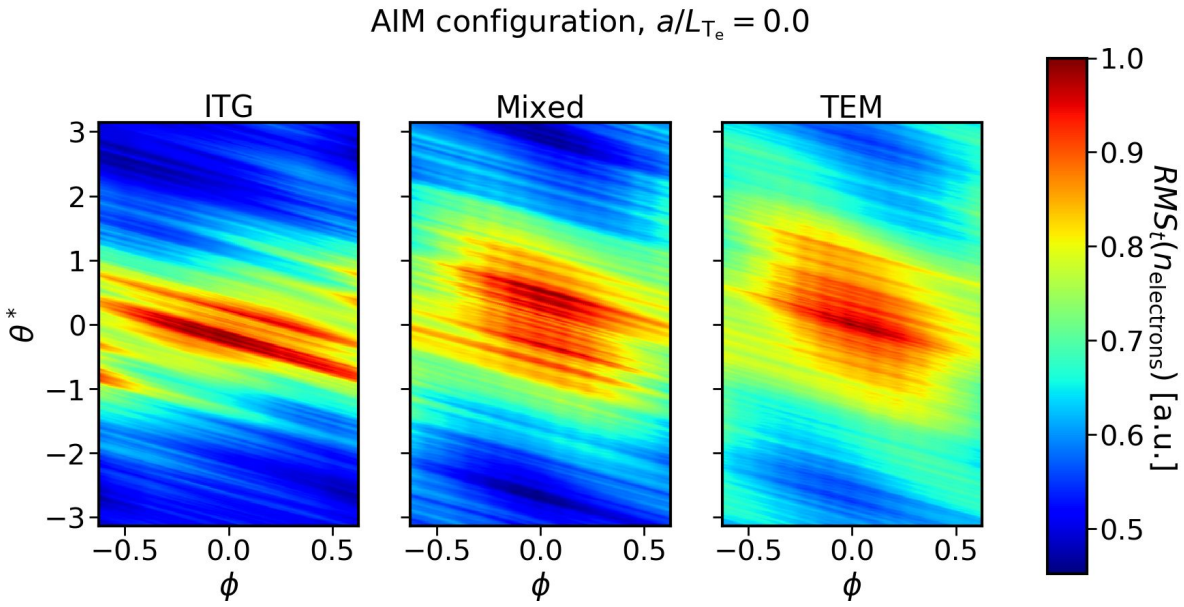

Figure 5.8: Root mean squared density fluctuations of the ITG, Mixed and TEM case in the low-mirror (AIM) configuration, normalised to their respective maximum value, as a function of the poloidal and toroidal PEST angles.

We see that the density fluctuations seem to be somewhat more pronounced for the ITG scenario in comparison with the one shown in figure 5.4, which can be expected since the overall transport is higher in the low-mirror configuration. Nevertheless, the density perturbation seems to vary only by slightly more than a factor of two over the entire surface, with all other qualitative trends being the same as in the standard configuration. Since the same trends were observed regarding the transport levels and the structure of turbulent fluctuations, we expect core plasmas in standard and low-mirror configurations for the scenarios under consideration to behave similarly overall. Therefore, we will only focus on the former configuration from now on.

5.3 Influence of a radial electric field

One distinctive feature that separates flux-tube from full-flux-surface simulations is the fact that the latter can be influenced by the presence of a constant background radial electric field $E_\mathrm{r}(x) = -\nabla\phi_0(x)$, usually originating from neoclassical physics. As the background

quantities do not depend on the binormal direction, it can be shown that the effect of the electric field can be eliminated through a Galilean transformation into a reference system that rotates with the corresponding ExB-velocity in this direction, therefore only causing a Doppler shift of mode frequencies. On the other hand, the binormal dependence of the operators in the gyrokinetic equation in flux-surface simulations breaks this invariance, not only causing a Doppler shift. The previous discussion did not consider taking into account a sheared electric field, which can potentially have a significant impact on flux-tube and flux-surface simulations and will be part of the investigation presented in chapter 6.

Nevertheless, simulations in [23] show an order-of-magnitude reduction of ITG transport and a substantial dislocation of the maximum amplitude of turbulent fluctuations on the flux-surface. These results are again in contrast to global simulations shown in [91], both using adiabatic electrons, in which the stabilising effect on ITG turbulence as well as the dislocation through the electric field was reported to be substantially smaller. In this section, we want to enter this discussion again using a kinetic electron model to assess the electric field's impact on different kinds of electrostatic turbulence. To this end, we repeat the three full-flux-surface scenarios of section 5.1. However, this time we add a normalised electric field with Mach number $M_{\mathrm{ExB}} = -\hat{v}_{\mathrm{E}_0} = \pm 0.015$, where $\hat{v}_{\mathrm{E}_0}$ is the normalised velocity associated with the background electric field, given in section 3.2. This Mach number corresponds approximately to a radial electric field of $\pm 19\,\mathrm{kV/m}$ for the reference temperature $T_{\mathrm{ref}} = 3.41\,\mathrm{keV}$ used in the simulation. A comparison between the heat fluxes with and without the electric field is given in figure 5.9. We can see that the effect on turbulence is relatively small, especially compared with the variation of the gradients. While there is a stabilisation of approximately 16% for the ITG scenario, all three flux-surface simulations of the TEM and Mixed case scenarios agree within error bars, respectively. Therefore, we see that, besides the overall small influence of the electric field on the flux levels, there is no noticeable impact of the sign of the electric field.

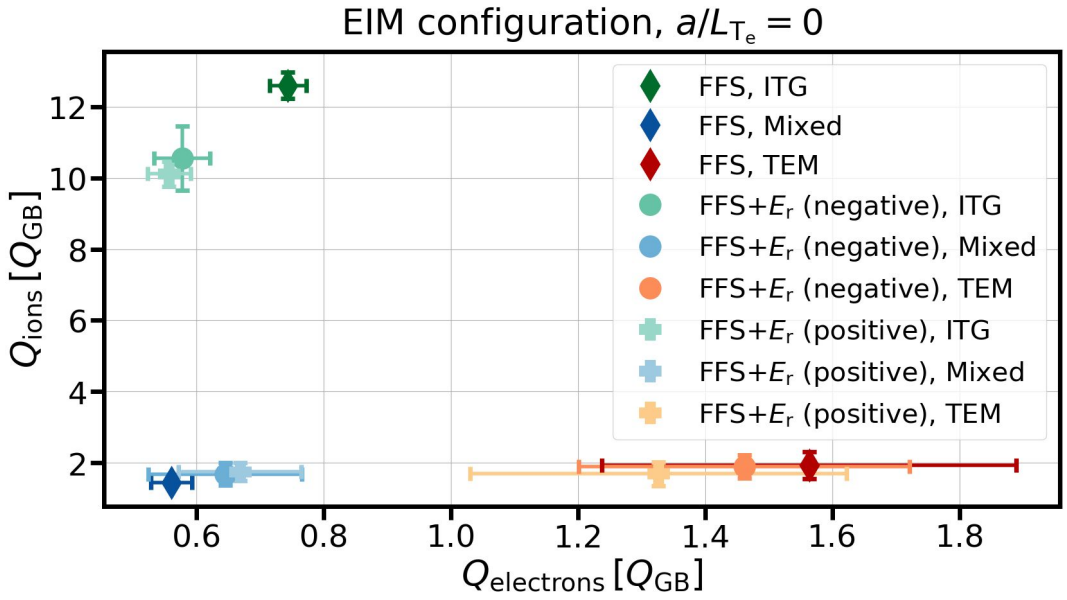

Figure 5.9: Averaged ion and electron heat fluxes of all three turbulence scenarios for full-flux-surface simulations with and without radial electric field.

The weak transport stabilisation is accompanied by a slight shift of the turbulent density fluctuations, as shown in figure 5.10.

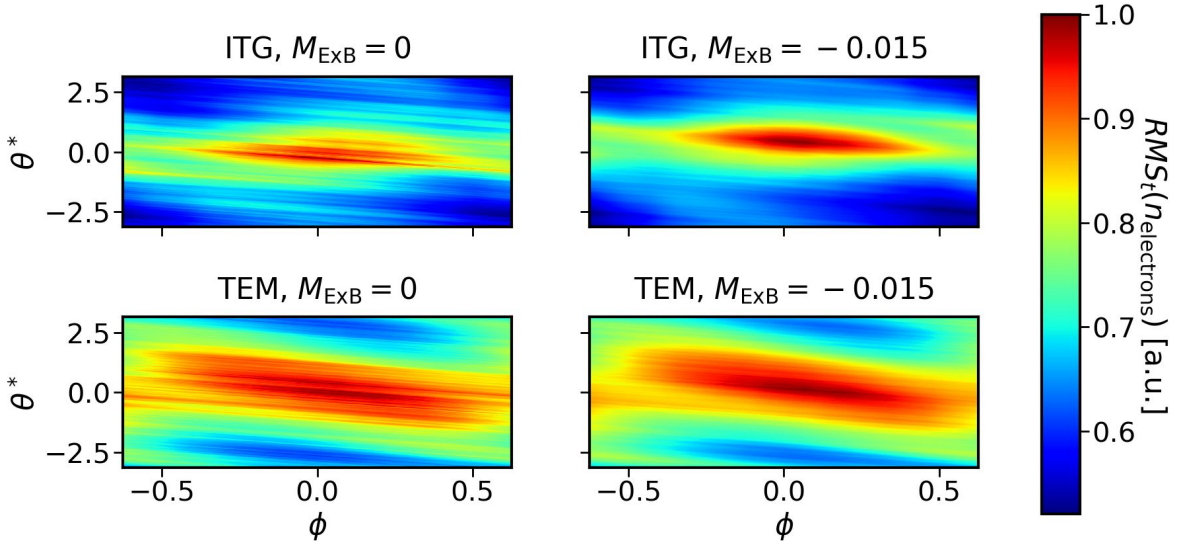

Figure 5.10: Root mean squared density fluctuations of the ITG and TEM case, with and without radial electric field, normalised to their respective maximum value, as a function of the poloidal and toroidal PEST angles.

The explanation given at the beginning of this section, along with the findings of section 5.1, make it clear why these results also are in agreement with what was shown in [91]: the radial electric field's dislocating effect cannot be felt unless turbulence is sufficiently localised. This is easily understood by imagining an extreme case in which all turbulence is uniformly distributed, and any kind of dislocation would go undetected. The turbulence is weakly localised in all three scenarios under discussion, as was already demonstrated in figure 5.4. Furthermore, as can be observed in figure 5.10, our examples had far less dislocation than the findings in [23]. To prove that the dislocation is not affected in a significant way by the choice of the electron model, we again repeat the ITG simulations with adiabatic electrons, observing also only a reduction in transport by around 8% from $8.42\,Q_{\mathrm{GB}}$ to $7.42\,Q_{\mathrm{GB}}$. Furthermore, one can see in figure 5.11 that the dislocation of density fluctuations is equally small as the ones shown in figure 5.10. Additionally, we propose that even in the situation of strong localisation, the electric field can only result in dislocations on equilibrium lengthscales if the corresponding velocities, specifically the ExB- and thermal velocities, are comparable with one another, which necessitates that $M_{\mathrm{ExB}} \sim 1$. During the study of the examples examined in section 5.4, we provide evidence to support this.

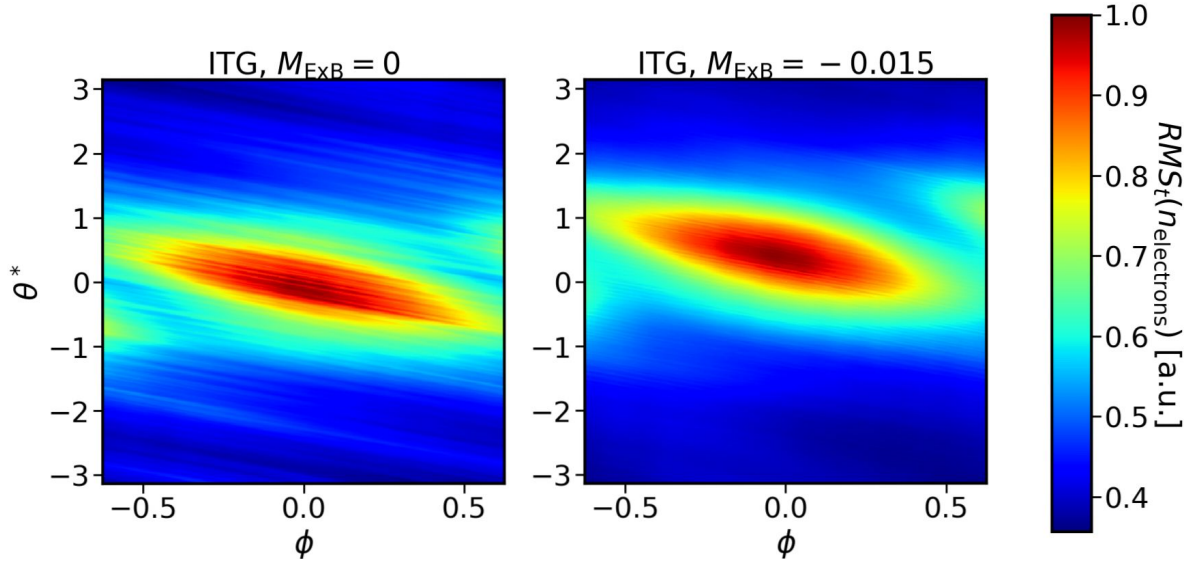

Figure 5.11: Root mean squared density fluctuations of the ITG case, run with adiabatic electrons, with and without radial electric field, normalised to their respective maximum value, as a function of the poloidal and toroidal PEST angles.

5.4 Effect of a finite electron temperature gradient

As a final step, we will look at the effect of a finite electron temperature gradient on different types of turbulence and the behaviour of flux-tube and flux-surface simulations. We, therefore, run the flux-tube and full-flux-surface simulations of section 5.1 again, but this time we add an electron temperature gradient of $a/L_{T_e} = 2.5$. The corresponding heat fluxes can be found in figure 5.12. The first thing one can notice is the substantial increase in ion and electron transport for the ITG cases, which we attribute to the excitation of hybrid ITG-TEM turbulence, where the trapped electron part is driven by the electron temperature gradient. This claim is based on the fact that both the flux-tube and surface simulations have a substantial amount of electron heat flux, which is atypical for pure ITG turbulence.

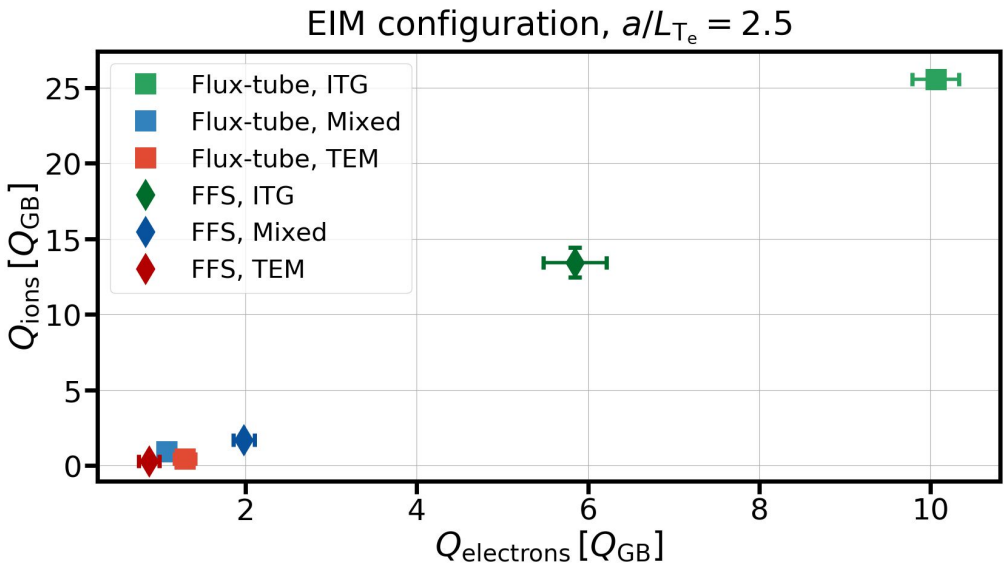

Figure 5.12: Averaged ion and electron heat fluxes of all three turbulence scenarios for flux-tube and full-flux-surface simulations, including a finite electron temperature gradient.

Furthermore, one can take a look at the heat flux structure along the magnetic field, for simplicity in the case of the flux-tube simulation only, and compare the ITG cases with and without electron temperature gradient with each other in figure 5.13. In there, we see that the structure of the ion heat flux is relatively unaffected by the electron temperature gradient, having a strong peak on the outboard-midplane and a sharp fall-off towards the inboard side. The electron heat flux, however, while having a very similar structure for the pure ITG case as its ion counterpart, starts to develop several local maxima along the magnetic field line, something that can also be observed in the electron heat flux structure of the density gradient driven TEM case in the rightmost plots of figure 5.13.

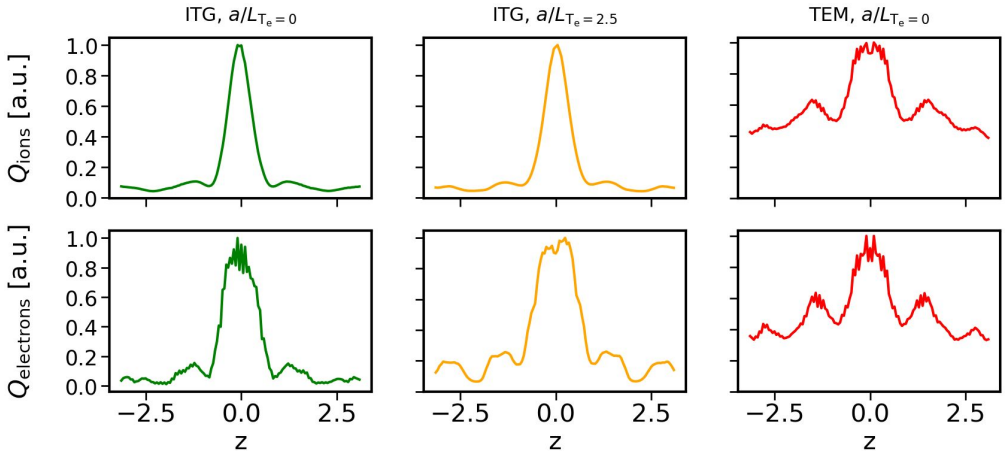

Figure 5.13: Ion (top) and electron (bottom) heat flux structures parallel to the magnetic field, obtained by flux-tube simulations, normalised to their respective maximum; shown, from left to right, are the pure ITG case, the ITG case with finite electron temperature gradient, and the TEM case.

We can now continue to compare the flux-tube to the flux-surface results for the cases under consideration. Compared with the scenarios considered in section 5.1, the flux-tube simulations produce heat fluxes that are almost twice as large as the ones obtained with the full-flux-surface model for the ITG case. Even further, one can see that the two models now do not only differ quantitatively but also qualitatively for the Mixed and TEM case: while the flux-tube simulations predict that the Mixed case produces similar levels of total transport compared with the TEM case, the full-flux-surface simulations predict that the former produces noticeably more transport than the latter, differing by roughly a factor of two. This can be seen in figure 5.14, where the same heat fluxes as in figure 5.12 are plotted without the ITG results for clarity.

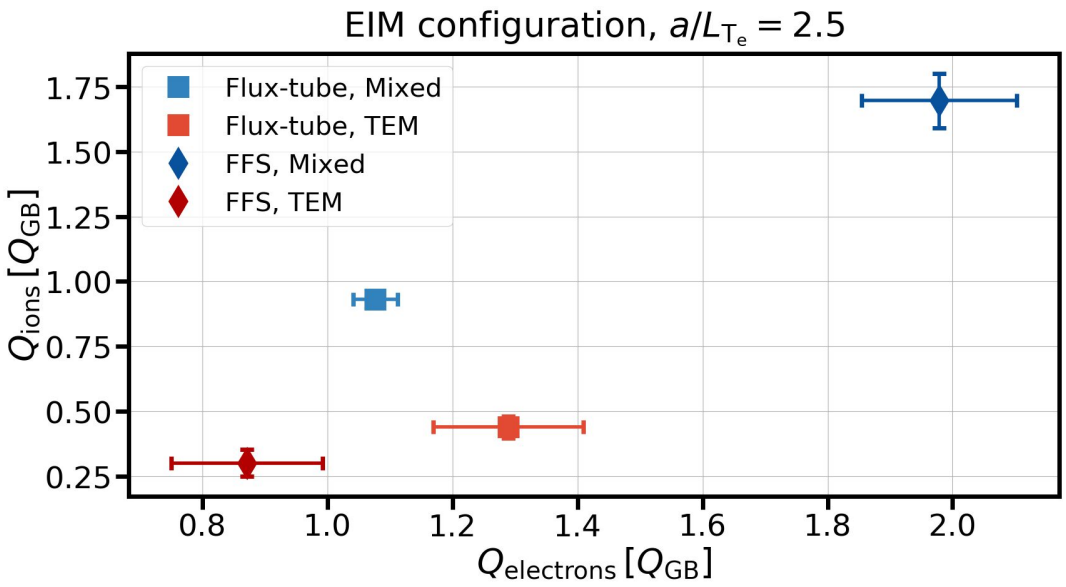

Figure 5.14: Averaged ion and electron heat fluxes of the TEM and Mixed case turbulence scenarios for flux-tube and full-flux-surface simulations, including a finite electron temperature gradient.

To explore these differences further, we show the heat flux variation along the field-line label for all three full-flux-surface simulations in figure 5.15. Like in figure 5.2, the corresponding transport levels obtained by flux-tube simulations are placed on top and marked by crosses. As the two different simulation domains produce the largest discrepancy for the ITG case, we perform additional local simulations at $\alpha = (0.25, 0.5, 0.75) * (2\pi/5)$, on top of the one at $\alpha = 0$. As shown in figure 5.15, even averaging the flux levels over multiple tubes still results in a difference of the two domains by a factor of approximately 1.5. Furthermore, we see that, while the full-flux-surface simulation produces a mostly homogeneous spreading of heat flux, the local simulations predict a strong peaking of the fluxes in the $\alpha = 0$-tube, with a rapid fall-off towards the other tubes. Therefore, it becomes apparent that the two different simulation domains do not only produce significantly different transport levels but also a different spatial profile of turbulence.

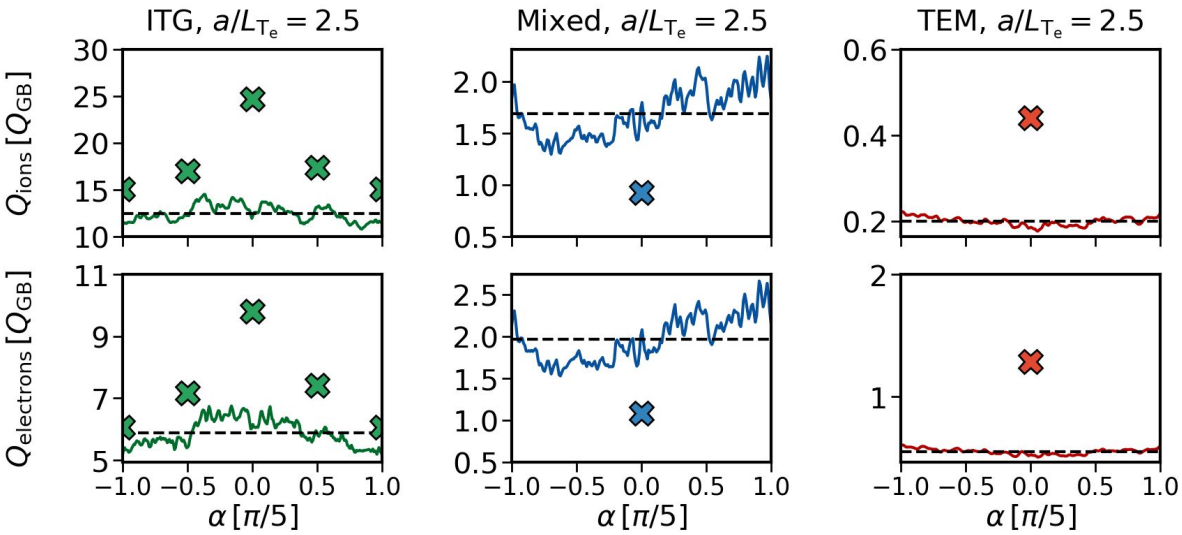

Figure 5.15: Variation of the ion and electron heat fluxes for the three turbulence scenarios as a function of the field-line label. The dashed black lines indicate the mean value, whereas the crosses represent the heat flux obtained by the corresponding flux-tube simulation.

Similar behaviour can be seen in the same picture for the Mixed and TEM examples, where local simulations, in turn, either underestimate or overestimate the heat fluxes. Additionally, as can be shown, the full-flux-surface simulation for both situations seems to predict a slightly increased transport towards the $\alpha = \pi/5$-flux-tube as opposed to the ITG scenario, which has a little increased transport around $\alpha = 0$. This suggests that one should compare many flux tubes while conducting turbulence investigations because there is no assurance that the transport would always peak in the same binormal position.

As a next step, we look again at the structure of the turbulent density fluctuations between the three cases in figure 5.16. Comparing these variations of density fluctuations with those in figure 5.4, it becomes apparent that the ITG and TEM scenarios behave similarly with or without an electron temperature gradient: both cases show a relatively weak localisation around the outboard midplane, with the ITG case being slightly more peaked than the TEM case. In contrast to the previous case, however, the Mixed scenario produces a strongly localised fluctuation pattern that peeks on the inboard side of the flux-surface. The reason for this unfamiliar pattern is not yet understood but has been confirmed in flux-tube benchmarks between GENE and GENE-3D in order to ensure the correctness of the results produced by GENE-3D, as can be seen in figure 5.17.

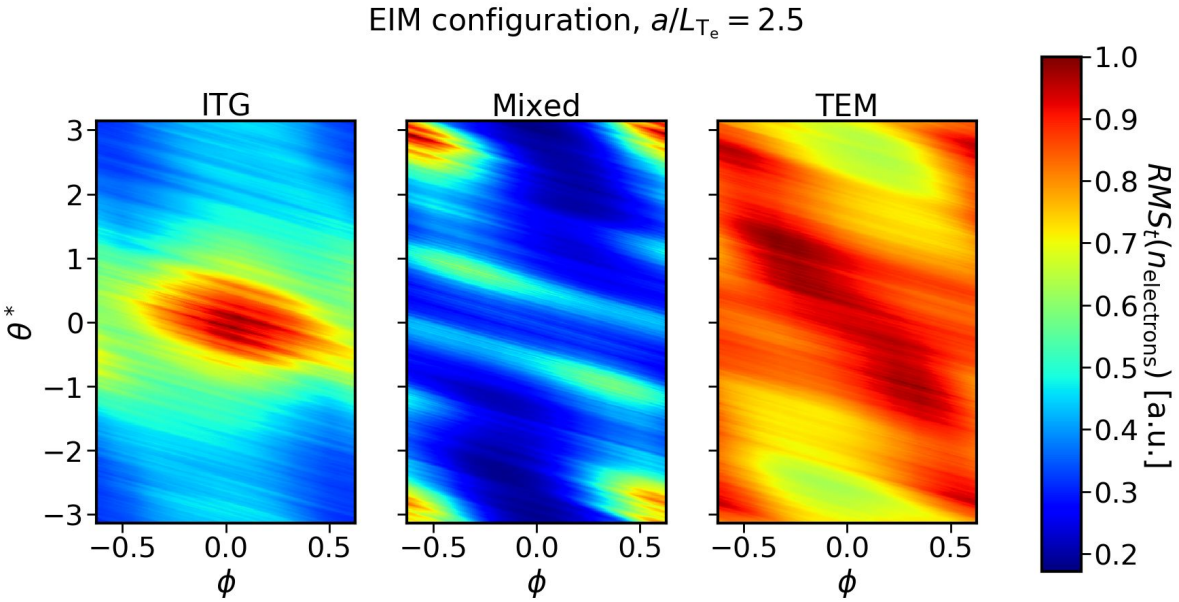

Figure 5.16: Root mean squared density fluctuations of the ITG, Mixed and TEM case with finite electron temperature gradient, normalised to their respective maximum value, as a function of the poloidal and toroidal PEST angles.

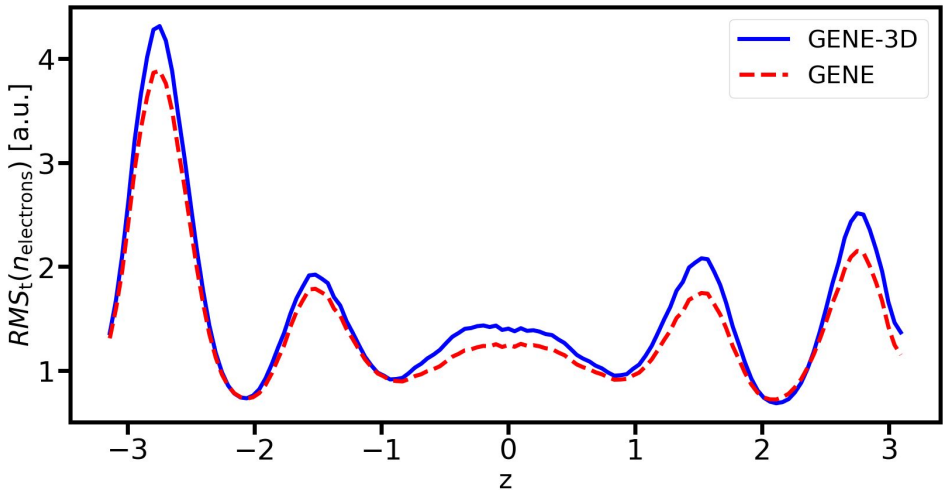

Figure 5.17: Root mean squared density fluctuations of the Mixed case with finite electron temperature gradient obtained by flux-tube simulations, as a function of the parallel coordinate. The density obtained by GENE-3D is marked in blue, and the one by GENE in red.

While a dedicated investigation of this behaviour is left for future work, such highly localised turbulence can indeed serve as a proper candidate to test the possibility of the electric field dislocating turbulence. Adding an electric field with $M_{\mathrm{ExB}} = -0.015$ to the Mixed case scenario, the ion heat flux reduces from $(1.70 \pm 0.10)\, Q_{\mathrm{GB}}$ to $(1.26 \pm 0.11)\, Q_{\mathrm{GB}}$ and the electron flux from $(1.98 \pm 0.12)\, Q_{\mathrm{GB}}$ to $(1.46 \pm 0.13)\, Q_{\mathrm{GB}}$. As shown for all cases considered in section 5.3, the density fluctuations are again only shifted very slightly, as

can be seen in figure 5.18, which overall implies that the radial electric field does not seem to significantly impact the spatial location of ion and electron fluctuations, even for highly localised cases, supporting the hypothesis about the flow strength made in section 5.3. It remains to be seen in the future how much the radial electric field will affect the behaviour of heavy impurities, as their higher mass makes them more susceptible to its influence.

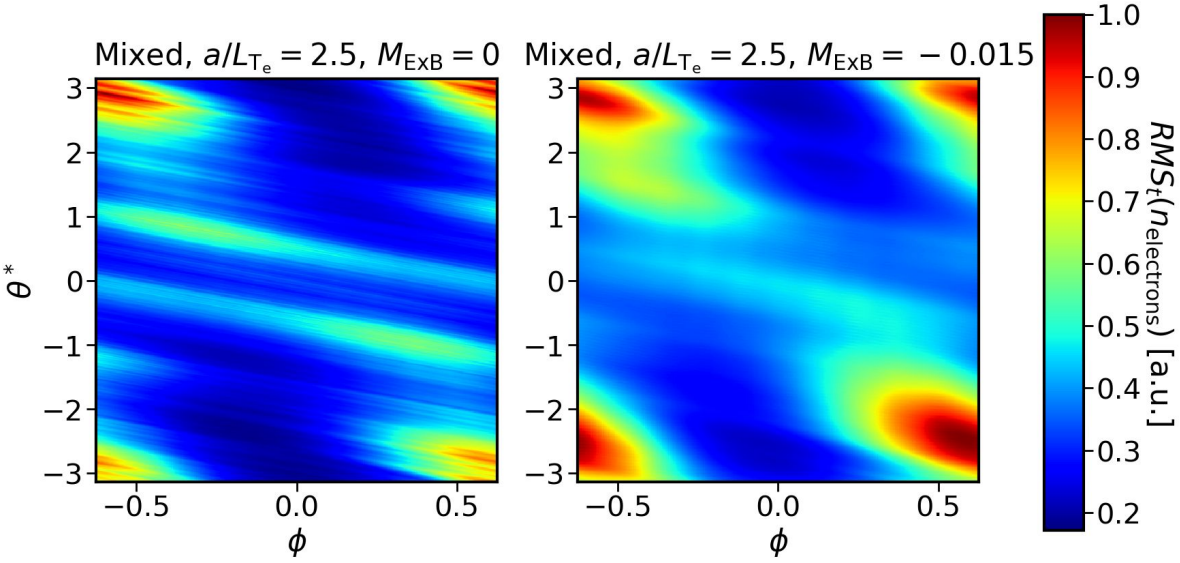

Figure 5.18: Root mean squared density fluctuations of the Mixed case with finite electron temperature gradient, with and without radial electric field, normalised to their respective maximum value, as a function of the poloidal and toroidal PEST angles.

5.5 Chapter summary

This section dealt with the investigation of full-flux-surface effects on ITG- and TEM-driven turbulence, as well as on the interaction between the two, in Wendelstein 7-X-like configurations. By performing the first-ever full-flux-surface simulations with kinetic electrons, we confirmed the stabilisation of ITG-dominated turbulence by a finite density gradient originally predicted by flux-tube simulations. We have further shown that turbulence is spread out fairly evenly on the surface for the cases under consideration, different from what has been proposed in previous full-flux-surface studies that used an adiabatic electron model. Beyond that, we have shown that while flux-tube simulations can be a sufficient approximation of transport levels for some cases, other cases under consideration showed significant disagreement compared with flux-surface simulations, especially in cases where transport is comparatively large. Especially in these cases, the predicted spreading of heat flux between different field lines was heavily favoured towards a more localised distribution in the case of the flux-tube simulations. In contrast, the higher-fidelity model produced a rather uniform variation. Finally, we showed that an external radial electric field without flow shear only affects turbulence weakly for the cases under consideration, both in terms of the strength of turbulent transport and in terms of the location of turbulent fluctuations, not even in cases where the latter are highly localised.

While the parameters under consideration can be considered representative of the main

types of electrostatic turbulence relevant to the first operational campaign of W7-X, the study can still be improved in the sense of extending it to fully experimental parameters, including multiple radial positions, experimentally consistent profiles, electromagnetic effects, and more. For this reason, we will extend our investigation of different simulation models to the analysis of an experimental ECRH-heated discharge of Wendelstein 7-X, as well as an analysis of the underlying turbulence characteristics, in the next chapter.

Chapter 6

Analysis of an ECRH discharge in Wendelstein 7-X

In the preceding two chapters, we have demonstrated on multiple occasions that the predicted turbulence levels can significantly differ based on the fidelity of the underlying model and the physical effects taken into account. However, all simulations conducted so far have employed artificial background profiles, raising the question of the relevance of these findings in real-world experimental scenarios. Similar concerns also apply to most existing literature on gyrokinetic stellarator simulations. For instance, studies like [92, 93] employ simulations of experimental parameters in flux-tube domains, whereas publications like [94] present radially global simulations using analytical background profiles in the collisionless and electrostatic limit.

In this chapter, we will bridge this gap by presenting a global simulation of experimental discharge parameters of Wendelstein 7-X, using a kinetic electron model while accounting for electromagnetic and collisional effects and considering a finite equilibrium radial electric field. The only effect missing is magnetic compression, which is expected to have a minor influence in the case considered due to the low overall plasma-β. To the author's knowledge, this simulation is the first of its kind. We will compare the outcomes with those obtained from flux-tube and full-flux-surface simulations to extend the comparative analysis presented in chapter 5 to parameters relevant to experimental setups. Additionally, we will explore the hypothesis regarding the weakness of trapped-electron modes in the core of Wendelstein 7-X plasmas [16, 26], using the radially local and global simulation results obtained before. Moreover, we will investigate the relative influence of ion- and electron-scale turbulence on the overall transport levels. Identifying the different types of turbulence is highly important, as they require different mitigation strategies [95, 96]. The findings in this chapter are currently being prepared for submission to a peer-reviewed journal.

The rest of the chapter is structured as follows. We begin by introducing the discharge considered in section 6.1, followed by expanding upon the studies introduced in chapter 5, extending them to realistic experimental scenarios in section 6.2. Subsequently, we investigate the characteristics of the ion-scale turbulence found in the discharge's core region in section 6.3. Through a comprehensive analysis involving the different simulation types and a comparison against power balance analysis, we present compelling evidence supporting trapped-electron activity manifested in ITG-TEM hybrid turbulence. This discovery contradicts earlier literature findings. In section 6.4, we explore the influence of ETG turbulence

on the overall transport and identify factors contributing to its varying strength at different radial positions. Finally, in section 6.5, we justify the significance of these results in the experimental context, even though they may not align perfectly with the power balance analysis.

6.1 Details of the discharge

In the rest of the chapter, we consider an experimental Electron-Cyclotron-Resonance-Heated (ECRH) discharge of Wendelstein 7-X. Specifically, our focus is on the W7-X programme 20181016.037, for which the corresponding time traces can be found in figure 6.1.

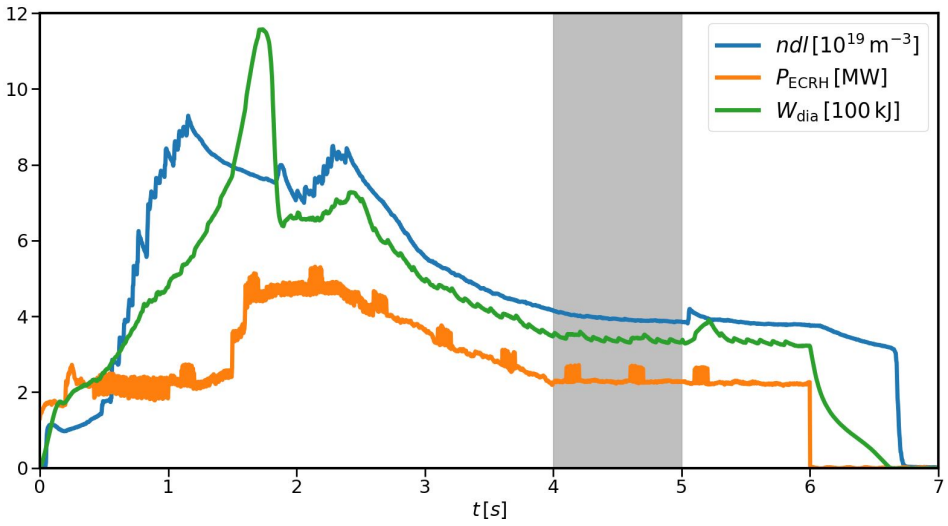

Figure 6.1: Time traces of the line-integrated density (blue), ECRH heating power (orange) and diamagnetic energy (green) of the W7-X programme 20181016.037. The area marked in grey at $t = 4 - 5\,\mathrm{s}$ corresponds to the shot phase considered in this investigation.

For our purposes, the discharge phase of $t = 4 - 5\,\mathrm{s}$ is particularly well-suited. It can be considered a representative scenario for gas-fuelled standard discharges within W7-X. The relevant background density and temperature profiles were obtained using the NTSS code [97], together with the neoclassical transport code DKES [98] computing the neoclassical fluxes as well as the equilibrium radial electric field. Figure 6.2 shows the background profiles and the electric field. One thing to note is that $T_\mathrm{i} \geq T_\mathrm{e}$ for some positions beyond $x/a \approx 0.5$. This contradicts the expectations for a plasma solely heated by ECRH, as the ions are only heated through equipartition with the electrons. However, this discrepancy, resulting from the specific configuration of NTSS used in this scenario, is of minor concern to us. To analyse turbulent dynamics beyond a comparison between the different simulation models, we largely focus on the region $x/a \leq 0.5$, as will become clear in subsequent discussions.

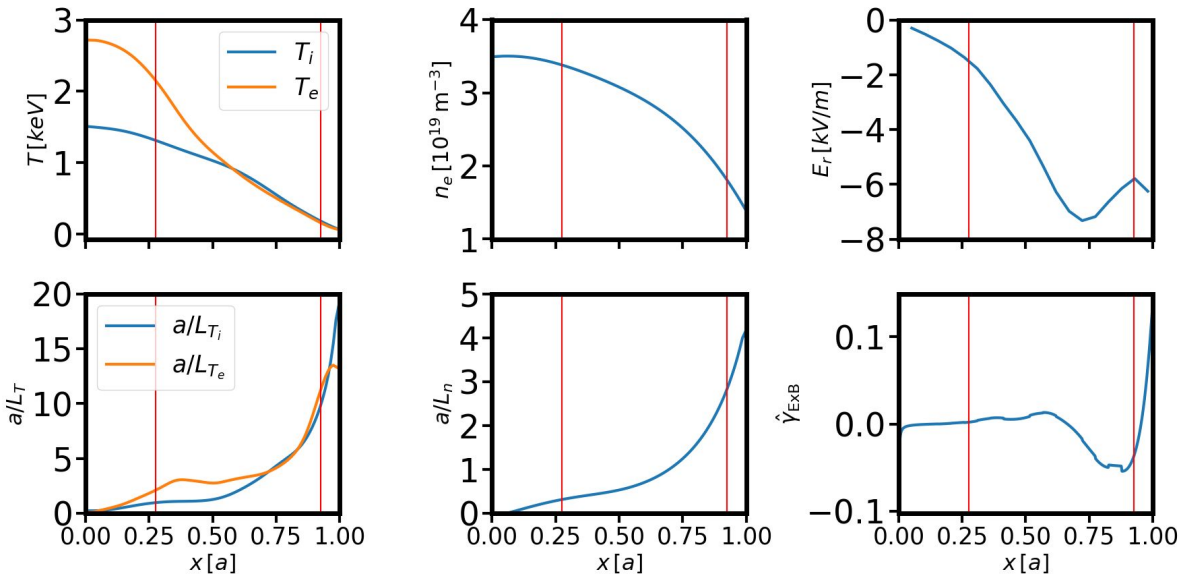

Figure 6.2: Density, temperature and radial electric field profiles corresponding to the grey area in figure 6.1. Top: profiles, bottom: corresponding (normalised) gradients. Bottom right: normalised flow shear rate, defined in equation 6.2.2 The red lines indicate the limits of the domain simulated with GENE-3D. The data was provided by Thomas Windisch (IPP Greifswald).

6.2 Comparison of computational domains

In this section, we begin our investigation of the discharge by comparing the predicted heat fluxes and turbulent fluctuation levels between flux-tube, full-flux-surface and radially global simulations. The latter serves as a benchmark, offering a reference point to assess the outcomes of the other two simulation models. Beyond the extension of the studies presented in chapter 5, the comparison enables the utilisation of the distinct diagnostic capabilities of each model, provided the overall transport predictions align reasonably well. For instance, while flux-surface and global simulations can provide the spatial patterns of turbulence across the entire surface, flux-tube simulations can isolate single toroidal modes in linear simulations, which will prove valuable in the subsequent sections.

The global simulation, performed with GENE-3D, considers a radial domain of $x/a \in [0.275, 0.925]$, which accounts for roughly 65% of the entire inner plasma volume. The grid employs resolutions of $(325, 256, 126, 64, 16)$ points in the $(x, y, z, v_{||}, \mu)$-directions, respectively. The corresponding box dimensions are $(L_\mathrm{x}, L_\mathrm{y}, L_{\mathrm{v}_{||}}, L_\mu) =$
$(259.437, \rho_\mathrm{s}, 265.472, \rho_\mathrm{s}, 3.45, v_{\mathrm{th},\sigma}(x_0), 11.9, T_{0,\sigma}(x_0)/B_\mathrm{ref})$. Using approximately 2.8 million core hours on the MPCDF cluster Raven, the simulated plasma is saturated based on the time traces of the volume-averaged heat fluxes illustrated in figure 6.3. To the author's knowledge, this simulation marks the first instance of a global gyrokinetic simulation conducted with experimental discharge parameters from W7-X, incorporating kinetic electrons and accounting for electromagnetic effects.

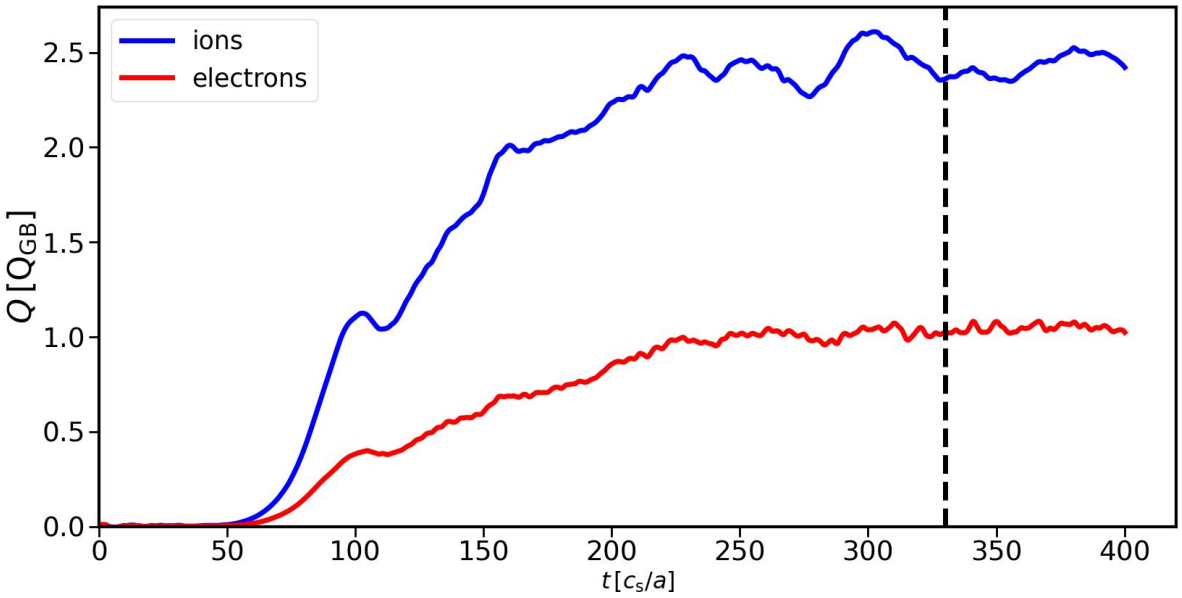

Figure 6.3: Time trace of the volume-averaged heat flux of the global simulation.

The resulting heat flux profiles are compared with the outcomes of radially local simulations, as depicted in figure 6.4. These local simulations are carried out at the radial positions $x/a = [0.4, 0.5, 0.6, 0.7, 0.8]$. The full-flux-surface simulations are performed using GENE-3D, covering one fifth of the respective surface. Using numerical boxes with $(L_{\mathrm{x}}, L_{\mathrm{v}_{||}}, L_\mu) = (225\,\rho_{\mathrm{s}}, 3\,v_{\mathrm{th},\sigma}(x_0),$
$9\,T_{0,\sigma}(x_0)/B_{\mathrm{ref}})$ and a resolution of $(n_{\mathrm{x}}, n_{\mathrm{y}}, n_{\mathrm{z}}, n_{\mathrm{v}_{||}}, n_\mu) = (225, 256, 128, 32, 9)$ was sufficient for most cases. However, the velocity grids had to be changed to $(L_{\mathrm{v}_{||}}, L_\mu, n_{\mathrm{v}_{||}}, n_\mu) = (6, 12, 64, 12)$ for the simulations at $x/a = 0.4$ and 0.5. Unless stated otherwise, a finite equilibrium flow corresponding to the local value of the nominal radial electric field is considered. The flux-tube simulations are conducted using GENE, as the two codes have been benchmarked extensively against each other. Nevertheless, GENE employs a much more efficient treatment of flux-tube domains due to the spectral representation in the radial and binormal directions. Four flux-tubes at $\alpha = [0, 0.25, 0.5, 0.75]2\pi/5$ are considered at each radial position. Here, a setup of $(k_{\mathrm{y,min}}, L_{\mathrm{v}_{||}}, L_\mu) = (0.05\,\rho_{\mathrm{s}}^{-1}, 3\,v_{\mathrm{th},\sigma}(x_0), 9\,T_{0,\sigma}(x_0)/B_{\mathrm{ref}})$ and $(n_{\mathrm{k_x}}, n_{\mathrm{k_y}}, n_{\mathrm{z}}, n_{\mathrm{v}_{||}}, n_\mu) = (128, 64, 128, 32, 9)$ was found to be sufficient. The radial box sizes are selected to be approximately $L_{\mathrm{x}} \approx 225\rho_{\mathrm{s}}$ and are adjusted according to the magnetic shear $\hat{s}$. In cases where the shear becomes too small, periodic boundary conditions in the z direction are assumed [99].

Figure 6.4 shows decent agreement of heat flux levels between the local and global simulations in the core while exhibiting significant disagreement between flux-tube and global results in the outer region, up to a factor of 2 at $x/a = 0.8$. In contrast, the alignment between full-flux-surface and global simulations is better, with a relative error of approximately 30%.

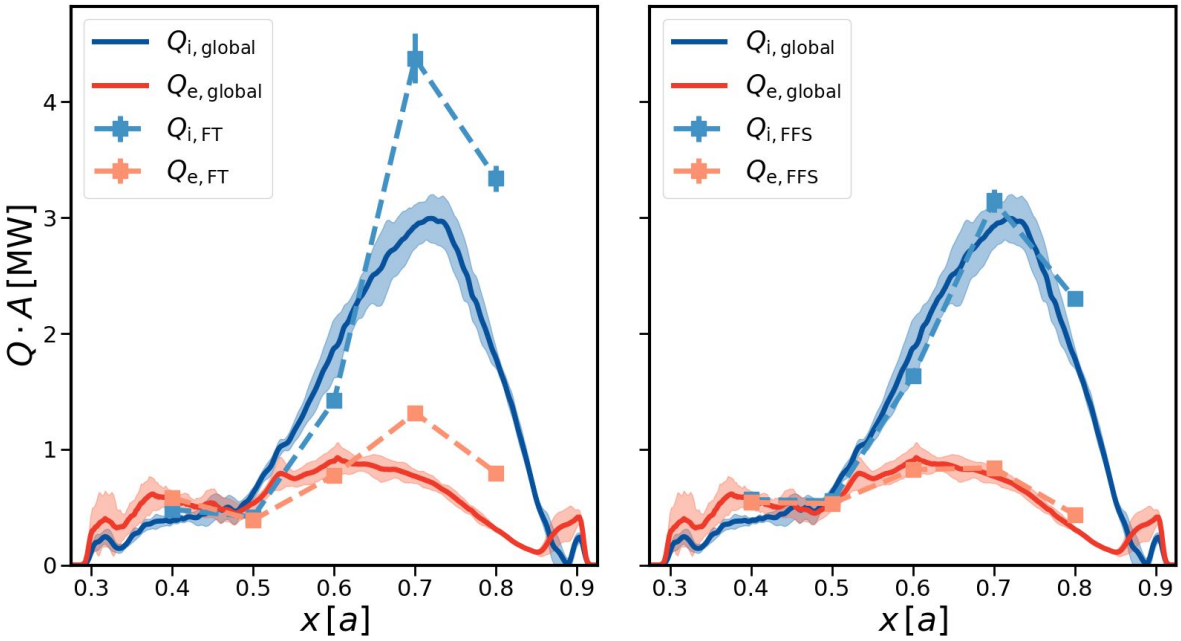

Figure 6.4: Comparison of the radial heat flux profile obtained from the global simulation with those obtained by flux-tube (left) and full-flux-surface (right) simulations. Shaded regions indicate standard deviation in time of the global simulation.

The discrepancies seen in figure 6.4 can partly be explained by the different treatment of the radial electric field within the three simulation models. As was discussed in section 5.3, a constant radial electric field can be eliminated in flux-tube simulations by an appropriate coordinate transformation, whereas full-flux-surface simulations are impacted by it. Moreover, global simulations account for the radial variation of the electric field, which naturally includes a shearing effect in the system. This shearing effect is known to have a stabilising impact on turbulence. However, it is possible to introduce this flow shear approximately in local simulations by linearising the flow velocity around the reference position according to

$$\hat{v}_{\mathrm{E}_0} = -\frac{\hat{E}_\mathrm{r}(x)}{\hat{\mathcal{C}}(x)} \approx -\left(\frac{\hat{E}_\mathrm{r}(x_0)}{\hat{\mathcal{C}}(x_0)} - \hat{\gamma}_{\mathrm{ExB}}(x_0)\,(\hat{x}-\hat{x}_0)\right), \tag{6.2.1}$$

where we have introduced the normalised ExB-flow shear rate

$$\hat{\gamma}_{\mathrm{ExB}}(x_0) \equiv -\frac{d}{d\hat{x}}\left(\frac{\hat{E}_\mathrm{r}(x)}{\hat{\mathcal{C}}(x)}\right)\Bigg|_{x=x_0} = -\left[\frac{d\hat{E}_\mathrm{r}}{d\hat{x}} - \frac{\hat{E}_\mathrm{r}}{\hat{x}}\,(1-\hat{s})\right]\Bigg|_{x=x_0}. \tag{6.2.2}$$

The Fourier representation of the radial direction employed by GENE necessitates using a sophisticated algorithm proposed in [100]. In contrast to this, it is straightforward to incorporate equation (6.2.1) into the gyrokinetic equation (3.2.7) of GENE-3D if Dirichlet boundary conditions are assumed in the radial direction.

When accounting for the sheared ExB-flow in the radially local simulations, we observe a noticeable impact in the outer radial region, as indicated in figure 6.5. Since the shear rate is comparatively low in the inner region, it is understandable that one does not see a significant change in the transport levels. However, one can see a substantial reduction around $x/a = 0.8$,

where the flow shear is strongest.

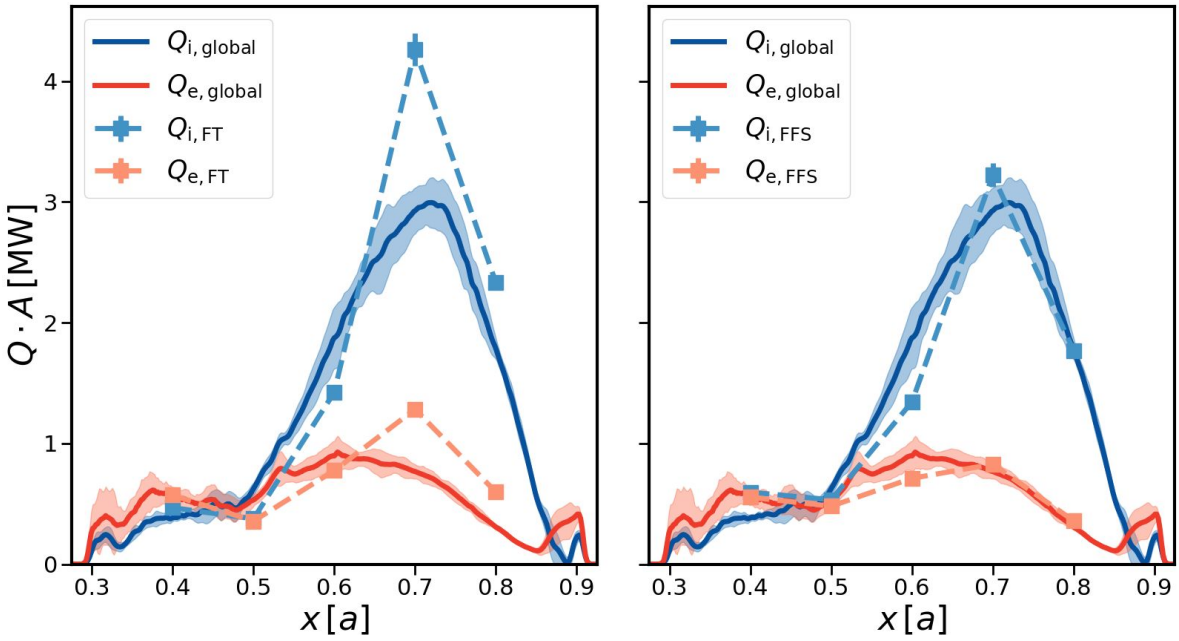

Figure 6.5: Same as figure 6.4 but linearised flow shear was added for the radially local simulations.

	$Q_{\text{ions}} \cdot A$ [MW]	$Q_{\text{electrons}} \cdot A$ [MW]
Flux-tube	3.34 ± 0.11	0.80 ± 0.02
Flux-tube (with $\hat{\gamma}_{\text{ExB}}$)	2.34 ± 0.04	0.60 ± 0.01
Flux-surface (no E_{r})	2.32 ± 0.06	0.44 ± 0.01
Flux-surface (with E_{r})	2.30 ± 0.05	0.44 ± 0.01
Flux-surface (with E_{r} & $\hat{\gamma}_{\text{ExB}}$)	1.77 ± 0.03	0.36 ± 0.01
Global	1.77 ± 0.08	0.30 ± 0.02

Table 6.1: Ion and electron heat fluxes at $x/a = 0.8$ as predicted by different models

By repeating the full-flux-surface simulation at $x/a = 0.8$ while neglecting the equilibrium ExB-flow, one can infer from table 6.1 that the local radial electric field has no significant impact on the transport levels at this position. Taking into account the flow shear, on the other hand, reduces the heat fluxes in both local models by approximately 20-25%, making the ion heat flux computed by the flux-surface simulation agree with the global results within error bars. This highlights that the shearing of equilibrium ExB-flows significantly impacts turbulence levels in stellarators and should, therefore, always be considered in gyrokinetic simulations. This is especially true in advanced scenarios, such as those with pellet fuelling, where one can see an even stronger radial variation of the electric field [23].

While the ion heat flux is only overpredicted by approximately 30% by the flux-tube simulations, the electron heat flux is still larger by a factor of 2 compared with the global results. Interestingly, however, one can see in figure 6.6 that the different flux-tubes are stabilised to a different extent by adding flow shear.

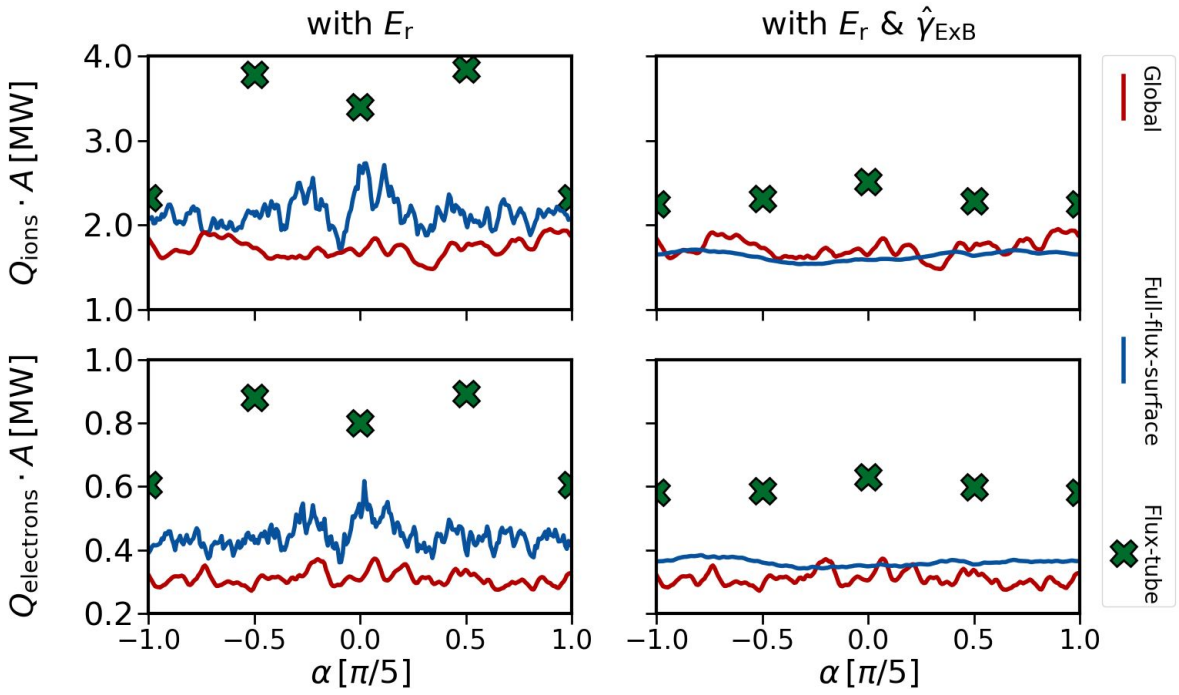

Figure 6.6: Variation of the ion and electron heat fluxes along the field-line label α centred around $x/a = 0.8$. Red and blue lines represent the fluxes obtained by global and full-flux-surface simulations, respectively, while green crosses mark the flux-tube results.

The ion heat flux reduces by approximately 40% within the $\alpha = \pi/10$-flux-tube, dropping from 3.85 MW to 2.28 MW. On the other hand, it only shows a slight decrease of about 3% at $\alpha = \pi/5$, from 2.32 MW to 2.24 MW. The electrons exhibit a slightly weaker stabilisation, with their heat flux decreasing from 0.89 MW to 0.60 MW at $\alpha = \pi/10$ and from 0.6 MW to 0.58 MW at $\alpha = \pi/5$, which translates to stabilisation of 32% and 3%, respectively. One can see that the overall variation of the different flux-tubes is greatly reduced by the addition of the shear to a level comparable with that of the flux-surface and global simulations. The mechanism driving this phenomenon will be subject to investigation in future research.

We complete the comparison of the different computational domains in experimental parameter regimes by considering the turbulent density fluctuations as a function of the field-line angles for different radial positions. According to the theory presented in [28] and [89], turbulent fluctuations are expected to become more localised as ρ^* decreases. However, as demonstrated in figure 6.7, even at $x/a = 0.8$, where $\rho^* \approx 1/580$, the density fluctuations exhibit a factor of variance of only up to 2.5, which aligns with our earlier considerations in chapter 5.

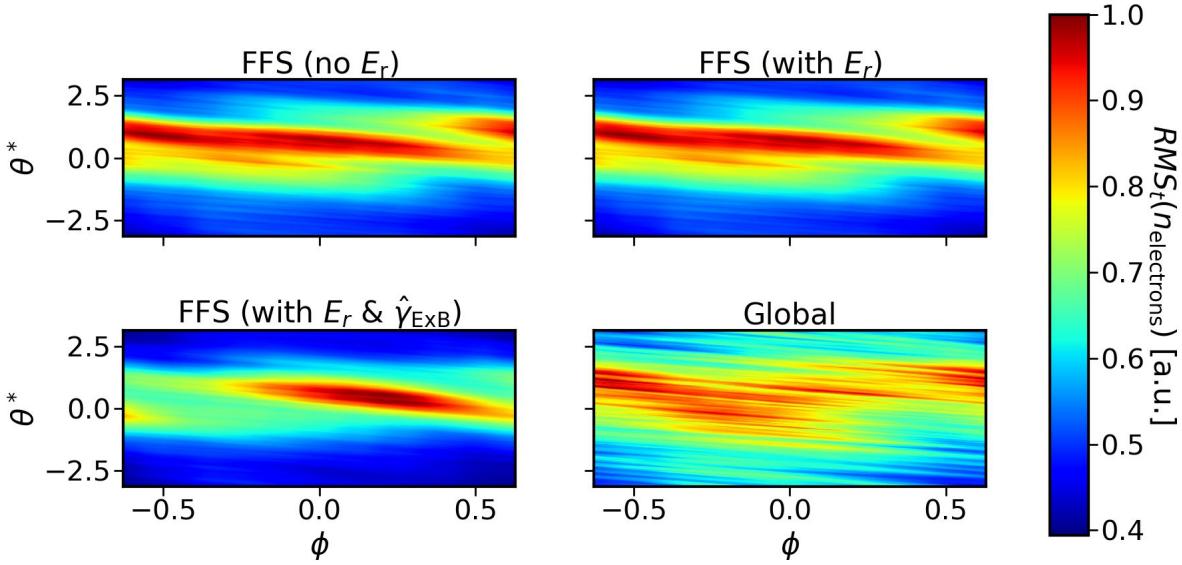

Figure 6.7: Root-mean-square of the electron density fluctuations at $x/a = 0.8$, normalised to the respective maximum value for full-flux-surface simulations with and without E_r, with finite ExB-flow shear as well as obtained by the global simulation. Fluctuations of the global simulations are averaged over $x/a \in [0.79, 0.81]$ to reduce statistical noise.

Furthermore, it is noteworthy that retaining the constant radial electric field does not significantly alter the spatial structure of the density fluctuations computed by the full-flux-surface simulations, in accordance with the results and subsequent explanation presented in sections 5.3 and 5.4. Interestingly, including finite $\hat{\gamma}_{\mathrm{ExB}}$ noticeably decreases the extent of the fluctuations along the toroidal direction. This behaviour is, however, inconsistent with the global results, also shown in figure 6.7, which has a relatively homogeneous structure in the toroidal direction. This effect is to be studied in the future.

6.3 Analysis of ion-scale turbulence in the core

After evaluating the predictive capacities of various simulation models for the current ECRH discharge, we focus on examining the system's inherent turbulence characteristics. To this end, we compare the global heat flux profiles predicted by GENE-3D against the anomalous heat fluxes obtained with NTSS in figure 6.8. The latter is given by the difference between total and neoclassical heat fluxes, where the latter are calculated with DKES.

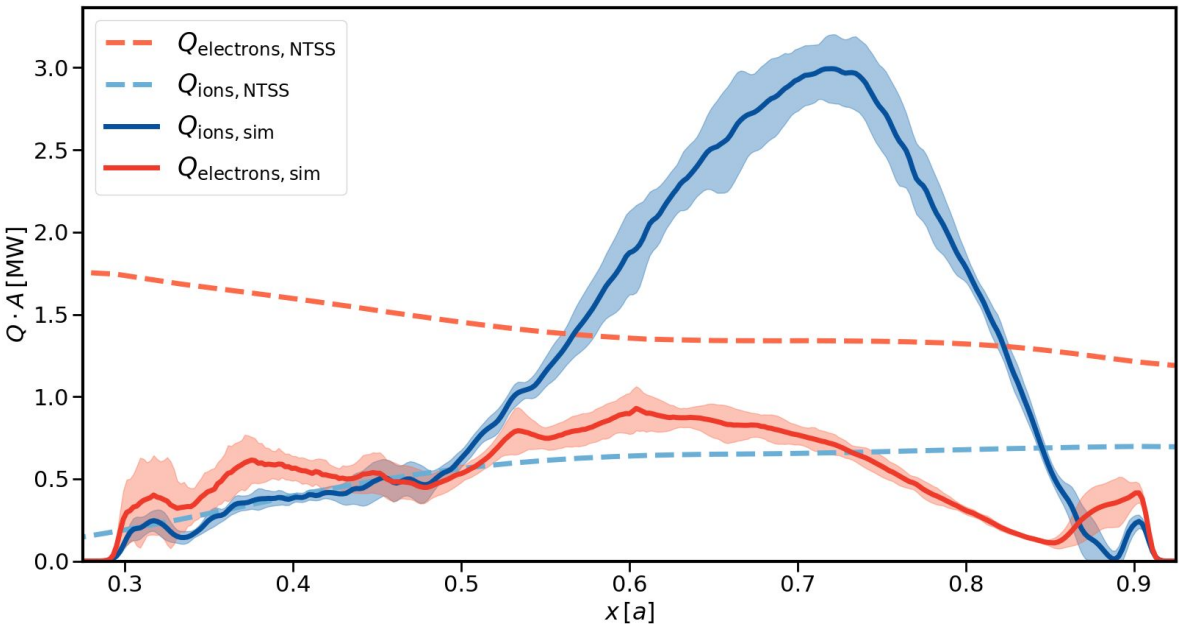

Figure 6.8: Comparison of the radial heat flux profile obtained from the global simulation with the power balance obtained by NTSS. Shaded regions indicate standard deviation in time of the global simulation.

The comparison between the power balance and GENE-3D shows good agreement of the ion heat flux up to $x/a = 0.5$. However, as we move further out of the core, the simulated ion heat flux increases substantially, reaching up to 3 MW, which exceeds even the total ECRH heating power injected into the system, as illustrated in figure 6.1. In contrast, the electron heat flux computed by GENE-3D appears notably lower across the entire radial domain. Consequently, our primary focus will be on the region with $x/a \leq 0.5$ for in-depth investigations of turbulence characteristics.

As was already mentioned in the introduction of chapter 6, it was postulated [16, 26] that ITG should be the dominant type of turbulence in the plasma core, while TEMs, if at all, should be expected in the plasma edge. However, the results obtained with GENE-3D and NTSS, as displayed in figure 6.8, suggest that this hypothesis can only be partially accurate. 'Pure' ITG turbulence drives only limited electron heat flux in comparison with the ion channel [101], as can also be observed in figure 5.1. In contrast, GENE-3D and NTSS predict either $Q_\mathrm{e} \geq Q_\mathrm{i}$ or $Q_\mathrm{e} \gg Q_\mathrm{i}$ in the core, as can be expected for plasmas where the only direct heating is applied to the electrons. Given that electromagnetic turbulence should be subdominant for the plasma-β of the discharge, TEM turbulence emerges as a likely candidate, as it was shown in chapter 5 that it could drive both ion and electron heat flux.

To explore this, we have selected the radial position $x/a = 0.4$ as a representative flux-surface within the inner plasma core. In figure 6.9, we present the spatial distribution of heat flux for both electron and ion channels along the parallel coordinate z and the field-line label α. Here, one can see that the ion heat flux exhibits primarily a single central peak, while the electron heat flux has multiple maxima along z at fixed α.

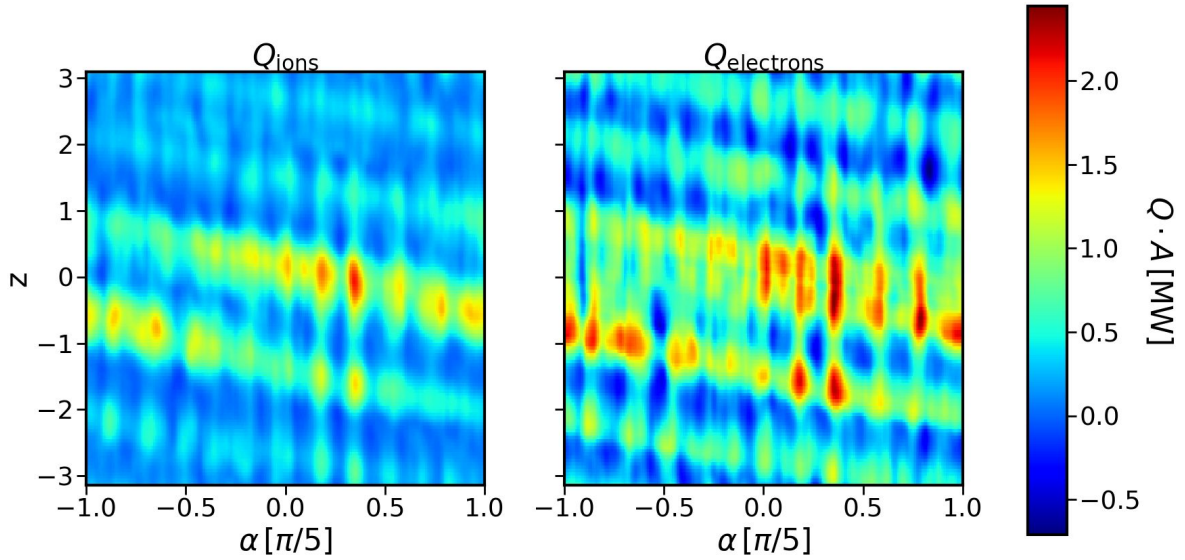

Figure 6.9: Electron and ion heat fluxes at $x/a = 0.4$, obtained by the global simulation, as a function of the parallel coordinate z and the field-line label α.

This distinction becomes even more evident when comparing the parallel structure at $\alpha = 0$ from flux-tube simulations against the magnetic field structure as well as the curvature drive $\mathcal{K}_\text{y}$ in figure 6.10.

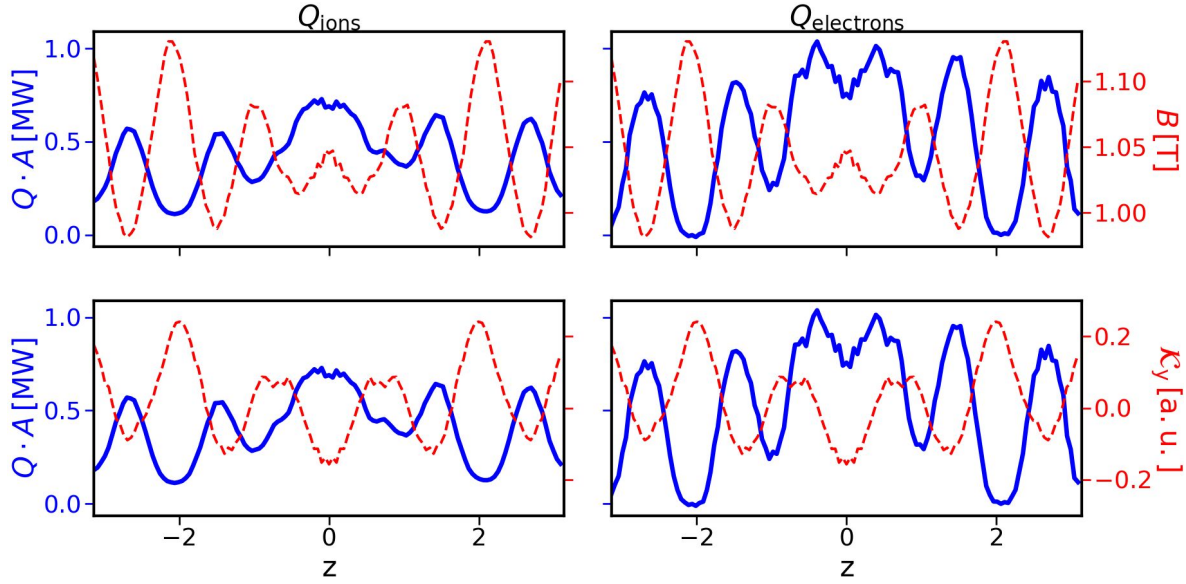

Figure 6.10: Blue: parallel ion (left) and electron (right) heat flux structures for the flux-tube simulation at $x/a = 0.4$, $\alpha = 0$ with nominal parameters; red: parallel structure of the equilibrium magnetic field strength (top) and the curvature-drive term $\mathcal{K}_\text{y}$ (bottom).

In the case of ion heat flux, it appears to peak at positions where $\mathcal{K}_\text{y}$ is the most negative. In contrast, the electron heat flux is additionally influenced significantly by the structure of magnetic wells. This becomes apparent as the latter has a local minimum at $z = 0$ despite

the curvature having a local minimum, closely followed by local maxima coinciding with the minima of the magnetic wells. The structural differences indicate the existence of a hybrid ITG-TEM mode, corroborated by linear simulations in figure 6.11.

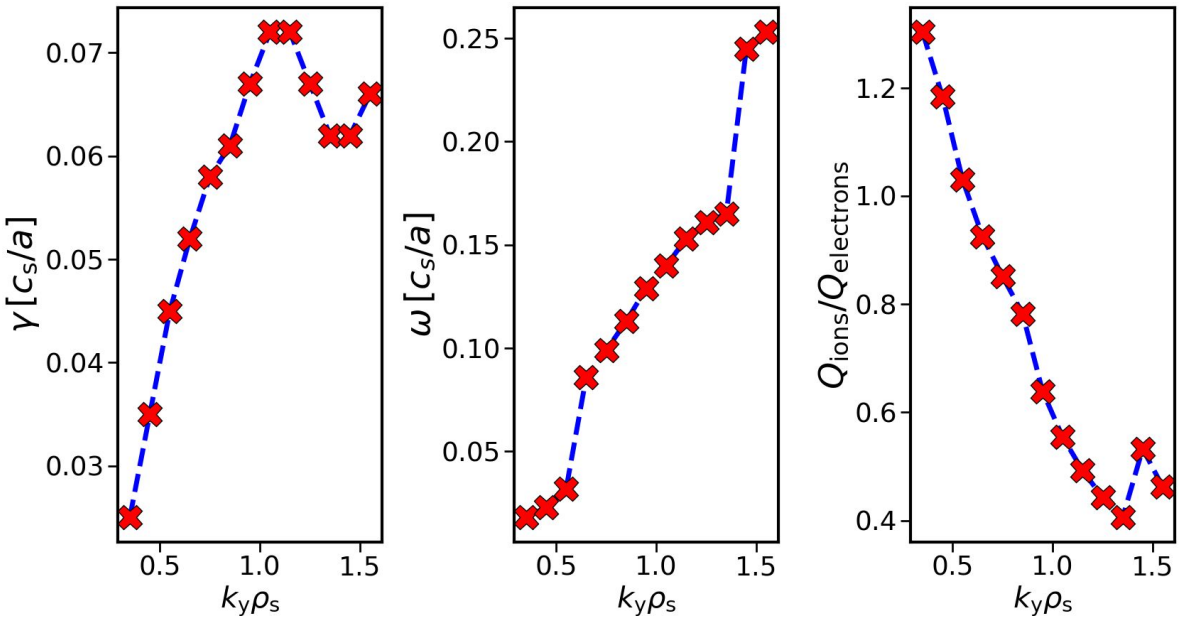

Figure 6.11: Linear flux-tube wavenumber-scan for the bean-shaped flux-tube at $x/a = 0.4$; left: growth rates, middle: mode frequencies, right: quasilinear estimates of the ion-to-electron heat flux ratio.

In there, all the analysed modes exhibit a positive frequency, indicating their propagation in the ion-diamagnetic direction. However, both particle channels have comparable strength regarding their quasilinear heat flux estimates. This points to a tight coupling between ions and electrons, a clear indication of the presence of ITG-TEM hybrid modes [102]. As can also be seen, the growth rate spectrum does not decrease within the scanned wavenumber range. Nevertheless, it becomes apparent that those small-scale modes do not contribute significantly to the nonlinear transport since the corresponding nonlinear heat flux spectra shown in figure 6.12 are predominantly determined by wavenumbers up to $k_y\rho_s \approx 1$.

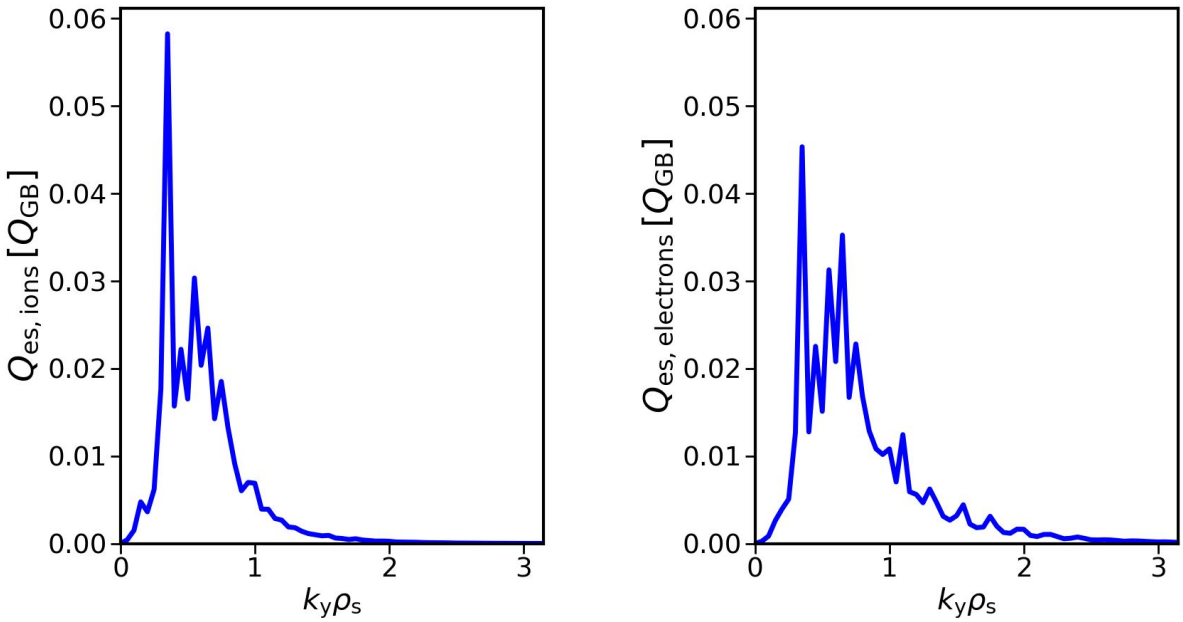

Figure 6.12: Nonlinear heat flux spectra for the bean-shaped flux-tube at $x/a = 0.4$; left: ion heat flux, right: electron heat flux.

We finalise this investigation by exploring the influence of each of the two temperature gradients on the overall transport levels. While this approach is not fully rigorous, it offers some insights into the contributions of different turbulence types to the overall dynamics.

Case	$Q_{\mathrm{ions}} \cdot A\,[\mathrm{MW}]$	$Q_{\mathrm{electrons}} \cdot A\,[\mathrm{MW}]$
Nominal	0.42 ± 0.05	0.49 ± 0.07
$a/L_{\mathrm{T_e}} = 0$	0.49 ± 0.06	0.07 ± 0.01
$a/L_{\mathrm{T_i}} = 0$	0.01 ± 0.00	0.18 ± 0.01

Table 6.2: Heat fluxes of flux-tube simulations at $x/a = 0.4$, $\alpha = 0$, for nominal parameters and either electron or ion temperature gradient set to zero.

Table 6.2 shows that, when compared to the nominal parameters, excluding the normalised electron temperature gradient has a negligible effect on the ion heat flux, as it remains similar to the nominal case within error bars. In contrast, the electron heat flux reduces by approximately 85% in this case, resulting in a scenario dominated by the ion channel. As can be seen in figure 6.13, the new ion heat flux has a rather ballooning-type structure along the magnetic field lines with substantially stronger contributions at the magnetic hills close to $z = 0$ compared with the ion heat flux shown in figure 6.10. Similar structures were observed in [23] for a case classified as ITG-driven, which we conclude is also the dominant type of turbulence here.

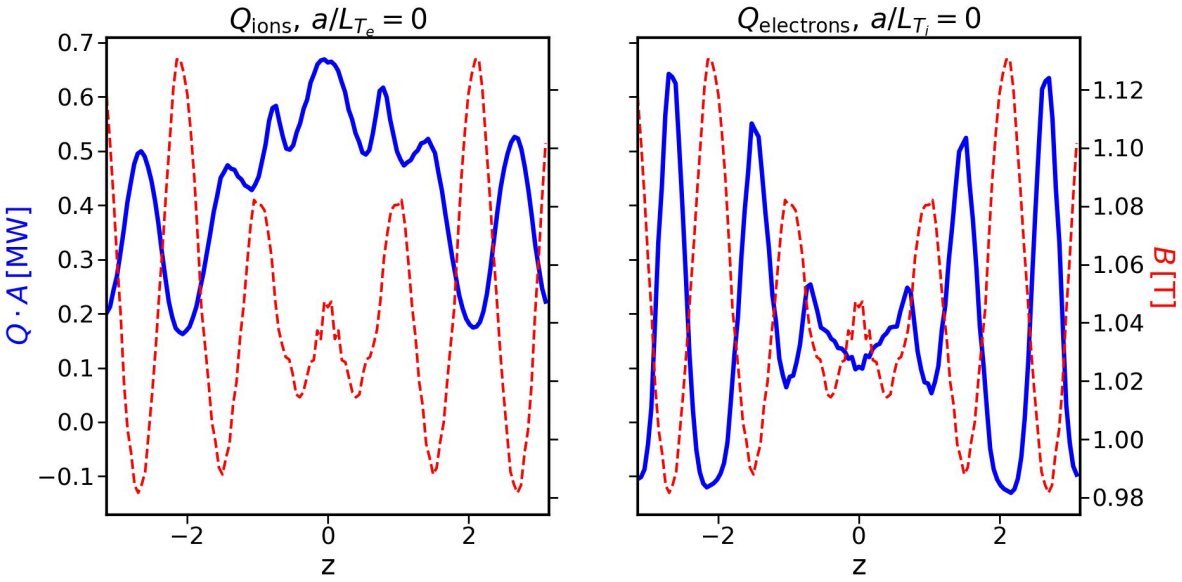

Figure 6.13: Left: parallel ion heat flux structure for the flux-tube simulation with $a/L_{\mathrm{T_e}} = 0$; right: parallel electron heat flux structure for the flux-tube simulation with $a/L_{\mathrm{T_i}} = 0$. While the heat fluxes are shown in blue, the parallel structure of the magnetic field strength is represented by red dashed lines.

Moreover, the ion heat flux vanishes almost completely when the ion temperature gradient is zero. In this case, the electron heat flux no longer peaks at $z = 0$, where the magnetic field strength has a local maximum, as shown in figure 6.13. Unlike the nominal case shown in figure 6.10, we conclude that the transport is now primarily driven by TEM turbulence, drawing its energy from the electron temperature gradient ∇T_{e}. Since one can also see in table 6.2 that the electron heat flux drops by a factor of 7 when the electron temperature gradient is neglected, one can see the importance of this branch of trapped-electron-modes compared with those that are primarily driven by an electron density gradient, which have garnered more attention in the literature thus far [22, 23, 103, 104].

Collectively, the evidence from the power balance, heat flux structure, and linear flux-tube analysis in this section leads us to conclude that, contrary to the proposition in [16, 26], trapped-electron-mode turbulence seems to be present in the core of gas-fuelled discharge in W7-X, at least for the discharge under consideration. However, the generality of this observation should be explored across various scenarios, a task reserved for future investigations.

6.4 Impact of ETG turbulence

As shown in figure 6.8, one can obtain satisfactory agreement between the predicted anomalous ion transport via power balance analysis and the one computed with GENE-3D within the core. In contrast, the electron transport remains too low. It is, however, essential to note that, thus far, we have primarily considered turbulence on the ion-scale. Therefore, the missing contribution to the electron flux could be driven by ETG turbulence.

To this end, we perform additional flux-tube simulations using the adiabatic ion model presented in section 2.7. We consider the flux-tubes at $\alpha = [0, 0.25, 0.5, 0.75]2\pi/5$ for $x/a = [0.3, 0.4, 0.5, 0.6, 0.7, 0.8, 0.9]$. The numerical resolution and box sizes remain the same as

those used in the ion-scale simulations in section 6.2, with the exception being the use of the electron Larmor radius ρ_e for normalisation instead of the ion sound Larmor radius ρ_s.

The resulting fluxes, given in megawatts, are then averaged over the field-line labels and are added to the ion-scale electron heat flux of GENE-3D via linear interpolation in the radial coordinate. Figure 6.14 shows the updated global flux profiles. In there, we observe that the contribution from electron-scale turbulence is negligible in the outer radial region. However, in the plasma core, ETG turbulence appears to account for over 50% of the turbulent electron heat flux. Our results align with [21], where ETG turbulence was identified as the potential main driver for electron heat transport in the core for some cases. However, the electron-scale contribution to the discharges was identified as even stronger than for the present case.

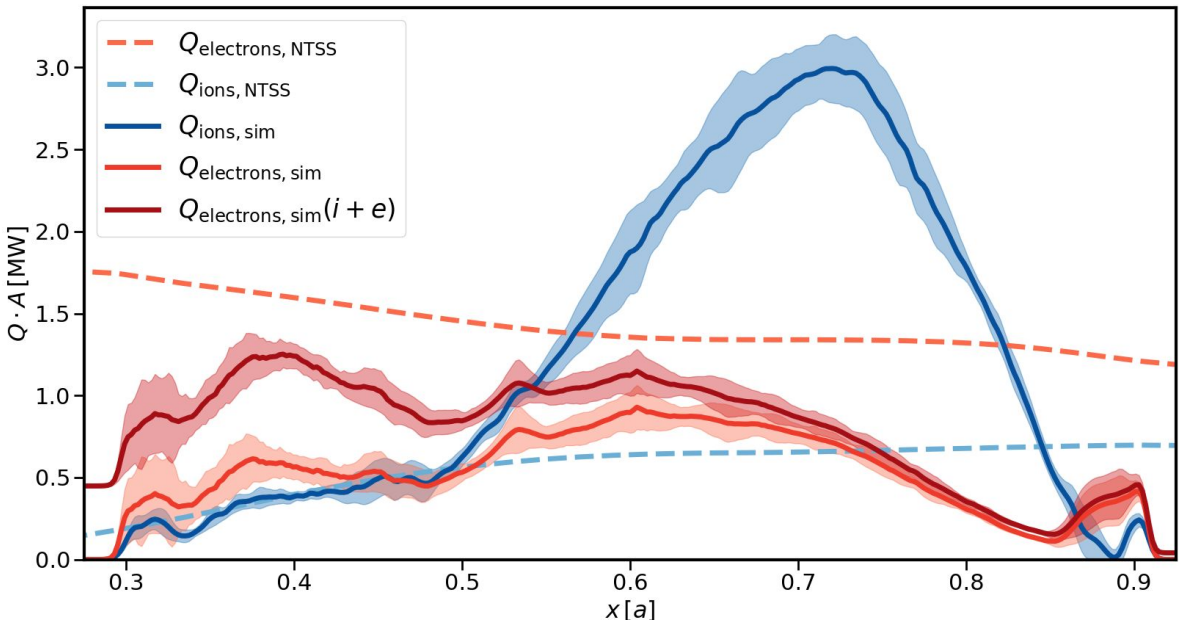

Figure 6.14: Comparison of the radial heat flux profile with the power balance obtained by NTSS. The dark red line shows the sum of electron heat fluxes of (separated) ion- and electron-scale simulations. Shaded regions indicate standard deviation in time of the global simulation.

In order to understand the discrepancy between the electron-scale contributions at different radial positions, one has to consider several possible factors. Figure 6.15 shows that the heat flux is nearly constant under variation of the field-line label so that the choice of the flux-tube or subsequent averaging procedures should have negligible impact on the discussion.

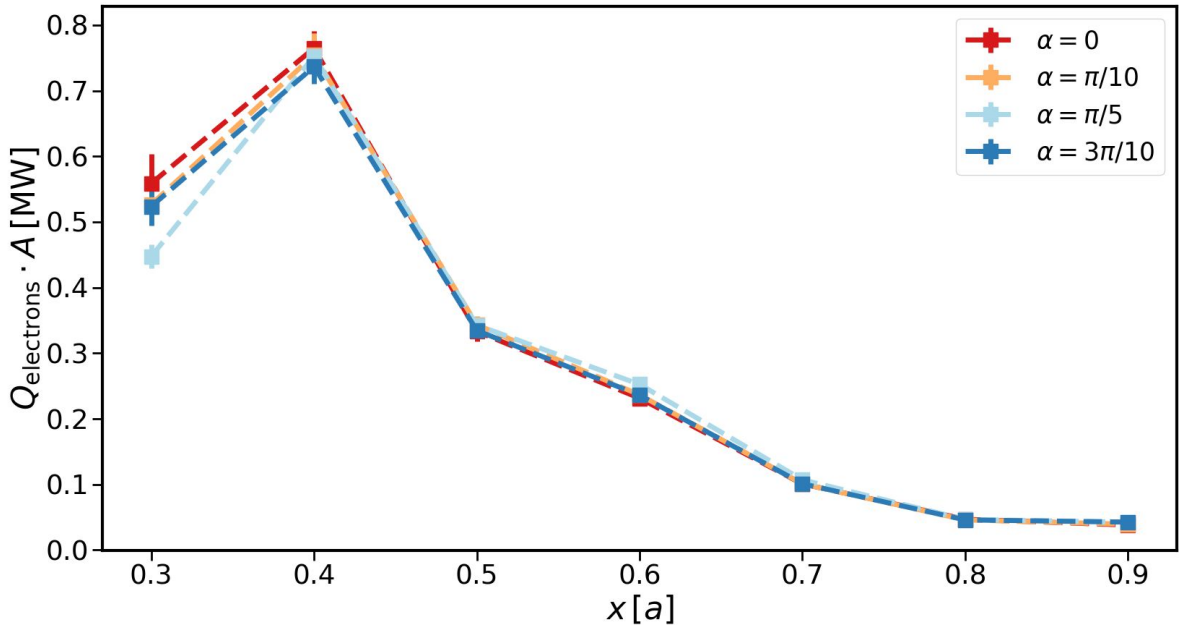

Figure 6.15: Electron heat fluxes obtained by local ETG simulations as a function of the radial coordinate for different field-line labels.

Previous studies of ETG dynamics in Wendelstein 7-AS [19] and similar simulations in tokamaks [105] have indicated that the collisionality and plasma-β have only a minor impact. However, the electron-to-ion temperature ratio $\tau = T_\mathrm{e}/T_\mathrm{i}$ and the normalised Debye length $\hat{\lambda}_\mathrm{De} = \lambda_\mathrm{De}/\rho_\mathrm{e} = \sqrt{B_\mathrm{ref}^2/(4\pi c^2 m_\mathrm{e} n_\mathrm{e}(x))}$ were reported to influence ETG turbulence significantly. Figure 6.16 shows that the decrease in τ is not responsible for the diminishing contribution of ETG to the total flux. The decrease in τ should lead to a destabilisation towards the outer region.

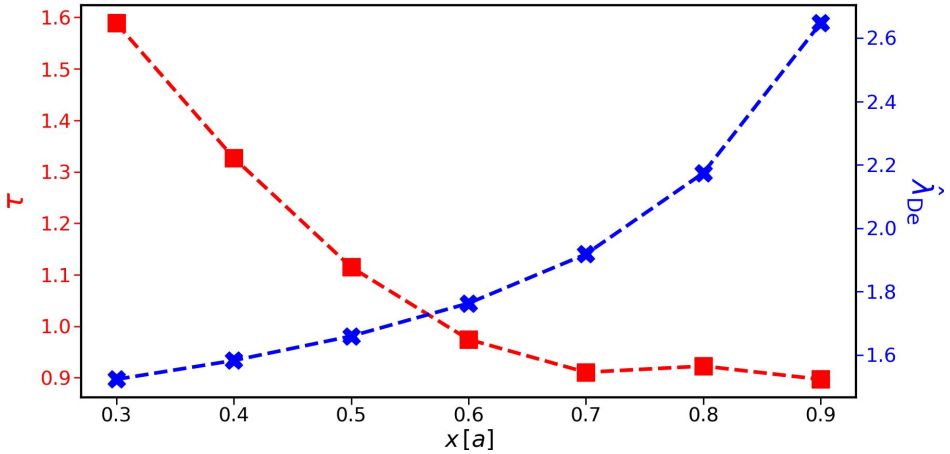

Figure 6.16: Variation of the temperature ratio $\tau = T_\mathrm{e}/T_\mathrm{i}$ (red) and the normalised Debye length $\hat{\lambda}_\mathrm{De} = \sqrt{B_\mathrm{ref}^2/(4\pi c^2 m_\mathrm{e} n_\mathrm{e}(x))}$ (blue) as a function of the radial coordinate.

Besides the change in τ, figure 6.16 also indicates that $\hat{\lambda}_\mathrm{De}$ increases towards the edge,

which is thought to have a stabilising influence on ETG turbulence. By repeating the flux-tube simulations while artificially setting $\hat{\lambda}_{\mathrm{De}} = 0$, we observe in figure 6.17 that the stabilisation resulting from Debye shielding remains inadequate to account for the radial variation in electron-scale transport, as the difference between both models becomes negligible towards the edge.

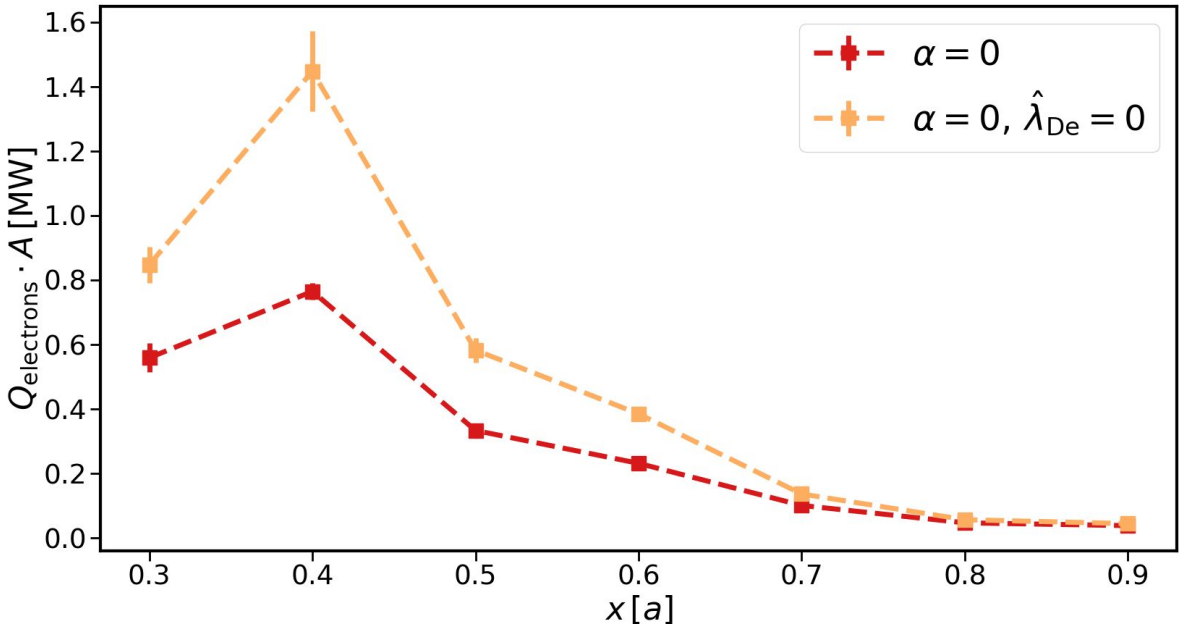

Figure 6.17: Radial electron-scale heat flux profiles of the $\alpha = 0$-flux-tube with (red) and without (orange) including $\hat{\lambda}_{\mathrm{De}}$.

In addition to geometrical factors, such as the magnetic field curvature, the normalised gradient ratio $\eta_{\mathrm{e}} = L_{\mathrm{n}}/L_{\mathrm{T_e}}$ is known to play a significant role, as a decrease has a stabilising effect on ETG turbulence. This effect was argued to explain the low ETG turbulence in the outer region of a discharge considered in [20]. If this was the leading cause, setting the density gradient to zero should naturally result in a radial profile that grows larger towards the edge, together with the normalised electron temperature gradient driving ETG turbulence. Although the decrease of η_{e} in the radial direction, shown in figure 6.18, would, in fact, support the hypothesis of stabilisation through the density gradient, we can see in the same figure that setting the density gradient to zero still results in the heat flux decreasing towards the edge.

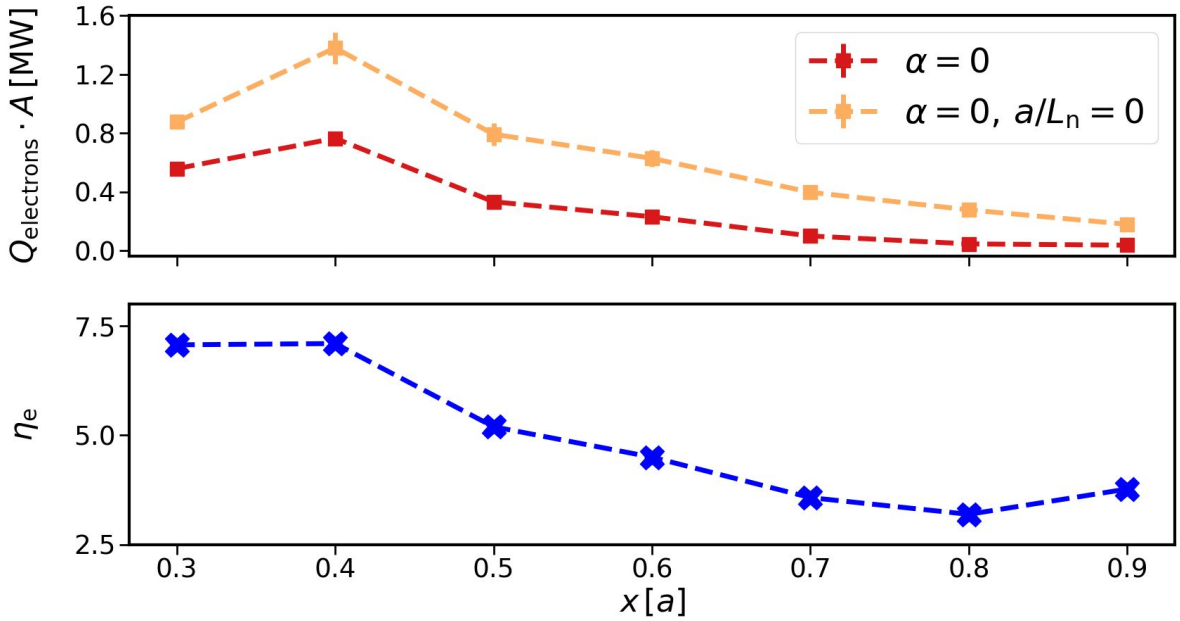

Figure 6.18: Top: Radial electron-scale heat flux profiles of the $\alpha = 0$-flux-tube with finite a/L_n (red) and with $a/L_n = 0$ (orange); bottom: radial variation of the normalised gradient ratio η_e.

Having eliminated all other options, we conclude that ETG transport is not stiff enough to compensate for the decrease in density and temperature towards the outer regions. To confirm this, we present the radial profile of the normalised heat flux and the Gyrobohm scaling factor profile in figure 6.19.

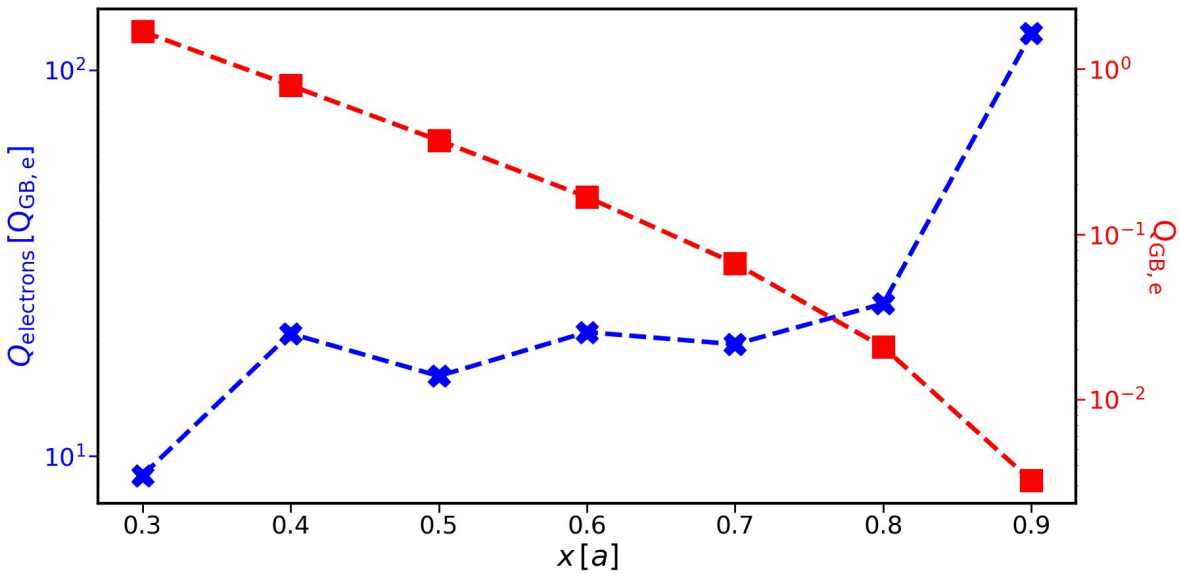

Figure 6.19: Blue: Radial electron-scale heat flux profile in Gyrobohm units, averaged over all field lines considered, using nominal simulation parameters; red: radial variation of Gyrobohm transport. The subscript 'e' indicates that the electron mass was used as reference mass m_{ref}.

Here, we observe that the former increases by approximately an order of magnitude towards the edge, aligning with the rise in the normalised electron temperature gradient. Simultaneously, the Gyrobohm scaling factor rapidly decreases by more than two orders of magnitude between the core and the edge. Therefore, we see that the normalised flux does not grow fast enough with increasing background drive, so the product of the two will decrease with increasing radial position.

Concluding this investigation, we summarise that we have shown electron-scale turbulence to be equally important as its ion-scale counterpart to explain the anomalous electron heat flux in the core of the gas-fuelled ECRH discharge under consideration. Conversely, we observed only minor contributions in the outer radial regions compared with the electron transport generated by hybrid ITG-TEM turbulence. Having considered multiple avenues of potential parametric causes for this, we conclude that ETG transport is less stiff than what is required by Gyrobohm scaling in order to compensate for the lower density and temperature in the edge. Whether this statement can be generalised to other discharges remains to be seen. Furthermore, it will be interesting to study the impact of the magnetic field geometry on transport stiffness.

6.5 Final remarks on power balance

While we have presented a first-of-its-kind simulation of experimentally relevant parameters of a gas-fuelled ECRH discharge in W7-X, one might rightfully question the validity of the conclusions drawn. The scepticism is justified since the simulated heat fluxes still do not align with the power balance, even with the additional electron-scale contributions. This is certainly true if one tried to establish a link between simulation and experiment for the outer region beyond $x/a = 0.5$ due to the overshoot in the ion heat flux calculated by GENE-3D. A more robust approach would involve a comprehensive coupling of various codes, including GENE-3D, GENE (for the ETG simulations), a neoclassical solver like KNOSOS [106] and other codes, with a transport code like Tango [107–109], to evolve the background profiles self-consistently until power balance is matched. Although this approach is routinely employed for tokamaks [110, 111], such simulations were either done globally using adiabatic electrons [112] or with kinetic electrons using a flux-tube approach [113] for stellarator geometries. Extending the GENE-3D-Tango approach to include kinetic electrons is beyond the scope of this thesis due to the high computational cost, but targeted as a project for the future.

Nevertheless, we can fortify the argument for TEM and ETG turbulence being relevant in the core of gas-fuelled ECRH plasmas without matching power balance by looking at the electron particle flux contributions. Although the experimental value of the flux is unknown due to substantial systematic uncertainties, it is reasonable to assume that, in the context of a purely gas-fuelled discharge, the total particle flux should tend towards zero or, at the very least, be relatively small deep within the core of the plasma.

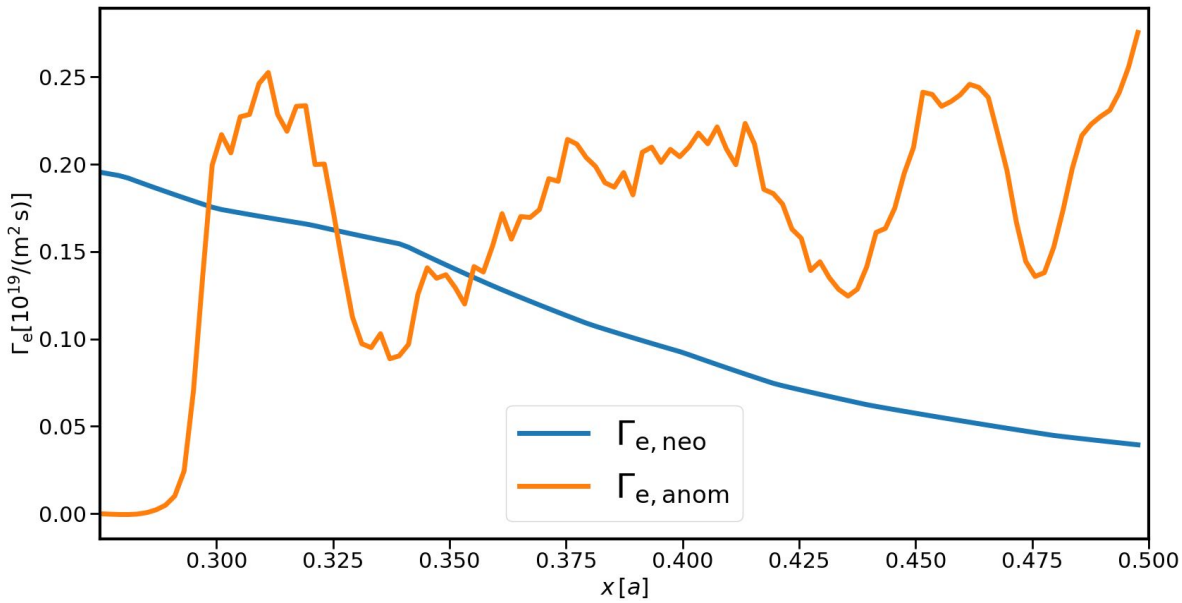

Figure 6.20: Radial profiles of contributions to the electron particle flux. The neoclassical particle flux, calculated with DKES, is shown in blue, while the anomalous flux, calculated with GENE-3D, is shown in orange.

A qualitative comparison of the particle flux levels presented in figure 6.20 with those documented in [93] indicates that the anomalous particle flux predicted by GENE-3D is too positive to fit the experiment. Since neoclassical transport often produces outward transport [114, 115], the turbulent particle flux has to become negative towards the magnetic axis, which is not the case here. Furthermore, as demonstrated in [93], an inward anomalous particle flux can be achieved by decreasing the density gradient, increasing the electron temperature gradient, or a combination of the two. Since both of these adjustments would enhance the drive of ∇T_e-TEM and ETG turbulence, it is reasonable to assume that, when matching power and particle balance, the contributions of electron-induced turbulence to the electron heat flux will be even more pronounced than under the nominal profiles employed in this analysis.

In summary, our evidence strongly supports the existence of trapped-electron turbulence in the core of gas-fuelled ECRH discharges in the form of an ITG-TEM hybrid and ETG turbulence. Their relevance in high-performance discharges, such as those with pellet fuelling, remains to be explored, given that robust density gradients have been shown to suppress ETG transport, as detailed in the previous section.

6.6 Chapter summary

This chapter presents the analysis of plasma turbulence in an experimental ECRH-discharge of Wendelstein 7-X using GENE-3D and GENE. We have shown that while flux-tube and full-flux-surface simulations decently approximate the heat flux levels in the plasma core predicted by a radially global simulation, the former significantly overpredicts transport in the outer region of the plasma. This discrepancy can be mitigated to some extent if the shearing of external ExB-flow is considered, highlighting its importance on turbulence stabilisation even in standard stellarator discharges.

Beyond that, we have provided substantial evidence for trapped-electron-mode turbulence in the plasma core for the case under consideration, in contrast to what has been proposed in the literature [16, 26]. While not being the sole contributors to transport, they were clearly shown to exist in the form of ITG-TEM hybrids, with the primary drive being the electron temperature gradient.

Additionally, we have demonstrated, within the scope of our specific case, that electron-scale simulations are responsible for a significant portion of electron heat flux compared with ion-scale simulations, deviating from the proposition of weak ETGs in W7-X made in [20]. In the outer radial regions of the plasma, their contribution diminishes, which we have shown to be caused by the normalised ETG transport not increasing sufficiently fast enough towards the outer region in order to offset the decrease in the Gyrobohm scaling factor caused by the lower electron temperature and density in the edge.

Finally, we argue for the validity of our claims despite not matching the transport predictions provided by power balance analysis, as the impact of electron-induced turbulence will only be strengthened if the background profiles are changed to obtain experimentally realistic particle fluxes.

Chapter 7

Conclusions

Throughout this thesis, the global gyrokinetic stellarator code GENE-3D has been upgraded to include electromagnetic effects arising through finite vector potential perturbations parallel to the magnetic field. In addition, GENE-3D has been used to study various effects relevant to the plasma performance in Wendelstein 7-X, with particular interest in comparing the predictive capabilities between flux-tube, full-flux-surface and radially global simulations. Below is a brief review of the most important accomplishments and insights. Furthermore, an outlook on possible future research topics is given.

7.1 Summary of the thesis

Upgrading GENE-3D to an electromagnetic turbulence code

Former versions of GENE-3D only used a formulation of the gyrokinetic equations in the electrostatic limit. While restricting the realm of physical phenomena that can be studied with the code, this limitation also made simulations including kinetic electrons unfeasible, as the numerical time step necessary for algorithmic stability was too small for simulations of meaningful timescales due to the so-called ω_H-mode [53]. Therefore, one of the main tasks was to include electromagnetic effects caused by finite vector potential perturbations $A_{1,||}$ into the code.

For this, Ampére's law and an equation for the inductive electric field had to be implemented, which had to be done with a conservative finite-difference scheme inspired by [71] in order to obtain numerically stable solutions. Besides other modifications, such as the inclusion of external ExB-flow-shear, an additional model for the inclusion of finite $B_{1,||}$-effects at arbitrary wavelengths for the global version of GENE has been developed that can be adopted readily for GENE-3D in the future. The electromagnetic upgrade has also been verified against GENE in linear and nonlinear global electromagnetic tokamak simulations, giving confidence in the correct model implementation.

Electromagnetic ITG simulation in stellarators

After initial verification studies against GENE, the code was applied to perform the first-ever global electromagnetic turbulence simulation with realistic electron mass in a stellarator geometry. The aim was to show the stabilising influence of finite plasma-β on ITG instabilities and turbulence in a Wendelstein 7-X-like plasma at already moderate levels of β, highlighting

the importance of retaining electromagnetic effects for quantitative investigations of experimental scenarios.

Full-flux-surface effects on electrostatic turbulence in Wendelstein 7-X-like plasmas

Besides the investigation of electromagnetic turbulence, upgrading GENE-3D also allowed for much more efficient simulations of electrostatic turbulence, as a small but finite β allows for a much larger time step while not changing the underlying electrostatic turbulence by any meaningful amount. Therefore, full-flux-surface simulations with kinetic electrons in stellarator geometry have been performed. Using this higher-fidelity setup, we have confirmed the stabilising effect of a finite density gradient on ITG-driven turbulence in stellarators, originally proposed through flux-tube simulations. We have furthermore shown that, while flux-tube simulations might predict similar transport levels compared with full-surface simulations for some of the cases under consideration, significant disagreement between the models was found in terms of the magnitude of the heat fluxes as well as the spatial distribution for cases that had a stronger turbulence drive. For most cases considered, we show that turbulent density fluctuations are only weakly localised on a flux-surface, in contrast to what has been suggested in previous full-flux-surface literature. Finally, it was found that for all cases considered, an external radial electric field neither caused any significant dislocation of the density fluctuations on the surface nor stabilised ITG turbulence significantly compared with an increase in the background density gradient.

Turbulence analysis of experimental ECRH-discharge in Wendelstein 7-X

GENE-3D was pushed to full operability in this chapter by performing simulations of experimental parameters of Wendelstein 7-X. The profiles under consideration are based on a discharge from the first operational campaign and can be considered representative of low-power ECRH-heated discharges with gas-puff fuelling. The discharge was investigated by performing flux-tube, full-flux-surface and radially global simulations, including kinetic electrons, electromagnetic and collisional effects, and a finite radial electric field. To the author's best knowledge, the full-surface and global simulations performed here were the first-of-a-kind studies of Wendelstein 7-X using experimental parameters. The subsequent analysis of the simulation results in this chapter was split into two parts.

In the first part, the comparison between flux-tube and full-flux-surface simulations was extended to experimentally relevant parameters, further comparing the approaches against predictions of a radially global simulation. In agreement with the previous chapter, we also found that, although flux-tube simulations can provide a suitable alternative to investigate the transport in the plasma's core, significant disagreement with the higher-fidelity models was found in the outer regions. We have also shown that including a sheared equilibrium-scale ExB-flow reduced the disagreement with the global results to some extent if the normalised flow shear rate is sufficiently large.

The second part of the analysis focused on the characterisation of turbulence found in the plasma's inner region for the profiles under consideration. In contrast to what was proposed in the literature, we find significant levels of trapped-electron turbulence in the form of ITG/TEM-hybrids in the core, where we propose that the trapped-electron contribution is the main contributor to the anomalous electron heat flux on ion scales. Furthermore, we

have found that electron-scale turbulence in the form of ETGs provides an equally important contribution to the electron heat flux as TEMs in the core. In contrast, their influence is negligible in the outer regions. This behaviour was attributed to the fact that the normalised electron-scale transport under consideration was not stiff enough to compensate for the temperature and density decrease towards the edge, lowering the Gyrobohm scaling factor.

7.2 Outlook for future projects

Beyond the suggestions for future projects given in the previous chapters, there are several projects that require improvements to the current version of GENE-3D.

Turbulence simulations of highly electromagnetic regimes

Future fusion reactors will likely operate at significantly higher plasma-β than those obtained in the first operational campaign of Wendelstein 7-X. Therefore, it is necessary to investigate the excitation of kinetic ballooning modes and their impact on plasma performance in great detail. Since previous studies have already shown magnetic compression effects to play a significant role, it is desirable to incorporate finite $B_{1,||}$ into the gyrokinetic system solved by GENE-3D. In order to use the model (2.7.6), presented in section 2.7, an alternative quadrature scheme for the μ-coordinate has to be introduced in order to use the arbitrary-wavelength model of the Poisson equation at a reasonable cost. One promising candidate is the discretisation scheme presented in [116], which was shown to behave significantly better for values of the coordinate close to the origin.

Non-Maxwellian background distribution functions

Besides the already-mentioned implementation of magnetic compression effects, incorporating the possibility of using non-Maxwellian background distribution functions will open the door to studying the interaction between neoclassical and gyrokinetic timescales. For this, the code will have to undergo significant changes, as the several simplifications introduced by a Maxwellian background have to be revered, resulting, for example, in a coupling between the field equations for ϕ_1, $A_{1,||}$ and $B_{1,||}$, subsequently also making it necessary to solve a coupled system for their time derivatives.

Interaction between energetic ions and turbulence

In a first attempt, [117] has shown that energetic ions can potentially be used to suppress turbulence in stellarators through resonant effects similar to what is seen in tokamaks [118–120]. It will, therefore, be interesting to study whether stellarators could be optimised so that such resonances could be exploited, for example, in the presence of fusion-born α-particles. Since such studies usually deal with a significant difference between core and edge temperatures, especially those of the fast ions, it will be helpful to implement block-structured velocity space grids [121], in GENE-3D, as its implementation in GENE has been shown to lead to a substantial reduction of the numerical cost.

Plasma profile prediction in stellarators

Although gradient-driven simulations can give valuable insights into the turbulent behaviour of plasmas, it is desirable to perform simulations at transport timescales. This way, the impact of physical effects on the density and temperature profiles, and therefore on plasma performance, can be studied. For this, GENE-3D has already been coupled to the transport code Tango [109] and applied to various scenarios [112, 122] under the use of an adiabatic electron model. The extension to kinetic electrons is straightforward and allows for predicting all particle temperature and density profiles, whereas in the former model, only the ion temperature is allowed to vary. Since this approach requires multiple global simulations with GENE-3D, its numerical performance should be improved. Besides the already mentioned implementation of block-structured velocity space grids, it will be crucial to port GENE-3D to run on GPUs. For this, the code will be refactored to support an object-oriented approach that allows the porting procedure via the gtensor library [123], which has been used successfully for GENE.

Acknowledgements

I want to express my deepest gratitude to all the people who have helped me throughout my PhD journey. First and foremost, I would like to thank Frank Jenko for giving me the opportunity to join his group and work on such an exciting project. I would also like to thank my mentor, Alejandro Bañón Navarro. Despite my near-daily drop-ins into his office, he was always available for scientific discussions and helped me keep track of the tasks right in front of me.

Many thanks also go to Gabriele Merlo. Although we have never met in person so far, he was one of my closest collaborators, always having insightful comments and exciting new projects to work on together. I would also like to thank Tobias Görler and Daniel Told, who have helped tremendously whenever I was stuck in the depths of the GENE source code.

I would like to thank Gabriele Merlo, Don Fernando, Christoph Pitzal, Facundo Sheffield, Hugo Cu Castillo and Leonhard Leppin for proofreading parts of my thesis.

I would also like to thank my friends and family, of whom there are too many to list here, but my parents, Ernst and Petra, in particular. They always encouraged and supported me however they could, not only during this PhD but throughout the entire journey to get to this point. Whatever I managed to do, I owe a great deal to all of them.

Finally, I would like to thank my significant other, Sophie Buscher. Despite all of the obstacles both of us have faced throughout these four years, she has always been the greatest support I could wish for.

Bibliography

[1] Brian Walsh, Philippe Ciais, Ivan A Janssens, Josep Penuelas, Keywan Riahi, Felicjan Rydzak, Detlef P Van Vuuren and Michael Obersteiner. 'Pathways for balancing CO2 emissions and sinks'. *Nature communications* 8.1 (2017), p. 14856.

[2] Jonas Kristiansen Nøland, Juliette Auxepaules, Antoine Rousset, Benjamin Perney and Guillaume Falletti. 'Spatial energy density of large-scale electricity generation from power sources worldwide'. *Scientific Reports* 12.1 (2022), p. 21280.

[3] Rick Michal. 'Fifty years ago in December: Atomic reactor EBR-I produced first electricity'. *Nuclear News* 44.12 (2001), pp. 28–29.

[4] Kenneth S Krane. *Introductory nuclear physics*. John Wiley & Sons, 1991.

[5] Irving Friedman. 'Deuterium content of natural waters and other substances'. *Geochimica et Cosmochimica Acta* 4.1 (1953), pp. 89–103. ISSN: 0016-7037. DOI: https://doi.org/10.1016/0016-7037(53)90066-0. URL: https://www.sciencedirect.com/science/article/pii/0016703753900660.

[6] https://www.destatis.de/DE/Presse/Pressemitteilungen/2022/12/PD22_542_85.html. Accessed: 2023-11-02.

[7] David Maisonnier, Iau Cook, Sardain Pierre, Boccaccini Lorenzo, Giancarli Luciano, Norajitra Prachai, Pizzuto Aldo, PPCS Team et al. 'DEMO and fusion power plant conceptual studies in Europe'. *Fusion Engineering and Design* 81.8-14 (2006), pp. 1123–1130.

[8] Samuel E. Wurzel and Scott C. Hsu. 'Progress toward fusion energy breakeven and gain as measured against the Lawson criterion'. *Physics of Plasmas* 29.6 (June 2022), p. 062103. ISSN: 1070-664X. DOI: 10.1063/5.0083990. eprint: https://pubs.aip.org/aip/pop/article-pdf/doi/10.1063/5.0083990/16620690/062103_1_online.pdf. URL: https://doi.org/10.1063/5.0083990.

[9] Ulrich Stroth. *Plasmaphysik*. Springer, 2011.

[10] Martin Greenwald, JL Terry, SM Wolfe, S Ejima, MG Bell, SM Kaye and GH Neilson. 'A new look at density limits in tokamaks'. *Nuclear Fusion* 28.12 (1988), p. 2199.

[11] FC Schuller. 'Disruptions in tokamaks'. *Plasma Physics and Controlled Fusion* 37.11A (1995), A135.

[12] Per Helander and Dieter J Sigmar. *Collisional transport in magnetized plasmas*. Vol. 4. Cambridge university press, 2005.

[13] Per Helander. 'Theory of plasma confinement in non-axisymmetric magnetic fields'. *Reports on Progress in Physics* 77.8 (2014), p. 087001.

[14] RC Wolf et al. 'A stellarator reactor based on the optimization criteria of Wendelstein 7-X'. *Fusion Engineering and Design* 83.7-9 (2008), pp. 990–996.

[15] CD Beidler, HM Smith, A Alonso, T Andreeva, J Baldzuhn, MNA Beurskens, Matthias Borchardt, SA Bozhenkov, Kai Jakob Brunner, Hannes Damm et al. 'Demonstration of reduced neoclassical energy transport in Wendelstein 7-X'. *Nature* 596.7871 (2021), pp. 221–226.

[16] T Klinger, T Andreeva, S Bozhenkov, C Brandt, R Burhenn, B Buttenschön, G Fuchert, B Geiger, O Grulke, HP Laqua et al. 'Overview of first Wendelstein 7-X high-performance operation'. *Nuclear Fusion* 59.11 (2019), p. 112004.

[17] K Aleynikova, A Zocco, P Xanthopoulos, P Helander and C Nührenberg. 'Kinetic ballooning modes in tokamaks and stellarators'. *Journal of Plasma Physics* 84.6 (2018).

[18] Peter Manz. 'The microscopic picture of plasma edge turbulence'. PhD thesis. Technische Universität München, 2019.

[19] F Jenko and A Kendl. 'Stellarator turbulence at electron gyroradius scales'. *New Journal of Physics* 4.1 (2002), p. 35.

[20] GG Plunk, P Xanthopoulos, GM Weir, SA Bozhenkov, A Dinklage, G Fuchert, J Geiger, M Hirsch, U Hoefel, M Jakubowski et al. 'Stellarators resist turbulent transport on the electron larmor scale'. *Physical Review Letters* 122.3 (2019), p. 035002.

[21] GM Weir, P Xanthopoulos, M Hirsch, U Höfel, T Stange, N Pablant, O Grulke, S Äkäslompolo, J Alcuson, S Bozhenkov et al. 'Heat pulse propagation and anomalous electron heat transport measurements on the optimized stellarator W7-X'. *Nuclear Fusion* 61.5 (2021), p. 056001.

[22] JHE Proll, GG Plunk, BJ Faber, T Görler, P Helander, IJ McKinney, MJ Pueschel, HM Smith and P Xanthopoulos. 'Turbulence mitigation in maximum-J stellarators with electron-density gradient'. *Journal of Plasma Physics* 88.1 (2022), p. 905880112.

[23] P. Xanthopoulos, S. A. Bozhenkov, M. N. Beurskens, H. M. Smith, G. G. Plunk, P. Helander, C. D. Beidler, J. A. Alcusón, A. Alonso, A. Dinklage, O. Ford, G. Fuchert, J. Geiger, J. H. E. Proll, M. J. Pueschel, Y. Turkin, F. Warmer and the W7-X Team. 'Turbulence Mechanisms of Enhanced Performance Stellarator Plasmas'. *Phys. Rev. Lett.* 125 (7 Aug. 2020), p. 075001. DOI: 10.1103/PhysRevLett.125.075001. URL: https://link.aps.org/doi/10.1103/PhysRevLett.125.075001.

[24] JA Alcusón, P Xanthopoulos, GG Plunk, P Helander, F Wilms, Y Turkin, A Von Stechow and O Grulke. 'Suppression of electrostatic micro-instabilities in maximum-J stellarators'. *Plasma Physics and Controlled Fusion* 62.3 (2020), p. 035005.

[25] GG Plunk, JW Connor and P Helander. 'Collisionless microinstabilities in stellarators. Part 4. The ion-driven trapped-electron mode'. *Journal of Plasma Physics* 83.4 (2017), p. 715830404.

[26] O Grulke et al. 'Plasma Dynamics and Transport Studies in Wendelstein 7-X'. In: *27th IAEA Fusion Energy Conference (FEC 2018)*. 2018.

[27] Andreas Dinklage, CD Beidler, Per Helander, Golo Fuchert, H Maaßberg, Kian Rahbarnia, T Sunn Pedersen, Y Turkin, RC Wolf, A Alonso et al. 'Magnetic configuration effects on the Wendelstein 7-X stellarator'. *Nature Physics* 14.8 (2018), pp. 855–860.

[28] P Xanthopoulos, HE Mynick, P Helander, Yu Turkin, GG Plunk, F Jenko, T Görler, D Told, T Bird and JHE Proll. 'Controlling turbulence in present and future stellarators'. *Physical review letters* 113.15 (2014), p. 155001.

[29] Jim-Felix Lobsien, Michael Drevlak, Thomas Sunn Pedersen et al. 'Stellarator coil optimization towards higher engineering tolerances'. *Nuclear Fusion* 58.10 (2018), p. 106013.

[30] Maurice Maurer, A Bañón Navarro, Tilman Dannert, Marco Restelli, Florian Hindenlang, Tobias Görler, Daniel Told, Denis Jarema, Gabriele Merlo and Frank Jenko. 'GENE-3D: A global gyrokinetic turbulence code for stellarators'. *Journal of Computational Physics* 420 (2020), p. 109694.

[31] MDJ Cole, T Moritaka, R Hager, J Dominski, S Ku and CS Chang. 'Nonlinear global gyrokinetic delta-f turbulence simulations in a quasi-axisymmetric stellarator'. *Physics of Plasmas* 27.4 (2020), p. 044501.

[32] E Sánchez, A Mishchenko, JM García-Regaña, R Kleiber, A Bottino, L Villard et al. 'Nonlinear gyrokinetic PIC simulations in stellarators with the code EUTERPE'. *arXiv preprint arXiv:2004.14605* (2020).

[33] HY Wang, I Holod, Zhihong Lin, Jian Bao, Jing Yuan Fu, PF Liu, Javier H Nicolau, Donald Spong and Yong Xiao. 'Global gyrokinetic particle simulations of microturbulence in W7-X and LHD stellarators'. *Physics of Plasmas* 27.8 (2020), p. 082305.

[34] Felix Wilms, Alejandro Bañón Navarro, Gabriele Merlo, Leonhard Leppin, Tobias Görler, Tilman Dannert, Florian Hindenlang and Frank Jenko. 'Global electromagnetic turbulence simulations of W7-X-like plasmas with GENE-3D'. *Journal of Plasma Physics* 87.6 (2021).

[35] Anatoliĭ Aleksandrovich Vlasov. 'The vibrational properties of an electron gas'. *Soviet Physics Uspekhi* 10.6 (1968), p. 721.

[36] EA Frieman and Liu Chen. 'Nonlinear gyrokinetic equations for low-frequency electromagnetic waves in general plasma equilibria'. *The Physics of Fluids* 25.3 (1982), pp. 502–508.

[37] Alain J Brizard and Taik Soo Hahm. 'Foundations of nonlinear gyrokinetic theory'. *Reviews of modern physics* 79.2 (2007), p. 421.

[38] Alain J Brizard. 'Variational principle for the parallel-symplectic representation of electromagnetic gyrokinetic theory'. *Physics of Plasmas* 24.8 (2017).

[39] Natalia Tronko, Alberto Bottino and Eric Sonnendrücker. 'Second order gyrokinetic theory for particle-in-cell codes'. *Physics of Plasmas* 23.8 (2016).

[40] Tilman Dannert. 'Gyrokinetische Simulation von Plasmaturbulenz mit gefangenen Teilchen und elektromagnetischen Effekten'. PhD thesis. Technische Universität München, 2005.

[41] H Goldstein Classical Mechanics. *Addison-Wesley Series in Physics*. 1980.

[42] Robert G Littlejohn. 'Variational principles of guiding centre motion'. *Journal of Plasma Physics* 29.1 (1983), pp. 111–125.

[43] Robert G Littlejohn. 'Hamiltonian perturbation theory in noncanonical coordinates'. *Journal of Mathematical Physics* 23.5 (1982), pp. 742–747.

[44] John R Cary and Robert G Littlejohn. 'Noncanonical Hamiltonian mechanics and its application to magnetic field line flow'. *Annals of Physics* 151.1 (1983), pp. 1–34.

[45] T Görler, N Tronko, WA Hornsby, A Bottino, R Kleiber, C Norscini, V Grandgirard, F Jenko and E Sonnendrücker. 'Intercode comparison of gyrokinetic global electromagnetic modes'. *Physics of Plasmas* 23.7 (2016), p. 072503.

[46] Hideo Sugama. 'Gyrokinetic field theory'. *Physics of Plasmas* 7.2 (2000), pp. 466–480.

[47] Alain J Brizard. 'Exact energy conservation laws for full and truncated nonlinear gyrokinetic equations'. *Physics of Plasmas* 17.4 (2010), p. 042303.

[48] Y Idomura, M Ida, S Tokuda and L Villard. 'Conservative gyrokinetic Vlasov simulation using Morinishi scheme'. In: *33rd European Physical Society Conference on Plasma Physics*. 2006.

[49] William D D'haeseleer, William NG Hitchon, James D Callen and J Leon Shohet. *Flux coordinates and magnetic field structure: a guide to a fundamental tool of plasma theory*. Springer Science & Business Media, 2012.

[50] T. Görler, X. Lapillonne, S. Brunner, T. Dannert, F. Jenko, F. Merz and D. Told. 'The global version of the gyrokinetic turbulence code GENE'. *Journal of Computational Physics* 230.18 (2011), pp. 7053 –7071. ISSN: 0021-9991. DOI: https://doi.org/10.1016/j.jcp.2011.05.034. URL: http://www.sciencedirect.com/science/article/pii/S0021999111003457.

[51] Paul Crandall. 'Collisional and electromagnetic physics in gyrokinetic models'. PhD thesis. UCLA, 2019.

[52] John Van Wicheren Reynders. 'Gyrokinetic simulation of finite-beta plasmas on parallel architectures'. PhD thesis. Princeton University, 1993.

[53] H Doerk and Frank Jenko. 'Towards optimal explicit time-stepping schemes for the gyrokinetic equations'. *Computer Physics Communications* 185.7 (2014), pp. 1938–1946.

[54] Meng Li, Boris N Breizman and Linjin Zheng. 'Canonical straight field line magnetic flux coordinates for tokamaks'. *Journal of Computational Physics* 326 (2016), pp. 334–341.

[55] J. D. Huba. *NRL report*. 2011. URL: http://wwwppd.nrl.navy.mil/nrlformulary.

[56] T Görler. 'Multiscale effects in plasma microturbulence Ph. D'. PhD thesis. thesis University of Ulm, Germany, 2009.

[57] Milton Abramowitz and Irene A Stegun. 'Handbook of mathematical functions with formulas, graphs, and mathematical table'. In: *US Department of Commerce*. National Bureau of Standards Applied Mathematics series 55, 1965.

[58] Xavier Lapillonne. *Local and global Eulerian gyrokinetic simulations of microturbulence in realistic geometry with applications to the TCV Tokamak*. Tech. rep. Swiss Federal Institute of Technology EPFL, 2010.

[59] L. D. Landau. 'The transport equation in the case of Coulomb interactions'. *Physi. Z. der Sowjet.* 10 (154 1936).

[60] Michael Alan Beer, SC Cowley and GW Hammett. 'Field-aligned coordinates for nonlinear simulations of tokamak turbulence'. *Physics of Plasmas* 2.7 (1995), pp. 2687–2700.

[61] Peter Porazik and Zhihong Lin. 'Gyrokinetic simulation of magnetic compressional modes in general geometry'. *Communications in Computational Physics* 10.4 (2011), pp. 899–911.

[62] Ge Dong, Jian Bao, Amitava Bhattacharjee, Alain Brizard, Zhihong Lin and Peter Porazik. 'Gyrokinetic particle simulations of the effects of compressional magnetic perturbations on drift-Alfvenic instabilities in tokamaks'. *Physics of Plasmas* 24.8 (2017), p. 081205.

[63] Yuheng Yang, Lei Ye, Yang Chen, Nong Xiang and Youwen Sun. 'Gyrokinetic Particle-in-Cell simulation of the effect of compressional magnetic perturbations on the microscopic instabilities in Tokamak'. *Computer Physics Communications* (2023), p. 108892.

[64] F. Wilms, G. Merlo, F. Sheffield, T. Görler, A. Banon Navarro and F. Jenko. 'Implementation of magnetic compressional effects at arbitrary wavelength in the global version of GENE'. *Submitted to Computer Physics Communications* (2023).

[65] Florian Merz. 'Gyrokinetic simulation of multimode plasma turbulence'. PhD thesis. Universität Münster Münster, 2008.

[66] William H Press. 'Numerical recipes in Pascal: the art of scientific computing'. *(No Title)* (1989).

[67] Denis Jarema. 'Efficient eulerian gyrokinetic simulations with block-structured grids'. PhD thesis. Technische Universität München, 2017.

[68] Daniel Told. 'Gyrokinetic microturbulence in transport barriers'. PhD thesis. Universität Ulm, 2012.

[69] Mikhail Shashkov and Stanly Steinberg. *Conservative finite-difference methods on general grids*. CRC press, 2018.

[70] S Günter, Q Yu, J Krüger and K Lackner. 'Modelling of heat transport in magnetised plasmas using non-aligned coordinates'. *Journal of Computational Physics* 209.1 (2005), pp. 354–370.

[71] Sibylle Günter, Karl Lackner and C Tichmann. 'Finite element and higher order difference formulations for modelling heat transport in magnetised plasmas'. *Journal of Computational Physics* 226.2 (2007), pp. 2306–2316.

[72] Akio Arakawa. 'Computational design for long-term numerical integration of the equations of fluid motion: Two-dimensional incompressible flow. Part I'. *Journal of computational physics* 135.2 (1997), pp. 103–114.

[73] BF McMillan, S Jolliet, TM Tran, L Villard, A Bottino and P Angelino. 'Long global gyrokinetic simulations: Source terms and particle noise control'. *Physics of Plasmas* 15.5 (2008), p. 052308.

[74] Andris M Dimits, G Bateman, MA Beer, BI Cohen, W Dorland, GW Hammett, C Kim, JE Kinsey, M Kotschenreuther, AH Kritz et al. 'Comparisons and physics basis of tokamak transport models and turbulence simulations'. *Physics of Plasmas* 7.3 (2000), pp. 969–983.

[75] CM Greenfield, JC DeBoo, TH Osborne, FW Perkins, MN Rosenbluth and D Boucher. 'Enhanced fusion performance due to plasma shape modification of simulated ITER discharges in DIII-D'. *Nuclear fusion* 37.9 (1997), p. 1215.

[76] Alexey Mishchenko, Alessandro Biancalani, Alberto Bottino, Thomas Hayward-Schneider, Ph Lauber, Emmanuel Lanti, Laurent Villard, Ralf Kleiber, Axel Koenies and Matthias Borchardt. 'Numerics and computation in gyrokinetic simulations of electromagnetic turbulence with global particle-in-cell codes'. *Plasma Physics and Controlled Fusion* 63.8 (2021), p. 084007.

[77] Hideaki Masui, Akihiro Ishizawa, Kenji Imadera, Yasuaki Kishimoto and Yuji Nakamura. 'Global saturation physics of ion temperature gradient turbulence in finite normalized pressure tokamaks'. *Nuclear Fusion* 62.7 (2022), p. 074001.

[78] Joachim Geiger, Craig D Beidler, Y Feng, Henning Maaßberg, Nikolai B Marushchenko and Yuryi Turkin. 'Physics in the magnetic configuration space of W7-X'. *Plasma Physics and Controlled Fusion* 57.1 (2014), p. 014004.

[79] Daniel Carralero, Teresa Estrada, Emmanouil Maragkoudakis, Thomas Windisch, J Arturo Alonso, M Beurskens, S Bozhenkov, Ivan Calvo, Hannes Damm, O Ford et al. 'An experimental characterization of core turbulence regimes in Wendelstein 7-X'. *Nuclear Fusion* 61.9 (2021), p. 096015.

[80] F. Hindenlang, O. Maj, E. Strumberger, M. Rampp and E. Sonnendrücker. *GVEC: A newly developed 3D ideal MHD Galerkin Variational Equilibrium Code, Presentation given in 'Simmons Collaboration on Hidden Symmetries in Fusion Energy'*. 2019. URL: `https://hiddensymmetries.princeton.edu/meetings/simons-hour-talks`.

[81] E Sánchez, JM García-Regaña, A Bañón Navarro, JHE Proll, C Mora Moreno, A González-Jerez, I Calvo, R Kleiber, J Riemann, J Smoniewski et al. 'Gyrokinetic simulations in stellarators using different computational domains'. *arXiv preprint arXiv:2106.02828* (2021).

[82] MNA Beurskens, SA Bozhenkov, O Ford, P Xanthopoulos, A Zocco, Y Turkin, A Alonso, C Beidler, I Calvo, D Carralero et al. 'Ion temperature clamping in Wendelstein 7-X electron cyclotron heated plasmas'. *Nuclear Fusion* 61.11 (2021), p. 116072.

[83] J Baldzuhn, H Damm, CD Beidler, K McCarthy, N Panadero, C Biedermann, SA Bozhenkov, KJ Brunner, G Fuchert, Y Kazakov et al. 'Pellet fueling experiments in Wendelstein 7-X'. *Plasma Physics and Controlled Fusion* 61.9 (2019), p. 095012.

[84] Per Helander, Josefine Henriette Elise Proll and Gabriel Galad Plunk. 'Collisionless microinstabilities in stellarators. I. Analytical theory of trapped-particle modes'. *Physics of Plasmas* 20.12 (2013), p. 122505.

[85] Josefine Henriette Elise Proll, Pavlos Xanthopoulos and Per Helander. 'Collisionless microinstabilities in stellarators. II. Numerical simulations'. *Physics of Plasmas* 20.12 (2013), p. 122506.

[86] Felix Wilms, Alejandro Banon Navarro and Frank Jenko. 'Full-flux-surface effects on electrostatic turbulence in Wendelstein 7-X-like plasmas'. *Nuclear Fusion* (2023).

[87] Per Helander, T Bird, F Jenko, R Kleiber, GG Plunk, JHE Proll, J Riemann and P Xanthopoulos. 'Advances in stellarator gyrokinetics'. *Nuclear Fusion* 55.5 (2015), p. 053030.

[88] H Thienpondt, JM García-Regaña, I Calvo, M Barnes, F Parra and R Davies. *Turbulent heat flux versus density gradient at finite ion temperature gradient: An intermachine study with the gyrokinetic code stella, Presentation given in '23rd International Stellarator-Heliotron Workshop'*. 2022.

[89] P Xanthopoulos, GG Plunk, A Zocco and P Helander. 'Intrinsic turbulence stabilization in a stellarator'. *Physical Review X* 6.2 (2016), p. 021033.

[90] GT Roberg-Clark, GG Plunk, P Xanthopoulos, C Nührenberg, SA Henneberg and HM Smith. 'Critical gradient turbulence optimization toward a compact stellarator reactor concept'. *arXiv preprint arXiv:2301.06773* (2023).

[91] Edilberto Sanchez, Alejandro Banon Navarro, Felix Wilms, Matthias Borchardt, Ralf Kleiber and Frank Jenko. 'Instabilities and turbulence in stellarators from the perspective of global codes'. *Nuclear Fusion* (2022).

[92] Teresa Estrada, D Carralero, T Windisch, E Sánchez, JM García-Regaña, J Martínez-Fernández, A de la Peña, JL Velasco, JA Alonso, M Beurskens et al. 'Radial electric field and density fluctuations measured by Doppler reflectometry during the post-pellet enhanced confinement phase in W7-X'. *Nuclear Fusion* 61.4 (2021), p. 046008.

[93] H Thienpondt, JM García-Regaña, I Calvo, JA Alonso, JL Velasco, A González-Jerez, M Barnes, K Brunner, O Ford, G Fuchert et al. 'Prevention of core particle depletion in stellarators by turbulence'. *Physical Review Research* 5.2 (2023), p. L022053.

[94] Tajinder Singh, Javier H Nicolau, Zhihong Lin, Sarveshwar Sharma, Abhijit Sen and Animesh Kuley. 'Global gyrokinetic simulations of electrostatic microturbulent transport using kinetic electrons in LHD stellarator'. *Nuclear Fusion* 62.12 (2022), p. 126006.

[95] JHE Proll, HE Mynick, P Xanthopoulos, SA Lazerson and BJ Faber. 'TEM turbulence optimisation in stellarators'. *Plasma Physics and Controlled Fusion* 58.1 (2015), p. 014006.

[96] Sven Stroteich, Pavlos Xanthopoulos, Gabriel Plunk and Ralf Schneider. 'Seeking turbulence optimized configurations for the Wendelstein 7-X stellarator: ion temperature gradient and electron temperature gradient turbulence'. *Journal of Plasma Physics* 88.5 (2022), p. 175880501.

[97] Yu Turkin, H Maaßberg, CD Beidler, J Geiger and NB Marushchenko. 'Current control by ECCD for W7-X'. *Fusion Science and Technology* 50.3 (2006), pp. 387–394.

[98] WI Van Rij and SP Hirshman. 'Variational bounds for transport coefficients in three-dimensional toroidal plasmas'. *Physics of Fluids B: Plasma Physics* 1.3 (1989), pp. 563–569.

[99] Mike F Martin, Matt Landreman, Pavlos Xanthopoulos, Noah R Mandell and William Dorland. 'The parallel boundary condition for turbulence simulations in low magnetic shear devices'. *Plasma Physics and Controlled Fusion* 60.9 (2018), p. 095008.

[100] GW Hammett, W Dorland, NF Loureiro and T Tatsuno. 'Implementation of large scale E× B shear flow in the GS2 gyrokinetic turbulence code'. In: *48th Annual Meeting of the Division of Plasma Physics*. 2006.

[101] M Kotschenreuther, X Liu, DR Hatch, S Mahajan, L Zheng, A Diallo, R Groebner, JC Hillesheim, CF Maggi, C Giroud et al. 'Gyrokinetic analysis and simulation of pedestals to identify the culprits for energy losses using 'fingerprints''. *Nuclear Fusion* 59.9 (2019), p. 096001.

[102] P Xanthopoulos and F Jenko. 'Gyrokinetic analysis of linear microinstabilities for the stellarator Wendelstein 7-X'. *Physics of plasmas* 14.4 (2007).

[103] JA Alcusón, Th Wegner, A Dinklage, A Langenberg, J-P Bähner, B Buttenschön, EM Edlund, G Fuchert, JM García-Regaña, O Grulke et al. 'Quantitative comparison of impurity transport in turbulence reduced and enhanced scenarios at Wendelstein 7-X'. *Nuclear Fusion* 63.9 (2023), p. 094002.

[104] Josefine Henriette Elise Proll, Per Helander, John William Connor and GG Plunk. 'Resilience of quasi-isodynamic stellarators against trapped-particle instabilities'. *Physical Review Letters* 108.24 (2012), p. 245002.

[105] Frank Jenko, W Dorland, M Kotschenreuther and BN Rogers. 'Electron temperature gradient driven turbulence'. *Physics of plasmas* 7.5 (2000), pp. 1904–1910.

[106] Jose Luis Velasco, I Calvo, Felix I Parra and JM García-Regaña. 'KNOSOS: a fast orbit-averaging neoclassical code for stellarator geometry'. *Journal of Computational Physics* 418 (2020), p. 109512.

[107] Jeffrey B Parker, Lynda L LoDestro, Daniel Told, Gabriele Merlo, Lee F Ricketson, Alejandro Campos, Frank Jenko and Jeffrey AF Hittinger. 'Bringing global gyrokinetic turbulence simulations to the transport timescale using a multiscale approach'. *Nuclear Fusion* 58.5 (2018), p. 054004.

[108] Jeffrey B Parker, Lynda L LoDestro and Alejandro Campos. 'Investigation of a multiple-timescale turbulence-transport coupling method in the presence of random fluctuations'. *Plasma* 1.1 (2018), pp. 126–143.

[109] AI Shestakov, RH Cohen, JA Crotinger, LL LoDestro, A Tarditi and XQ Xu. 'Self-consistent modeling of turbulence and transport'. *Journal of Computational Physics* 185.2 (2003), pp. 399–426.

[110] A Di Siena, A Bañón Navarro, T Luda, G Merlo, M Bergmann, L Leppin, T Görler, JB Parker, L LoDestro, T Dannert et al. 'Global gyrokinetic simulations of ASDEX Upgrade up to the transport timescale with GENE–Tango'. *Nuclear Fusion* 62.10 (2022), p. 106025.

[111] A Di Siena, P Rodriguez-Fernandez, NT Howard, A Bañón Navarro, R Bilato, T Görler, E Poli, G Merlo, J Wright, M Greenwald et al. 'Predictions of improved confinement in SPARC via energetic particle turbulence stabilization'. *Nuclear Fusion* 63.3 (2023), p. 036003.

[112] A Bañón Navarro, A Di Siena, JL Velasco, F Wilms, G Merlo, T Windisch, LL LoDestro, JB Parker and F Jenko. 'First-principles based plasma profile predictions for optimized stellarators'. *Nuclear Fusion* 63.5 (2023), p. 054003.

[113] Noah Mandell, William Dorland, Felix Parra, Tony Qian, Jai Sachdev and Jose Luis Velasco. 'Stellarator profile prediction and evolution using the Trinity3D+ GX+ KNOSOS multi-scale gyrokinetic framework'. *Bulletin of the American Physical Society* (2023).

[114] H Maaßberg, CD Beidler and EE Simmet. 'Density control problems in large stellarators with neoclassical transport'. *Plasma physics and controlled fusion* 41.9 (1999), p. 1135.

[115] CD Beidler, Y Feng, J Geiger, F Köchl, H Maßberg, NB Marushchenko, C Nührenberg, HM Smith and Y Turkin. '(Expected difficulties with) density-profile control in W7-X high-performance plasmas'. *Plasma Physics and Controlled Fusion* 60.10 (2018), p. 105008.

[116] Matt Landreman and Darin R Ernst. 'New velocity-space discretization for continuum kinetic calculations and Fokker–Planck collisions'. *Journal of Computational Physics* 243 (2013), pp. 130–150.

[117] Alessandro Di Siena, A Bañón Navarro and Frank Jenko. 'Turbulence suppression by energetic particle effects in modern optimized stellarators'. *Physical Review Letters* 125.10 (2020), p. 105002.

[118] N Bonanomi, P Mantica, A Di Siena, E Delabie, C Giroud, Thomas Johnson, E Lerche, S Menmuir, M Tsalas, D Van Eester et al. 'Turbulent transport stabilization by ICRH minority fast ions in low rotating JET ILW L-mode plasmas'. *Nuclear Fusion* 58.5 (2018), p. 056025.

[119] A Di Siena, T Görler, H Doerk, E Poli and R Bilato. 'Fast-ion stabilization of tokamak plasma turbulence'. *Nuclear Fusion* 58.5 (2018), p. 054002.

[120] A Di Siena, T Görler, E Poli, R Bilato, H Doerk and A Zocco. 'Resonant interaction of energetic ions with bulk-ion plasma micro-turbulence'. *Physics of Plasmas* 26.5 (2019).

[121] Denis Jarema, Hans-Joachim Bungartz, Tobias Görler, Frank Jenko, Tobias Neckel and Daniel Told. 'Block-structured grids in full velocity space for Eulerian gyrokinetic simulations'. *Computer Physics Communications* 215 (2017), pp. 49–62.

[122] A Bañón Navarro, GT Roberg-Clark, GG Plunk, D Fernando, A Di Siena, F Wilms and F Jenko. 'Assessing global ion thermal confinement in critical-gradient-optimized stellarators'. *arXiv preprint arXiv:2310.18705* (2023).

[123] Kai Germaschewski, Bryce Allen, Tilman Dannert, Markus Hrywniak, John Donaghy, Gabriele Merlo, Stephane Ethier, Ed D'Azevedo, Frank Jenko and Amitava Bhattacharjee. 'Toward exascale whole-device modeling of fusion devices: Porting the GENE gyrokinetic microturbulence code to GPU'. *Physics of Plasmas* 28.6 (2021).